

Computational Modeling of Photonic Crystal Microcavity Single-Photon Emitters

Submitted in partial fulfillment of the requirements for
the degree of
Doctor of Philosophy
in
Electrical and Computer Engineering

Nicole A. Saulnier

B.S., Electrical and Computer Engineering, Carnegie Mellon University
M.S., Electrical and Computer Engineering, Carnegie Mellon University

Carnegie Mellon University
Pittsburgh, PA

May 2011

Acknowledgments

This research was supported in part by the National Science Foundation through the Graduate Research Fellowship and through TeraGrid resources provided by the Pittsburgh Supercomputing Center

Thesis Committee:

Elias Towe, Chair

T.E. Schlesinger

Lisa Porter

David Lambeth

Abstract

Conventional cryptography is based on algorithms that are mathematically complex and difficult to solve, such as factoring large numbers. The advent of a quantum computer would render these schemes useless. As scientists work to develop a quantum computer, cryptographers are developing new schemes for unconditionally secure cryptography. Quantum key distribution has emerged as one of the potential replacements of classical cryptography. It relies on the fact that measurement of a quantum bit changes the state of the bit and undetected eavesdropping is impossible. Single polarized photons can be used as the quantum bits, such that a quantum system would in some ways mirror the classical communication scheme. The quantum key distribution system would include components that create, transmit and detect single polarized photons.

The focus of this work is on the development of an efficient single-photon source. This source is comprised of a single quantum dot inside of a photonic crystal microcavity. To better understand the physics behind the device, a computational model is developed. The model uses Finite-Difference Time-Domain methods to analyze the electromagnetic field distribution in photonic crystal microcavities. It uses an 8-band $k \cdot p$ perturbation theory to compute the energy band structure of the epitaxially grown quantum dots. We discuss a method that combines the results of these two calculations for determining the spontaneous emission lifetime of a quantum dot in bulk material or in a microcavity. The computational models developed in this thesis are used to identify and characterize microcavities for potential use in a single-photon source. The computational tools developed are also used to investigate novel photonic crystal microcavities that incorporate 1D distributed Bragg reflectors for vertical confinement. It is found that the spontaneous emission enhancement in the quasi-3D cavities can be significantly greater than in traditional suspended slab cavities.

Contents

List of Tables	vii
List of Figures	viii
1 Introduction	1
1.1 Overview of Single-photon Sources	5
1.1.1 The Role of Optical Cavities	6
1.2 Novel Microcavity Design and Computational Model Development	12
1.3 Overview of this Thesis	15
2 Methodology	21
2.1 Overview of physical models	21
2.2 Spontaneous Emission Rates in Quantum Dots	24
2.3 Optical simulations: the Finite-Difference Time-Domain Method	29
2.3.1 The Perfectly Matched Layer	32
2.3.2 Band Diagrams	36
2.3.3 FDTD for Photonic Crystal Microcavity Analysis	43
2.3.4 Spontaneous Emission Enhancement	44
3 Quantum Dot Modeling and Spontaneous Emission Lifetimes	51
3.1 Quantum Dot Modeling Using Nextnano++	53

3.2	Material Parameters	61
3.3	Pyramidal Quantum Dots	68
3.4	Calculation of the Spontaneous Emission Lifetime	73
3.5	Summary	82
4	Quasi-3D Photonic Crystal Microcavities	87
4.1	2D Photonic Crystal Slab Microcavities	88
4.2	1D Distributed Bragg Reflection Microcavities	101
4.3	Quasi-3D Photonic Crystal Band Diagrams	103
4.4	Hybrid Photonic Crystal Microcavities	110
5	Photonic Crystal Microcavity Single-Photon Emitter	127
5.1	Mode Identification and Cavity Analysis	130
5.2	Spontaneous Emission Lifetimes	143
5.3	Fabrication Non-idealities	150
6	Summary and Recommendation for Future Work	163
6.1	General Conclusions	163
6.2	Recommendation for Future Work	166
.1	Transition Rates with Time-Dependent Perturbation Theory	168

List of Tables

- 3.1 Material Parameters 63
- 3.2 Influence of Variation of Material Parameters 65
- 3.3 Spontaneous Emission Lifetimes 79

- 4.1 Examination of Extraction Efficiency Calculations 120

- 5.1 Spontaneous Emission Lifetimes in Various L3 Cavities 145
- 5.2 Extraction Efficiency from L3 Microcavity 148

List of Figures

1.1	Quantum Key Distribution Setup	4
1.2	Distributed Bragg Reflector	7
1.3	One Dimensional Microcavities	8
1.4	Higher Dimension Photonic Crystals	9
1.5	2D Photonic Crystal Slab Microcavity	10
1.6	Photonic Crystal Laser and Single Photon Source	13
1.7	Electrical Injection - Coulomb Blockade	14
2.1	Microcavity Component Parameters	22
2.2	Computational Model Flowchart	24
2.3	Three dimensional Yee grid	30
2.4	2D Square Lattice Unit Cell in Real and Reciprocal Space	37
2.5	Square Lattice Photonic Band Diagram	38
2.6	Triangular Lattice Unit Cells	38
2.7	Triangular Lattice Band Diagram	41
2.8	Effect of Blackman Window	41
2.9	Modes in a 2D Photonic Crystal Slab Microcavity	44
2.10	Spontaneous Emission Enhancement from a Dipole in a Planar Metal Cavity	46
3.1	Piezoelectric Charging in Quantum Dots	58
3.2	Pyramidal Quantum Dot	62

3.3	Electron and Hole Energies in Pyramidal Quantum Dots	64
3.4	Effect of Parameters on 8×8 $k \cdot p$ Calculations	66
3.5	Wavefunctions for 101 Faceted Quantum Dots	67
3.6	Energy States and Transitions in Pyramidal Quantum Dots	68
3.7	Ground State Emission Wavelengths in Pyramidal Quantum Dots	69
3.8	Energy States and Transitions in Small Pyramidal Quantum Dots	70
3.9	Wavefunctions for $b = 14\text{nm}$, 20nm , and 28.6nm Quantum Dots	71
3.10	Wavefunctions for $b = 10\text{nm}$, $h = 6\text{nm}$ and 3nm Quantum Dots	72
3.11	L3 Microcavity Geometry and Photonic Band Diagram	77
3.12	L3 Microcavity Mode Frequencies and Profiles	79
3.13	Relative Spontaneous Emission Rates for a L3 Cavity	80
3.14	Spontaneous Emission Lifetimes	81
4.1	2D Photonic Crystal Lattices	88
4.2	2D Triangular Lattice Band Diagram	89
4.3	Effect of Changing Dielectric Constant or Hole Radius on Band Gap for Triangular Lattice	90
4.4	2D Photonic Crystal Slab	91
4.5	2D Triangular Slab Band Diagram	92
4.6	Effect of Slab Thickness on Bandgap Size	94
4.7	2D PC Slab with Single Defect - Dipole Modes	94
4.8	Change in Dipole Mode Frequency and Quality Factor	95
4.9	Spontaneous Emission of Centered Ex-polarized Dipole	97
4.10	Spontaneous Emission of Centered Ez-polarized Dipole	97
4.11	Spontaneous Emission as Function of Location in Cavity	98
4.12	Spontaneous Emission Rates and Extraction Efficiency for Varied Rows of Holes	99

4.13 Spontaneous Emission Rate and Extraction Efficiency for Varied Slab Thickness	100
4.14 DBR and Its Projected Band Diagram	101
4.15 Omnidirectional Reflection from a DBR	102
4.16 DBR Cavity Mode Frequencies	103
4.17 Quasi-3D Photonic Crystal	104
4.18 Quasi-3D Photonic Crystal Band Diagrams	105
4.19 Light Line in Quasi-3D Photonic Crystal	106
4.20 DBR TE Modes in Quasi-3D Photonic Crystal	107
4.21 Quasi-3D Photonic Crystal Band Diagrams	109
4.22 Quasi-3D Microcavities	111
4.23 Quasi-3D Microcavity Mode Frequencies	111
4.24 Quality Factor for Various Microcavities	113
4.25 Quality Factor for Various Hole Depths	114
4.26 Field Leakage in Microcavity with DBR Below	114
4.27 a) The spontaneous emission rate for the cavities of Fig. 4.22 for 3, 5 or 7 holes. b) The extraction efficiency for the cavities of Fig. 4.22 for 3, 5 or 7 holes.	115
4.28 Magnitude of Wavevector Along Brollouin Zone for y-dipole Mode	117
4.29 Spontaneous Emission Rate and Extraction Efficiency for Varied Hole Depth	118
4.30 Spontaneous Emission Rate and Extraction Efficiency for Top DBR Periods	119
4.31 Mode Frequencies for Quasi-3D Cavity	120
4.32 Radiation Rates for Slab and Quasi-3D Cavity	121
4.33 Dipole Mode Frequencies on Band Diagram	122
4.34 Magnitude of Wavevector Along Brollouin Zone for x-dipole Mode	123
5.1 Band Diagram for Quasi-3D Photonic Crystal	130

5.2	Single Defect Cavity With Side Hole Perturbation	131
5.3	Dipole Mode Profile and Field Pattern	132
5.4	Single Defect Cavity With Reduced Hole Radii	133
5.5	Mode Frequencies in a Single Defect Cavity With Reduced Inner Hole Radii	134
5.6	Mode Profiles and Field Vectors for Cavity With Reduced Inner Hole Radii	135
5.7	L3 Microcavity Geometry	136
5.8	Mode Frequencies in a L3 Microcavity	137
5.9	L3 Cavity Mode Profile and Field Pattern	138
5.10	Mode Frequencies in a L3 Microcavity for Shifted and Elongated Holes . .	139
5.11	Monopole Mode Electric Fields in Slab and Quasi-3D Cavities	140
5.12	Reciprocal Space Representation of Monopole Mode	142
5.13	Radiation Rates in L3 Microcavity with Elongated Holes	143
5.14	Radiation Rates in Quasi-3D L3 Microcavity with Elongated Holes	145
5.15	Spontaneous Emission Lifetime in L3 Microcavities vs. Lattice Constant .	147
5.16	Radiation Rate and Extraction Efficiency vs. Number Of Top DBR Periods for L3 Cavity	149
5.17	Radiation Rate and Extraction Efficiency vs. Number Of Bottom DBR Periods for L3 Cavity	150
5.18	Spontaneous Emission Lifetime in L3 Microcavities vs. Lattice Constant .	152
5.19	Reciprocal Space Representation of Monopole Mode	153
5.20	Radiation Rates with Dipoles at Maximum Field Locations	155
5.21	Radiation Rates for x, y, z Dipoles in a L3 Cavity	156
5.22	Spontaneous Emission Lifetime as a Function of Quantum Dot Location . .	158
5.23	Spontaneous Emission Lifetime Along 2 Planes	159

Chapter 1

Introduction

Accurate modeling of a single-photon source is a complex and important problem. A particularly promising single-photon source is made by placing a quantum dot inside of a microcavity. Quantum dots have discrete energy levels and are often thought of as artificial atoms. In small dots, there is only one state in the conduction band for the electron to occupy and one state in the valence band for the hole to occupy; therefore a single generation-recombination event can be isolated. The result of the recombination of one electron with one hole is a single photon. Because there are no photons to induce a transition, the photon will be emitted spontaneously. The field from an emitted photon must occupy an allowed electromagnetic mode and in free space there is an infinite number of modes. A microcavity can be used to tailor the number of modes available to the emitted photon, providing the necessary control over the photon polarization and direction.

Modeling of a quantum dot in a microcavity may at first appear to be straightforward. It is tempting to consider the single-photon source as a limiting case of a traditional semiconductor laser and to apply the extensive laser design tool kit to develop this source. But lasers and single-photon sources operate on distinctly different principles. Specifically, lasers rely primarily on stimulated emission and single-photon sources on spontaneous emission. Another flaw of this approach is that traditional laser modeling ignores individual

electrons and photons in favor of considering their populations. How a single excited electron in a quantum dot recombines spontaneously to emit a single photon into the microcavity cannot be deduced from traditional modeling methods. The quantum dot and microcavity form a coupled system and their interaction must be taken into account. To tackle this problem, principles from electromagnetics, solid state physics, and quantum mechanics must be combined. A complete set of modeling tools to analyze quantum dots in microcavities has not yet been developed. The primary goal of this thesis is to develop a tool set to model and optimize such a single-photon source.

Single-photon sources are necessary for implementing quantum key distribution systems. Quantum-based cryptography is superior to classical cryptography because it remains secure even after a quantum computer is developed. Cryptographers commonly refer to this as an unconditionally secure system. Classical cryptography methods are only secure under the assumption that sufficiently long keys can not be cracked with modern computing resources. While this is certainly true today, many of the cryptography schemes could be cracked easily with a quantum computer. These cryptography systems are thus only conditionally secure. In the future, quantum cryptography will be essential for secure communication.

Quantum cryptography was developed by Bennett and Brassard [1]. It is based on the laws of quantum mechanics and, according to these laws, any test to determine information about a non-orthogonal quantum state will perturb that state. A set of quantum states can be constructed from single photons of various polarizations. Imagine a photon with polarization axis α that encounters a filter oriented at an angle β with respect to the photon polarization. If the polarization axis aligns with the filter then the photon will always pass through. If the axes are perpendicular then the photon will always be absorbed. When α and β are neither parallel nor perpendicular to one another, the photon behaves probabilistically. A photon will be transmitted through the filter with probability $\cos^2(\alpha - \beta)$ and will be absorbed with probability $\sin^2(\alpha - \beta)$. Placing a filter in the path of

the photon and monitoring what happens corresponds to making a measurement on a quantum state (in this case the polarization of the photon). The photons that happen to pass through the filter are now in a new state with polarization β . All information about the photon polarization, α , prior to passing through the filter is lost. This is due to the uncertainty principle which guarantees that measurement of a photon can only reveal one bit about the polarization.

The state of a single polarized photon can be described by a two dimensional space. This means that if we choose two orthonormal vectors, say $v_{r1} = (1, 0)$ and $v_{r2} = (0, 1)$ we can express any polarization as a linear combination of these two vectors $v = a*v_{r1} + b*v_{r2}$. This is called the rectilinear basis, where v_{r1} is the horizontal polarization and v_{r2} is the vertical polarization. Another basis, called the diagonal basis can also be defined. The two basis vectors, $v_{d1} = (0.707, 0.707)$ and $v_{d2} = (-0.707, 0.707)$, correspond to a polarization angle of 45° and 135° respectively. These two bases have a special relationship to one another. Because they are offset by 45° , a vector originally prepared in one of the bases will have equal projections onto the basis vectors of the other basis. As a result, a photon prepared with polarization along an axis in one basis will behave randomly when subjected to a measurement in the other basis. This means that the rectilinear and diagonal bases are conjugates.

To illustrate the quantum key distribution protocol, we will follow the steps that two people, commonly referred to as Alice and Bob, take to communicate securely. Alice will choose either the rectilinear or diagonal basis for each single photon she sends to Bob. She will also choose whether to encode a 1 or a 0, which corresponds to polarization along one of the unit vectors in the chosen basis. When Bob receives a single photon, he must guess which basis Alice used and make the corresponding measurement. If he guesses correctly he knows with certainty if Alice sent a 1 or a 0. If he guesses incorrectly then he has a 50% chance of measuring either a 1 or a 0 owing to the fact that the two bases are conjugates. After Alice has sent Bob all of the photons she reveals which basis she used for each single

photon. Bob will only keep the data points corresponding to photons that he measured in the correct basis. Using the classical channel, they will check a subset of these data points to make sure that Bob measured the same value that Alice sent. If their data do not correlate, then an eavesdropper, commonly called Eve, made measurements on the single photons before they reached Bob. After Eve’s measurement, the photons are no longer in their original state. The result of Bob’s measurements on these photons will not match the polarizations that Alice used, and Eve is detected. If Alice and Bob agree on most of the data points they compare, they can be sure that the key is secure and use it to encode future messages. This is referred to as the BB84 protocol for quantum cryptography. The general setup is outlined in Fig. 1.1.

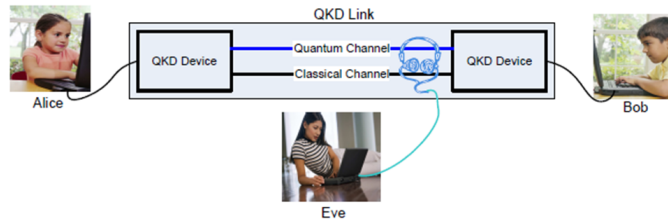


Figure 1.1: Quantum Key Distribution Setup: Image taken from [2]

Photon transmission through optical fibers has been studied extensively, but creating and detecting single photons with specific polarizations remains a difficult task. True single-photon sources are necessary because any multi-photon transmission compromises the security of the system by allowing Eve to listen in undetected. To counter attacks that can result from non-ideal single-photon sources, decoy pulses were demonstrated experimentally in [3]. Other groups have proposed changing the BB84 protocol [4] or adjusting the components used for single photon emission and detection [5, 6, 7]. But the advent of a perfect single-photon source would eliminate the need for many of these adjustments to the BB84 protocol. This would greatly simplify the implementation of quantum cryptography in current networks.

1.1 Overview of Single-photon Sources

The ideal single-photon source should generate single photons on demand, be electrically driven, and control the photon polarization. When a single photon is desired a single electron should recombine with a hole to emit a photon. If the electron and hole are injected electrically, the device will be more easily integrated into systems and will be less bulky than an optically driven alternative. This section describes various single-photon sources that were initially demonstrated in the literature. These single-photon emission schemes all fall short of the design requirements for a single-photon source that could be used in a real quantum cryptography system. The following sections will illustrate the advantages of using a single quantum-dot inside of a photonic-crystal microcavity in order to meet the design requirements.

Many groups are currently working to develop a single-photon source that can be used for quantum key distribution. The earliest work demonstrated single photon emission from single atoms [8] or ions [9] in traps. Single molecules [10] and single quantum dots [11] also released single photons. Quantum dots are more stable over long periods of time and have the potential of being incorporated into devices. Atoms, ions, or molecules are more challenging to isolate and require complex setups that are better suited for laboratory research than real world applications. The major drawback of all these single-photon sources is that they are optically pumped. Additional problems include limited speed, poor photon collection efficiency and no polarization control.

To demonstrate an electrically driven single-photon source, Yuan *et al.* [12] proposed a pin diode with a quantum-dot active layer. A metal aperture was used to select only one dot for emission. The device demonstrated the ability to electrically drive single photon emitters but did not efficiently couple the photons to the outside. To improve the directionality of the emitted photons, other groups placed a distributed Bragg reflector (DBR) below the quantum dot layer using a metal aperture [13] or an oxide aperture [14]

to select a single quantum dot. Although the collection efficiency was improved, these devices still do not provide any control over the photon polarization.

1.1.1 The Role of Optical Cavities

In traditional optical devices, such as lasers, the photon polarization is controlled by stimulated emission and the emitted photons have the same polarization and direction as the inducing photon. Microcavities are used in single-photon sources instead of stimulated emission to control the properties of the spontaneously emitted photon. In a microcavity, only certain field profiles are allowed, each corresponding to a particular mode. Unlike free space where all frequencies have corresponding modes, many frequencies in a cavity will have no associated mode. For example, in a simple one-dimensional cavity of length d , the modes exist only at discrete frequencies corresponding to $\nu_r = mc/2dn$ where c is the speed of light in vacuum, n is the index of refraction of the cavity medium and $m = 1, 2, \dots$ is an integer. Because the polarization of the photon is that of its mode, by controlling which modes exist in the microcavity one can control the photon polarization.

An optical cavity traps light between reflective surfaces. Reflection occurs at an interface between two materials with different indices of refraction. When light is incident from a medium of high refractive index to one of lower refractive index, total internal reflection of the electromagnetic field is possible. For this to occur the incident angle of the incoming field, θ_I must be larger than a critical angle θ_C . This special case is known as total internal reflection (TIR). Light can also be reflected from a distributed Bragg reflector (DBR) which is a multilayer stack of materials with alternating refractive indices as indicated in Fig. 1.2. The thickness of the layers is on the order of the wavelength of light to be reflected. Reflection from a DBR can be thought of in two different ways. One way is to consider the sum of the reflections and refractions of a propagating plane wave at each interface. Another way is to consider the periodicity of the structure. Any wave

that propagates through the DBR must be periodic. Because of the two different dielectric materials in the unit cell, all wavelengths will no longer be periodic and those that are not will be prevented from traveling through the DBR.

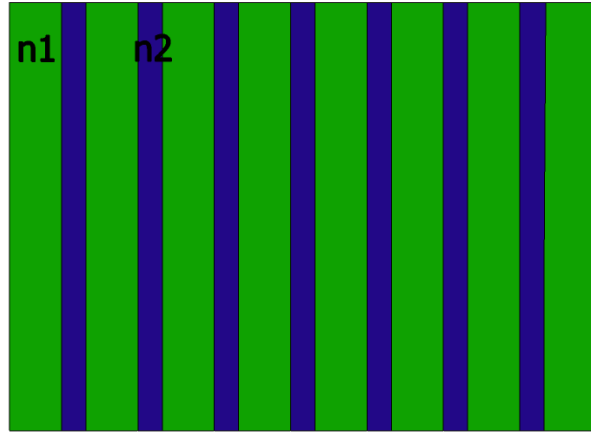


Figure 1.2: Distributed Bragg reflector, periodic dielectric structure in one dimension.

The reflectivity of a DBR is not only wavelength dependent but is highly dependent on the characteristics of the DBR as well. Changes in the number of periods, the indices of refraction or the material thicknesses will affect the reflectivity profile. Thus with proper design, it is possible to create a DBR to reflect almost any wavelength range with any reflectivity. For maximum reflection the thicknesses are typically chosen as a quarter wavelength, $\lambda_n/4$.

By placing two reflective surfaces parallel to but at some distance from one another, an optical cavity is formed. Light originating from within the cavity will remain there for some finite time before leaking out to the surrounding medium. The amount of time the light is trapped depends on the surface reflectivity, the orientation of the reflecting surfaces, and the absorption loss in the material separating the mirrors. These simple two-surface cavities are one-dimensional systems and are constructed by using the principle of either total internal reflection or distributed Bragg reflection for the mirrors. Figure 1.3 shows the cavities corresponding to each type of reflection. It is possible to confine light in two or

even all three dimensions. When the high index material of Fig. 1.3(a) is reduced to a finite thickness in one (two) additional direction(s), light is confined in two (three) dimensions by total internal reflection. Using distributed Bragg reflection for two and three dimensional cavities is not as straightforward.

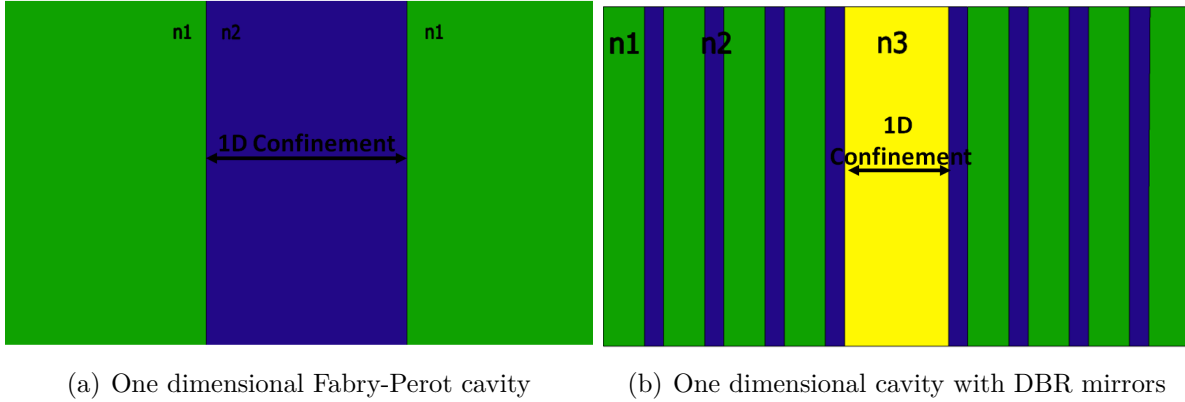
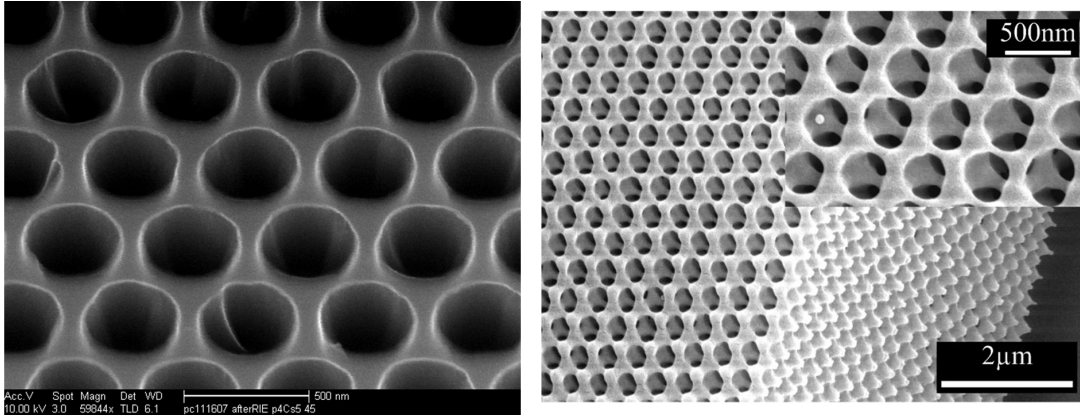


Figure 1.3: Two types of one dimensional cavities

A DBR is essentially a periodic arrangement of materials of different dielectric constants in one dimension. To obtain reflectivity in more than one direction requires a two or three dimensional periodic arrangement of the materials. Some common periodicities for 2D and 3D are shown in Fig. 1.4. Structures with periodic arrangements of dielectric constants on the order of the wavelength of light in 1, 2 or 3D are referred to as photonic crystals. Photonic crystals were first introduced by Yablonovitch who proposed that a complete photonic band gap would exist for a properly designed 3D photonic crystal [15]. The range of wavelengths which are prohibited from traveling through a periodic structure is referred to as the band gap. Much of the terminology used to describe photonic crystals is borrowed from solid state physics. The periodic refractive index is the photon equivalent of the periodic potential experienced by electrons traveling through a solid state crystal.

To create a two or three dimensional cavity using distributed Bragg reflection, 2D or 3D photonic crystals are used. A cavity is formed by a defect in the perfect periodic crystal. Light emitted into a photonic crystal cavity will be confined if the wavelength corresponds



(a) 2D Photonic Crystal

(b) 3D Photonic Crystal [16]

Figure 1.4: 1.4(a) two dimensional photonic crystal, periodic in two dimensions only. 1.4(b) three dimensional photonic crystal, periodic in all three dimensions.

to a frequency within the photonic band gap of the bulk photonic crystal.

More complicated cavities can be formed by combining both total internal reflection and distributed Bragg reflection to create quasi-3D cavities. One such cavity is formed by placing a defect in a 2D photonic crystal slab. This forms a quasi-3D cavity where the dielectric periodicity confines light in-plane and total internal reflection (TIR) is responsible for vertical confinement as shown in Fig. 1.5. The cavity modes of a 2D photonic crystal slab microcavity are more complicated than those of a rectangular cavity because any defect to the perfect periodic structure forms a microcavity. Slightly decreasing the size of one hole will pull up a state from the lower band (dielectric band) of the gap. Increasing the size of one hole will first bring one state down from the upper band (air band). As the radius is increased further a series of higher order modes will enter the band gap. The ability to precisely control the number of modes in the cavity as well as the frequencies at which the modes appear is one of the most remarkable things about photonic crystal cavities.

The cavity also enhances the rate of spontaneous emission which will lead to faster emission of a photon. When a microcavity is used in a single-photon source, the operating speed of the device should increase. The spontaneous emission rate is inversely

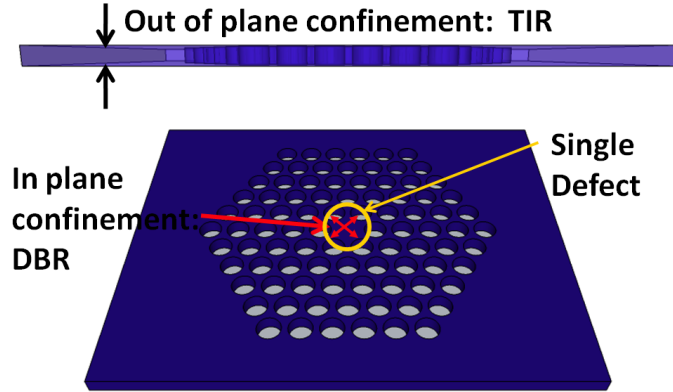


Figure 1.5: 2D Photonic Crystal Slab Microcavity

proportional to the spontaneous emission lifetime, τ_{spont} , which is a measure of how long an electron remains in its excited state before spontaneously emitting a photon. The amount of spontaneous emission enhancement is proportional to the ratio of the density of modes in the cavity to the density in free space. The density of modes is the number of modes per unit frequency range. In free space this is given by the following equation

$$\rho_o(\omega) = \frac{2\omega^2 V}{\pi c^3} \quad (1.1)$$

where ω is frequency, V is volume, and c is the speed of light [17].

For microcavities the density of modes is cavity specific. In photonic crystal microcavities, the density of modes falls to 0 inside the photonic band gap except at mode frequencies there the density is represented by a Dirac delta function. At the mode frequencies the density of modes is higher than in free space and spontaneous emission enhancement occurs. For all other frequencies in the photonic band gap, the photonic crystal microcavity exhibits spontaneous emission suppression because the density of modes is significantly reduced from the free space density.

An exact expression for the spontaneous emission enhancement can be derived by taking

the ratio of the spontaneous transition rate in a cavity to the rate in bulk material. In bulk material the spontaneous transition rate can be written as

$$W_{if}^{bulk} = \frac{4n\omega^3}{3\hbar c^3} |d_{fi}|^2 \quad (1.2)$$

where d_{fi} is the transition matrix element and n is the index of refraction of the bulk material. In a microcavity the transition rate is

$$W_{if}^{cavity} = \frac{4}{\hbar^2 \Delta\omega} |d_{fi}|^2 (\alpha E_{max})^2 \quad (1.3)$$

where α is the normalization factor of the fields given by

$$\alpha^2 = \frac{2\pi\hbar\omega_{fi}}{\int \epsilon(r) E^2(r) d^3r} \quad (1.4)$$

Derivation of the bulk and cavity spontaneous emission rates can be found in Appendix.1. Introducing the cavity quality factor $Q = \omega_{fi}/\Delta\omega$ and the mode volume [17]

$$V_{eff} = \frac{\int \epsilon(r) E^2(r) d^3r}{(\epsilon(r) E^2(r))_{max}} \quad (1.5)$$

and taking the ratio of equations (1.3) and (1.2), one obtains the following equation for the spontaneous emission enhancement

$$F_p = \frac{3}{4\pi^2} \left(\frac{\lambda}{n}\right)^3 \frac{Q}{V_m} \quad (1.6)$$

This result is commonly referred to as the 'Purcell' spontaneous emission enhancement factor. It is the amount of enhancement or suppression of the spontaneous emission rate due to the modified density of modes in a microcavity.

Purcell noted that the radiation rate for a radio frequency oscillator was modified when

connected to a resonant circuit. The difference was quantified by equation (1.6). At radio frequencies, the cavities are quite large and so the effects are difficult to observe. As microelectronic processing techniques improved, it was possible to make smaller and smaller cavities and thus to see this effect in a more pronounced way. Small cavities designed for optical wavelengths are extremely common today. A photonic crystal microcavity, for example, typically has a cavity diameter of approximately $1\mu m$. Refer to the 2D photonic crystal of Fig. 1.4(a) and imagine removing one hole. In these structures the Purcell effect is observed due to the relatively high quality factor and the small mode volume.

1.2 Novel Microcavity Design and Computational Model Development

Introducing a microcavity as part of a single-photon source would control the photon polarization and lead to faster operating speeds. To take advantage of these benefits, several groups have experimentally demonstrated microcavity single-photon sources. Specifically, quantum dots in microring resonators [18], micropillar cavities [19] and photonic crystal cavities [20] have been presented. The major disadvantage of these devices is that they are optically pumped with a pulsed laser source. There is little chance that an electrical connection could be made to either the micropillar or the microring resonator without disturbing the optical properties of the cavity. Although making an electrical connection to a photonic crystal cavity is also challenging, an electrically driven photonic crystal laser [21] demonstrated that it is possible to electrically pump these structures. This laser, shown in Fig. 1.6(a), consists of a 2D photonic crystal slab suspended in air with a quantum well active region. A central conducting post delivered holes to the gain region and a conducting metal pad circled the photonic crystal to inject electrons into the device. With an optimized post and cavity design, Park *et al.* [21] showed that the post did not degrade

the optical cavity quality. This device was not optimized for single photon emission, but it represents a significant step toward, demonstrating the feasibility of an electrically driven microcavity single-photon source.

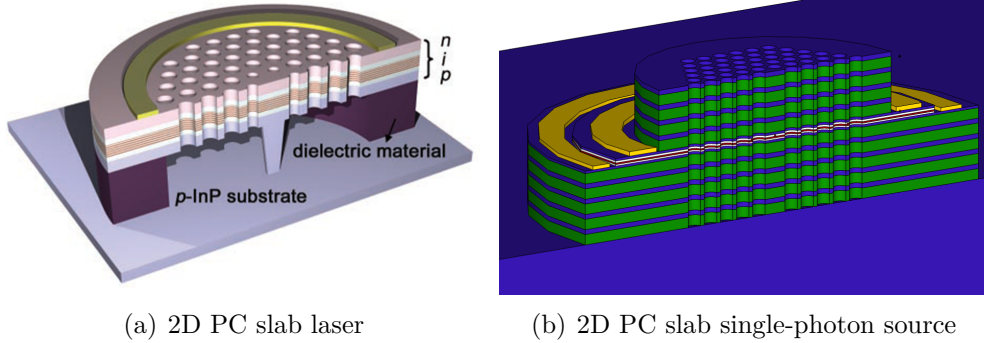


Figure 1.6: 1.6(a) The electrically driven single defect 2D photonic crystal laser presented by Park *et al.* [21]. 1.6(b) Proposed quantum dot photonic crystal microcavity single-photon source.

Although a significant research effort has been devoted to experimental studies of single-photon sources, not much theoretical work has been presented. The focus of this research is to address the theoretical side of the problem by modeling a single quantum dot in a photonic crystal microcavity. The specific device structure, shown in Fig. 1.6(b), is a modified version of the photonic crystal laser proposed by Park *et al.* [21]. To achieve single-photon emission, the quantum well layer would be replaced by a sparse quantum-dot layer. The quantum dots must be sparse enough that there is a high probability that only one quantum dot would be located inside of the photonic crystal microcavity, ensuring single photon operation. Instead of the simple 2D photonic crystal slab microcavity of Fig. 1.6(a), the microcavity of Fig. 1.6(b) combines a 2D photonic crystal for in-plane confinement with a distributed Bragg reflector (DBR) for vertical confinement. Whereas total internal reflection is a naturally occurring phenomenon, the reflection from a DBR can be almost fully controlled. This additional level of control gives the hybrid-microcavity an advantage over the photonic crystal slab suspended in air.

The single-photon source of Fig. 1.6(b) could be electrically pumped by controlling

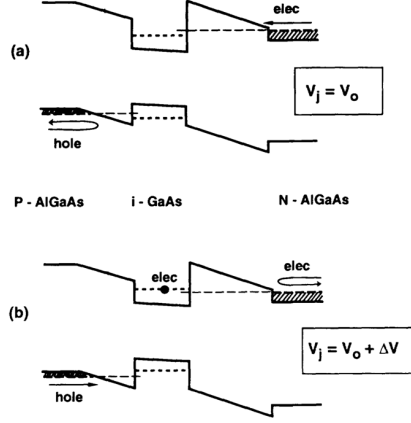


Figure 1.7: The energy-band diagram of the pin AlGaAs-GaAs heterojunction with (a) and without (b) the applied voltage pulse. For $V_j = V_0$ ($V_j = V_0 + \Delta V$), the Fermi energy of the n (p) type AlGaAs layer is at least $e^2/2C_{ni}$ ($e^2/2C_{ni}$) higher (lower) than the energy of the quantum-dot electron (hole) subband. Image taken from [22].

the injection of electrons and holes into the quantum dot. One method that has been demonstrated, is an AlGaAs/GaAs pin device with either a quantum well or quantum dot located in the intrinsic region [22]. In this structure, the intrinsic region acts as a barrier to carriers that otherwise would occupy one of the lower discrete energy levels of the conduction band in the quantum dot. If the voltage across the pin junction $V(t)$ is less than the built-in potential, V_{bi} , the carriers can only enter the quantum dot by resonant tunneling. The conditions for resonant tunneling are given by

$$\begin{aligned} E_{fn} - e^2/2C_{ni} &\geq E_{res,e} \geq E_{nc} - e^2/2C_{ni} \\ E_{fp} + e^2/2C_{pi} &\leq E_{res,h} \leq E_{pv} + e^2/2C_{pi} \end{aligned} \quad (1.7)$$

where $E_{res,e}$ and $E_{res,h}$ are the energies of the electron and hole subbands, E_{nc} and E_{pv} are the energy of the conduction and valence band in the n/p-type AlGaAs, C_{ni} and C_{pi} are the capacitances between the dot and the n/p-type AlGaAs, and E_{fn} and E_{fp} are the Fermi levels in the n/p-type AlGaAs. The Fermi energy of the n-type(p-type) AlGaAs must be at least $e^2/2C_{ni}$ higher(lower) than the energy of the quantum dot electron(hole) subband for electron(hole) tunneling to occur. This is represented pictorially in Fig. 1.7.

To inject a single electron-hole pair into the quantum dot the following process will take place. At an applied voltage, $V(t_1) = V_o$, an electron will tunnel into the quantum dot. The presence of the electron changes the capacitance and the condition for resonant tunneling of an electron is no longer satisfied. Additional electrons will not enter the quantum dot. This is referred to as the Coulomb blockade. The voltage is then changed to $V(t_2) = V_o + \Delta V$. Now a hole will tunnel into the quantum dot and again the Coulomb blockade prevents additional holes from entering the quantum dot. The electron and hole will recombine spontaneously to emit a photon. By using this method to pump the photonic crystal microcavity single-photon source of Fig. 1.6(b), the device will meet all of the requirements of a single-photon source.

1.3 Overview of this Thesis

A promising single-photon source for quantum cryptography is composed of a single quantum dot inside a photonic crystal microcavity because it can be electrically driven and emits photons of a designed polarization on demand. A detailed understanding of the device operation is essential for achieving high performance.

This thesis focuses on using computational modeling techniques to study this single-photon source and to reach a set of optimal device parameters. There are two key modeling tools: finite-difference time-domain techniques for modeling the optical properties of the device, and electronic band structure calculations using $k \cdot p$ perturbation theory to include the effects of strain on the energy bands. In Chapter 2, the finite-difference time-domain techniques are discussed in detail using brief illustrative examples. This chapter also provides an outline of the theoretical equations used to model the interaction between the quantum dot and the photonic crystal microcavity which is described by the spontaneous emission rate. Discussion of $k \cdot p$ perturbation theory and the specifics of the spontaneous emission lifetime calculation are saved for Chapter 3. Here, the active medium of the de-

vice, the InAs quantum dot, will be examined in detail. The numerical methods used to calculate the energy levels and wavefunctions in the quantum dot through $k \cdot p$ perturbation theory will be discussed first. A set of general trends will then be established to assist in determining the proper quantum dot size during the design process. Here we will also examine how changes in the quantum dot size change the energy bands and subsequently the wavelength of the emitted photon. Finally this chapter introduces a method to calculate the actual spontaneous emission lifetime of the system. The theoretical results are compared to experimentally available data to prove the accuracy of the method.

The following chapters focus on how the computational model is used to design an optimal single-photon source. Chapter 4 discusses light confinement in three dimensions. The Chapter begins with an overview of microcavities in 2D photonic crystals and distributed Bragg reflectors. Cavities that consist of a 2D photonic crystal slab suspended in air will then be compared with cavities that use DBRs for vertical confinement. Studies of the mode frequencies, mode profiles, cavity quality factors and radiation rates will be presented. 3D finite-difference time-domain photonic band structure calculations are also used to compare various quasi-3D cavities. Chapter 5 combines the knowledge of quasi-3D microcavity design with the quantum dot photon emission trends to analyze an optimal single-photon source. The Chapter begins with an examination of the cavity modes that arise in candidate cavities. A summary of the performance will be given including: band diagrams, mode frequencies and profiles, and key lifetimes. The most promising of the microcavities will be examined further to investigate the affect of fabrication non-idealities on the spontaneous emission lifetime. The final chapter of this thesis contains concluding remarks and suggestions for future investigation.

Chapter 2

Methodology

2.1 Overview of physical models

The single-photon source introduced in Chapter 1 utilizes a quasi-3D photonic crystal microcavity to control the emission of a photon from a single quantum dot. The effect of the microcavity is twofold. First, the number of modes is suppressed so that only a few modes exist within the photonic bandgap, each having their own corresponding resonant field distribution. Second, the spontaneous emission lifetime, or the time that the electron remains excited, is perturbed. When a cavity mode lies at the electron transition frequency there is an enhancement in the emission and the lifetime becomes shorter. Conversely when there is no mode at the transition frequency then the electron remains in the excited state longer than it would in the absence of the cavity. After the photon is emitted from the quantum dot, it will remain in the cavity for some amount of time. This time is referred to as the photon lifetime. A long photon lifetime will limit the operating speed of the device because the photon must leave the cavity before another excitation emission cycle occurs. In general, it is expected that the hybrid-photonic crystal microcavity will have a higher quality factor and larger Purcell factor due to the increased confinement in the vertical direction. As a result, the spontaneous emission lifetime should decrease and the photon

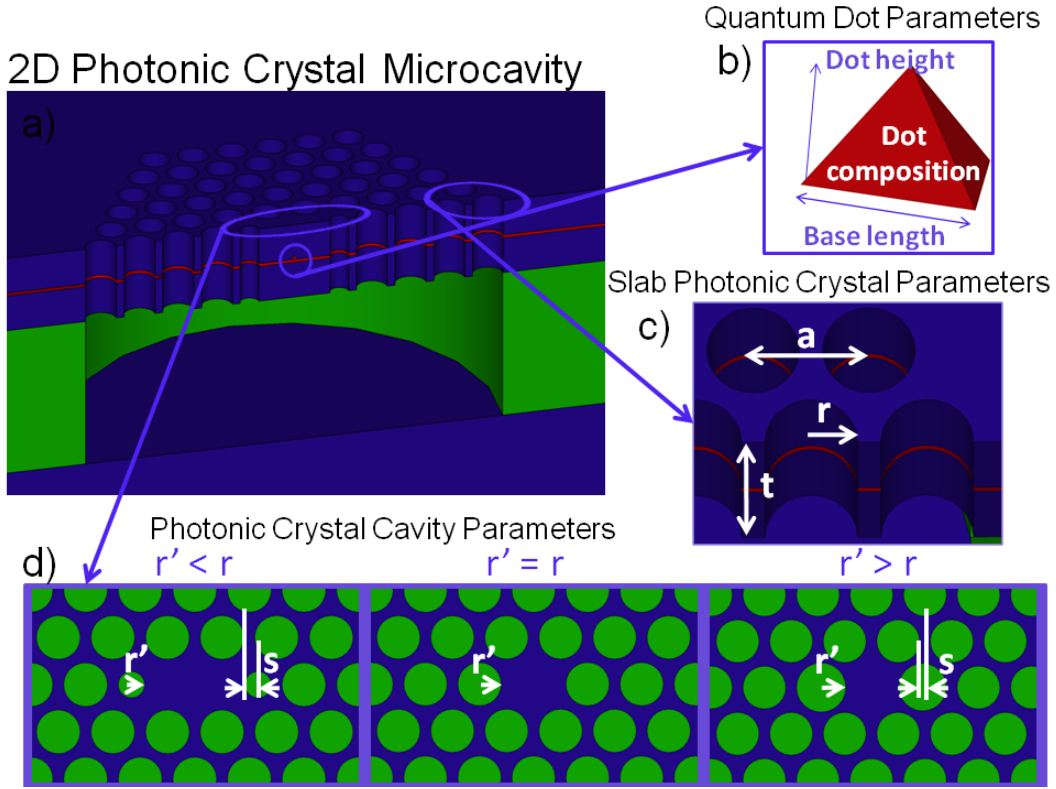


Figure 2.1: Illustrative view of the relevant components and parameters for a quantum dot photonic crystal microcavity single photon source. a) A basic single photon emitter. b) The quantum dot's parameters are the dot height, size, and composition. c) The 2D photonic crystal's parameters are the lattice constant, a , the hole radius, r , and the slab thickness, t . d) The photonic crystal cavity parameters depend on the geometry of the defect. Here a single hole is removed and two neighboring holes are perturbed to break the mode degeneracy.

lifetime increase.

Before fabricating such a complex device, it is imperative that an accurate computational model be developed to optimize the key parameters. In order to predict how the device will operate, it is necessary to determine the electron transition frequency, the cavity mode frequencies, the mode profiles, the spontaneous emission lifetime and the photon lifetime. The device performance depends on several parameters that describe the quantum dot and the microcavity. For example, the dot-size and material system determine the energy level spacings and subsequently the electron transition frequency. As explained in Chapter 3, the quantum dot parameters also affect the electron wavefunctions which are

used to compute the spontaneous emission lifetime. For the photonic crystal, the lattice constant, a , the hole radius, r , and the slab thickness, t , determine where the photonic bandgap will lie. The cavity mode frequencies and the mode profiles then depend on these parameters as well as the type of defect that forms the microcavity. Because the spontaneous emission lifetime is a function of the density of photon modes available in the microcavity, this lifetime is also affected by the photonic crystal parameters and the defect. A summary of the key parameters is shown in Fig. 2.1.

The complete model devised for this thesis is divided into two parts. The first is for the design of a quantum dot and photonic crystal microcavity to operate at a user defined frequency. The energy levels and wavefunctions for the quantum dot are found for a particular dot material and size by using $k \cdot p$ perturbation theory. Then the photonic crystal and the microcavity are designed using Finite-Difference Time-Domain methods to ensure that a mode occurs at the quantum dot electron transition frequency. After this basic microcavity is designed, the DBRs can be added. For the DBRs, the important parameters are the number of periods for the top and bottom mirror as well as the layer indices of refraction and thicknesses. The bottom mirror will likely be over 99% reflective at the operating frequency of the device to prevent photons from traveling back toward the substrate. Because photons will exit the device from the top, the top DBR will have a lower reflectivity, likely between 0% and 50%. The second part of the model assesses how well the device functions by computing the key lifetimes and mode profiles. If the device does not meet the desired goals, then the microcavity can be redesigned and the functionality reassessed. A flowchart for the computational model is shown in Fig. 2.2.

It is obvious that some parts of the design process allows for the quantum dot and the photonic crystal microcavity to be considered separately, however their interaction is a key advantage of using this structure as a single photon source. Calculation of the spontaneous emission lifetime of an electron in the quantum dot photonic crystal microcavity system is thus the main feature of the computational model. Due to the importance of this

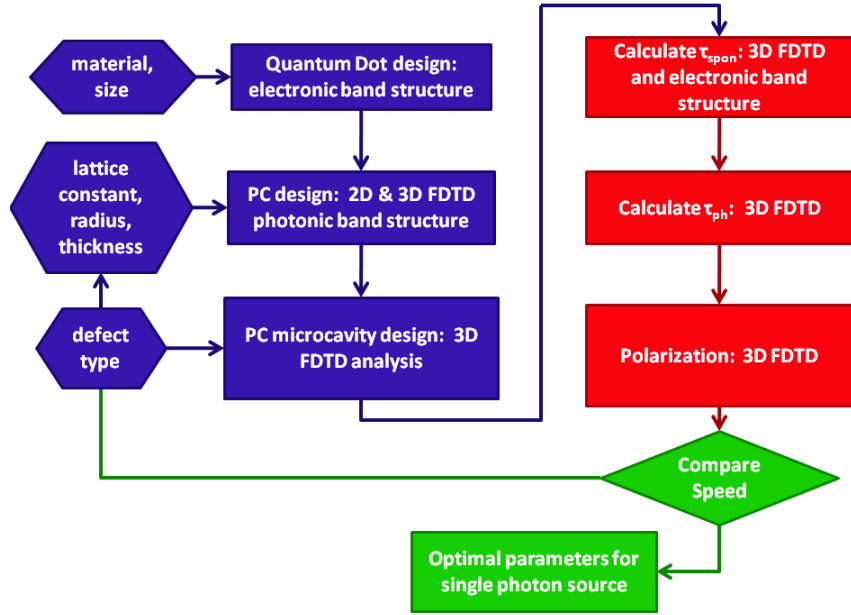


Figure 2.2: Computational Model Flowchart - the left hand side contains the input parameters, the middle the design portions of the model and the right hand side has the analysis tools.

calculation, the details will be discussed in Chapter 3 where the modeling of the quantum dot will also be covered. The general equations for spontaneous emission rates are discussed briefly in this Chapter to provide a frame of reference for the radiation rate calculations. The focus of this Chapter, however, is on the computational modeling methods that are used for the photonic crystal microcavity. This discussion includes an overview of the Finite-Difference Time-Domain method which is used in the design and characterization process.

2.2 Spontaneous Emission Rates in Quantum Dots

Time-dependent perturbation theory is used to determine the transition rates for an atomic electron in the presence of electromagnetic radiation. Assuming that the Hamiltonian will

vary harmonically, the key equation that results is Fermi's golden rule, given by

$$W_{i \rightarrow f} = \int \Gamma_{if} \rho(E_f) dE_f = \frac{2\pi}{\hbar} |\langle \Phi_f | \hat{H}'(t) | \Phi_i \rangle|^2 \rho(E_f) |_{E_f = E_i + \hbar\omega} \quad (2.1)$$

with

$$\Gamma_{if} = \frac{2\pi}{\hbar} |\langle \Phi_f | \hat{H}'(t) | \Phi_i \rangle|^2 \delta(E_f - E_i + \hbar\omega). \quad (2.2)$$

Here $W_{i \rightarrow f}$ is the transition rate from some initial state Φ_i to some final state Φ_f , E_f and E_i are the final and initial energies of the electron respectively, $\rho(E_f)$ is the density of final electron states, $\hat{H}'(t)$ is the time varying perturbation that results from the electromagnetic radiation, and ω is the angular frequency of the electromagnetic field. The difference between these two equations is that equation (2.2) is the transition rate for one specific transition and equation (2.1) is the transition rate from an initial state to a continuum of final states. To obtain equation (2.1), Γ_{if} is integrated over the number of final states that fall within the energy interval $E_f \rightarrow E_f + dE_f$ which is equivalent to $\rho(E_f)dE_f$.

Fermi's Golden Rule is a general equation used to obtain transition rates for either absorption or emission of photons. In our case we are concerned with the spontaneous emission of a photon from a quantum dot in a microcavity. The remainder of this section will focus on how equation (2.1) must be tailored for this situation. Specifically, the electron is initially in one of the discrete energy levels of the quantum dot and the field is in a photonic state with 0 photons. These form a coupled system that can be expressed as $|\Phi_i\rangle = |\psi_i\rangle |0\rangle$. After some time, the electron recombines with a hole and a photon is emitted. The coupled quantum dot/microcavity system is then in state $|\Phi_f\rangle = |\psi_f\rangle |1\rangle$ with 1 photon. The transition occurs as a result of the time varying Hamiltonian $\hat{H}'(t)$ which is given by

$$\hat{H}'(t) = \frac{q}{2m_e} \vec{A}(\vec{r}, t) \cdot \vec{P}, \quad (2.3)$$

where $\vec{A}(\vec{r}, t)$ is the magnetic vector potential of the electromagnetic field, \vec{P} is the mo-

momentum operator, m_e is the mass of the electron, q is the charge on the electron and c is the speed of light. The magnetic vector potential can be thought of classically or quantum mechanically. Because the classical treatment does not account for spontaneous transitions, the quantum mechanical treatment must be used and the electromagnetic field must be quantized. Derivation of equation (2.1) and other supplemental information pertinent to this section are given in Appendix .1.

Quantization of the electromagnetic field results in the following equation for the perturbation operator for photon emission

$$\hat{H}'(t) = \sum_k \sum_\lambda \sqrt{\frac{\hbar}{2\omega_k V \epsilon}} \frac{q}{m_e} a_{\lambda k}^\dagger e^{-i\vec{k}\cdot\vec{r}} \epsilon_{\lambda}^* \cdot \vec{P} e^{i\omega_k t} \quad (2.4)$$

where ω_k is the angular frequency of the radiation, V is the volume of the field, \vec{k} is the wavevector of the radiation, ϵ is the dielectric constant, ϵ_{λ} are two polarization unit vectors in the plane perpendicular to \vec{k} , and $a_{\lambda k}^\dagger$ is the quantum mechanical raising operator. Substituting (2.4) and the initial and final states into (2.2), the equation for the spontaneous transition rate that results in a photon of wavenumber \vec{k} and polarization λ becomes

$$\Gamma_{i \rightarrow f}^{spon} = \frac{\pi q^2}{m_e^2 \omega_k V \epsilon} |\langle \psi_f | e^{-i\vec{k}\cdot\vec{r}} \epsilon_{\lambda}^* \cdot \vec{P} | \psi_i \rangle|^2 \delta(E_f - E_i + \hbar\omega_k). \quad (2.5)$$

The dipole approximation is typically used to simplify equation (2.5) and $e^{-i\vec{k}\cdot\vec{r}} \approx 1 \pm i\vec{k}\cdot\vec{r} - \frac{1}{2}(\vec{k}\cdot\vec{r})^2 \mp \dots \approx 1$. This approximation is reasonable because the term $\vec{k}\cdot\vec{r}$ and all higher order terms will be much smaller than 1 owing to the fact that the wavelength of the radiation is much larger than the size of the quantum dot. To determine the total spontaneous transition rate, Γ_{if}^{spon} must be integrated over the density of final states. Because the quantum dot has discrete energy levels the density of the final electron states is a delta function. The spontaneous transition rate will then only depend on the integration of Γ_{if} over the density of the final photonic states. The spontaneous emission rate is given

by

$$W_{i \rightarrow f}^{spon} = \int \Gamma_{if}^{spon} \rho_C(\omega) d\omega = \frac{\pi}{\hbar \epsilon} | -q \langle \psi_f | \vec{r} | \psi_i \rangle |^2 \rho_C(\omega_{if}). \quad (2.6)$$

In this equation

$$\vec{d}_{fi} = -q \langle \psi_f | \vec{r} | \psi_i \rangle \quad (2.7)$$

is the dipole matrix element and $\rho_C(\omega_{if})$ is the photon density of modes in the microcavity evaluated at the electron transition frequency ω_{if} . Direct solution of the density of photon modes in a cavity is somewhat tricky as will be discussed in Section 2.3.4. An easier approach will be taken in Chapter 3, where it will be shown that the rate can be found from a combination of the spontaneous emission rate in bulk and the FDTD radiation rate calculations. The FDTD calculations essentially determine the change in radiation rates of an emitter in a specific cavity geometry relative to the bulk rate. This change in radiation rate is ultimately a result of a change in the density of photon modes and Eq. 2.6 is still a valid description of the calculation.

Equation 2.6 can not be solved without first calculating the initial and final wavefunctions, ψ_i and ψ_f and subsequently the dipole matrix element, \vec{d}_{fi} . The energy levels involved in the transition are also required so that the photon frequency can be determined. These quantities all depend on the quantum dot size, geometry and material system. The quantum dots proposed for the single-photon source would be grown by molecular beam epitaxy (MBE) and formed through the Stranski-Krastanov growth process. A likely material system for the single-photon source would be GaAs with InAs quantum dots because the quantum dots can be designed to emit light at the important telecommunications wavelength of $1.3\mu m$. To form the quantum dots, a few monolayers of InAs are deposited on top of GaAs. There is a lattice mismatch between these two materials and the layers are subsequently strained. After the amount of the InAs deposited reaches a critical thickness, the strain is relaxed by the formation of small islands, or quantum dots. Although the strain is relaxed from the 2D growth case, a significant amount of strain remains in quan-

tum dots grown by MBE. This will have a profound impact on the energy levels and the wavefunctions in the quantum dot and can not be ignored in favor of simplified approaches that consider only the 3D confinement potential.

The energy levels and wavefunctions are determined through an 8×8 $k \cdot p$ perturbation theory at the beginning of the single photon device design process so that the frequency corresponding to the transition can be used to design the photonic crystal microcavity. By using 8×8 $k \cdot p$ perturbation theory, the strain is easily accounted for. The wavefunctions for the ground state and the excited state are substituted into equation (2.7) to find the dipole matrix element.

The spontaneous emission lifetime can be found from the spontaneous transition rate through the simple calculation

$$\tau_{spont} = \frac{1}{W_{i \rightarrow f}} \quad (2.8)$$

The difficulty in finding τ_{spont} then lies in determining the dipole matrix element from equation (2.7) and the relative radiation rates from the FDTD calculations. Because the actual energy levels, wavefunctions and dipole matrix element of the quantum dot will be used to calculate the transition rates, absolute lifetimes will be found for the quantum dot microcavity system. Most researchers currently just compute the relative change in lifetimes as a result of a particular microcavity. They are essentially de-coupling the quantum dot microcavity system for computational ease. To understand how a single-photon source operates, simple calculations of the Purcell factor do not suffice and models of the actual lifetimes of the device are needed.

2.3 Optical simulations: the Finite-Difference Time-Domain Method

Simulations based on the Finite-Difference Time-Domain (FDTD) method provide valuable information about the behavior of electromagnetic fields in the presence of various dielectric structures. These simulations are often used to show field propagation with time as in the case of mode propagation in a waveguide. The FDTD method is also useful for simulations of optical cavities where information about the mode frequencies, profile, cavity quality factor Q , and radiation rate is easily collected. Additionally, it is possible to use the FDTD method to solve for the band structure of photonic crystals. The following discussion provides a brief overview of the techniques used in the application of the FDTD method to these problems. We will begin with a discussion of how Maxwell's equations are converted to a form that can be implemented in a computer code.

The FDTD method solves Maxwell's equations,

$$\nabla \times H = \epsilon \frac{\partial E}{\partial t} \quad (2.9)$$

$$\nabla \times E = -\mu \frac{\partial H}{\partial t} \quad (2.10)$$

directly by approximating the temporal and spatial derivatives with central differences on a discretized grid. In our simulations we use the method of Yee [1] to discretize the problem space as shown in Fig. 2.3. Here the electric and magnetic fields are interleaved in space and time and a leap-frog approach is used to update the fields. Using the method of Yee, the FDTD equations can be solved for one, two or three dimensional problems based on the requirements of the simulation. Although 2D and 3D applications are used to obtain the results in this thesis, we only consider the 3D case here as it is the most general.

Examination of Maxwell's equations reveals that (2.9) and (2.10) can be separated into

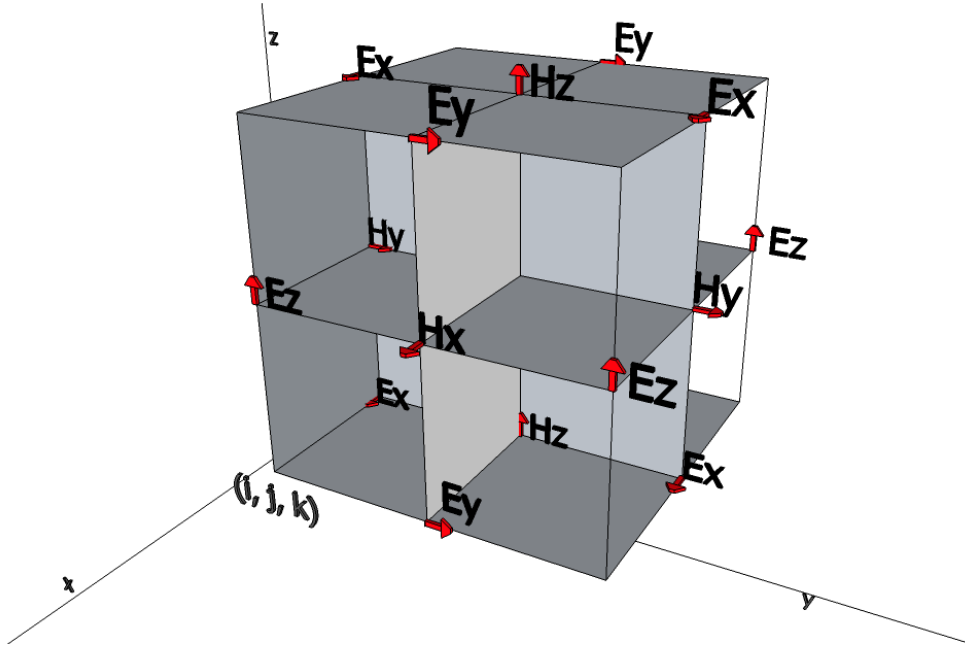


Figure 2.3: Yee Grid

6 equations describing the time variation of the x, y, and z components of the electric and magnetic fields. These equations are

$$\frac{\partial H_z}{\partial y} - \frac{\partial H_y}{\partial z} = \epsilon(r) \frac{\partial E_x}{\partial t} \quad (2.11)$$

$$\frac{\partial H_x}{\partial z} - \frac{\partial H_z}{\partial x} = \epsilon(r) \frac{\partial E_y}{\partial t} \quad (2.12)$$

$$\frac{\partial H_y}{\partial x} - \frac{\partial H_x}{\partial y} = \epsilon(r) \frac{\partial E_z}{\partial t} \quad (2.13)$$

$$\frac{\partial E_z}{\partial y} - \frac{\partial E_y}{\partial z} = -\mu \frac{\partial H_x}{\partial t} \quad (2.14)$$

$$\frac{\partial E_x}{\partial z} - \frac{\partial E_z}{\partial x} = -\mu \frac{\partial H_y}{\partial t} \quad (2.15)$$

$$\frac{\partial E_y}{\partial x} - \frac{\partial E_x}{\partial y} = -\mu \frac{\partial H_z}{\partial t} \quad (2.16)$$

Central difference approximations are then used for the spatial and time derivatives in

these equations. The difference approximations for time derivatives of the electric and magnetic fields are written as

$$\frac{\partial E}{\partial t} = \frac{E^{n+1/2} - E^{n-1/2}}{\Delta t} \quad (2.17)$$

$$\frac{\partial H}{\partial t} = \frac{H^{n+1} - H^n}{\Delta t}. \quad (2.18)$$

The spatial derivatives are different for each field component but follow directly from the Yee grid. As an example we can write

$$\frac{\partial E_y}{\partial x} = \frac{E_y^{n+1/2}(i+1, j+1/2, k) - E_y^{n+1/2}(i, j+1/2, k)}{\Delta x} \quad (2.19)$$

$$\frac{\partial H_y}{\partial x} = \frac{H_y^n(i+1/2, j, k+1/2) - H_y^n(i-1/2, j, k+1/2)}{\Delta x} \quad (2.20)$$

The variable n is an integer used as a time index and $n\Delta t$ corresponds to some time in seconds. The variables i, j, k are integers used to index the fields in the x, y, z direction respectively so that $i\Delta x$ corresponds to some distance along the x direction. For most cases it is convenient to choose $\Delta x = \Delta y = \Delta z$ and that is done here. Applying the central difference approximations to equations (2.11) to (2.16) we obtain the following equations that are used to update the electric and magnetic field components

$$E_x^{n+1/2}(i+1/2, j, k) = E_x^{n-1/2}(i+1/2, j, k) + \frac{\Delta t}{\epsilon(r)\Delta x} [H_z^n(i+1/2, j+1/2, k) - H_z^n(i+1/2, j-1/2, k) + H_y^n(i+1/2, j, k-1/2) - H_y^n(i+1/2, j, k+1/2)] \quad (2.21)$$

$$E_y^{n+1/2}(i, j+1/2, k) = E_y^{n-1/2}(i, j+1/2, k) + \frac{\Delta t}{\epsilon(r)\Delta x} [H_x^n(i, j+1/2, k+1/2) - H_x^n(i, j+1/2, k-1/2) + H_z^n(i-1/2, j+1/2, k) - H_z^n(i+1/2, j+1/2, k)] \quad (2.22)$$

$$E_z^{n+1/2}(i, j, k+1/2) = E_z^{n-1/2}(i, j, k+1/2) + \frac{\Delta t}{\epsilon(r)\Delta x} [H_y^n(i+1/2, j, k+1/2) - H_y^n(i-1/2, j, k+1/2) + H_x^n(i, j-1/2, k+1/2) - H_x^n(i, j+1/2, k+1/2)] \quad (2.23)$$

$$\begin{aligned}
H_x^{n+1}(i, j + 1/2, k + 1/2) &= H_x^n(i, j + 1/2, k + 1/2) + \frac{\Delta t}{\mu \Delta x} [E_y^{n+1/2}(i, j + 1/2, k + 1) \\
&\quad - E_y^{n+1/2}(i, j + 1/2, k) + E_z^{n+1/2}(i, j, k + 1/2) - E_z^{n+1/2}(i, j + 1, k + 1/2)]
\end{aligned} \tag{2.24}$$

$$\begin{aligned}
H_y^{n+1}(i + 1/2, j, k + 1/2) &= H_y^n(i + 1/2, j, k + 1/2) + \frac{\Delta t}{\mu \Delta x} [E_z^{n+1/2}(i + 1, j, k + 1/2) \\
&\quad - E_z^{n+1/2}(i, j, k + 1/2) + E_x^{n+1/2}(i + 1/2, j, k) - E_x^{n+1/2}(i + 1/2, j, k + 1)]
\end{aligned} \tag{2.25}$$

$$\begin{aligned}
H_z^{n+1}(i + 1/2, j + 1/2, k) &= H_z^n(i + 1/2, j + 1/2, k) + \frac{\Delta t}{\mu \Delta x} [E_x^{n+1/2}(i + 1/2, j + 1, k) \\
&\quad - E_x^{n+1/2}(i + 1/2, j, k) + E_y^{n+1/2}(i, j + 1/2, k) - E_y^{n+1/2}(i + 1, j + 1/2, k)]
\end{aligned} \tag{2.26}$$

These equations are easily implemented in a programming language such as C.

Since most interesting situations occur in a medium of inhomogeneous dielectric constant, $\epsilon(r)$, it is necessary that the FDTD method be applicable when the dielectric constant varies across the simulation space. The FDTD method obeys the basic boundary conditions for electromagnetic fields at the interface of two materials of different dielectric constants. It is thus valid to set ϵ_r at every grid point in the simulation space to correspond with the structure of interest and then apply the normal FDTD field update equations.

Finite-difference time-domain simulations also require various sources depending on the application. All of the simulations described in this thesis use a hard source. When a hard source is used, one of the fields is set to the value of a desired input signal at each time step. Hard sources can be specified for a single point, a line, or a plane. They typically have a Gaussian and/or sinusoidal profile. The details of the input excitation required for each calculation will be discussed below.

2.3.1 The Perfectly Matched Layer

One of the most straightforward applications of the basic FDTD method just described is the variation of the electromagnetic fields with time. This class of simulations for example can show light traveling down a waveguide, light reflecting off of the interface between two

materials of different dielectric constants, or the profile of an optical cavity mode. In all of these cases it is necessary to simulate an unbounded problem in some finite computational domain. When the electromagnetic fields reach the outer boundary of the simulation space, they will be totally reflected. These reflected waves will propagate back into the region of interest making the results difficult to decipher. One solution is to make the problem space so large that the fields do not reach the outer boundary during the time of simulation. Since the field update equations are solved for each grid point at each time step adding additional grid points to the simulation outside of the structure of interest has a negative effect on both the computation time and storage. Instead it is wise to use a boundary condition at the edge of the simulation space that absorbs outgoing waves.

Many absorbing boundary conditions have been proposed, but the most popular method was introduced by Berenger [2]. The Berenger Perfectly Matched Layer (PML) splits the electric and magnetic fields into parallel and perpendicular components. By varying the electric conductivity and the magnetic loss in the split field equations around the boundary of the problem space, waves propagate into the PML with little reflection and are attenuated. The advantage of the PML is that it affectively absorbs waves of any frequency and any incident angle. The major drawback of the Berenger PML is the unnatural field splitting at the boundaries which requires the use of different field update equations in these regions. While the Berenger PML is a mathematical model based on a non-physical medium, if such physical absorbing medium were to exist it must be anisotropic. Sacks used the idea of this anisotropic material to create the uniaxial PML (UPML) [3]. In these simulations we implement the UPML because unlike the PML it allows the traditional field update equations to be computed across the entire problem space. The coefficients used for the field updates are constant except for in the boundary regions.

To implement the UPML, Maxwell's equations 2.9 and 2.10 are modified and are shown

in 2.27 and 2.28.

$$\nabla \times H = j\omega\epsilon \begin{bmatrix} \frac{s_y s_z}{s_x} & 0 & 0 \\ 0 & \frac{s_x s_z}{s_y} & 0 \\ 0 & 0 & \frac{s_x s_y}{s_z} \end{bmatrix} E \quad (2.27)$$

$$\nabla \times E = -j\omega\mu \begin{bmatrix} \frac{s_y s_z}{s_x} & 0 & 0 \\ 0 & \frac{s_x s_z}{s_y} & 0 \\ 0 & 0 & \frac{s_x s_y}{s_z} \end{bmatrix} H \quad (2.28)$$

with

$$s_x = \kappa_x + \frac{\sigma_x}{j\omega\epsilon_0}, \quad s_y = \kappa_y + \frac{\sigma_y}{j\omega\epsilon_0}, \quad s_z = \kappa_z + \frac{\sigma_z}{j\omega\epsilon_0} \quad (2.29)$$

Here κ_i , $i = x, y, z$, determines the absorption and σ_i the loss. In the interior of the problem space $\kappa_i = 1$ and $\sigma_i = 0$ and equations (2.27) and (2.28) reduce to the original Maxwell's equations (2.9) and (2.10). The premise of the UPML is that the values for κ_i and σ_i vary slowly at the edge of the UPML and the interior of the problem space. Accordingly, we use a polynomial grading for these parameters that increases with depth into the UPML so that

$$\sigma_x(x) = (x/d)^m \sigma_{x,max}, \quad \kappa_x(x) = 1 + (\kappa_{x,max} - 1)(x/d)^m \quad (2.30)$$

where

$$\sigma_{x,max} = -\frac{(m+1) \ln[R(0)]}{2\eta d} \quad (2.31)$$

and m is the degree of the polynomial usually 3 or 4, η is the impedance, d is the thickness of the UPML, and x is the distance into the UPML. Typically the UPML is between 10 and 20 computational cells thick. $R(0)$ is the desired reflection error at normal incidence to the UPML. Through a series of numerical experiments, the optimal value for a $d = 10$ cell layer UPML is $R(0) = e^{-16}$. The variable $\kappa_{x,max}$ in equation (2.30) is the maximum attenuation coefficient which is a number less than or equal to 1. Note that η is taken as the impedance of free space regardless of the dielectric profile of the problem space. This is necessary to

maintain field continuity within the UPML but does not require that the dielectric constant be 1 within the boundary region of the simulation. The dielectric profile is instead specified by the $\epsilon(r)$ of equation (2.27) and can be separated from the UPML parameters.

Equations (2.27) and (2.28) are difficult to discretize as given. The process is simplified by introduction of the electric and magnetic flux, D and B , respectively. We define these variables as

$$D_x = \epsilon(r) \frac{s_z}{s_x} E_x, \quad D_y = \epsilon(r) \frac{s_x}{s_y} E_y, \quad D_z = \epsilon(r) \frac{s_y}{s_z} E_z \quad (2.32)$$

$$B_x = \mu \frac{s_z}{s_x} H_x, \quad B_y = \mu \frac{s_x}{s_y} H_y, \quad B_z = \mu \frac{s_y}{s_z} H_z \quad (2.33)$$

The equations for the electric and magnetic fields then become

$$\begin{bmatrix} \frac{\partial H_z}{\partial y} - \frac{\partial H_y}{\partial z} \\ \frac{\partial H_x}{\partial z} - \frac{\partial H_z}{\partial x} \\ \frac{\partial H_y}{\partial x} - \frac{\partial H_x}{\partial y} \end{bmatrix} = j\omega \begin{bmatrix} s_y & 0 & 0 \\ 0 & s_z & 0 \\ 0 & 0 & s_x \end{bmatrix} \begin{bmatrix} D_x \\ D_y \\ D_z \end{bmatrix} \quad (2.34)$$

$$\begin{bmatrix} \frac{\partial E_z}{\partial y} - \frac{\partial E_y}{\partial z} \\ \frac{\partial E_x}{\partial z} - \frac{\partial E_z}{\partial x} \\ \frac{\partial E_y}{\partial x} - \frac{\partial E_x}{\partial y} \end{bmatrix} = -j\omega \begin{bmatrix} s_y & 0 & 0 \\ 0 & s_z & 0 \\ 0 & 0 & s_x \end{bmatrix} \begin{bmatrix} B_x \\ B_y \\ B_z \end{bmatrix} \quad (2.35)$$

Equations (2.32) through (2.34) form a set of 12 equations that must be discretized and evolved in time to implement a 3D FDTD algorithm. First the electric fluxes $D_{x,y,z}$ are found from the magnetic fields $H_{x,y,z}$ using equation (2.34). Next the electric fields $E_{x,y,z}$ are found from the electric flux by equation (2.32). Then the magnetic fluxes $B_{x,y,z}$ are updated from the electric fields using equation (2.35). Finally the magnetic fields are found from the magnetic flux by equation (2.33). The 12 field update equations are discretized using the same procedure that was used to obtain equations (2.21) to (2.26) from equations (2.11) to (2.16). The discretized form of these equations is used in the 3D FDTD code.

2.3.2 Band Diagrams

The first application of the FDTD method that is used in the single photon source model is calculation of the band structure of a photonic crystal. In the model, these calculations are used to design a photonic crystal with a band gap centered around the electron transition frequency. Although our device is three dimensional, it is possible to use a 2D FDTD calculation to reduce computation time during the initial stages of the design process. Here, a finite slab thickness is represented by an effective refractive index. A single unit cell is discretized in 2 dimensions and is excited by a delta function in space and a wide frequency content Gaussian pulse in time. Monitor points are scattered throughout the unit cell to collect the time varying field data. It is important that neither the input excitation nor the monitor points are located at points of high symmetry as this could result in undetected modes. Periodic boundary conditions are used to ensure that fields leaving one side of the unit cell appear immediately on the other side multiplied by the appropriate phase factor. The boundary conditions for the E_z field are given as an example.

$$\begin{aligned} E_z|_{i=0} &= E_z|_{i=max} e^{j\vec{k}\cdot\vec{L}} \\ E_z|_{j=j_{max}+1} &= E_z|_{j=1} e^{-j\vec{k}\cdot\vec{L}} \end{aligned} \quad (2.36)$$

where \vec{L} is a real space vector with length a in this case and \vec{k} is a vector in reciprocal space pointing from the origin to a point along the outside of the irreducible Brillouin zone (see Fig. 2.4). The variable i is an index along the x direction and j an index along the y direction. The unit cell spans points 1 to $max + 1$.

Photonic band structure calculations are easily illustrated with a square lattice photonic crystal of dielectric cylinders in air with lattice constant $a = 574nm$. The real space lattice, the unit cell, and the reciprocal lattice with the irreducible Brillouin zone are shown in Fig. 2.4. The radius of the rods is $r = 0.2a = 114.8nm$ and the index of refraction is $n = 2.9833$. The simulations must be run multiple times. Each time the boundary conditions are

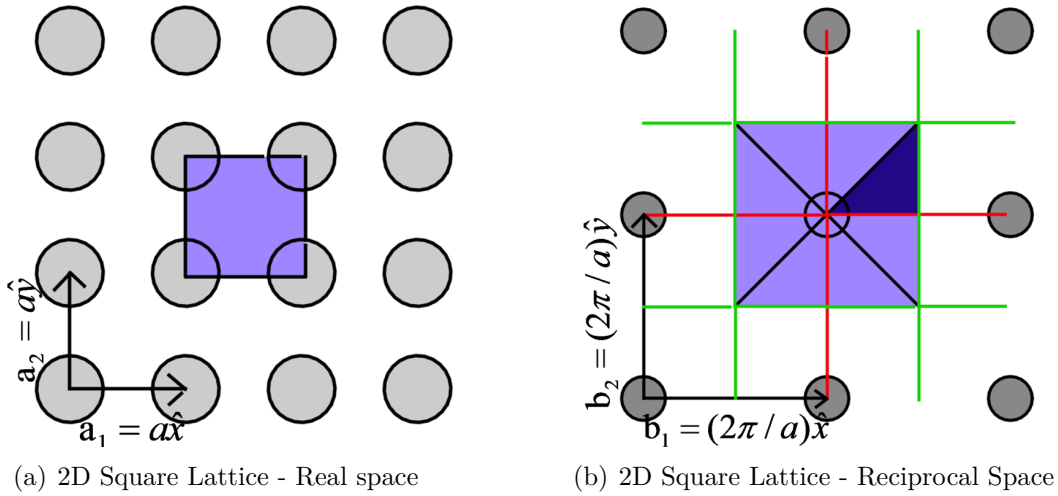


Figure 2.4: The square lattice photonic crystal with lattice constant a . 2.4(a) the real space lattice with the unit vectors a_1 and a_2 . The shaded region represents the unit cell of the square lattice. 2.4(b) the reciprocal lattice space. The Brillouin zone is shaded light blue and is found by taking the perpendicular bisector (green lines) of the lines connecting the origin and the nearest lattice points (orange lines). The dark blue region is the irreducible Brillouin zone.

adjusted to correspond to a different k vector. By taking the discrete Fourier transform (DFT) of the sampled field data it is possible to determine the supported modes for each k vector. Through a series of simulation runs with \vec{k} tracing the irreducible Brillouin zone edge, it is possible to construct the band diagram. The FDTD calculated band structure for the photonic crystal of Fig. 2.4 is shown in Fig. 2.5.

The photonic crystal structure proposed for the single-photon source is a triangular array of air holes in a dielectric slab sandwiched between two DBRs. In this case, a more accurate photonic band diagram will be required and a full 3D FDTD simulation must be implemented. Periodic boundary conditions are still used in the plane of the slab but UPML boundary conditions are used at the top and bottom of the mesh. To illustrate how band diagrams for 3D structures are found using the FDTD method, consider the following case: a triangular array of air holes in a dielectric slab of finite thickness.

Implementation of periodic boundary conditions for a triangular lattice is not as straightforward as for the square lattice. In order to make implementation of the boundary condi-

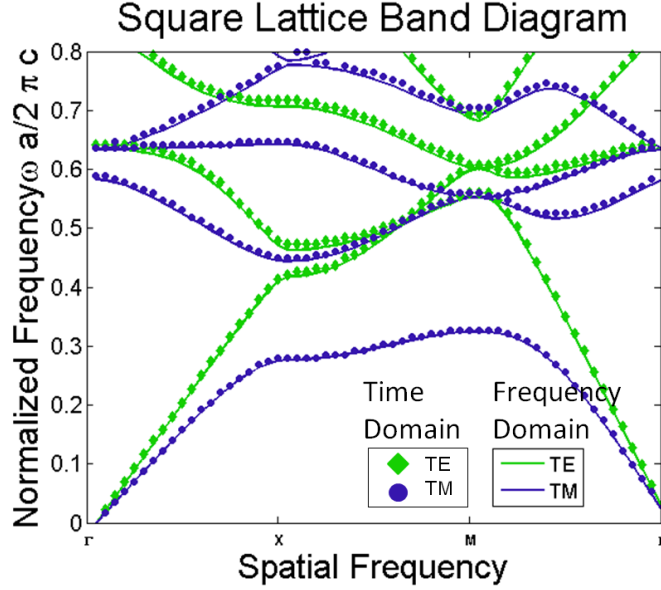


Figure 2.5: Band diagram for a square lattice photonic crystal. Data points, either dots or diamonds, were found using the 2D FDTD method. To verify the 2D FDTD implementation, the bands were also calculated using the MIT Photonic Bands software which is a planewave expansion program (frequency domain technique). These results, solid lines, agree well with the 2D FDTD bands.

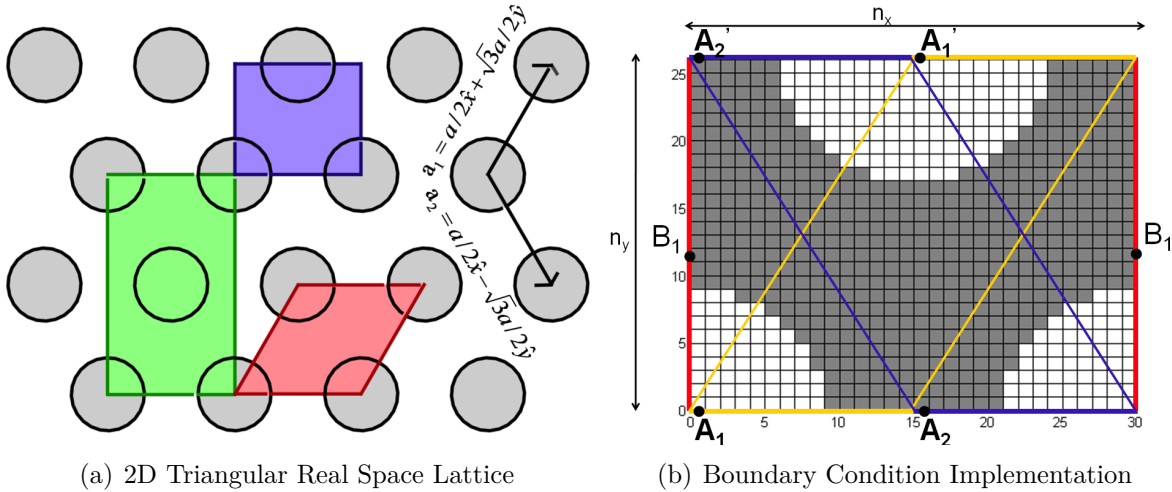


Figure 2.6: a) The real space triangular lattice with unit vectors a_1 and a_2 . Three possible unit cells for FDTD band structure calculations are shown. Red is the conventional rhombus unit cell. Green is a large rectangle resulting in folded bands. Blue is the single cell that is used in this thesis. b) Pictorial representation of the field mapping for the 2D triangular lattice photonic crystal with small rectangular single unit cell. Fields A and B are mapped to A' and B' .

tions easier, several unit cells have been used to tile the triangular lattice as shown in Fig. 2.6(a). The most obvious unit cell is a rhombus, but this requires copying field values along the non-linear sides of the cell [4]. Another proposed method is to use a large rectangular unit cell, shown in green in Fig. 2.6(a) [5]. This rectangle actually contains two unit cells and the true band diagram is difficult to separate from the folded version that results. Umenyi proposed using the unit cell shown in blue in Fig. 2.6(a) [6]. This unit cell has several advantages over the other two approaches. First, the fields are copied along the edges of the unit cell and no approximations along a slanted edge are necessary. Second, the boundary conditions are implemented over a true unit cell so that no bands are folded. The small rectangle also minimizes the simulation space which leads to less computational demand. This is particularly important for the 3D simulations. For the triangular lattice 3D FDTD band diagram simulations performed in this thesis, the single rectangular unit cell is used.

To see how the boundary conditions are implemented, consider first the 2D case as shown in Fig. 2.6(b). The Bloch boundary conditions along the y axis are implemented in two parts: first the fields along the bottom left half of the cell are translated by $a/2$ in x and $\sqrt{3}a/2$ in y (point $A1$ is mapped to $A1'$), then the fields in the second half of the cell are translated by $a/2$ in the negative x direction and $\sqrt{3}a/2$ in y (point $A2$ is mapped to $A2'$). In the x axis the Bloch boundary conditions translate the fields by a (point $B1$ is mapped to $B1'$). The boundary conditions can then be written as

$$A1' = A1 \times e^{(-i(k_x/2 + \sqrt{3}k_y/2)a)} \quad (2.37)$$

$$A2' = A2 \times e^{(-i(-k_x/2 + \sqrt{3}k_y/2)a)} \quad (2.38)$$

$$B1' = B1 \times e^{(-ik_x a)} \quad (2.39)$$

where k_x and k_y are reciprocal space vectors to some point along the edge of the irreducible

Brouillon zone. The reciprocal space unit cell and the Brouillon zone are shown in Fig. 2.7(a). For the triangular lattice, the rows of holes are separated from one another by $\sqrt{3}a/2$. In order to have an integer number of cells in both the x and y direction, Δx and Δy must be slightly different. To determine Δy we first set $\Delta x = a/n_x$, where n_x is the chosen number of cells in the x direction. Using Δx we can then determine a Δy that will tile the y direction in an integer number of cells n_y . This occurs when

$$\Delta y = a' / \lceil a' / \Delta x \rceil \quad (2.40)$$

where $a' = \sqrt{3}/2a\Delta x$ and $\lceil \rceil$ is the "ceil" function, which corresponds to rounding up to the next integer. The denominator of equation (2.40) is the smallest integer number of cells that could be used to tile the y direction, n_y . Δy is the absolute distance between rows, a' , divided by the number of cells in the y direction. For numerical stability Δt is automatically adjusted so that $\Delta t \leq 1/c\sqrt{1/(\Delta x)^2 + 1/(\Delta y)^2}$ for 2D and $\Delta t \leq 1/c\sqrt{1/(\Delta x)^2 + 1/(\Delta y)^2 + 1/(\Delta z)^2} = 1/c\sqrt{2/(\Delta x)^2 + 1/(\Delta y)^2}$ for 3D where $\Delta x = \Delta z$.

The 3D triangular unit cell is shown as an inset in Fig. 2.7(b). This structure has a lattice constant $a = 30\text{cells}$, hole radius $r = 0.3a$, slab thickness $t = 0.4a$, and slab dielectric constant $\epsilon_r = 11.56$. The band diagram for this structure is shown in Fig. 2.7(b). The gray shaded region in Fig. 2.7(b) is the light cone. Mathematically, the light cone is written as $|k| \leq \omega/c$. Modes lying below the light cone undergo total internal reflection when encountering the dielectric slab/air interface. Those that lie above the cone are lossy as some portion of the fields propagate across the interface and enter the air region surrounding the slab. The line defined by $|k| = \omega/c$ is referred to as the light line. In Fig. 2.7(b), the solid lines represent the modes that are found using plane-wave expansion techniques. Specifically, the MIT Photonic Bands software was used in this case. There is good agreement between the two methods, especially at low frequencies.

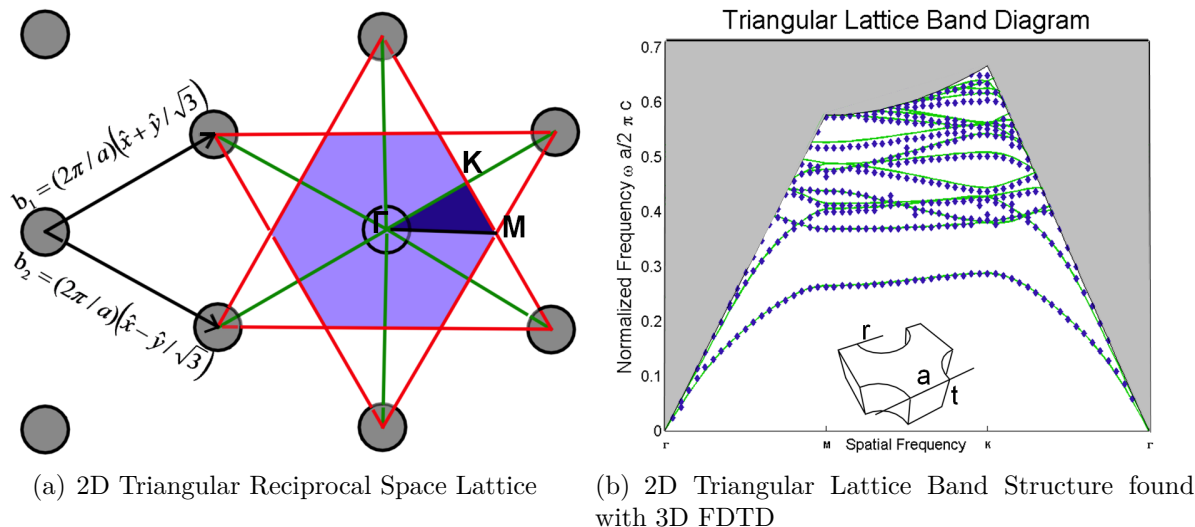


Figure 2.7: a) The triangular lattice reciprocal space representation with unit vectors b_1 and b_2 . b) Band diagram for the 2D triangular lattice photonic crystal slab. Data points show results from 3D FDTD methods and lines show the results of planewave expansion techniques (MIT Photonic Bands software). Inset is the 3D unit cell for the finite slab 2D photonic crystal.

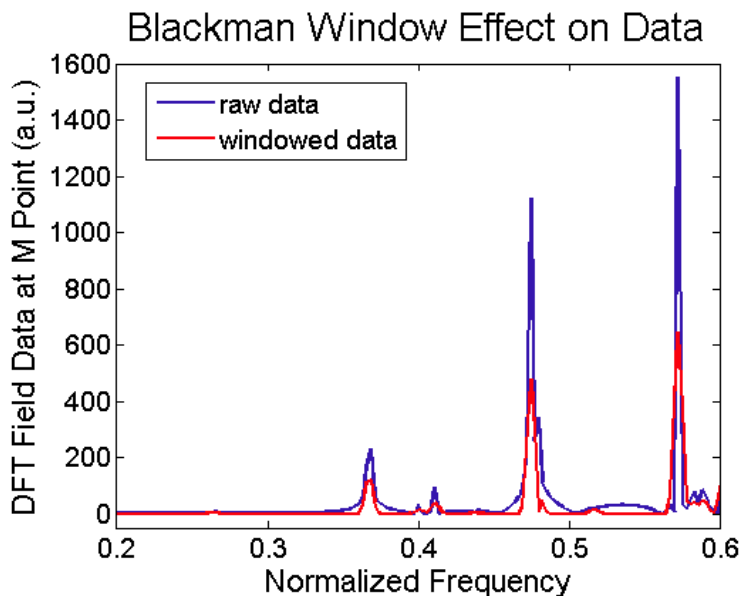


Figure 2.8: The DFT of the raw field data (blue) and the windowed data (red) at the M point of the reciprocal lattice unit cell is shown. The peaks in both data sets are practically co-located. The windowed data has less background ripple leading to better peak detection.

To determine the band structure using FDTD methods, a Gaussian pulse with wide frequency content is used to excite both the Ex and Ez fields. As the fields propagate to the outer boundary in the plane of the slab, they encounter the periodic boundary conditions. Waves that escape from the slab and travel towards the top and bottom of the problem space are absorbed by a perfectly matched layer. As in the 2D FDTD band structure calculations, the simulation is run multiple times (typically 60) with a different value for (k_x, k_y) each time. There are several monitor points located in the unit cell to capture the time varying fields and the peaks of the Fourier transformed field data give the resonant modes for the particular k vector. The simulations are necessarily run for a finite period of time. This is numerically equivalent to taking an infinitely long data set and multiplying it by a rectangular window that is 1 between $t = 0 - T, T$ being the length of the finite simulation. Multiplication in the time domain corresponds to convolution in the frequency domain, so it is instructive to consider the frequency domain representation of the rectangular window. The DFT of the rectangular window function has a main lobe with a series of side lobes whose magnitudes decrease gently with frequency. The first lobe is only 13dB lower than the main lobe. It is the presence of these pronounced sidelobes that leads to substantial ripples in the DFT of the raw FDTD field data. To minimize the effect of these ripples and allow the resonant frequencies to be more easily detected, it is possible to use other windowing functions that have more desirable frequency domain representations. One such window is the Blackman window, the first side-lobe of which is ≈ 60 dB lower than the main lobe. The time representation of the Blackman window is

$$f(t) = a_0 - a_1 \cos\left(2\pi \frac{t}{t_{max}}\right) + a_2 \cos\left(4\pi \frac{t}{t_{max}}\right) \quad (2.41)$$

where $a_0 = (1-\alpha)/2$, $a_1 = 1/2$, and $a_2 = \alpha/2$ [7]. For the Blackman window the convention

is to choose $\alpha = 0.16$, which gives

$$f(t) = 0.42 - 0.5 \cos\left(2\pi \frac{t}{t_{max}}\right) + 0.08 \cos\left(4\pi \frac{t}{t_{max}}\right). \quad (2.42)$$

As shown in Fig. 2.8, the locations of the peaks remain almost unchanged by use of the Blackman window. The peaks are much easier to discern especially those that are close together.

2.3.3 FDTD for Photonic Crystal Microcavity Analysis

Another important application of the FDTD method is the analysis of photonic crystal microcavities. Introduction of a defect to the photonic crystal will not change the frequencies of the photonic bandgap, instead certain modes will move into the gap. To determine the number of modes and their frequencies, the cavity is modeled using 3D FDTD methods with UPML boundary conditions on all 6 sides of the problem space. The input should be a short Gaussian pulse or a delta function. Several monitor points are placed at low symmetry points in the cavity to record the time varying fields. After a sufficient number of time steps, the DFT of the recorded fields will have peaks at the cavity mode frequencies. The main requirement on simulation time is that the frequency bins of the DFT provide enough resolution to accurately determine the mode frequencies. To determine the field profiles associated with each mode, the cavity is excited with a pulse of narrow frequency content centered on the frequency of the mode of interest. In the case of degenerate modes, it is necessary to use inputs of a particular symmetry to isolate a single mode. The electric and magnetic field components are recorded in a plane of the problem space to determine the field profile.

To illustrate this method, the mode frequencies and profiles for the modified single defect cavity examined by Park *et al.* [8] will be presented. The photonic crystal slab is made of InGaAsP and has a lattice constant $a = 0.57\mu m$, radius $r = 0.35a$ and a slab

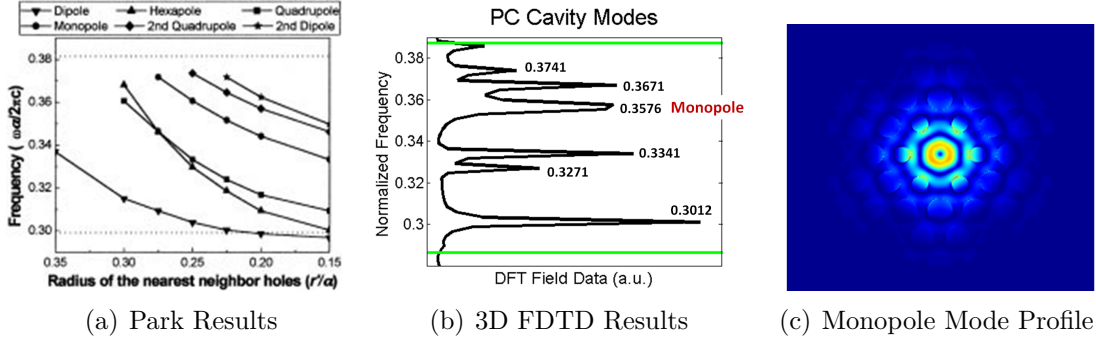


Figure 2.9: Characterization of a photonic crystal microcavity. 2.9(a)) The number of modes appearing in the photonic band gap as a function of the inner hole radius. Taken from [8]. 2.9(b)) Comparison of 3D FDTD results with those of Fig. 2.9(a). Here $r'=0.25a$ and there are 6 modes. Simulations were run for 34,000 time steps. The green lines denote the edges of the photonic bandgap. 2.9(c)) The mode profile of the monopole mode which appears at the normalized frequency $0.3576 = 188.08THz$.

thickness $t = 0.40a$. The index of refraction corresponding to this material system is $n = 3.4$. A microcavity was formed by removing the central hole and reducing the radii of the nearest neighbor holes. Park *et al.* showed that the number of modes in the cavity changes as the inner radii of holes varies, see Fig. 2.9(a). When the inner hole radii are $r' = 0.25a$ there are 5 modes inside of the photonic bandgap. The results of the 3D FDTD simulation with $r' = 0.25a$ are shown in Fig. 2.9(b) and agree well with the frequencies shown in Fig. 2.9(a). There is an extra mode in Fig. 2.9(b) that may be the result of the longer runtime that was used to obtain this data. The profile of the monopole mode is shown in Fig. 2.9(c).

2.3.4 Spontaneous Emission Enhancement

As discussed in Chapter 1, shrinking the size of a high quality optical cavity to the same order of magnitude as the wavelength of emitted light can have a profound impact on the emission properties. The spontaneous emission enhancement factor can be found by taking the ratio of the radiation rate of a dipole in a microcavity to the radiation rate of a dipole in free space. The radiation rate of a dipole can be simulated using 3D FDTD methods.

Following the method of Hwang *et al.* [9], Maxwell's equations are written as

$$\nabla \cdot \epsilon(r)E(r, t) + P_d(r, t) = 0 \quad (2.43)$$

$$\nabla \cdot H(r, t) = 0 \quad (2.44)$$

$$\nabla \times E(r, t) = -\mu(r)\frac{\partial}{\partial t}H(r, t) \quad (2.45)$$

$$\nabla \times H(r, t) = \frac{\partial}{\partial t}\epsilon(r)E(r, t) + P_d(r, t) \quad (2.46)$$

where $P_d(r, t)$ is the polarization from a dipole source and $\epsilon(r)$ and $\mu(r)$ are the permittivity and permeability, respectively. The radiation rate is calculated by integrating the normal component of the Poynting vector over a closed surface containing the dipole. For our cubic grid the choice of a cube enclosing the cavity is appropriate for the surface of integration. The radiation rate is then found by computing

$$P_{rad} = \frac{1}{2} \int \int Re(\langle E \times H^* \rangle \cdot \hat{n}) dS \quad (2.47)$$

$$= \frac{\Delta x^2}{2} Re \left(\sum_y \sum_z (E \times H^*) \cdot \hat{x} + \sum_x \sum_z (E \times H^*) \cdot \hat{y} + \sum_x \sum_y (E \times H^*) \cdot \hat{z} \right) \quad (2.48)$$

This method can be used to determine the spontaneous emission enhancement factors for the photonic crystal microcavity. These enhancement factors will be used in Chapter 3 to calculate the spontaneous emission lifetimes. For these calculations, 3 sets of radiation simulations are required to determine the enhancement factors for a x , y , and z -oriented dipole. Because the spontaneous emission enhancement can also be thought of as the ratio of the density of modes in a cavity to the density in free space, the density of photon modes in the microcavity, $\rho_c(\omega)$ can be derived from these FDTD calculations. Direct use of this density may lead to numerical errors that are minimized by taking the ratio of the radiation rate in the cavity to the radiation rate in bulk. For this reason, the spontaneous emission lifetime calculations in Chapter 3 are designed to use the ratio of the radiation

rates as opposed to the mode density.

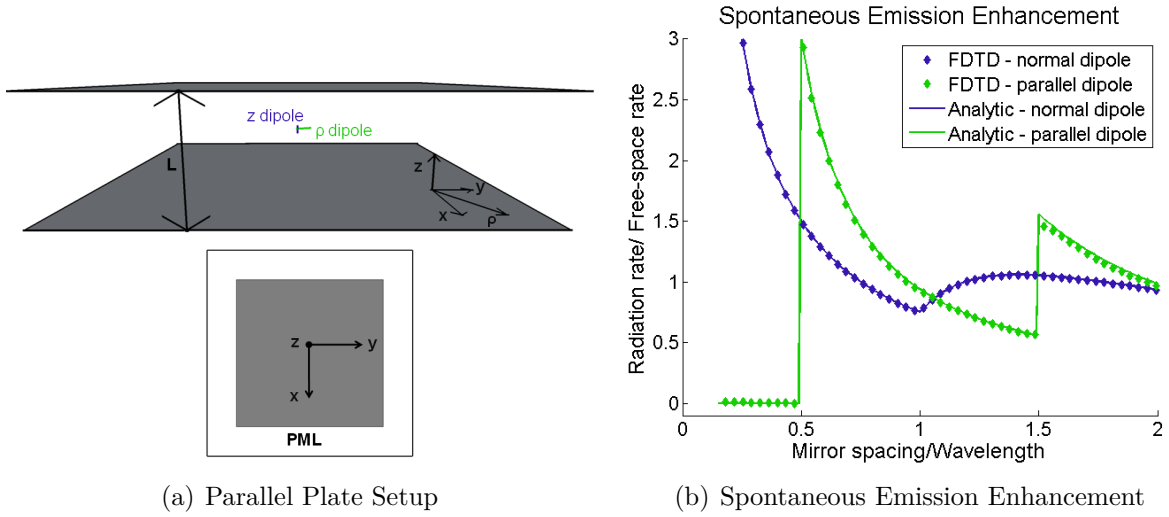


Figure 2.10: a) Pictorial representation of a dipole centered between two parallel metal plates. The dipole can be oriented perpendicular to the plates (along z) or parallel to the plates (in the x,y plane). b) Analytic (lines) and FDTD results (data points) of the spontaneous emission enhancement for a dipole centered between the metal plates.

To ensure that this method is implemented correctly, it is valuable to calculate the spontaneous emission enhancement factor for a planar microcavity. The planar microcavity consists of two perfectly conducting plates that extend infinitely in the plane. The separation between them is taken as L and the dipole is located halfway between the two plates. These simulations are done with 3D FDTD and somewhat thick 20-cell UPML boundary conditions terminate all 6 sides of the problem space. The setup is shown in Fig. 2.10(a). It is possible to solve this problem analytically to determine the radiation rate for a dipole positioned normal to the mirrors γ_z and parallel to the mirrors γ_ρ . These rates are given as a function of the rate in free space γ_o in 2.49 and 2.50 [10].

$$\gamma_z = \gamma_o \left(\frac{3\lambda}{4L} \right) \left(1 + \sum_{n=1}^{[2L/\lambda]} 2 \left[1 - \left(\frac{n\lambda}{2L} \right)^2 \right] \cos^2 \left(\frac{n\pi z}{L} \right) \right) \quad (2.49)$$

$$\gamma_\rho = \gamma_o \left(\frac{3\lambda}{4L} \right) \sum_{n=1}^{[2L/\lambda]} \left[1 + \left(\frac{n\lambda}{2L} \right)^2 \right] \sin^2 \left(\frac{n\pi z}{L} \right) \quad (2.50)$$

The spontaneous emission enhancement factors γ_z/γ_o and γ_ρ/γ_o are plotted in Fig. 2.10(b) (the solid lines) along with the results obtained from the FDTD method just described (data points). The good agreement between the results verifies that the FDTD method is a valid way to determine the spontaneous emission enhancement factors.

Photon Lifetime

The photon lifetime, τ_{ph} , is also calculated with 3D FDTD after the photonic crystal microcavity has been designed. It is related to the cavity quality factor, Q through the relationship [11]

$$\tau_{ph} = \frac{Q}{2\pi\nu_o} \quad (2.51)$$

where ν_o is the resonant frequency. The cavity quality factor of the mode of interest is calculated with the FDTD method by discretizing the cavity and implementing a UPML at all 6 outer boundaries of the problem space. First, the cavity is excited with a Gaussian pulse excitation centered at the frequency of the mode of interest. The quality factor can be calculated by monitoring either the energy decay from the cavity or the relative amount of power leaving the simulation space. When the cavity has a high Q , the energy decay will be extremely slow and the time required for the energy to reach 0 will be long. In this case, monitoring the energy decay can be challenging.

Alternatively, by using the relative power leaving the simulation space the calculation can be performed in a more reasonable amount of time. The equation for the quality factor in this case is [11]

$$Q = 2\pi\nu_o \frac{U(t)}{P(t)} \quad (2.52)$$

where $U(t)$ is the energy in the mode and $P(t)$ is the power leaving the simulation space. There are two main points of caution. The first is that the flux must reach a steady state before the data is recorded. The second requires that the input Gaussian have a bandwidth that is neither too narrow nor too wide. A wide Gaussian in frequency would

result in the injection of power to multiple modes instead of just the desired one. If the frequency domain Gaussian is too narrow a high Q output may be the spectral width of the excitation and not the cavity resonance. A key advantage of this approach is that it is possible to separate the in-plane and out-of-plane quality factors. This provides a better understanding of where the loss occurs and how the device performance could be improved.

For the single-photon source, the cavity quality factor should, in general, be low. This leads to shorter photon lifetimes and faster operation of the device. A typical cavity quality factor for a photonic crystal designed to operate at $\lambda = 1.3\mu\text{m}$ is around $Q = 300$. The corresponding frequency is $\nu = 230.6\text{THz}$ and the resulting photon lifetime would be, $\tau_{\text{photon}} = 0.207\text{ps}$. This lifetime is much smaller than the anticipated spontaneous emission lifetimes which are expected to fall between $0.1 - 5\text{ns}$. Due to the relatively low quality factors required for these devices and the straightforward implementation of the energy decay calculation, this method is primarily used to calculate quality factors in this thesis.

Chapter 3

Quantum Dot Modeling and Spontaneous Emission Lifetimes

One of the most critical lifetimes limiting the operating speed of the single photon source is the spontaneous emission lifetime. As discussed in Chapter 2, this lifetime depends on the photon density of modes and on the dipole matrix element through the equation

$$\tau_{spont} = \frac{1}{W_{fi}} \quad (3.1)$$

where

$$W_{fi} = \frac{\pi}{\hbar\epsilon} |\vec{\epsilon}_\lambda \cdot \vec{d}_{fi}|^2 \rho_{photon}(\omega_{fi}), \quad (3.2)$$

$\vec{\epsilon}_\lambda$ is the polarization of the emitted light and $\rho_{photon}(\omega_{fi})$ is the photon mode density at the frequency of the emitted photon, ω_{fi} . The matrix element for the electron's dipole moment is expressed as

$$d_{fi} = -q \langle \psi_f | \vec{r} | \psi_i \rangle \quad (3.3)$$

where ψ_f and ψ_i are the final and initial wavefunctions respectively, q is the charge on an electron, and \vec{r} is the position vector. Derivations of these equations are given in Appendix

.1.

The aim of this chapter is to discuss a method for calculating the spontaneous emission lifetime, given in Equation 3.1, for a quantum dot in bulk or in a microcavity. In this case, the photon mode density will be that of bulk, ρ_B , or the photonic crystal microcavity, ρ_C , at the frequency of the emitted photon. Additionally, ψ_f becomes the wavefunction of a hole in the valance band ground state and ψ_i the wavefunction of an electron in the conduction band ground state. The photon frequency is related to the transition energy through

$$E_i - E_f = \hbar\omega_{fi}. \quad (3.4)$$

where E_i is the ground state electron energy and E_f is the hole ground state energy. To solve for the spontaneous emission lifetime, the energy levels and wavefunctions of the confined states in the quantum dot must be determined.

Using Bloch's theorem and traditional $k \cdot p$ perturbation theory, calculation of the energy levels and wavefunctions for bulk III-V direct bandgap materials is fairly straightforward. The modeling of nanostructures, such as quantum dots, is more complicated due to the abrupt interfaces between different materials and the loss of discrete translational symmetry. Fortunately, the main principles of Bloch's theorem and $k \cdot p$ perturbation theory can be extended to nanostructures through the envelope-function theory developed by Burt [1]. The situation is further complicated for InAs quantum dots grown on GaAs through the Stranski-Krastanov growth process, where strain has a significant effect on the conduction and valance bands. This strain is accounted for through the use of deformation potentials [2].

To determine the energy levels and wavefunctions in the InAs quantum dots through $k \cdot p$ perturbation theory, we use the Nextnano++ software [3]. Nextnano++ was developed as a full 3D nanodevice simulator and has extensive capabilities. This Chapter begins with a brief overview of the Nextnano++ numerical calculations used for quantum dot

modeling. Next, the InAs and GaAs material parameters used in our calculations are discussed. A brief overview of the energy bands, wave functions, and transition matrix elements for pyramidal InAs quantum dots grown on GaAs is then given with the goal of identifying quantum dots that emit photons at wavelength $\lambda = 1.3\mu m$. The remainder of the Chapter is devoted to outlining the proposed method for calculating the spontaneous emission lifetime.

3.1 Quantum Dot Modeling Using Nextnano++

The calculations performed by the Nextnano++ software are based on Bloch's theorem, the $k \cdot p$ perturbation theory, the envelope-function theory, and deformation potentials [4]. Bloch's theorem states that for a perfectly periodic crystal the eigenfunctions, $\psi_{n,k}(r)$, can be written as a product of a plane wave, $\exp(ik \cdot r)$, and a Bloch factor, $u_{n,k}(r)$. Substitution of the eigenfunction, or Bloch function, into the one-body Schrödinger equation gives the following relation for the Bloch factors

$$E_n(k)u_{n,k}(r) = H(k)u_{n,k}(r) \quad (3.5)$$

$$= \left[\frac{\hat{P}^2}{2m_0} + V(r) \right] u_{n,k}(r) \quad (3.6)$$

where $E_n(k)$ are the eigenenergies, $\hat{P}^2/2m_0$ is the kinetic energy and $V(r)$ is the potential set up by the atoms in the crystalline lattice. The eigenvalue problem can then be solved in the reciprocal space for a single unit cell. The result, $E_n(k)$, is a set of energies that vary continuously with the reciprocal space vector k and form the electronic band structure of the solid.

Many well developed techniques exist for calculating the band structure, including the $k \cdot p$ approximation [5, 6, 7]. The $k \cdot p$ method provides extremely accurate results but only for particular values of k near a point or points of interest. This method is then

acceptable only when knowledge of the entire band structure is unnecessary. The electronic and optical properties of many semiconductors depend only on the electronic states at the bottom of the conduction band and the top of the valance band. Calculation of the band structure only around these extrema, by the $k \cdot p$ method, therefore provides the necessary information about the material.

To obtain the electronic band structure of the quantum dot, Nextnano++ uses $k \cdot p$ perturbation theory. The eigenequation for an electron moving in a periodic potential, $V(r + R) = V(r)$, is

$$H\Psi = \left(\frac{\hat{P}^2}{2m} + V(r) \right) \Psi = E\Psi \quad (3.7)$$

Writing the wavefunction Ψ in Bloch form as $\Psi = e^{ik \cdot r} u_{nk}(r)$ where $u_{nk}(r + R) = u_{nk}(r)$ and substituting into (3.7) we obtain

$$\left(\frac{\hat{P}^2}{2m} + V(r) + \frac{\hbar}{m} k \cdot \hat{P} + \frac{\hbar^2 k^2}{2m} \right) u_{nk}(r) = (H_0 + H_{kp} + H_{k^2}) u_{nk}(r) = E_n(k) u_{nk}(r) \quad (3.8)$$

For any particular choice of k , the eigenfunctions $u_{nk}(r)$ form a complete set as long as the functions' periodicity matches that of the potential $V(r)$. Choosing the wavefunctions at $k = k_o$ as our basis, it is possible to express the eigenfunctions for any other k as

$$u_{nk}(r) = \sum_{n'} c_{n'n}(k - k_o) u_{n'k_o}(r) \quad (3.9)$$

This is referred to as the k_o representation. If we define

$$H_{k_o} = \left(\frac{\hat{P}^2}{2m} + \frac{\hbar}{m} k_o \cdot \hat{P} + \frac{\hbar^2 k_o^2}{2m} + V(r) \right) \quad (3.10)$$

then

$$H_{k_o} u_{nk_o} = E_n(k_o) u_{nk_o} \quad (3.11)$$

and

$$\left[H_{k_0} + \frac{\hbar}{m}(k - k_0) \cdot \hat{P} + \frac{\hbar^2}{2m}(k^2 - k_0^2) \right] u_{nk} = E_n(k)u_{nk} \quad (3.12)$$

which is converted to a matrix eigenvalue equation by the familiar process of multiplication by $u_{nk}^*(r)$ and integration over the unit cell. The eigenvalue problem is given by

$$\sum_{n'} \left[\left(E_n(k_0) + \frac{\hbar^2}{2m}(k^2 - k_0^2) \right) \delta_{nn'} + \frac{\hbar}{m}(k - k_0) \cdot p_{nn'} \right] c_{n'n}(k - k_0) = E_n(k)c_{nn}(k - k_0) \quad (3.13)$$

where

$$p_{nn'} = \int_{\text{unitcell}} u_{nk_0}^*(r) \hat{P} u_{n'k_0}(r) dr. \quad (3.14)$$

The off-diagonal terms all come from the $k \cdot p$ term which is treated as a perturbation when solving for the eigenvalues. For many semiconductors, only a few of the energy bands are important and it is possible to create a finite dimensional matrix eigenvalue problem from equation 3.13. Nextnano++ uses the Löwdin method to divide the bands into two groups [8]. Bands in group A are near the Fermi energy, interact with one another and have a drastic effect on the energy levels, while group B contains all of the remaining bands. For quantum dot calculations, the pertinent bands are the conduction band and the first three valance bands. These bands are all included in group A when an 8-band $k \cdot p$ model is used. The finite dimensional $k \cdot p$ Hamiltonian matrix is

$$H_{nn'}^{kp}(k) = \left[\left(E_n(k_0) + \frac{\hbar^2}{2m}(k^2 - k_0^2) \right) \delta_{nn'} + \frac{\hbar}{m}(k - k_0) \cdot p_{nn'} \right] + \sum_{\gamma \in B} \frac{H_{n\gamma}(k)H_{\gamma n'}(k)}{E_n(k_0) - E_\gamma(k_0)} \quad (3.15)$$

where n and n' now only run over the 8 bands in group A. The last term in this equation is due to the renormalization of the interaction matrix that removes the interactions of states in A and B to the lowest order [8].

To accurately model many materials, the spin-orbit coupling must be accounted for

when solving the Schrödinger equation. This is done by adding the term

$$H_{SO} = \frac{\hbar}{4m^2c^2} (\nabla V \times p) \cdot \sigma \quad (3.16)$$

to the Hamiltonian, $H_{nn'}^{kp}$. Here σ is the Pauli spin matrix vector $\sigma = (\sigma_1, \sigma_2, \sigma_3)^T$. The additional spin-orbit coupling term, given by

$$H_{SO'} = \frac{\hbar}{4m^2c^2} (\nabla V \times k) \cdot \sigma \quad (3.17)$$

is insignificant because the $\hbar k$ terms of $H_{SO'}$ are much smaller than the matrix elements of p . For this reason, only H_{SO} is added to the Hamiltonian in Nextnano++.

The envelope approximation is used to extend the $k \cdot p$ method to nanostructures, such as quantum dots. In this approximation, the electron wave functions are written as a superposition of the Bloch functions, $\psi_{nk_0}(\vec{r})$, yielding

$$\psi(\vec{r}) = \sum_n F_n(\vec{r}) \psi_{nk_0}(\vec{r}). \quad (3.18)$$

Here F_n are the envelope functions that are assumed to vary slowly with respect to the crystal lattice. The envelope functions and the potential that arises from the nanostructure are then expanded in terms of a Fourier series,

$$F_n(\vec{r}) = \sum_k c_{nk} e^{ik \cdot \vec{r}} \quad (3.19)$$

$$V_{struc}(\vec{r}) = \sum_k V_k^{struc} e^{ik \cdot \vec{r}} \quad (3.20)$$

and the Schrödinger equation including the new potential becomes

$$(H(k_0) + V_{struc}(\vec{r})) \psi(\vec{r}) = E \psi(\vec{r}). \quad (3.21)$$

Substitution of equations 3.18-3.20 into equation 3.21 gives a matrix eigenvalue problem of the same form as equation 3.13. The 8-band $k \cdot p$ approximation can then be used to solve for the coefficients $c_{n'n}$.

In order to solve the eigenvalue problem, the conduction band minimum and the valance band maximum must be known at all points in space. These values depend on the band edges of the bulk semiconductor materials comprising the nanostructure. While the bandgaps for these different materials are well known, the discontinuities in band energies at material interfaces is less obvious due to the lack of an absolute energy scale for determining semiconductor band edges. Van de Walle proposed a method for determining the proper band alignment at semiconductor interfaces in the presence of strain[2]. Through a set of deformation potentials and knowledge of the hydrostatic and biaxial strain in the nanostructure, the band values can be determined. The conduction band energy becomes

$$E_c = E_c + a_c \epsilon_h \quad (3.22)$$

where a_c is the absolute deformation potential for the conduction band and $\epsilon_h = \epsilon_{xx} + \epsilon_{yy} + \epsilon_{zz}$ is the hydrostatic strain. For the valance bands, the situation is not as simple. Here the strain leads to an additional term in the $k \cdot p$ Hamiltonian matrix that is given by

$$S(\epsilon) = n \begin{bmatrix} \epsilon_{xx} & \epsilon_{xy} & \epsilon_{xz} \\ \epsilon_{yx} & \epsilon_{yy} & \epsilon_{yz} \\ \epsilon_{zx} & \epsilon_{zy} & \epsilon_{zz} \end{bmatrix} + (l - n) \begin{bmatrix} \epsilon_{xx} & 0 & 0 \\ 0 & \epsilon_{yy} & 0 \\ 0 & 0 & \epsilon_{zz} \end{bmatrix} + m \begin{bmatrix} \epsilon_{yy} + \epsilon_{zz} & 0 & 0 \\ 0 & \epsilon_{xx} + \epsilon_{zz} & 0 \\ 0 & 0 & \epsilon_{xx} + \epsilon_{yy} \end{bmatrix}. \quad (3.23)$$

The parameters l , m , and n are found from the absolute deformation potential for the valance band, a_v , and the sheer deformation potentials, b and d , through the following

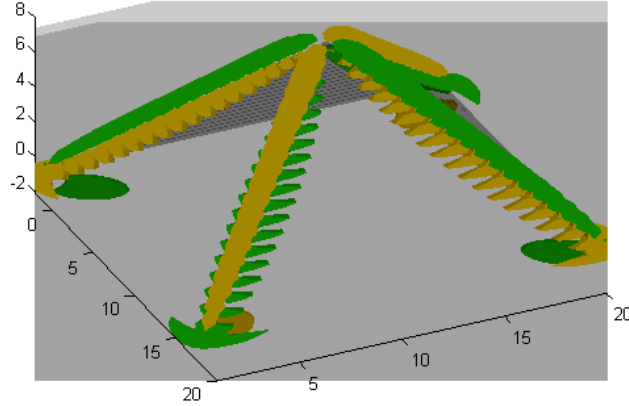


Figure 3.1: The piezoelectric charges for a pyramidal quantum dot. The charges lie along the edges of the pyramids and alternate in sign. This breaks the symmetry of the dot and leads to a favorable direction for the electron and hole wavefunctions [9].

relationships

$$l = a_v + 2b \quad (3.24)$$

$$m = a_v - b \quad (3.25)$$

$$n = \sqrt{3}d \quad (3.26)$$

The deformation potentials for InAs and GaAs as well as the other relevant parameters used in the Nextnano++ calculations are given in Table 3.1 of Sec. 3.2.

Nextnano++ also takes into account the piezoelectric charges that arise from the strain in quantum dots. When a material is strained, the positive and negative charges can be displaced from their normal position resulting in microscopic electric dipoles. This leads to macroscopic charges at the interfaces of the quantum dot. For pyramidal quantum dots, the charges tend to lie along the edges of the pyramid as shown in Fig. 3.1. The presence of the piezoelectric charges breaks the symmetry of the dot and drastically changes the wavefunctions. The piezoelectric charges are incorporated in Nextnano++ through solution

of the Poisson equation, which is given by

$$\nabla \cdot [\epsilon(\vec{r}) \nabla \phi(\vec{r})] = -\rho(\vec{r}) \quad (3.27)$$

where $\epsilon(\vec{r})$ is the position dependent dielectric tensor, $\rho(\vec{r})$ is the piezoelectric charge density and $\phi(\vec{r})$ is the electrostatic potential. The piezoelectric charges are found from

$$\rho(\vec{r}) = -\nabla \cdot P^{piezo}(\vec{r}) \quad (3.28)$$

where, $P^{piezo}(\vec{r})$ is the piezoelectric polarization and is proportional to the strain tensor

$$P_i^{piezo} = e_{ijk} \epsilon_{jk} \quad (3.29)$$

Although the proportionality constants, e_{ijk} , form a third rank tensor with 27 entries, in the zincblend crystal there is only one non-zero entry, e_{14} . The piezoelectric polarization can then be written as a function of space,

$$P^{piezo}(\vec{r}) = e_{14}(\vec{r}) \begin{pmatrix} 2\epsilon_{yz}(\vec{r}) \\ 2\epsilon_{xz}(\vec{r}) \\ 2\epsilon_{xy}(\vec{r}) \end{pmatrix}. \quad (3.30)$$

To account for the band edge shifts and the piezoelectric charges, the strain in the pyramidal quantum dot must be found at all locations. Away from the dot the strain will tend toward zero as the crystal lattice retains its bulk geometry. Near the dot, however, there will be significant strain due to the lattice mismatch of the dot and surrounding material. There are several ways to solve for the strain in the quantum dot. One method, developed by Stroleru [10], expands the Eshelby inclusion theory [11] developed for elliptical dots in isotropic systems to the more practical case of pyramidal and truncated pyramidal

quantum dots. The method used in Nextnano++ is a strain minimization technique based on the Euler-Cauchy stress principle and Cauchy's fundamental postulate [12]. The Cauchy stress tensor σ_{ij} can be written in differential form as

$$\nabla \cdot \sigma_{kl}(\vec{r}) = -F_l = 0 \quad (3.31)$$

where F_i , the external volume force, is equal to 0 because we are interested only in the strain from the internal lattice mismatch. Using Hooke's Law, the stress tensor can be written in terms of the strain tensor through the relation

$$\sigma_{kl} = C_{klmn}\epsilon_{mn} \quad (3.32)$$

where C_{klmn} are the compliance coefficients. In a strained crystal lattice, the positive and negative charges are displaced from their rest positions by some distance. It is possible to write the strain tensor in terms of the displacement, u , as

$$\epsilon_{kl} = \frac{1}{2} \left(\frac{\delta u_k}{\delta x_l} + \frac{\delta u_l}{\delta x_k} \right) \quad (3.33)$$

where l and k refer to two different directions in the coordinate system. For instance if $l = x$ and $k = z$, the strain component, ϵ_{zx} would depend on the sum of the derivative of the displacement along z with respect to x and the derivative of the displacement along x with respect to z . Similar to a stretched or compressed spring, charges displaced from their normal lattice site will increase the potential energy of the system. This elastic energy, when summed over the volume, is expressed in terms of the strain tensor as

$$E_{elastic} = \frac{1}{2} \int_V C_{klmn}\epsilon_{kl}\epsilon_{mn} dr^3. \quad (3.34)$$

Nextnano++ solves for the strain distribution in the quantum dots that minimizes the

elastic energy. Once the strain tensors have been determined, they are used to calculate the strain-dependent components of the Hamiltonian as well as the piezoelectric charging.

This section only briefly outlines the mathematical models for simulating pyramidal quantum dots using Nextnano++. The capabilities of the Nextnano software are extensive and the interested reader is referred to the online documentation for Nextnano++ [13] and Nextnano3 [3].

3.2 Material Parameters

Modeling of nanoscale heterostructures is sensitive to the choice of material parameters. For the 8×8 $k \cdot p$ perturbation calculations, there are approximately 20 material parameters that must be entered into the database for each material. Some of the parameters, such as the bulk energy band gaps, have well established values. Other parameters, such as the deformation potentials, have a range of acceptable values. By entering the appropriate parameters into the database, Nextnano++ is able to replicate the results of several published papers. The general trends in these papers agree, however each author uses slightly different quantum dot sizes and parameters which makes direct comparison a challenge. Still more difficult is the choice of the correct set of parameters that lead to the most accurate energy level transitions and wavefunctions. The majority of the parameters used in this thesis are those of Stoleru [10], because they best match experimental results. As seen in table 3.1, these parameters come from well respected references such as the Landolt-Börnstein database [14] and are used by several authors.

There are two main differences between these parameters and those used in Ref. [10]. The first is that the piezoelectric charging at the interface of the pyramidal dot and the background is ignored in Ref. [10] by setting $e_{14} = 0$. Consider a quantum dot with base width, $b = 16\text{nm}$, and height, $h = 6\text{nm}$. See Fig. 3.2 for a schematic representation of the pyramidal quantum dot. Taking into account the piezoelectric charging increases the

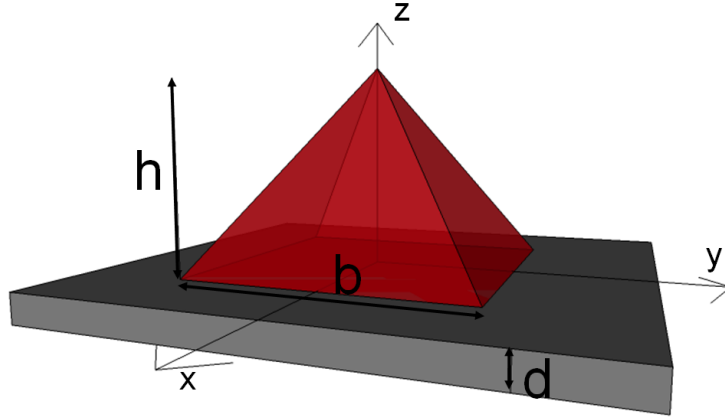


Figure 3.2: Schematic representation of the pyramidal quantum dot used in the Nextnano++ simulations. The dot has height, h , and base width, b . The wetting layer thickness is given by d .

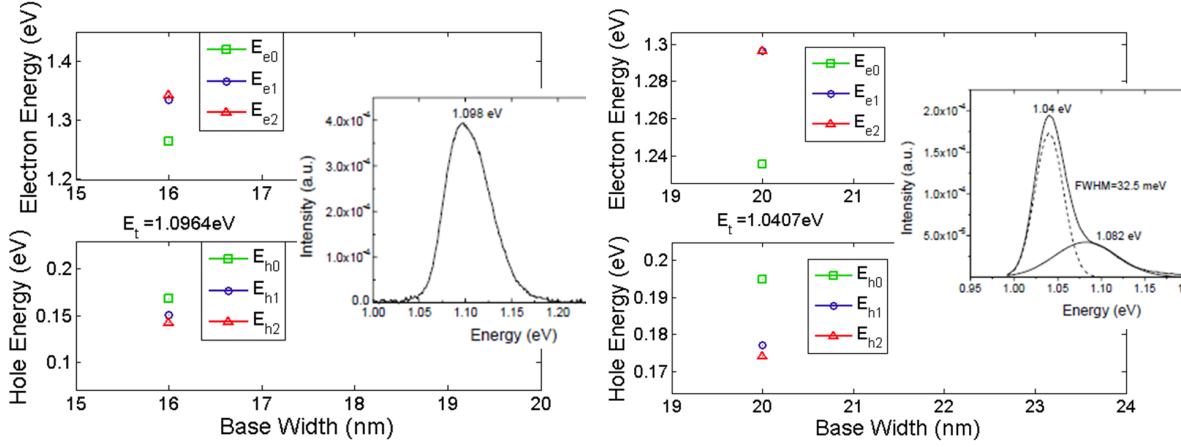
energy transition in this dot from 1.096eV to 1.0964eV, a change of only $\approx 0.04\%$. As discussed at the end of Section 3.1, the wavefunctions are affected by the piezoelectric charging. This changes the transition matrix element and subsequently the spontaneous emission lifetime. Piezoelectric charging can not be ignored for accurate modeling of the quantum dot in the single photon source. The other parameter that is neglected by Stoleru [10] is the shear valence band deformation potential arising from the uniaxial strain along the (111) direction, d . Compared to the effect of the shear deformation potential resulting from the biaxial strain, the affect of d is negligible. It is however, still included in our calculations for completeness.

To verify the validity of the parameters in Table 3.1, the energy bands and energy levels for a pyramidal InAs quantum dot with base width $b = 16\text{nm}$ and height $h = 6\text{nm}$ are shown in Fig. 3.3(a). The transition energy of 1.097eV matches the photoluminescence peak of a sample with dots of the same size, inset of Fig. 3.3(a), and the theoretical results of Stoleru [10]. The energy separation between the electron ground state and the first excited state is 70meV. Similarly the results for a quantum dot with base width $b = 20\text{nm}$ and height $h = 6\text{nm}$ are shown in Fig. 3.3(b). Again the energy transition,

landoltbornstein vandewalle1989band stier1999electronic

Table 3.1: Material Parameters for Nextnano++

Parameter	GaAs	InAs	References
a (Å)	5.6503	6.0553	[10, 14]
E_g (eV)	1.518	0.413	[10, 2, 9, 14]
E_g (eV)	1.424	0.324	[10, 14]
Δ_0 (eV)	0.34	0.38	[10, 2]
$E_{v,av}^0$ (eV)	-6.92	-6.747	[10, 2, 9]
m_e^*	$0.0667m_0$	$0.02226m_0$	[10, 9]
a_c (eV)	-8.013	-5.08	[10, 2, 9]
a_v (eV)	1.16	1.00	[10, 2, 9]
b (eV)	-1.7	-1.8	[10, 2, 9]
d (eV)	-5.062	-3.6	[2, 9]
E_p (eV)	25.7	22.2	[10, 9, 15]
C_{11}	118.8	83.3	[10, 9, 14]
C_{12}	53.8	45.3	[10, 9, 14]
C_{44}	59.4	39.6	[9, 14]
e_{14}	-0.16	-0.045	[9]
ϵ_s	13.18	14.6	[9]
γ_1	7.1	19.7	[9, 14]
γ_2	2.02	8.4	[9, 14]
γ_3	2.91	9.3	[9, 14]



(a) Electron and Hole Energies 16nm Pyramidal Quantum Dot (b) Electron and Hole Energies 20nm Pyramidal Quantum Dot

Figure 3.3: The electron and hole energy levels for an InAs pyramidal quantum dot, a) $b = 16\text{nm}$ and $h = 6\text{nm}$ with transition energy $E_T = 1.097\text{eV}$ and b) $b = 20\text{nm}$ and $h = 6\text{nm}$ with transition energy $E_T = 1.0407\text{eV}$. The transition energies closely match the peak of the photoluminescence spectrum shown as insets [10].

$E_T = 1.04\text{eV}$, found using Nextnano++ with the parameters given in Table 3.1 agrees well with photoluminescence experiments of a real InAs quantum dot sample.

In order to better understand how the material parameters affect the results, the parameters of Table 3.1 are varied according to Table 3.2. Figure 3.4 shows how the first electron and hole energies vary as the material parameters are changed. As expected, neglecting the piezoelectric charging, data set 2, and shifting the valence band offset, data set 3, do not significantly affect the energies. Changing the optical matrix parameter, E_p , changes the 8×8 $k \cdot p$ parameters, L' , M , and N' , and subsequently the electron and hole energies (data sets 4-6). L' , M , and N' , are the Kane parameters and are material dependent constants. They are related to the Dresselhaus parameters, L , M , and N through

$$\begin{aligned}
 L' &= L + \frac{E_p}{E_g} \\
 M &= M \\
 N' &= N + \frac{E_p}{E_g}
 \end{aligned}
 \tag{3.35}$$

Table 3.2: Influence of Variation of Material Parameters

Data Set	Parameter Varied	Units	GaAs	InAs
1	reference, table 3.1		—	—
2	like 1, but e_{14}	Cm^{-2}	$0.16 \rightarrow 0$	$0.045 \rightarrow 0$
3	like 2, but E'_v	meV	—	$-6.747 \rightarrow -6.67$
4	like 3, but E_p	eV	$25.7 \rightarrow 28.8$	—
5	like 4, but a_c	meV	—	—
	a_g	meV	$-9.173 \rightarrow -8.233$	—
	b_v	meV	$-1.7 \rightarrow -1.824$	—
	d_v	meV	$0 \rightarrow -5.062$	$0 \rightarrow -3.6$
6	like 2, but E_p	eV	$25.7 \rightarrow 28.8$	—
7	like 2, but a_v	meV	$1.16 \rightarrow 0.22$	—
	a_g	meV	$-9.173 \rightarrow -8.233$	—
	b_v	meV	$-1.7 \rightarrow -1.824$	—
	d_v	meV	$0 \rightarrow -5.062$	$0 \rightarrow -3.6$
8	Vurgaftman parameters			
9	like 2, but S		$-0.904 \rightarrow -0.905$	$-0.324 \rightarrow -0.2434$
10	like 8, but m_e	m_0	—	$0.026 \rightarrow 0.0226$
11	Stier parameters			

where E_g is the band gap energy. The Dresselhaus parameters can be expressed in terms of the Luttinger parameters, γ_1 , γ_2 and γ_3 . Well accepted values for these parameters are found in the Landolt-Börnstein database [14]. The effect of altering the deformation potentials is not as significant and results in a 0.1% change in the transition energy; compare data set 4 and 5 or 1 and 7. Data set 8 is calculated using parameters recommended by Vurgaftman [16]. Almost every parameter is shifted somewhat from the values in Table 3.1 above. For this data set, the transition energy is decreased by 1.6% from the value for data set 1. By changing the electron effective mass, m_e , for InAs in data set 10 to the value used in Ref. [10], the transition energy is shifted up from data set 8 by 0.8%. The transition energy is most significantly affected by changing the value of S , data set 9, which affects the $k \cdot p$ parameters. The value of S is dependent on the energy band gap, the electron mass, the spin orbit splitting parameter, Δ_0 , and the optical matrix parameter. The final data set, 11, uses the full set of parameters in Ref. [9] and results in a transition energy shift of 1.5% from the reference. Of the parameters that vary among authors, the most

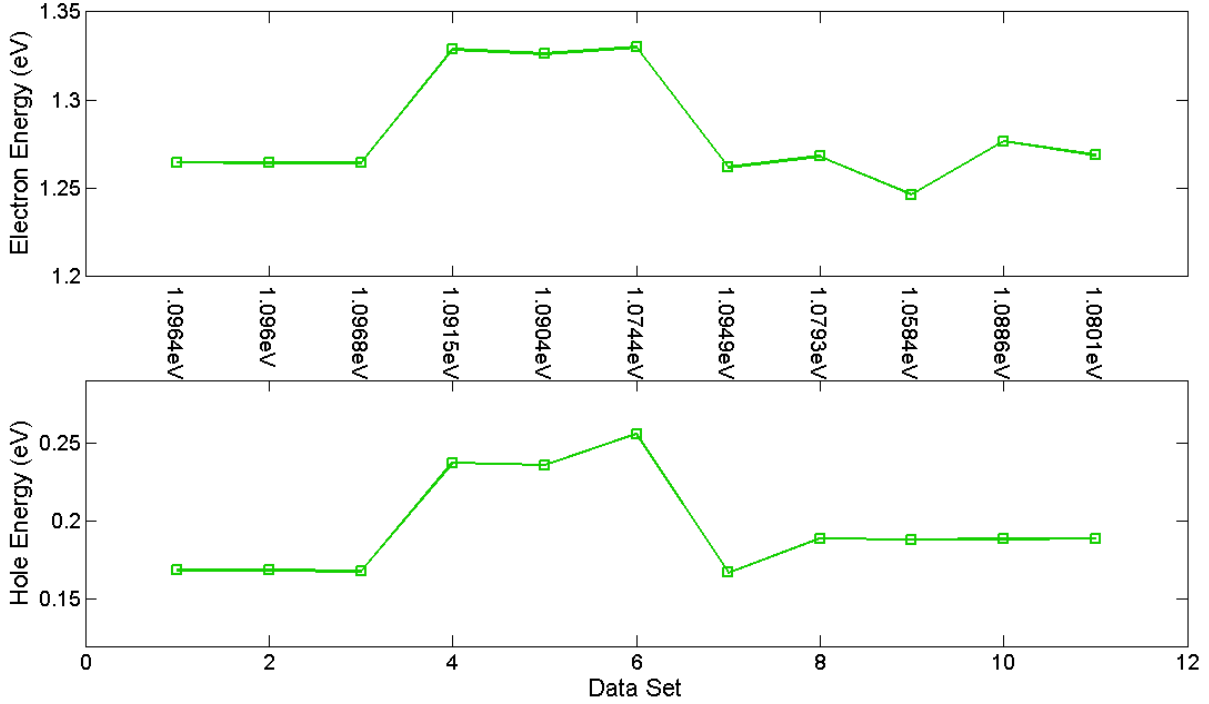


Figure 3.4: The first electron (top) and hole (bottom) energies for a pyramidal InAs quantum dot, $b = 16\text{nm}$ and $h = 6\text{nm}$, for the various parameters given in Table 3.2. The transition energy is in the center of the plot. Energies are given with respect to the GaAs valance band energy far from the dot set to 0eV .

significant ones are the effective masses and those that affect the $8 \times 8 \mathbf{k} \cdot \mathbf{p}$ parameters.

Nextnano++ can also be used to determine the wavefunctions in the quantum dots. In order to visualize the wavefunctions, $|\psi\rangle$, it is useful to plot the probability density isosurfaces, $\langle\psi|\psi\rangle$. Figure 3.5 shows the first 3 electron and hole probability density isosurfaces for pyramidal quantum dots with 101 facets and base widths $b = 13.6\text{nm}$ and $b = 20.4\text{nm}$. The electron wavefunctions are similar for the two different size dots, and tend to extend along the $[110]$ direction. When the dots are larger, there is not much difference between the hole ground state and first excited state wavefunction. They are both concentrated around the corners of the pyramid base along the $[1\bar{1}0]$ direction. In the smaller dots, the hole wavefunctions still tend to extend along the $[1\bar{1}0]$ direction, however the ground state wavefunction is no longer split into two regions. It is also possible to decompose the

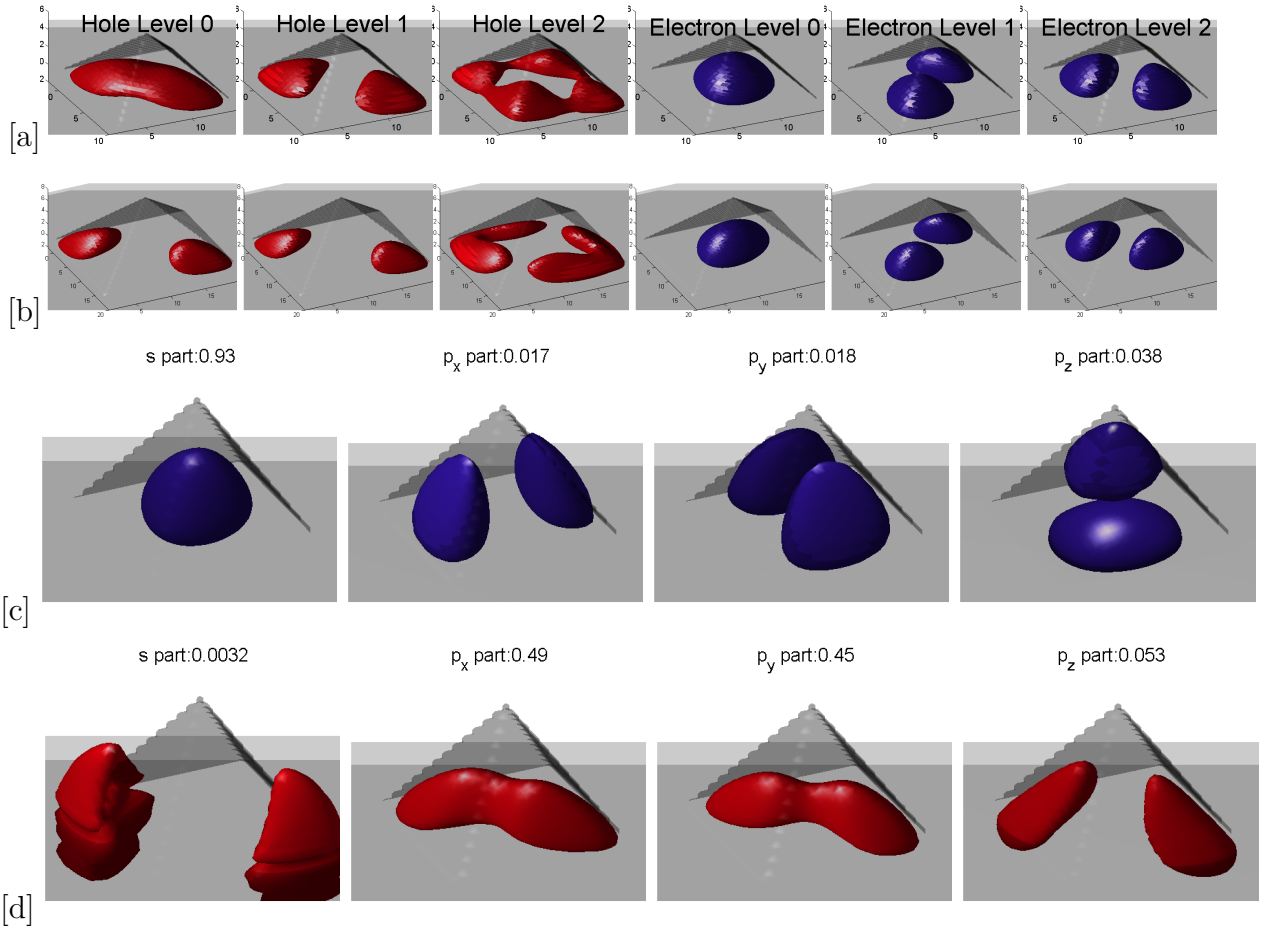
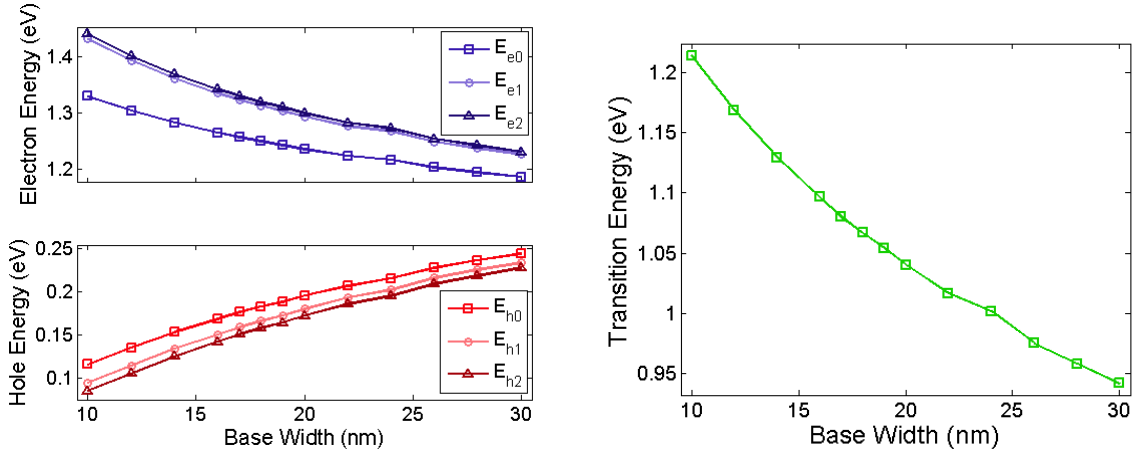


Figure 3.5: The ground state and first two excited states for the electron and hole in a pyramidal InAs quantum dot with base width, a) $b = 13.6\text{nm}$ and b) $b = 20.4\text{nm}$. The decomposition of the c) electron and d) hole ground state wavefunctions into their envelope components. The proportional contribution of each envelope is given above the dots.

wavefunctions into their basis wavefunctions, $|s\rangle$, $|p_x\rangle$, $|p_y\rangle$, $|p_z\rangle$. The probability density isosurfaces of each basis function is shown in Fig. 3.5(c) for the electron ground state and in Fig. 3.5(d) for the hole ground state. Above each function is the integral probability of the state after summing over both spins. For the electron wavefunction the largest contribution to the ground state is from the $|s\rangle$ function. The hole wavefunctions are mostly comprised of $|p_x\rangle$ and $|p_y\rangle$ functions. All of these wavefunction plots agree well with those of Stier [9] and confirm that nextnano++ is providing reasonable wavefunctions.



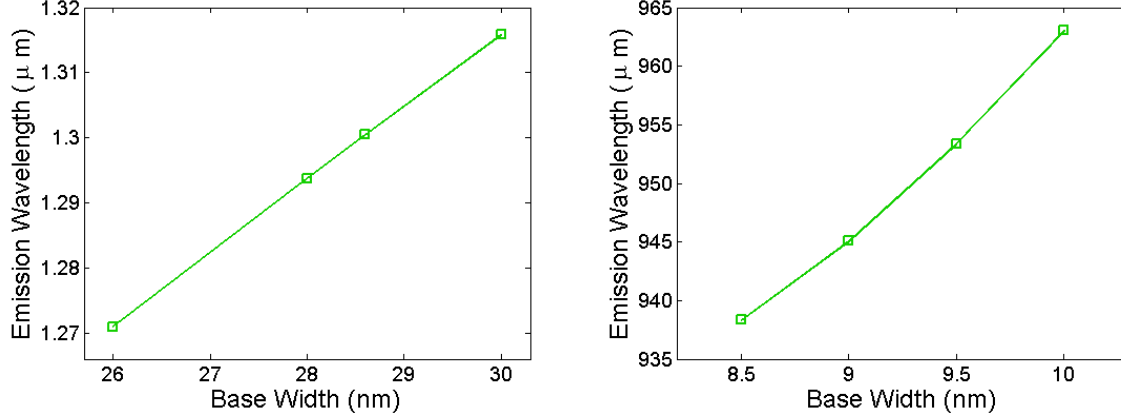
(a) Electron and Hole Energies in Pyramidal Quantum Dots (b) Transition Energies Pyramidal Quantum Dots

Figure 3.6: a) The electron and hole energy levels for an InAs pyramidal quantum dot with $h = 6\text{nm}$ and height $h = 10\text{nm}$ to $h = 30\text{nm}$. b) Transition energies for these quantum dots.

3.3 Pyramidal Quantum Dots

Although the exact shape of epitaxially grown quantum dots has been debated, most researchers now agree that a square based pyramid or truncated pyramid is the most likely geometry. For this reason and also to compare my results with published work, this Section examines pyramidal InAs quantum dots grown on GaAs. In the Nextnano++ calculations, the wetting layer is assumed to be 0.5nm thick. The presence of the wetting layer does not significantly alter the results because it is essentially a quantum well with electron (hole) energies above (below) the energy levels in the quantum dot.

As the quantum dot is made larger, the transition energy decreases. Figure 3.6(a) shows the electron and hole energies for pyramidal quantum dots of fixed height, $h = 6\text{nm}$, and various base widths. Smaller quantum dots have energies that approach the GaAs band edges. Larger dots have lower electron (higher hole) energies that are closer to the lower conduction (higher valence) band level in the quantum dot. Note that only the first three electron and hole energy levels are shown for the dots and that more energy states may exist, especially in larger dots. The transition energy for the first electron and hole states,

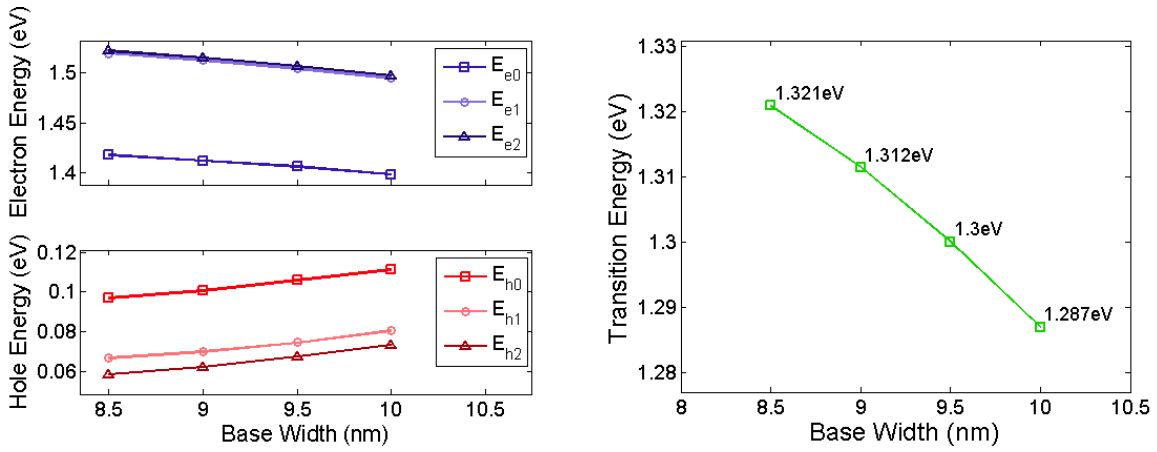


(a) Ground State Emission Wavelengths in Large Pyramidal Quantum Dots (b) Ground State Emission Wavelengths in Small Pyramidal Quantum Dots

Figure 3.7: The photon emission wavelength for an electron and hole ground state recombination in a) large and b) small InAs pyramidal quantum dots. a) The target emission wavelength, $\lambda = 1.3\mu\text{m}$ is obtained for a dot with $h = 6\text{nm}$ and $b = 28.6\text{nm}$. b) The target emission wavelength, $\lambda = 945.1\text{nm}$, is obtained for a dot with $h = 3\text{nm}$ and $b = 9\text{nm}$.

$E_T = E_{e0} - E_{h0}$, is shown as a function of base width in Figure 3.6(b). For a quantum dot with base width of $b = 28\text{nm}$, the transition energy is approximately 0.958eV and the photons emitted from the dot will have a wavelength of $\lambda = 1.294\mu\text{m}$. This is close to the target emission wavelength of $\lambda = 1.3\mu\text{m}$. From the figure, a dot of height, $h = 6\text{nm}$, and base width between $b = 28\text{nm}$ and $b = 30\text{nm}$ should give the desired emission. Figure 3.7(a) shows the photon wavelength for the ground state transition as a function of the dot base width. A dot with $b = 28.6\text{nm}$ has emission wavelength $\lambda = 1.3005\mu\text{m}$. Although this dot will emit photons at the low-loss wavelength for optical fiber transmission, it has several excited states for the electron to occupy. The implications will be discussed further in the next Chapter.

To validate the spontaneous emission calculations through comparison with experimental results, it will also be necessary to have dots that emit photons with wavelength near $\lambda = 942.4\text{nm}$. This corresponds to a transition energy of $E_T = 1.312\text{eV}$. In Fig. 3.6(b), even small quantum dots with $b = 10\text{nm}$ and $h = 6\text{nm}$ have only a transition energy $E_T = 1.2\text{eV}$. Continuing to decrease the base width of the dots will not result in the tran-



(a) Electron and Hole Energies in Small Pyramidal Quantum Dots (b) Transition Energies Small Pyramidal Quantum Dots

Figure 3.8: a) The electron and hole energy levels for an InAs pyramidal quantum dot with $h = 3\text{nm}$ and height $h = 8.5\text{nm}$ to $h = 10\text{nm}$. b) Transition energies for these quantum dots.

sition energy required. Instead, the height can be decreased which will result in a smaller overall InAs volume and higher transition energies. Figure 3.8(a) shows how the electron and hole energies vary when the dot height is reduced to $h = 3\text{nm}$ and the base width is varied from $b = 8.5\text{nm}$ to $b = 10\text{nm}$. The corresponding transition energies are shown in Fig. 3.8(b) and the photon wavelengths are shown in Fig. 3.7(b). When the quantum dots have $b = 9\text{nm}$ and $h = 3\text{nm}$, the photons emitted have wavelength $\lambda = 945.1\text{nm}$ which is within 0.2% of the desired wavelength. These quantum dots will be used in the next Section when the approach for calculating the spontaneous emission lifetimes is outlined. They may also be important for single photon source applications because unlike the larger $b = 28.6\text{nm}$ dots, only one excited electron state exists in the dot. The excited electron states actually lie above the GaAs conduction band edge and a single electron-hole recombination event can be isolated in these small dots. Such a dot is a valuable candidate for use in a single-photon source despite the fact that the photon wavelength is shorter than the target of $\lambda = 1.3\mu\text{m}$.

Because the wavefunctions will also be used to calculate the spontaneous emission

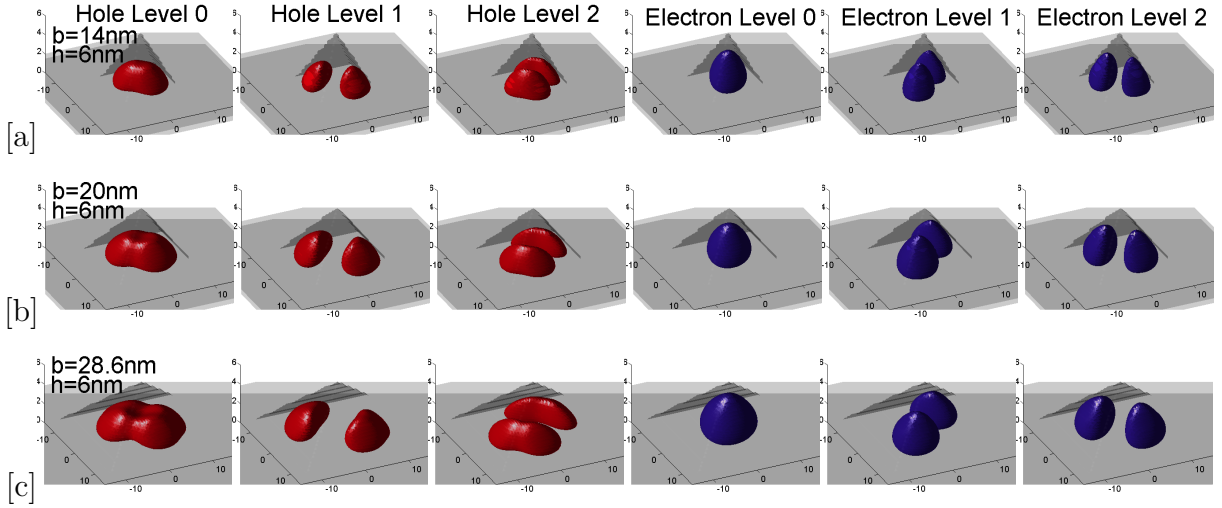


Figure 3.9: The ground state and first two excited states for the holes and electrons in a pyramidal InAs quantum dot. 3.9(a)-3.9(c) show the wavefunctions for dots with height $h = 6\text{nm}$ and base widths: 3.9(a) $b = 14\text{nm}$, 3.9(b) $b = 20\text{nm}$, 3.9(c) $b = 28.6\text{nm}$.

lifetimes, it is worthwhile to briefly discuss how they are affected for the two sets of quantum dots presented in this Section. A general dependence of the wavefunctions on quantum dot size was shown at the end of Sec. 3.2. For these two quantum dots, the facet was fixed to $\{101\}$ so that the base width was equal to twice the dot height. The result was two dots with the same geometry, but different sizes. In the majority of the energy calculations of this Section, the ratio of the base width to dot height was neither 2 : 1 nor held constant. The result is pyramids with facets that lie along different planes and a general change in the dot geometry. Figure 3.9, shows the first few electron and hole wavefunctions for a variety of dots.

The quantum dots in Fig. 3.9(a)-3.9(c) are all $h = 6\text{nm}$ high and have base widths $b = 14\text{nm}$, $b = 20\text{nm}$ and $b = 28.6\text{nm}$. As the base width increases, the hole ground state wavefunction spreads out along the $[1\bar{1}0]$ direction. This is similar to what was observed in Fig. 3.5 except that the ground state hole wavefunctions for dots with larger base widths are no longer split into two. The reduced dot height prevents the wavefunction splitting. Quantum dots with larger base to height ratios should have a larger overlap of the electron

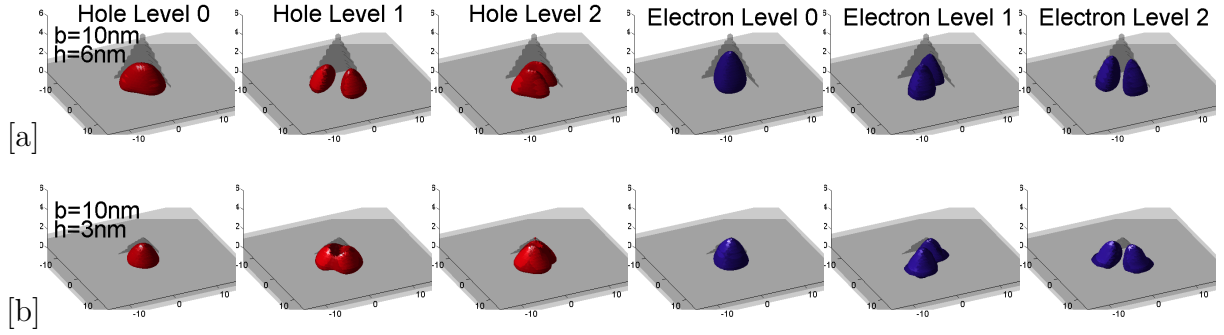


Figure 3.10: The ground state and first two excited states for the holes and electrons in a pyramidal InAs quantum dot. 3.10(b) A dot with base width $b = 10\text{nm}$ and height $h = 3\text{nm}$. 3.10(a) Shows the wavefunctions for a dot with base width $b = 10\text{nm}$ and height $h = 6\text{nm}$.

and hole ground state wavefunctions. This affects the transition matrix elements and subsequently the lifetimes.

For the first and second excited states the hole wavefunctions split along the $[1\bar{1}0]$ and $[110]$ directions respectively. The excited states of the electrons exhibit similar behavior except that the splitting occurs along the $[110]$ direction for the first excited state and the $[1\bar{1}0]$ direction for the second. A slight spreading of the electron ground state is observed along the $[110]$ direction as the base width is increased, but the wavefunction stays fairly localized at the center of the dot even for $b = 28.6\text{nm}$. Again this departure from the behavior of the wavefunctions in Fig. 3.5 is a result of the smaller dot heights.

As the dot height is reduced from 6nm in Fig. 3.10(a) to 3nm in Fig. 3.10(b) the wavefunctions fill the quantum dot volume almost completely. There is a significant portion of the wavefunction near the apex of the pyramid for both the electron and hole ground state wavefunctions. The hole excited state wavefunctions are no longer split, although they still spread along the $[1\bar{1}0]$ direction for the first state and $[110]$ direction for the second. Instead of coming together, the electron excited state wavefunctions are not as well confined to the pyramidal dot.

From the photoluminescence plot in Fig. 3.3 of Sec. 3.3, it is obvious that a real quantum dot sample does not have dots of uniform size. Even an extremely high quality sample

has some size dispersion. Consider the inset to Fig. 3.3(b), where the full width at half maximum is $FWHM = 32.5\text{meV}$. The peak transition energy is $E_T = 1.04\text{eV}$ and the FWHM spans from $E = 1.023\text{eV}$ to $E = 1.056\text{eV}$. According to Fig. 3.6(b), this corresponds to dots with base widths between $b = 19\text{nm}$ and $b = 21\text{nm}$. In order to model real single photon emitters, it is thus necessary to consider the performance of the device as the quantum dot size is varied over some range. This will be examined in the next Chapter. Some techniques, such as μPL , may be used during actual fabrication of the device to help minimize this variation through the location of quantum dots with the desired transition energy.

3.4 Calculation of the Spontaneous Emission Lifetime

Once the transition energies and wavefunctions are found with Nextnano++, they can be used to determine the dipole matrix elements which are then used to compute the spontaneous emission lifetime. The approach illustrated below solves for the lifetimes of quantum dots either in bulk or in a microcavity. Although we are specifically interested in photonic crystal microcavities, the method presented here applies to any microcavity that can be analyzed using FDTD methods. For bulk the spontaneous emission rate is given by [17]

$$W_{fi} = \frac{4n\omega^3}{2\hbar c^3} |\vec{\varepsilon}_\lambda \cdot \vec{d}_{fi}|^2 = \frac{4n\omega^3}{3\hbar c^3} |\vec{d}_{fi}|^2 \quad (3.36)$$

where c is the speed of light, n is the index of the bulk, ω is the angular frequency of the emitted photon, $\vec{\varepsilon}_\lambda$ is the unit vector denoting polarization, and \vec{d}_{fi} is the dipole matrix element. The simplification was made by noting that in bulk, there is no preferential direction for the polarization so that

$$\langle |d_{fi_x}|^2 \rangle = \langle |d_{fi_y}|^2 \rangle = \langle |d_{fi_z}|^2 \rangle = (1/3) \langle |\vec{d}_{fi}|^2 \rangle \quad (3.37)$$

and an average over the two polarizations yields $\sum_{\lambda} |\vec{\epsilon}_{\lambda} \cdot \vec{d}_{fi}|^2 = (2/3)|\vec{d}_{fi}|^2$.

To calculate the dipole matrix elements, we begin with the 8 complex spinors used in the 8×8 $k \cdot p$ calculations. For each eigenenergy, the complex wavefunctions are found by taking the weighted sums of the 8 spinors,

$$\psi(x, y, z) = s_1 |s+\rangle + s_2 |s-\rangle + p_1 |p_x+\rangle + p_2 |p_x-\rangle + p_3 |p_y+\rangle + p_4 |p_y-\rangle + p_5 |p_z+\rangle + p_6 |p_z-\rangle \quad (3.38)$$

where s_1, s_2 and p_1 - p_6 are the complex weighing factors and $\psi(x, y, z)$ is the complex wavefunction. The electron ground state wavefunction is denoted as $\psi_{e0}(x, y, z)$ and the hole ground state is $\psi_{h0}(x, y, z)$. These wavefunctions are coarse due to the large step size used in the 8×8 $k \cdot p$ calculations. To produce better results the wavefunctions can be interpolated to a smaller grid using either linear interpolation or splines. Next the wavefunctions are normalized by taking

$$\psi_{e0}(x, y, z) = \frac{\psi_{e0}(x, y, z)}{\sqrt{\int_x \int_y \int_z |\psi_{e0}(x, y, z)|^2 dx dy dz}} = \frac{\psi_{e0}(x, y, z)}{\sqrt{\sum_x \sum_y \sum_z |\psi_{e0}(x, y, z)|^2 \Delta x \Delta y \Delta z}} \quad (3.39)$$

$$\psi_{h0}(x, y, z) = \frac{\psi_{h0}(x, y, z)}{\sqrt{\int_x \int_y \int_z |\psi_{h0}(x, y, z)|^2 dx dy dz}} = \frac{\psi_{h0}(x, y, z)}{\sqrt{\sum_x \sum_y \sum_z |\psi_{h0}(x, y, z)|^2 \Delta x \Delta y \Delta z}}. \quad (3.40)$$

The dipole matrix element is found from the wavefunctions through solution of

$$\vec{d}_{fi} = -q \langle \psi_f | \vec{r} | \psi_i \rangle = -q \langle \psi_{h0} | \vec{r} | \psi_{e0} \rangle \quad (3.41)$$

where ψ_i is the ground state electron wavefunction ψ_{e0} , ψ_f is the ground state hole wavefunction ψ_{h0} , and

$$\vec{r} = x\hat{x} + y\hat{y} + z\hat{z}. \quad (3.42)$$

By substiting Equation 3.42 into Equation 3.41, the dipole matrix element along the three

coordinate axis, x , y , and z can be found through the following equations

$$d_{if}(x) = | -q \langle \psi_{h0} | \vec{x} | \psi_{e0} \rangle |^2 = q^2 \left| \sum_x \sum_y \sum_z (x_c - x) \psi_{h0}^* \psi_{e0} \Delta x \Delta y \Delta z \right|^2 \quad (3.43)$$

$$d_{if}(y) = | -q \langle \psi_{h0} | \vec{y} | \psi_{e0} \rangle |^2 = q^2 \left| \sum_x \sum_y \sum_z (y_c - y) \psi_{h0}^* \psi_{e0} \Delta x \Delta y \Delta z \right|^2 \quad (3.44)$$

$$d_{if}(z) = | -q \langle \psi_{h0} | \vec{z} | \psi_{e0} \rangle |^2 = q^2 \left| \sum_x \sum_y \sum_z (z_c - z) \psi_{h0}^* \psi_{e0} \Delta x \Delta y \Delta z \right|^2 \quad (3.45)$$

where x_c , y_c and z_c are the center points of the quantum dot in the x, y, and z directions respectively.

For a quantum dot in bulk, these values can be directly entered into Equation 3.36 to determine the bulk transition rate. The main assumption in simplifying this Equation was that there was no preferred direction for radiation in bulk. In a microcavity this assumption is no longer valid; each mode will have a distinct polarization that is determined by its field distribution. If the quantum dot is emitting into a microcavity, then the transition rate must be given by

$$W_{fi} = \frac{4n\omega^3}{2\hbar c^3} |\vec{\epsilon}_\lambda \cdot \vec{d}_{fi}|^2. \quad (3.46)$$

Instead of writing $\vec{\epsilon}_\lambda$ as a typical unit vector, it is possible to express this value as

$$\vec{\epsilon}_\lambda = R_x \hat{x} + R_y \hat{y} + R_z \hat{z} \quad (3.47)$$

where R_x , R_y , and R_z are weighing factors that denote the strength of a dipole radiating along the x, y, or z axis respectively. The value of $|\vec{\epsilon}_\lambda \cdot \vec{d}_{fi}|^2$ then becomes

$$|\vec{\epsilon}_\lambda \cdot \vec{d}_{fi}|^2 = \vec{\epsilon}_\lambda \cdot (2/3) |\vec{d}_{fi}|^2 = (2/3) (R_x d_{if}(x) + R_y d_{if}(y) + R_z d_{if}(z)). \quad (3.48)$$

In bulk, $R_x = R_y = R_z = 1$, because there is no preferential direction for emitted radiation.

When the quantum dot is placed in a microcavity, the density of modes and hence the weighing factors are altered. The weighing factors are found from three separate FDTD radiation rate calculations each with a dipole oriented along the x, y, or z direction. Details of these calculations were provided in Sec. 2.3.4. Specifically, the weighing factor is the ratio of the spontaneous emission rate in the cavity to the rate in bulk at the transition frequency corresponding to the energy transition in the quantum dot. These weighing factors signify how well an emitter, the quantum dot, couples to a cavity mode if it is placed at a particular location in the cavity and is emitting in a particular direction. The factor of (2/3) that was obtained by approximating $|\vec{\epsilon}_\lambda \cdot \vec{d}_{fi}|^2$ in bulk, remains in Equation 3.48 because the radiation rates in the cavity calculated by FDTD methods were normalized by the rates in bulk. Recall that the Purcell factor is the ratio of the radiation rate in a cavity to the rate in bulk. The weighing factors then are actually the Purcell factor of an emitter laying along the x, y, or z axis in the cavity.

The spontaneous emission rate for a quantum dot in bulk or in a microcavity can now be expressed as

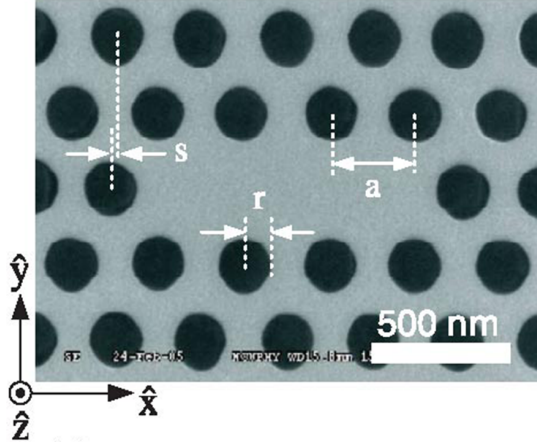
$$W_{fi} = \frac{4n\omega^3}{3c^3} |\vec{\epsilon}_\lambda \cdot \vec{d}_{fi}|^2 = \frac{4n\omega^3}{3c^3} (R_x d_{if}(x) + R_y d_{if}(y) + R_z d_{if}(z)) \quad (3.49)$$

and the spontaneous emission lifetime is

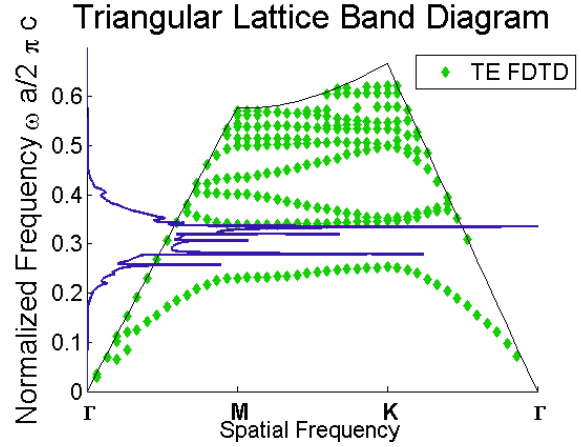
$$\tau_{spont} = 1/W_{fi} = \frac{3c^3}{4n\omega^3 (R_x d_{if}(x) + R_y d_{if}(y) + R_z d_{if}(z))}. \quad (3.50)$$

Equation 3.49 is equally valid for a quantum dot in bulk or in a microcavity. Upon substitution of $R_x = R_y = R_z = 1$, Equation 3.49 reduces to Equation 3.36. In Appendix .1, the explicit equations for the spontaneous emission rate in a cavity and in bulk are found to be

$$W_{i \rightarrow f}^{cavity} = \frac{4}{\hbar^2 \Delta\omega} |\vec{d}_{fi}|^2 |\alpha^2 E_{max}|^2 \quad (3.51)$$



(a) Chang Microcavity



(b) Chang Band Diagram and $s = 0.0a$ Mode Frequencies

Figure 3.11: a) An SEM image of the microcavity analyzed by Chang [18]. b) The band diagram and mode frequencies for the L3 microcavity, $a = 282.3\text{nm}$, $r = 0.31a$, and $s = 0.0a$. There are 5 peaks in the mode frequency plot, top and bottom correspond to the band edges and the 3 in the middle are modes within the band gap.

$$W_{i \rightarrow f}^{bulk} = \frac{4n\omega^3}{3\hbar c^3} |\vec{d}_{fi}|^2 \quad (3.52)$$

respectively. These equations differ in terms of the prefactor and at first glance it would appear that Eq. 3.49 above can not be correct for emission into both bulk and a microcavity. But the weighing factors, R_x , R_y and R_z , in Eq. 3.49 are determined with respect to the radiation from dipoles in bulk. Therefore, it is correct to begin with the spontaneous emission rate in bulk and use these weighing factors to determine how the presence of the microcavity perturbs the emission rates.

To verify this method for calculating the spontaneous emission lifetimes, we compare our theoretical results with the experiments of Chang [18]. The structure examined is a photonic crystal microcavity in a 180nm-thick GaAs slab with a single layer of $\text{In}_{0.5}\text{Ga}_{0.5}\text{As}$ quantum dots at the center. Specifically, the microcavity was formed by removing three holes in a line, which is commonly referred to as the L3 defect. The photonic crystal has a lattice constant near $a = 284.5\text{nm}$, with a hole radius, $r = 0.31a$. Control over the resonant mode frequency is provided by shifting the nearest neighbor holes, along the defect axis,

outward by some distance, $s = 0.0a$ to $s = 0.15a$. Figure 3.11(a) shows an SEM image of the microcavity [18] and the TE-like photonic band diagram for the bulk photonic crystal obtained from our 3D FDTD simulator. A photonic band gap exists for the TE-like modes in the frequency range spanning $f = 0.2534 - 0.3393(a/\lambda)$, which closely matches the values in [18]. The mode frequencies for the L3 cavity with $s = 0.0a$ are shown as an overlay in Fig. 3.11(b). There are 3 modes within the bandgap.

As shown in Fig. 3.12(a), the mode wavelength increases as the shift, s , is varied. The shift corresponds to an addition of high index material to the cavity volume resulting in a lower mode frequency and a longer wavelength. The second mode which is shown, lies within the same wavelength range as was reported by Chang [18] and also has a matching field profile. This mode is linearly polarized and the normalized E_y field profile is shown in Fig. 3.12(b). Chang also used finite-difference time-domain methods to locate the cavity resonant frequencies and calculate the field distributions. Although our mode frequencies match the theoretical results of Chang closely, there is some discrepancy between the theoretical results and the experimental cavity resonance. This is likely due to imperfections during the fabrication process that lead to variations in the hole sizes and spacings and the slab thickness. It is found that reducing the lattice constant to $a = 282.3\text{nm}$ leads to a resonance of the second mode for $s = 0.1a$ at $\lambda = 945.1\text{nm}$, which is closer to the experimental results. To compare the theoretical spontaneous emission lifetime with the experimental results, this adjustment is necessary.

Spontaneous emission calculations were performed using the 3D FDTD simulator. The results for an x, y, and z dipole are shown in Fig. 3.13 as a function of normalized frequency. For the x and y dipole, the radiation rate is suppressed within the band gap except at the resonant mode frequencies. In Fig. 3.13 there are only 2 modes within the band gap, because the field profile of the third mode has a null at the excitation point for all fields, E_x, E_y and E_z . No energy couples to this mode and it does not appear. At the normalized frequency $f = 0.2987$, which corresponds to $\lambda = 945.1\text{nm}$, the radiation rate from a y

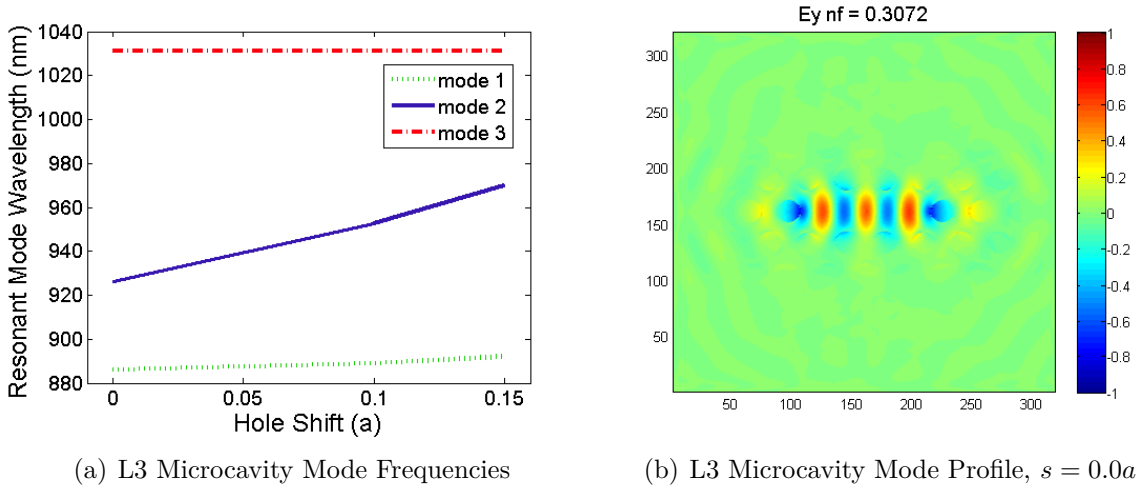


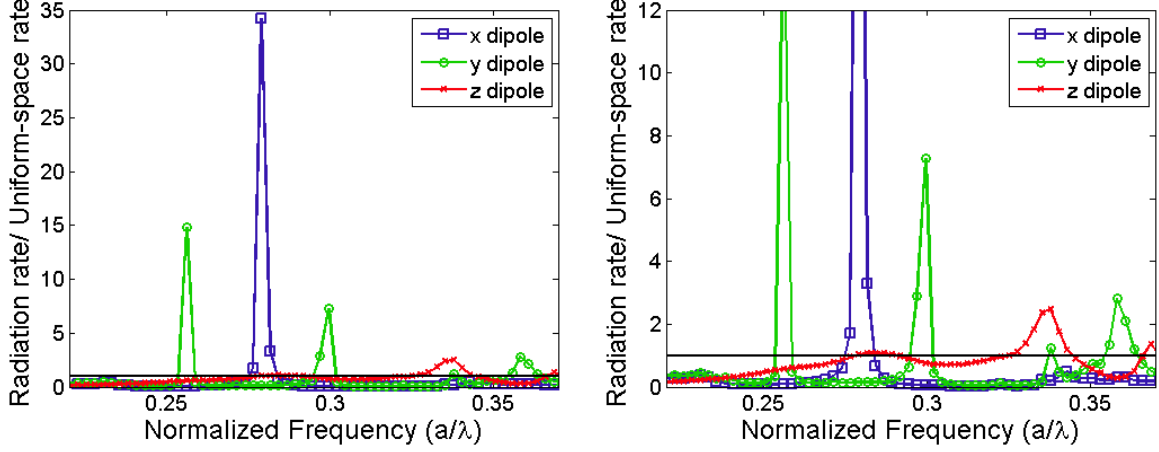
Figure 3.12: a) The mode frequencies versus the hole shift, s , for the second resonant mode in the L3 microcavity. b) The normalized E_y field for this mode when $s = 0.0a$.

Table 3.3: Spontaneous Emission Lifetimes L3 Microcavity, $s = 0.1a$

Dot b/h	$\lambda(nm)$	$d_{f_{ix}}$	$d_{f_{iy}}$	$d_{f_{iz}}$	R_x	R_y	R_z	τ_{spont} (ns)	experiment (ns)
9nm/3nm	945.1	71.3687	47.3168	56.9332	1	1	1	0.659	$0.65(\pm 0.05)$
9nm/3nm	945.1	71.3687	47.3168	56.9332	0.05335	7.278	0.7631	0.2955	0.21
9nm/3nm	945.1	71.3687	47.3168	56.9332	0.03859	0.1462	0.7028	2.329	2.52
8nm/3nm	926.4	34.0229	81.1823	67.1978	0.03859	0.1462	0.7028	1.804	2.52

dipole is much larger than 1. This will lead to the reduced spontaneous emission lifetime for the on-resonance quantum dot. The radiation factors used to calculate the spontaneous emission lifetimes are shown in Table 3.3. Also given in the Table are the lifetimes and the transition matrix elements along the x, y, and z directions for the InAs quantum dot with base width $b = 9\text{nm}$ or $b = 8\text{nm}$ and height $h = 3\text{nm}$, discussed in Sec. 3.3. Although the quantum dots in Ref. [18] have a material composition of $\text{In}_{0.5}\text{Ga}_{0.5}\text{As}$, we make the simplifying assumption that the dots are purely InAs.

The $b = 9\text{nm}$ dot is on resonance with the microcavity mode. In bulk this quantum dot has a spontaneous emission lifetime of $\tau_{0e} = 0.659\text{ns}$, in good agreement with the experimentally determined $\tau_{0e} = 0.65\text{ns}$. When the quantum dot is placed on resonance with the microcavity, the spontaneous lifetime decreases to $\tau_{1e} = 0.21\text{ns}$ in the experiments and to $\tau_{1c} = 0.2955\text{ns}$ in our calculations. These values correspond to an overall spontaneous



(a) Radiation Rates of an x, y, z Oriented Dipole (b) Close-up of a) Around Frequency of Interest

Figure 3.13: a) The relative radiation rates for an x, y, or z dipole located at the center of a L3 microcavity. In the band gap, 0.25 – 0.33, there is suppression of the rates for dipoles oriented along x or y except at cavity mode resonances. b) A zoomed in version of a). The black lines denote when the spontaneous emission in the cavity is equal to that of bulk.

emission enhancement factor of $\tau_{0e}/\tau_{1e} = 3$ for the experiments and $\tau_{0c}/\tau_{1c} = 2.23$ for the calculations. The discrepancy between the spontaneous emission lifetimes most likely results from an insufficient number of frequency points for the radiation factors. This results in smaller rate multipliers that lead to longer lifetime values. Another source of error in the calculations is the relatively small number of photonic crystal periods surrounding the defect. Fewer periods result in less tightly confined modes and a decrease in the radiation factors.

Off-resonance, the quantum dot would have a base width, $b = 8\text{nm}$, height, $h = 3\text{nm}$, and a calculated lifetime of $\tau_{2c} = 1.804\text{ns}$. For this quantum dot the photons emitted have a wavelength of $\lambda = 926.4\text{nm}$ which corresponds to a normalized frequency of $f = 0.3047$. The radiation rate multipliers at this frequency are all less than one, because this is a non-resonant frequency within the 2D photonic band gap. The experimentally observed lifetime of $\tau_{2e} = 2.52\text{ns}$ is even longer than the calculated value. Here the discrepancy is most likely due to insufficient number of photonic periods surrounding the defect.

The third line of Table 3.3 shows the spontaneous emission lifetime if the $b = 9\text{nm}$

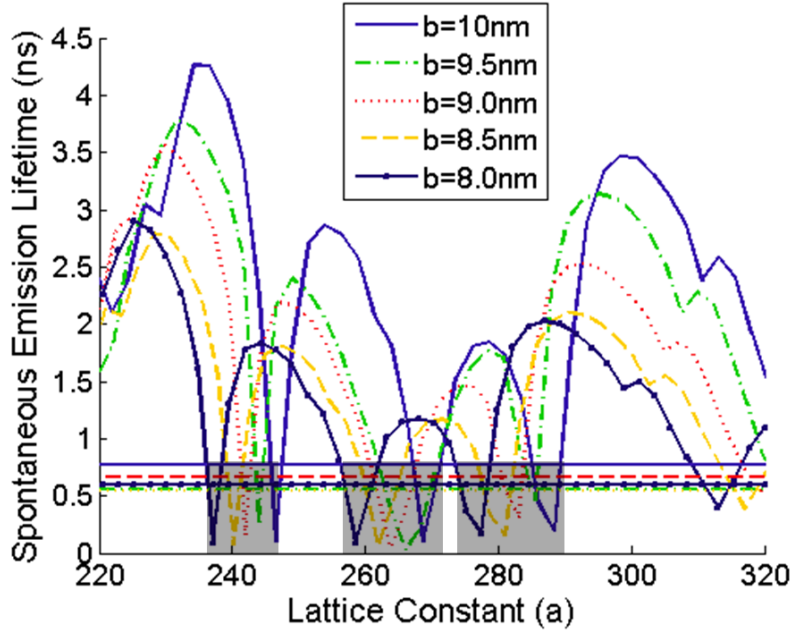


Figure 3.14: The spontaneous emission lifetimes for five different quantum dots in a L3 photonic crystal microcavity versus the photonic crystal lattice constant a . The three clusters of short lifetimes, denoted by the gray shaded regions, are for quantum dots on resonance with a cavity mode.

quantum dot is considered to be off-resonance. Since the results of the radiation rate calculations are relative, the absolute resonant frequency can be adjusted by tuning the value of the lattice constant, a . Increasing the lattice constant to $a = 287.9\text{nm}$, would shift the normalized quantum dot emission frequency from $f = 0.2987$ to $f = 0.3047$. For this quantum dot, the spontaneous emission lifetime is $\tau_{2c} = 2.329\text{ns}$. Although this is not the same as looking at the detuning of quantum dots from the resonant frequency in a fixed cavity, it does provide valuable information about the effects of fabrication errors.

If this concept is extrapolated then the spontaneous emission lifetime can be plotted as a function of the lattice constant. Figure 3.14 shows this dependence for 5 different quantum dots with base widths ranging from 8nm to 10nm. The range of base widths accounts for the non-uniformity of real quantum dot samples which was discussed in Sec. 3.3. In the Figure, the horizontal lines are the bulk radiation rates for each dot and the gray shaded regions denote the range of lattice constants for which the spontaneous emission

lifetime is less than in bulk due to coupling between a quantum dot and a cavity mode. If the lattice constant is tuned between $a = 277.5\text{nm}$ and $a = 288.5\text{nm}$, denoted by the right most gray shaded region, then one by one the quantum dots in the range $b = 8 - 10\text{nm}$ will be on resonance with the linearly polarized second cavity mode. The spontaneous emission lifetime is shortest for the dot with base width, $b = 8\text{nm}$, when $a = 277.5\text{nm}$ and for the $b = 10\text{nm}$ dot when $a = 288.5\text{nm}$. Consider a quantum dot sample grown for a laser that has a high density of dots with base widths between $b = 8 - 10\text{nm}$. This Figure illustrates that for a 10nm range of lattice constant there will be dots in the cavity that couple to the resonant mode and therefore have a short spontaneous emission lifetime. In a single photon source, there will be just one quantum dot within the cavity. Incorrect choice of the lattice constant could significantly hinder the device operation. If for example, the lattice constant is chosen to be $a = 277.5\text{nm}$ and the quantum dot inside of the microcavity has a base width other than $b = 8\text{nm}$ the emission will be suppressed and the operating speed would be slow.

The middle shaded region, $a = 258.5 - 268.7$, with short spontaneous emission lifetimes correspond to the first mode frequency in the L3 cavity. Although these lifetimes are even shorter than the second mode, they are not linearly polarized and are thus not suitable for a single photon source. It is interesting to note that for this mode, several quantum dots have enhanced spontaneous emissions for the same lattice constant. Such overlap would ease the fabrication precision required for single photon sources. The cluster of short lifetimes for $a = 237.1 - 246.5\text{nm}$, left shaded region, correspond to alignment of the quantum dot with the photonic band edge frequency.

3.5 Summary

This Chapter outlined a method of modeling the spontaneous emission lifetimes of quantum dots in bulk and in microcavities. The energy levels and the wavefunctions were obtained

from Nextnano++ [13]. A list of the parameters used in our calculations is given and the choices are justified through comparisons with experimental PL data from real quantum dot samples. Nextnano++ outputs the complex valued spinors which can be used to determine the complex wavefunctions. From these wavefunctions, the dipole matrix elements along the principal axis in the quantum dot are found. To calculate the spontaneous emission rates, these matrix elements are multiplied by weighing factors that represent the favorability of emission into a particular direction. The weighing factors are determined from 3D FDTD calculations that monitor the radiation leaving the problem space when x, y, or z dipoles radiate into the microcavity. It is found that this method provides spontaneous emission lifetimes that are in good agreement with experimental data.

Chapter 4

Quasi-3D Photonic Crystal

Microcavities

In Chapter 1, a quasi-3D photonic crystal microcavity was proposed for use in a single-photon source. This cavity utilizes the properties of both a 2D photonic crystal slab and a vertical distributed Bragg reflector (DBR) to enhance the rate of spontaneous emission while providing polarization control. A logical approach to designing the microcavity would be to begin with a 2D photonic crystal slab microcavity and to determine the effect of placing a DBR on either side. Thus, this Chapter begins with a brief discussion of 2D photonic crystal properties and photonic crystal slab microcavity designs. The effect and complexity of incorporating DBR mirrors in the single-photon source microcavity will be highlighted in a later part of the Chapter. As was discussed in Chapter 3, InAs quantum dots emit photons with wavelengths ranging from approximately $\lambda \approx 0.920\mu\text{m}$ (325.9THz) to $\lambda \approx 1.3\mu\text{m}$ (230.6THz). Since photonic crystals are described in normalized frequencies, i.e. ($\omega a/2\pi c = a/\lambda$), it is not necessary to know the exact design frequency at this point. The results presented here can be scaled to the proper frequency later. In fact, the trends illustrated in this chapter can be scaled for other applications that require a completely different operating frequency than for the single-photon source.

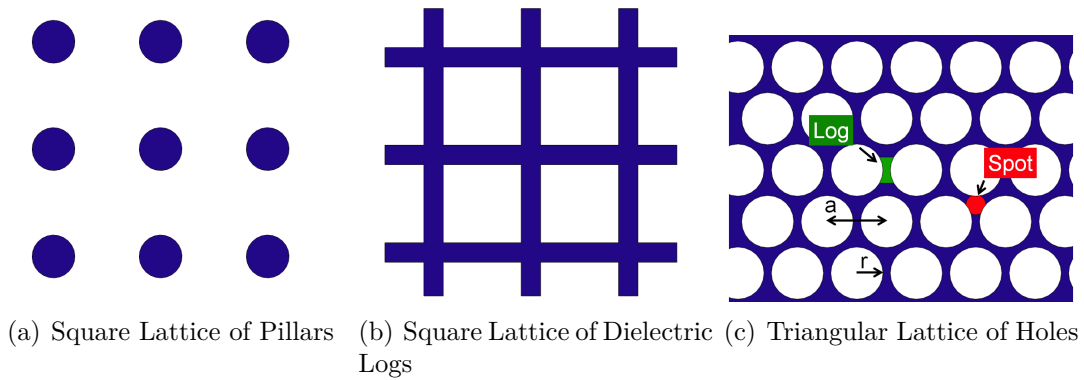


Figure 4.1: Three different 2D photonic crystal lattices are shown. Dark areas (blue) correspond to high dielectric material. a) A square lattice of dielectric pillars will have a TM band gap, b) 2D dielectric logs will have a TE band gap, and c) a triangular lattice of air holes in a dielectric can have both TE and TM band gaps.

4.1 2D Photonic Crystal Slab Microcavities

An ideal 2D photonic crystal is periodic in two dimensions and homogeneous in the third dimension. Although these structures do not have 3-dimensional periodicity, they nonetheless can exhibit band gaps for fields propagating on axis, with $k_z = 0$. If we assume on-axis propagation, then the fields can be split into two polarizations. In photonic crystals the convention is to define transverse electric (TE) modes as those with the electric field in the plane of the periodicity and the magnetic field normal. Transverse magnetic (TM) modes then have the magnetic field in the plane and the electric field normal.

Some common examples of 2D photonic crystals are shown in Fig. 4.1. For simplicity, we will choose air as the low index medium. A properly designed square lattice of dielectric pillars in air, shown in Fig. 4.1(a), can have a TM band gap. The presence and size of the band gap depends on the contrast between the dielectric constant of the pillars and that of the surrounding medium. The filling factor, or the fraction of dielectric material occupying a unit cell, also plays a role in determining the band structure. The frequency of a mode is associated with the corresponding electric field density: the larger the field concentration in the high index material, the lower the frequency of the mode. This follows from the

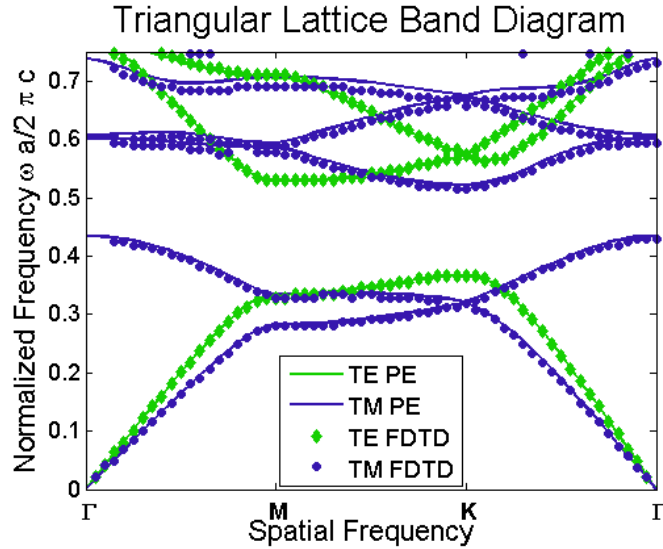
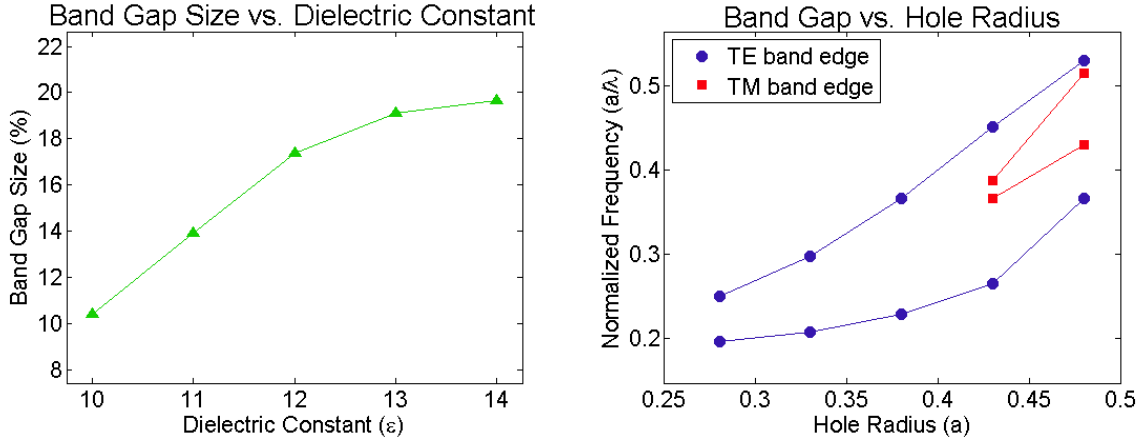


Figure 4.2: The band diagram for a 2D triangular lattice of air holes in dielectric slab with $\epsilon = 13.0$. The hole radius is $r = 0.48a$. The data points were obtained with FDTD methods (Sec. 2.3.2) and the solid lines were obtained with planewave expansion techniques (MIT Photonic Bands).

electromagnetic variational theorem [1]. A TE band gap is not possible in the square lattice of pillars because the electric field will always have to penetrate the air region. For the TE polarization, the field concentration will not vary significantly from the first mode to second and the variation in the frequencies will not be large enough to form a gap. A TE band gap can occur in a square lattice of dielectric logs, shown in Fig. 4.1(b). Here the high dielectric regions are continuous and the low frequency modes can be highly concentrated there. In order for the next mode to be orthogonal though, a portion of the field must penetrate the air region. The frequencies of the two bands will then be very different and a band gap will occur. For this structure, there is no TM band gap.

Consider now the photonic crystal of Fig. 4.1(c). This triangular lattice of air holes in a dielectric can be thought of as having both isolated pillars and interconnected logs. When properly designed, it can possess a band gap for both TE and TM polarized fields, making it particularly interesting. An overlap of the TE and TM band gaps occurs for air holes of radius $r = 0.48a$ in a dielectric slab with $\epsilon = 13$, as shown in Fig. 4.2. For



(a) Effect of Changing Dielectric Constant on Band Gap (b) Effect of Changing Hole Radius on Band Gap

Figure 4.3: a) As the dielectric constant of the bulk material is decreased, the TE and TM band gaps become smaller. For a wide range of semiconductor materials the band gap should remain. b) As the ratio of the hole radius to the lattice constant is decreased, the size of the TE and TM band gaps decrease. The TM band gap closes before the TE gap and the complete 2D gap is eliminated.

this structure the normalized midgap frequency is $0.4719(a/\lambda)$. To center the band gap around our frequency of interest, $f = 230.6THz$ ($\lambda = 1.3\mu m$), the lattice constant must be $a = 613nm$ and the hole radius $r = 294nm$. Because the properties of the photonic crystal can be scaled to any size that can be fabricated, the size of the band gap is given as a ratio of the frequency range of the gap to the midgap frequency. For this structure we obtain a band gap of 17.97%.

The size and position of the band gap change as the dielectric constant and r/a ratio change. Keeping the r/a ratio constant and decreasing the dielectric constant, $\epsilon < 13$, increases the band frequencies and decreases the gap size. Increasing the dielectric constant has the opposite effect and the gap size increases. The effect of the dielectric on the gap size is illustrated in Fig. 4.3(a). Most semiconductor materials of interest fall within the range of dielectric constants in Fig. 4.3(a), and they will have a complete band gap when $r = 0.48a$. If the dielectric constant is instead held constant at $\epsilon = 13$ and the hole radius is decreased, the complete band gap will decrease and eventually disappear, see Fig. 4.3(b).

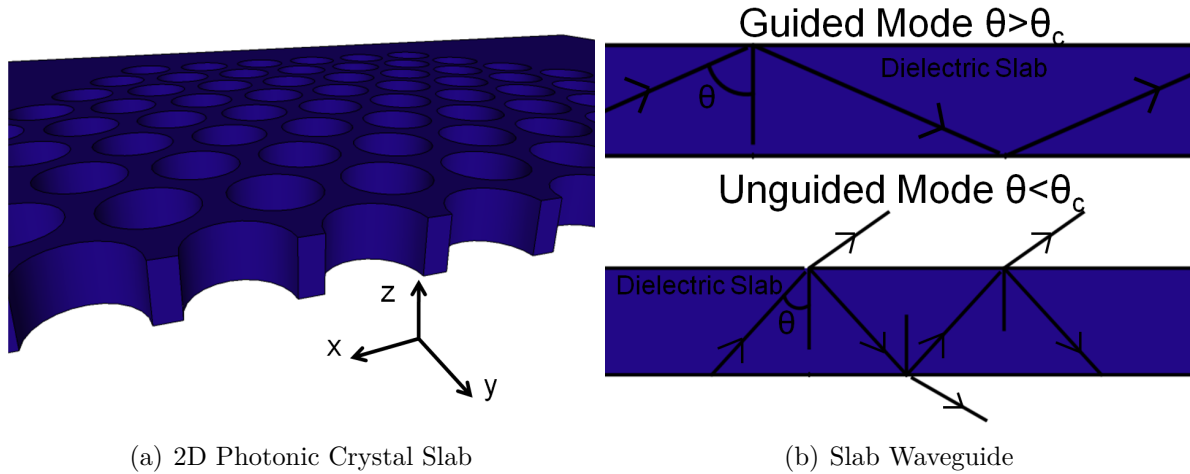


Figure 4.4: a) A 2D photonic crystal with a triangular lattice of air holes in a high index slab. b) A slab waveguide with the requirements for a guided mode.

As the holes become smaller, the photonic crystal no longer seems to have both pillars and logs. Once the TM band gap is closed no complete gap can exist. For a decrease in r/a from 0.48 to 0.43 the size of the band gap decreases from 17.97% to only 5.63%. Once $r/a = 0.38$, the TM band gap has entirely disappeared.

Thus far it has been assumed that the 2D photonic crystal is homogeneous in the third dimension. While this serves as an illustrative example, it is important to consider the more realistic case of a finite slab of high index material penetrated by air holes, Fig. 4.4(a). In this structure, reflections will occur from both distributed Bragg reflection off of the periodic lattice and total internal reflection at the air-dielectric interface. The 2D photonic crystal slab is essentially a combination of the infinite 2D photonic crystal and a dielectric slab waveguide. In a slab waveguide, light traveling at certain angles undergoes total internal reflection at the air-dielectric interface and remains inside the slab. This angle, shown in Fig. 4.4(b), is referred to as the critical angle and is given by $\Theta_c = \sin^{-1}(n_a/n_d)$ where n_a , n_d are the index of refraction for air and the dielectric, respectively. The thickness of the slab waveguide will determine the number of modes that can propagate, with thicknesses less than λ supporting only a single mode. Slab photonic

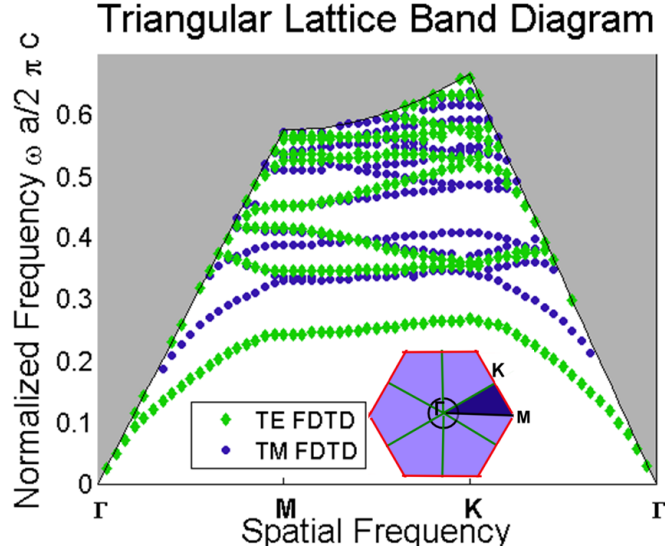


Figure 4.5: The band diagram for a 2D triangular lattice of air holes in InGaAsP, dielectric constant $\epsilon = 11.56$. The hole radius is $r = 0.3a$ and slab thickness is $t = 0.6a$. The data points were obtained with FDTD methods (Sec. 2.3.2). The inset shows the Brillouin zone, light blue, and the irreducible Brillouin zone, dark blue.

crystals are typically no thicker than a , the lattice constant. Thicker slabs can support more modes which can fill and close the band gap. Slabs that are thinner than $.5a$, have smaller band gaps and may not remain stable during the fabrication process. In this thesis, only slabs of reasonable thickness, $t = 0.5a - 0.9a$, are considered.

The thickness of the slab must now be taken into consideration when calculating the band diagrams, where 3D FDTD methods will be used. Figure 4.5 shows the band diagram for a $t = 0.6a$ thick InGaAsP slab with $\epsilon = 11.56$ and $r = 0.3a$. The slab structure is symmetric about the $z = 0$ plane, which allows the modes to be classified as either TE-like (even) or TM-like (odd). They are, however not strictly TE or TM because there are no x or y mirror symmetries to allow a full decoupling of the fields. The gray shaded region in Fig. 4.5 is the light cone. In a three-dimensional structure, the wavevector has three components. For the 2D photonic crystal, the wavevector is separated into two main components k_{\parallel} which refers to the in-plane wavevector (k_x, k_y) and k_z which is perpendicular to the plane. The band diagram of Fig. 4.5 is actually a projected band

diagram where $k_z = 0$. If k_z is non-zero, then at some point the fields will encounter the dielectric-air interface. As long as the angle of incidence is larger than the critical angle, the fields will be totally reflected. The light cone denotes which wavevectors will have a large enough angle of incidence to prevent the fields from leaking out into the surrounding air. The boundaries of the light cone are calculated by taking $\omega/c = |k_{||}| = \sqrt{k_x^2 + k_y^2}$ for each point along the Brillouin zone (inset of Fig. 4.5).

In Fig. 4.5 there is a band gap for the TE-like modes between 0.2682 – 0.3462, but no gap for the TM-like modes within this frequency range. This is not surprising because even for the ideal 2D photonic crystal with a higher index contrast, the TM band gap disappears from the TE gap once $r \leq 0.43a$, as shown in Fig. 4.3(b). It is tricky to obtain an overlap of the TE-like and TM-like band gaps in photonic crystal slabs but at sufficiently large r/a an overlap occurs [2]. When r/a is large, the logs are very thin and the holes are very large. Such a photonic crystal is particularly sensitive to fabrication errors and may not be structurally robust. For these reasons, smaller r/a ratios are typically chosen, like the one in this example. Even if there was an overlap of the TE and TM-like band gaps, this would not be considered a complete band gap. In photonic crystal slabs, band gaps exist only for modes that are guided in the slab waveguide. Once the bands enter the light cone the guided modes are eliminated and no band gaps can exist.

Although there is no complete band gap in photonic crystal slabs, the size of the TE-like gap is still important. The size of the band gap changes as the slab thickness is varied, as illustrated in Fig. 4.6. Here the dielectric slab has $\epsilon = 11.56$ and $r = 0.3a$. As the thickness of the slab is increased the size of the band gap increases and asymptotically approaches the ideal 2D case. For slab thicknesses greater than $1.1a$, the size of the gap is significantly reduced. This is expected since the guide is now thick enough to support multiple modes in the vertical direction.

Thus far the discussion has been limited to the band structures of perfectly periodic photonic crystals and photonic crystal slabs. The presence of defects in photonic crystal

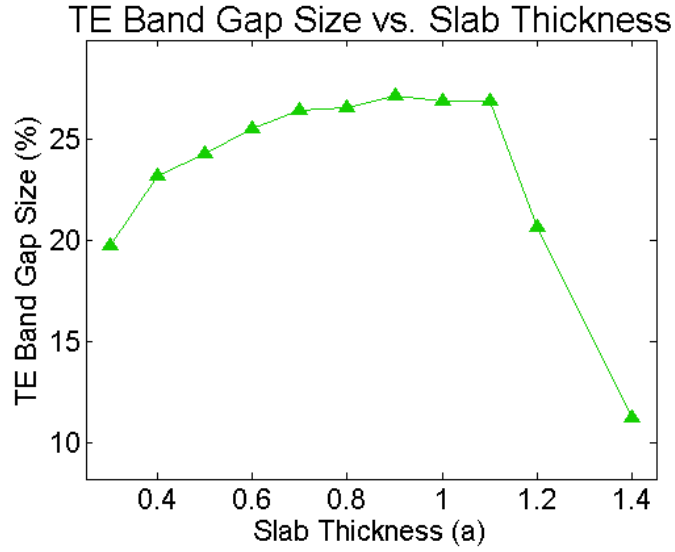


Figure 4.6: The size of the TE band gap for an InGaAsP slab, dielectric constant $\epsilon = 11.56$, is plotted versus the thickness of the slab. The hole radius is fixed to $r = 0.3a$ and the slab thickness varies from $t = 0.3a$ to $t = 1.2a$.

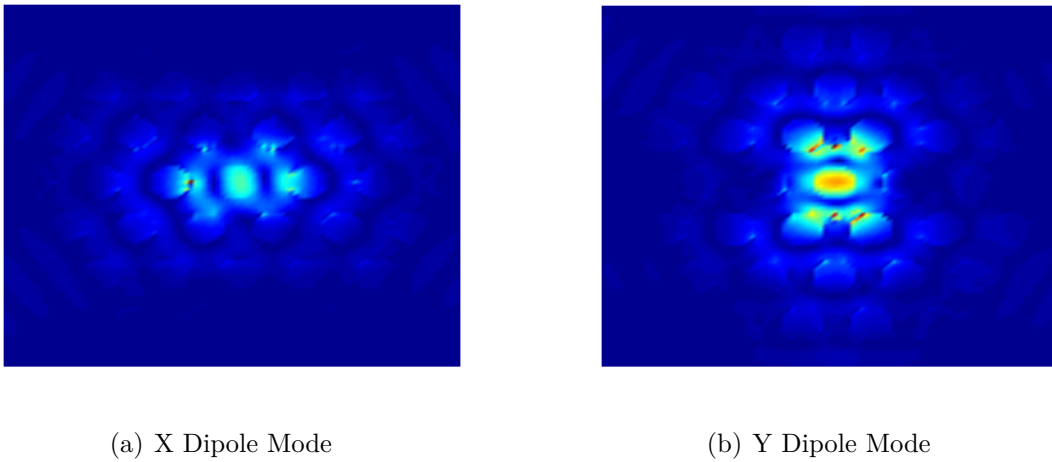


Figure 4.7: The mode profile for the a) x-dipole and b) y-dipole, found by taking the magnitude squared of the electric field across the z-plane at the slab center.

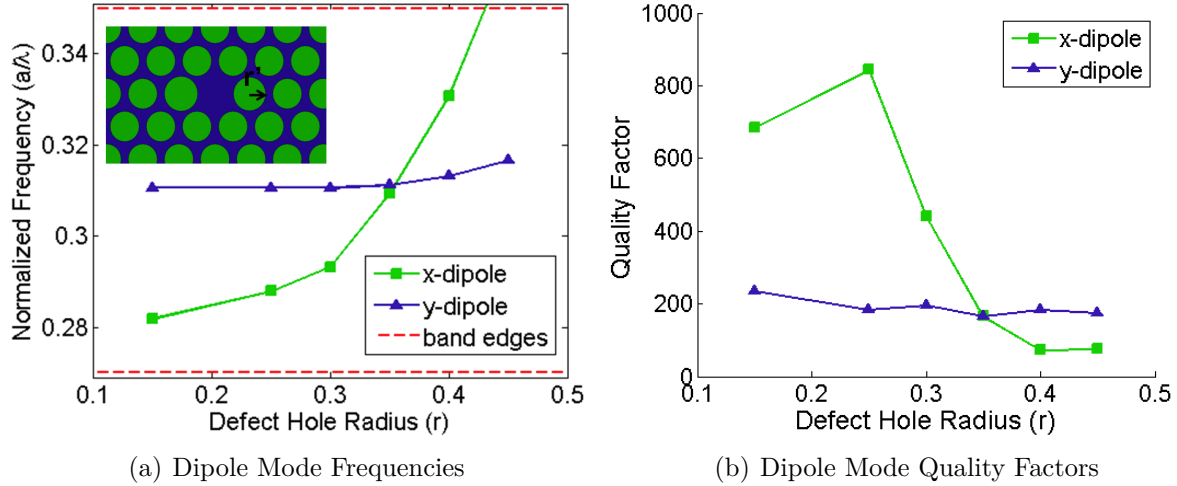


Figure 4.8: a) The degeneracy splitting of the dipole mode by changing r' (shown in inset). When $r' \neq r$ the frequencies of the x-dipole and y-dipole mode do not coincide. b) As the geometry of the cavity is changed the quality factor of the x and y dipole modes changes.

slabs will lead to localized modes that appear within the band gap. For the single-photon source, the mode should satisfy the following requirements: appear at $230.6THz$, have a distinct x or y polarization, have a low to moderate quality factor. When a single hole is removed from the photonic crystal slab, a dipole mode of double degeneracy is formed. For a slab of GaAs with dielectric constant $\epsilon = 12.96$, hole radius $r = 0.35a$, and slab thickness $t = 0.5a$, the mode appears at the normalized frequency $f = 0.312$. The physical dimensions of the photonic crystal would then be $a = 405nm$, $r = 142nm$, and $t = 203nm$ for operation at our target frequency. Figure 4.7 shows the mode profiles for the x-dipole and y-dipole.

The degeneracy of the dipole mode can be eliminated if the symmetry of the photonic crystal is broken [3]. One way to break the symmetry is to vary the size of the inner holes surrounding the defect as shown in the inset of Fig. 4.8(a). By adjusting the radii of the two holes that lie along the \hat{x} direction, see Fig. 4.4(a) for the axis, the frequency of the x-dipole mode can be adjusted. The y-dipole mode is favored in this geometry because the perturbation is along \hat{x} and the fields of the mode lie primarily along \hat{y} . These new

geometries will affect the mode frequency and the quality factor. Figure 4.8(a) shows how the mode frequencies vary as the hole radius is changed. When $r' \neq r$, there are two mode frequencies corresponding to the x-dipole or y-dipole mode. As the defect radius, r' , is made larger, the y-dipole mode frequency increases only slightly. The x-dipole is more sensitive to the perturbation of the cavity geometry. It is shifted up in frequency and eventually leaves the band gap. For $r' < r$, the frequency of the y-dipole again remains relatively unchanged. The x-dipole mode is shifted down in frequency towards the dielectric band edge. When $r' \neq r$, the degeneracy is lifted and single mode operation can be achieved by placing an emitter in the cavity that emits photons of either the x or y dipole mode frequency.

As discussed in Chapter 1 the spontaneous emission rate of a dipole source is drastically affected by its surroundings. When a dipole source is placed inside of a photonic crystal microcavity, its emission can be enhanced or suppressed depending on the oscillation frequency of the dipole and its location in the microcavity [4]. Section 2.3.4 discussed how FDTD methods can be used to obtain the spontaneous emission enhancement factor. The same techniques are applied here to study the spontaneous emission of a dipole located inside of a photonic crystal microcavity.

Consider first, the case of a $t = 0.5a$ thick GaAs slab suspended in air. The index of refraction is $n = 3.6$, the hole radius is $r = 0.3a$ and a doubly degenerate dipole mode is created by removal of a single air hole from the microcavity. Fig. 4.9 shows the spontaneous emission enhancement as a function of frequency for an E_x -polarized point dipole located at the center of the photonic crystal microcavity. This particular photonic crystal structure exhibits a band gap between the normalized frequencies $0.252 - 0.34$. Throughout this frequency range the spontaneous emission is suppressed except at the resonant mode frequency, 0.2933 , where the emission factor is strongly enhanced.

In Fig. 4.10 the spontaneous emission of an E_z -polarized point dipole located at the center of the cavity is shown. This source does not couple to the TE-like modes which

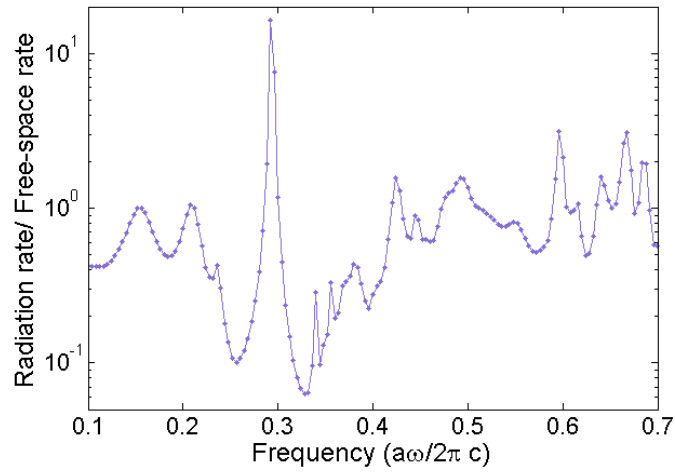


Figure 4.9: The spontaneous emission rate for an Ex-polarized dipole centered in a single defect GaAs slab microcavity. Here the spontaneous emission is normalized to the rate in a uniform dielectric. This source couples to the TE-like modes of the 2D photonic crystal slab and enhancement occurs at the resonant frequency.

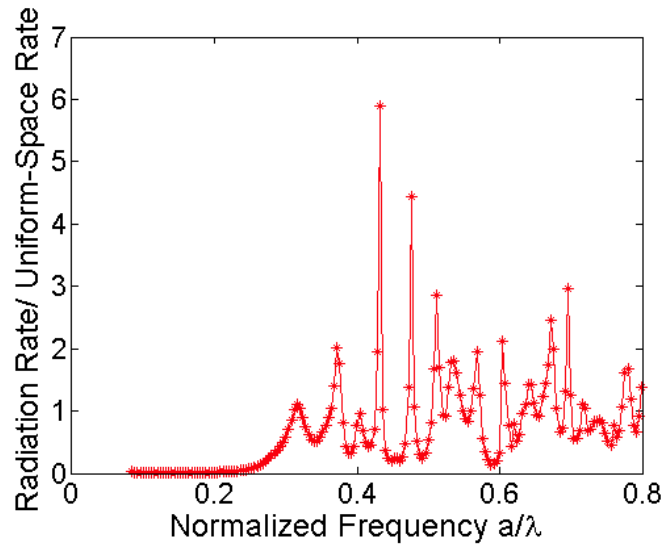


Figure 4.10: The spontaneous emission rate for an Ez-polarized dipole centered in a single defect GaAs slab microcavity. Here the spontaneous emission is normalized to the rate in a uniform dielectric. This mode couples to the TM-like modes of the slab PC structure.

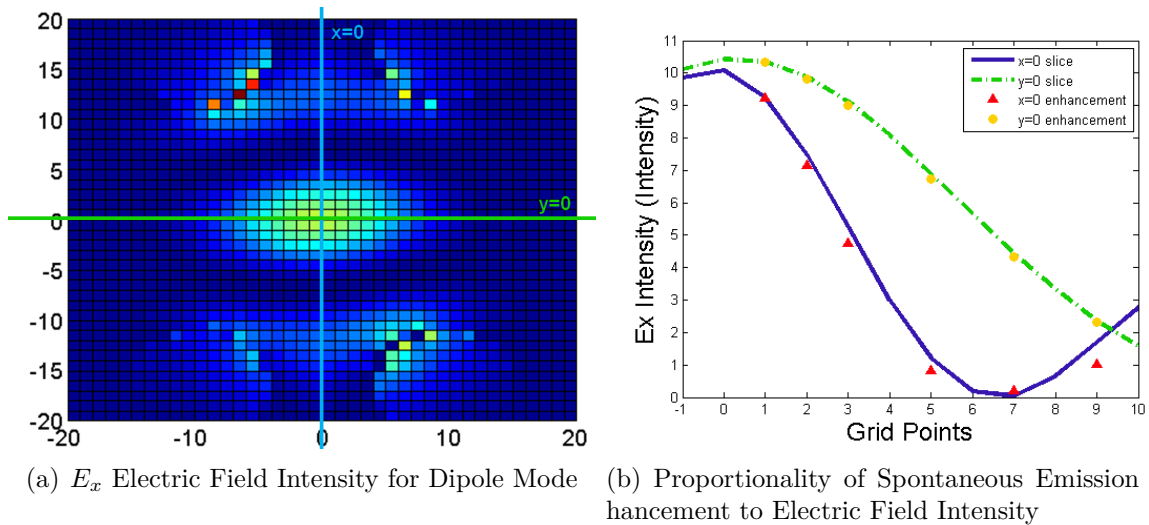


Figure 4.11: a) The electric field intensity is plotted along a slice at the center of the photonic crystal slab. b) The field intensity of a) is sliced along the $x = 0$ and the $y = 0$ axis and the magnitude of the intensity is normalized to the spontaneous emission rate at the $x = 1$ or $y = 1$ position respectively. The data points correspond to the spontaneous emission rates for a dipole located at various points along the axis.

is why there is no peak at the resonant mode frequency of 0.2933. Instead this source couples to the TM-like modes and has a peak within the TM band gap that lies between 0.4086 – 0.4473. The suppression of emission for frequencies below ≈ 0.25 is due to the fact that there are no TM-like modes or bands below this frequency.

The spontaneous emission enhancement is affected by the placement of the oscillating dipole within the microcavity. This dependence arises from the fact that the radiation rate of the dipole is proportional to the squared amplitude of the electric field [4]. If an E_x -polarized point dipole source is again placed inside of the slab microcavity and its position is varied, the spontaneous emission rate should change proportionally to the change in the magnitude of the electric field. Figure 4.11(a) shows the squared magnitude of the electric field and Fig. 4.11(b) shows the spontaneous emission enhancement for the resonant mode, $f = 0.2933$, as a function of position. The dipole was shifted from the center of the cavity along the x or y axis and the spontaneous emission enhancement was recorded at several points, shown as data points in Fig. 4.11(b). Here the solid lines are slices of the squared

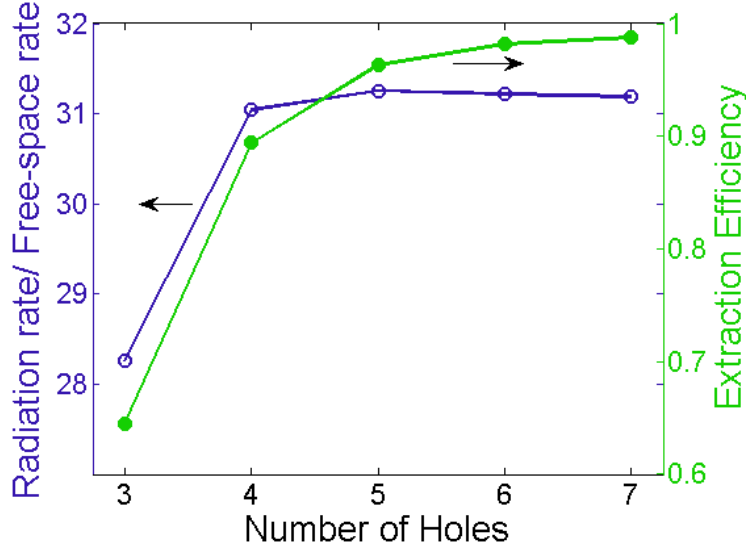


Figure 4.12: The spontaneous emission rate enhancement for an Ex-polarized dipole centered in a single defect GaAs slab microcavity, $r = 0.3a$ and $t = 0.5a$, for increasing rows of photonic crystal around the defect, open circles. The extraction efficiency is also shown and approaches 1 as the number of holes is increased, closed circles.

magnitude of the electric field along the x or y directions normalized to the spontaneous emission at the $x, y = 1$ point. As expected, the spontaneous emission enhancement is proportional to the electric field. We see that for a dipole shifted along the x -axis, the spontaneous emission rate slowly decreases. When the dipole is shifted along the y -axis the rate decreases rapidly and then increases again. The minimum value occurs around $(0, 7)$, which is where the electric field intensity is a minimum.

The extraction efficiency of the device can be found using the FDTD method as well. This efficiency is defined as the ratio of the flux through the top and bottom surfaces of the slab to the total outgoing flux [2]. During the course of the spontaneous emission calculations, the \hat{z} component of the Poynting vector is summed over the same surface used to compute the emitted power. By taking the ratio of these sums, the extraction efficiency as a function of frequency is obtained. As shown in Fig. 4.12, the extraction efficiency at the resonant frequency increases as the number of rows surrounding the defect increases. This is expected because the more holes surrounding the defect, the better the in-plane

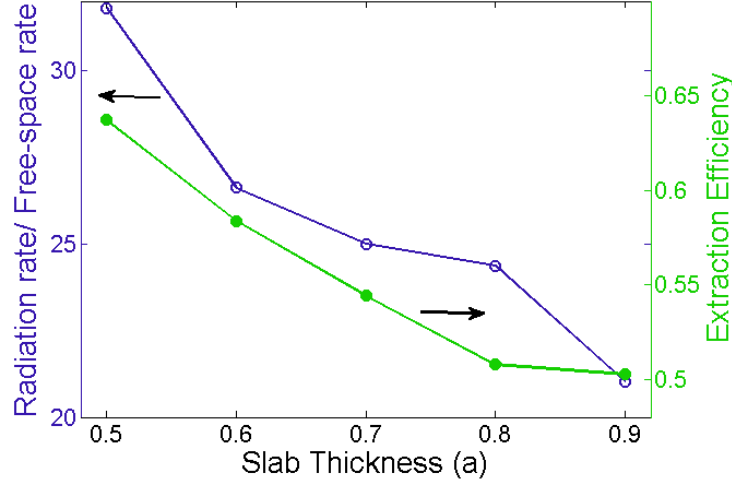


Figure 4.13: The spontaneous emission rate for an Ex-polarized dipole centered in a single defect GaAs slab microcavity as a function of the slab thickness.

confinement. There should be less leakage through the photonic crystal and more energy exiting the device through the top or bottom of the slab. The spontaneous emission rate is only slightly increased, although it also exhibits an asymptotic behavior. While 4 or 5 holes surrounding the defect is adequate to accurately determine the spontaneous emission rate, accurate calculation of the extraction efficiency requires closer to 6 or 7 rows of holes. It is worth noting that as expected, the resonant frequency does not change as rows of holes are added.

When the number of holes surrounding the defect is kept constant and the slab height is increased, the spontaneous emission enhancement and the extraction efficiency decrease. This is illustrated in Fig. 4.13 for a GaAs slab with 3 rows of holes surrounding the defect. As the slab thickness increases, there is a larger volume of high dielectric material for the electromagnetic fields to occupy. The magnitude of the electric field decreases which leads to a decrease in the spontaneous emission rate. For thicker slabs, the extraction efficiency decreases due to the fact that more of the fields satisfy the total internal reflection condition and remain in the slab.

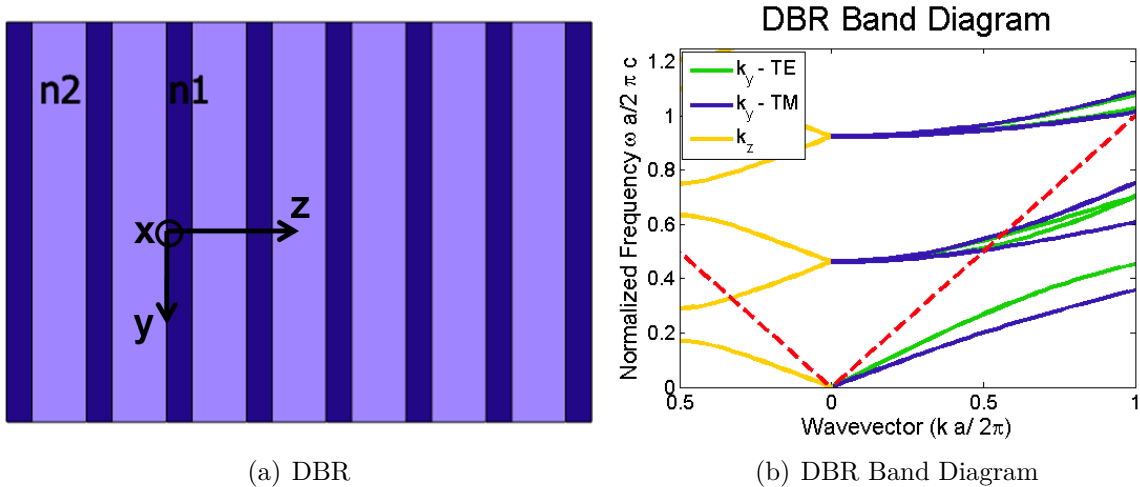


Figure 4.14: a) DBR with the coordinate axis used in this section. b) The band diagram for a quarter wave stack of GaAs $n = 3.6$ and oxidized AlGaAs $n = 1.544$ for propagation along $(0, 0, k_z)$, left, and $(0, k_y, 0)$, right. The red dashed line is the light line.

4.2 1D Distributed Bragg Reflection Microcavities

The concept of distributed Bragg reflection was first introduced in Chapter 1. Previously, only on-axis propagation was considered, $(0, 0, k_z)$, where z is the axis of periodicity; see Fig. 4.14(a). For on-axis propagation it was found that a photonic band gap exists and light with frequencies in the gap that is incident on the DBR will be completely reflected. When the incident light is not propagating on axis, then the symmetry is broken and light will be able to propagate through the crystal. The modes of a quarter-wave DBR made of GaAs, $n = 3.6$, and oxidized AlGaAs, $n = 1.544$, are shown in Fig. 4.14(b). On the left hand side, the bands are plotted for $(0, 0, k_z)$ and on the right they are plotted for $(0, k_y, 0)$. For on-axis propagation the TE (polarization along x direction) and TM (polarization along the yz plane) modes are degenerate, but this degeneracy is split for off-axis propagation.

Although there is no complete band gap for the DBR, it is possible to achieve omnidirectional reflection [5]. In fact the quarterwave stack of Fig. 4.14(b) can have an omnidirectional gap, as shown in Fig. 4.15. The TE bands are plotted on the left hand side and the TM are on the right. The green and blue shaded regions correspond to a continuum

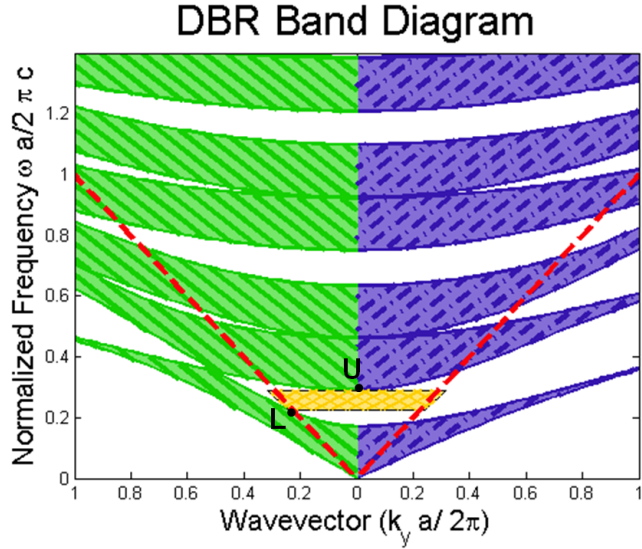


Figure 4.15: The DBR consists of a quarter wave stack of GaAs $n = 3.6$ and oxidized AlGaAs $n = 1.544$. The hatched regions on the left hand side are the continuum of TE modes for $k_z = 0$ to $k_z = 0.5$ and the right hand side are the TM modes. The red dashed line is the light line. Above the light line in the yellow cross-hatched region lies the region of omnidirectional reflectivity.

of modes for $k_z = 0$ to $k_z = 0.5$ and the red dashed line is the light line. Two conditions must be satisfied for the omnidirectional gap to exist. First, the index contrast between the two DBR materials must be high enough so that point U is above point L. Second, the light must be incident from a material with a lower index of refraction than either of the two materials of the DBR. The yellow hatched region in Fig. 4.15 is the omnidirectional reflection region. While the presence of an omnidirectional gap is an exciting feature of the DBR, it will not be useful for the single-photon device because light will originate from within the high index slab. The second condition for omnidirectional reflectivity will not be met. The possible advantage of using a DBR in the single-photon source will be examined in detail in Section 4.4.

Before concluding the discussion of DBRs, the design of single defect DBR microcavities is presented. For on-axis propagation, altering the thickness of one of the DBR layers introduces a state within the band gap and light is localized at the defect. The size of the

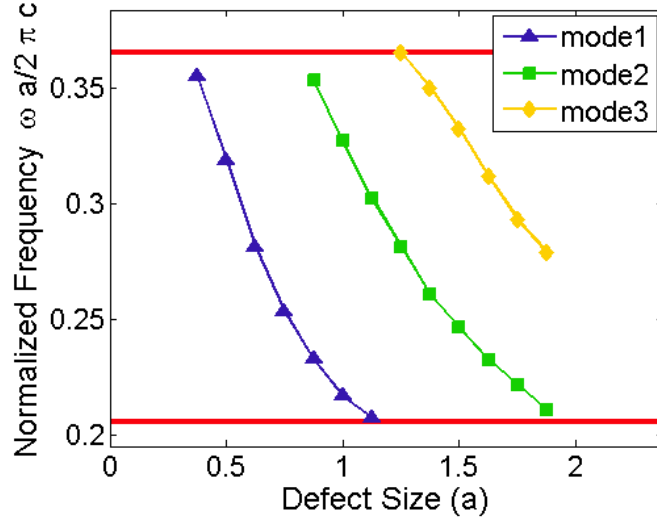


Figure 4.16: The DBR is a quarter wave stack of GaAs $n = 3.6$ and oxidized AlGaAs $n = 1.544$. The cavity consists of 4 DBR repetitions on either side of a central GaAs defect. As the defect is made larger higher order modes are pulled into the band gap from the air band.

defect layer will determine the mode frequency and profile. To illustrate this, consider the quarter-wave stack discussed earlier. If one layer of GaAs is increased slightly, then a mode will appear within the band gap near the air band edge. As the thickness is increased, the mode will sweep across the gap. When the thickness of the GaAs defect layer is doubled, the thickness corresponds to half of a wavelength at the center of the band gap. It is expected that one mode will be supported with a frequency of \tilde{c}/λ , where \tilde{c} is the speed of light in GaAs and λ is the wavelength of the mode. As the thickness is increased further, the mode moves down into the dielectric band. As the defect is made larger, higher order modes enter and traverse the band gap one by one. This is illustrated in Fig. 4.16.

4.3 Quasi-3D Photonic Crystal Band Diagrams

The 2D photonic crystal slabs examined in Sec. 4.1 used distributed Bragg reflection for in-plane confinement and total internal reflection for vertical confinement. Whereas total

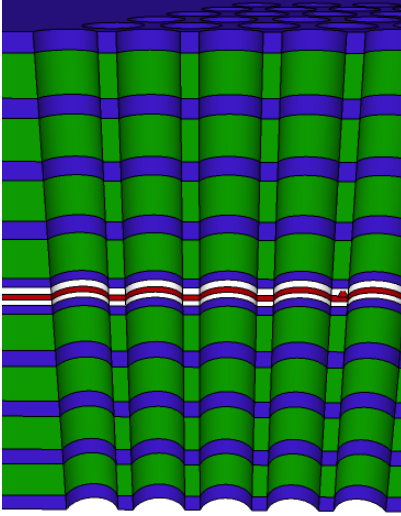


Figure 4.17: Schematic of the bulk quasi-3D photonic crystal. In-plane confinement and vertical confinement are caused by distributed Bragg reflection off of a 2D photonic crystal lattice and a vertical DBR, respectively.

internal reflection is completely dependent on the index contrast between the slab and the surrounding material, distributed Bragg reflection can be engineered by altering not only the materials but the layer thicknesses and the number of periods. Instead of relying on total internal reflection it may be beneficial to consider using 1D distributed Bragg reflectors. Before attempting to design microcavities in this quasi-3D photonic crystal, shown in Figure 4.17, it is beneficial to investigate the band structures of the bulk crystal.

Using 3D FDTD and symmetry approximations, it is possible to account for the DBR mirrors in the 2D photonic crystal band diagram. Figure 4.18 shows how the number of periods of the DBR affects the TE bands. The structure simulated here has GaAs slab thickness, $h = 0.5a$, and hole radius, $r = 0.3a$. The DBR is the same one used previously in this chapter, with alternating layers of GaAs and oxidized AlGaAs designed to be a quarter wave stack for $\lambda = 1.3\mu m$. With only 4 periods of this DBR, the reflectivity is greater than 98% for the normalized frequencies $0.2252 - 0.3551(a/\lambda)$. Here the lattice constant for the normalized frequencies is taken as the lattice constant of the 2D photonic

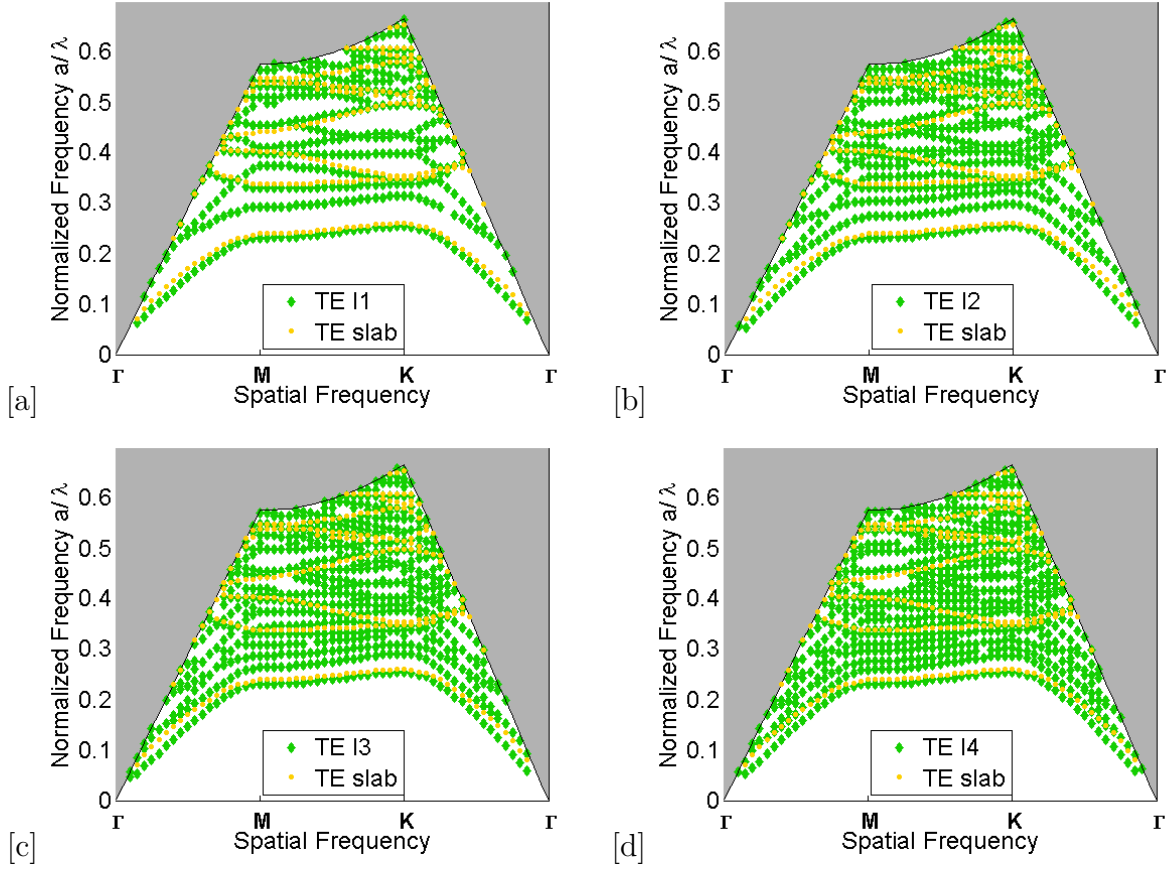


Figure 4.18: The band diagrams for a quasi-3D photonic crystal microcavity with 4.18(a) 1, 4.18(b) 2, 4.18(c) 3 or 4.18(d) 4 periods of DBR around the slab. The lattice constant was taken as $a = 30$, the GaAs layer thickness is $\approx 152.3\text{nm}$ and the oxidized AlGaAs layer is $\approx 348.2\text{nm}$ thick. The yellow circles overlaid on the band diagrams are the TE bands for the GaAs slab in air.

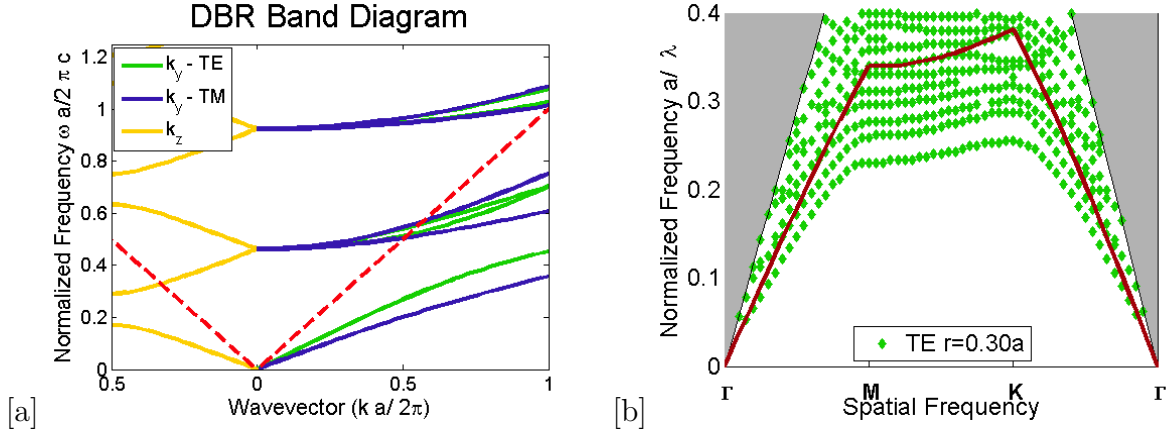


Figure 4.19: 4.19(a)) The on-axis (left) and off-axis (right) band diagrams for the DBR used to clad the 2D photonic crystal slab. 4.19(b)) The TE band diagram for the quasi-3D photonic crystal with 4 periods of DBR above and below the slab. The new light line, drawn as a bold red line, is determined from the DBR band diagram.

crystal and not the DBR to ensure frequency matching. The placement of the bottom TE band, the dielectric band, remains relatively constant as more periods of the DBR are added around the slab. This is expected because the dielectric band depends mostly on the thickness, filling factor, and dielectric constant of the slab and not the surrounding medium. Also shown in Fig. 4.18 as an overlay, is the band diagram for the GaAs slab suspended in air. As the periods of the DBR are added around the GaAs slab, these TE slab bands remain relatively intact but are shifted down slightly in frequency. Additional bands also begin to appear. By the time 3 periods of the DBR surround the slab, there are 4 bands within the original 2D photonic crystal band gap. It appears that the band gap of the 2D photonic crystal is completely eliminated by the DBR mirrors.

When the DBR mirrors are used to provide vertical confinement, the light line as discussed earlier is no longer relevant. The purpose of the light line in the band diagram for a 2D photonic crystal of finite slab thickness is to denote which frequency/wavevector combinations will satisfy the condition of total internal reflection and lead to guided slab modes. For the case of the DBR mirrors, the condition for reflection at the boundary of the GaAs slab is no longer dependent on total internal reflection. Instead the condition

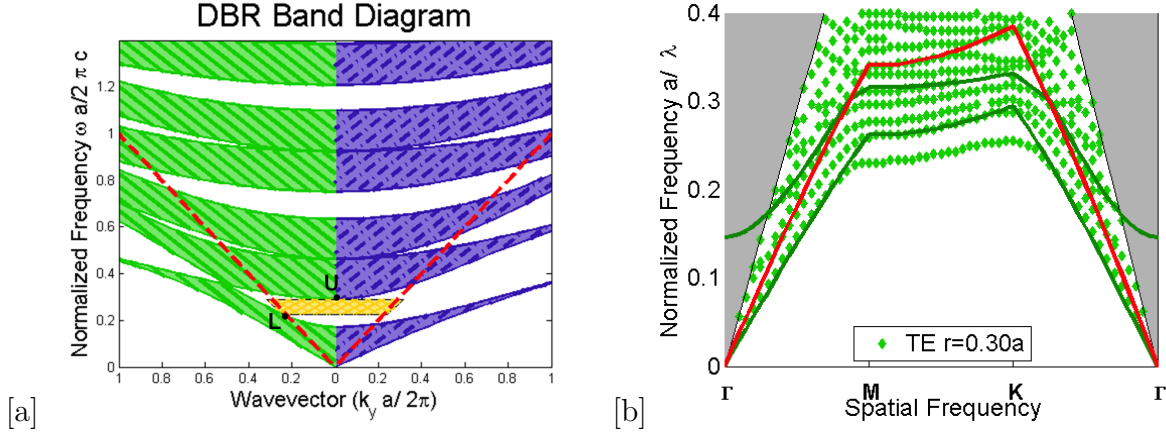


Figure 4.20: a) The TE (left) and TM (right) band diagrams for the DBR used to clad the 2D photonic crystal slab. b) The TE band diagram for the quasi-3D photonic crystal with 4 periods of DBR above and below the slab. The states in the 2D photonic crystal band gap are determined from the TE modes in the DBR band diagram.

for reflection will depend on the dispersion relation given by the lowest bands of the DBR band diagram for off-axis propagation, $k_y \neq 0$. The dispersion relation for the DBR was given in Fig. 4.14(b) but is repeated in Fig. 4.19(a) for convenience. This figure shows the on-axis bands on the left hand side and the off-axis bands on the right. In computing the band diagram for the DBR, $k_{||} = k_y$ was assumed. This choice is irrelevant due to the rotational symmetry in the plane perpendicular to the periodicity. To place the new light line on the 2D photonic crystal band diagram, first the magnitude of the wavevector, $|k| = \sqrt{k_x^2 + k_y^2}$, must be found at each point along the Brillouin zone. The light line frequency is then the frequency of the lowest TM band at $k = k_{||}$ in the right hand side of Fig. 4.19(a). The frequencies must be renormalized to the lattice constant of the 2D photonic crystal. Some additional scaling is also required because the air holes penetrate the DBR layers and reduce the overall effective index of the material. Because this new light line is generated from the DBR band diagrams, it will be referred to as the DBR light line. The band diagram for the GaAs slab with 4 periods of the DBR above and below the slab is shown in Fig. 4.19 with the DBR light line given by the bold red line. All modes above this line are able to pass through the DBR and are lossy.

For the quasi-3D band diagrams with 4 periods of the DBR around the GaAs slab, there are 4 bands that lie in the 2D photonic crystal band gap. Comparison of Fig. 4.20(a) and Fig. 4.20(b) reveals that the 4 bands are actually the same shape as the first shaded region on the left hand side of the DBR band diagram. The first and fourth bands appearing in the quasi-3D band diagram can be reproduced by mapping the TE bands of the DBR onto the quasi-3D photonic crystal band diagram in a manner similar to that used to determine the new light line. Using this method, and the same scaling factor, the dark green curves are found in Fig. 4.20(b). The first line corresponds to the case where $(0, k_y, 0)$ and the fourth to $(0, k_y, 0.5)$. These four bands denote a frequency range in the 2D photonic crystal band gap in which DBR TE modes exist. As opposed to the band diagram in Fig. 4.20(a) where there is a continuum of modes for $k_z = 0 - 0.5$, the modes in the quasi-3D band gap are discrete. The affect these bands have on the quasi-3D cavity resonances will depend on the mode profiles and will be investigated in the next section.

Any band gap that would exist in the quasi-3D structure must exist below the new light line and above the leaky DBR bands. Closer investigation of the band diagram in Fig. 4.19 reveals a small band gap between $0.3277 - 0.3306$. In Section 4.1, an increase in the hole radius lead to a larger band gap for a 2D suspended slab. Figure 4.21 shows the quasi-3D photonic crystal band diagrams for a GaAs slab of height $h = 0.5a$ with 4 periods of DBR cladding for radii, $r = 0.30a, 0.35a, 0.40a$, and $0.45a$. As the air hole radius is increased, the bands move upward in frequency due to the smaller effective index just as they would without the DBRs. The bands that result from the 2D photonic crystal also spread apart in frequency, however the overall size of the band gap is limited by the DBR bands. When $r = 0.30a$, the 2D photonic crystal band gap lies below the DBR light line. Increasing the hole radius to $r = 0.35a$ pushes the second TE 2D photonic crystal band up above the light line. The band gap now appears between the top of the leaky DBR band, $f = 0.3462(a/\lambda)$, and the bottom of the DBR light line, $f = 0.3556(a/\lambda)$. Of the 4 hole radii in Fig. 4.21, this 3% band gap is the largest. For larger radii, the DBR leaky band

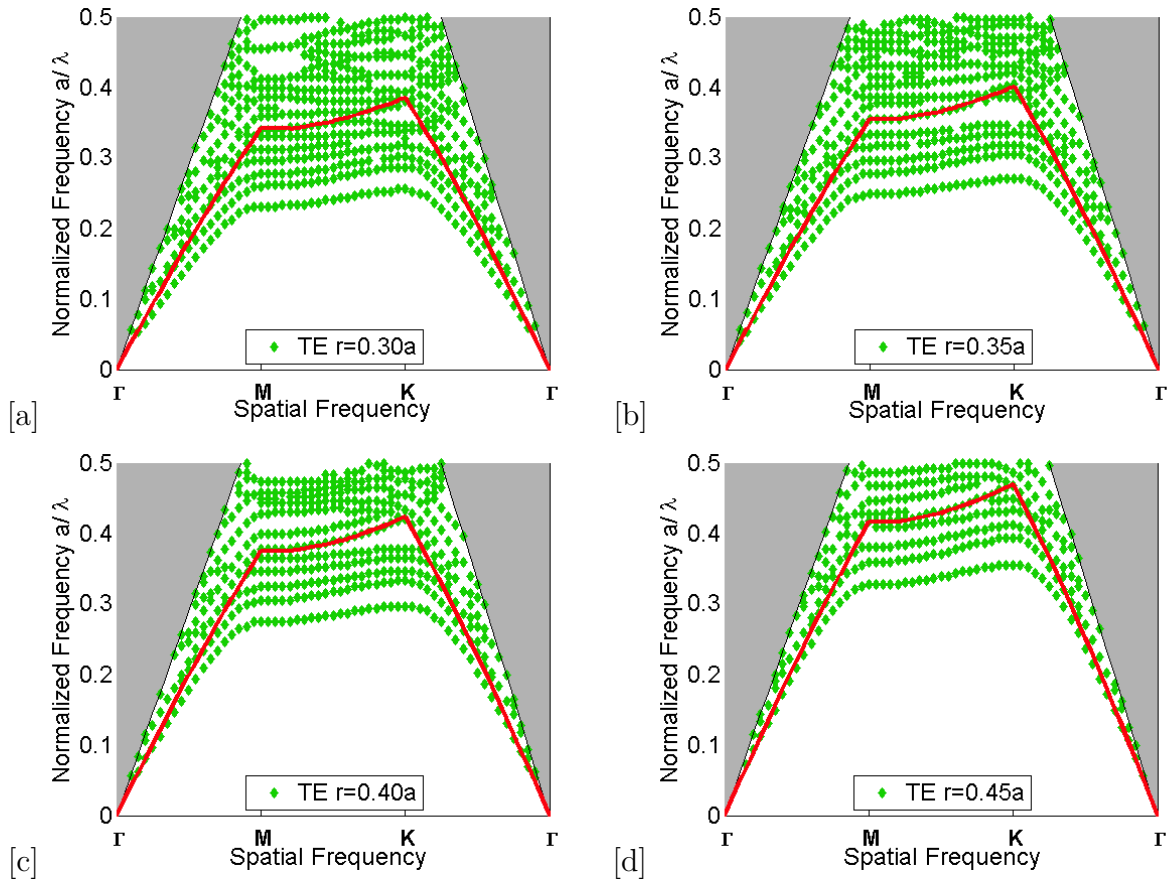


Figure 4.21: The band diagrams for a quasi-3D photonic crystal microcavity with 4 periods of DBR around the slab. The hole radius is 4.21(a) $0.30a$, 4.21(b) $0.35a$, 4.21(c) $0.40a$ or 4.21(d) $0.45a$. The lattice constant was taken as $a = 30$, the GaAs layer thickness is $\approx 152.3\text{nm}$ and the oxidized AlGaAs layer is $\approx 348.2\text{nm}$ thick.

and the dielectric band of the 2D photonic crystal are pushed upwards toward the DBR light line. Eventually, by the time $r = 0.45a$, the band gap is completely closed.

As the band diagrams reveal, there are additional states in the 2D photonic band gap caused by the DBR mirrors on the top and bottom of the slab. If one considers only the projected 1D and 2D band diagrams for the DBR and the 2D photonic crystal slab it would appear that there is a complete overlap of their band gaps. Although it is tempting to assume that this will lead to confinement in the quasi-3D microcavity, such an approach is flawed. Neither the DBR nor the 2D photonic crystal on their own have a complete band gap, so in both structures there are modes at every frequency that propagate. This is not always obvious from viewing the projected band diagrams where assumptions are made to restrict propagation in certain directions. One of the advantages of using the 3D FDTD method to determine the band diagram is that no assumptions or restrictions are made. This means that the more complex reflections that occur in the quasi-3D structure can be accurately simulated and a more realistic band diagram produced. Close attention must be paid when designing microcavities in these quasi-3D photonic crystals.

4.4 Hybrid Photonic Crystal Microcavities

Consider the microcavities shown in Fig. 4.22. Just as in Sec. 4.1, the in-plane confinement is due to a defect in a 2D photonic crystal. The various cavities, however, have different types of vertical confinement. Figure 4.22. b uses total internal reflection for the top mirror and distributed Bragg reflection for the bottom mirror. The cavities in c and d use DBRs for both the top and bottom mirrors, but have the 2D photonic crystal penetrating different numbers of layers. The particular types of mirrors will affect the device performance. For these devices, the thickness of the slab will also play a key role in determining the operating characteristics of the microcavity.

Consider first the simple case of a GaAs slab, ($\epsilon = 12.96$), with a triangular array of

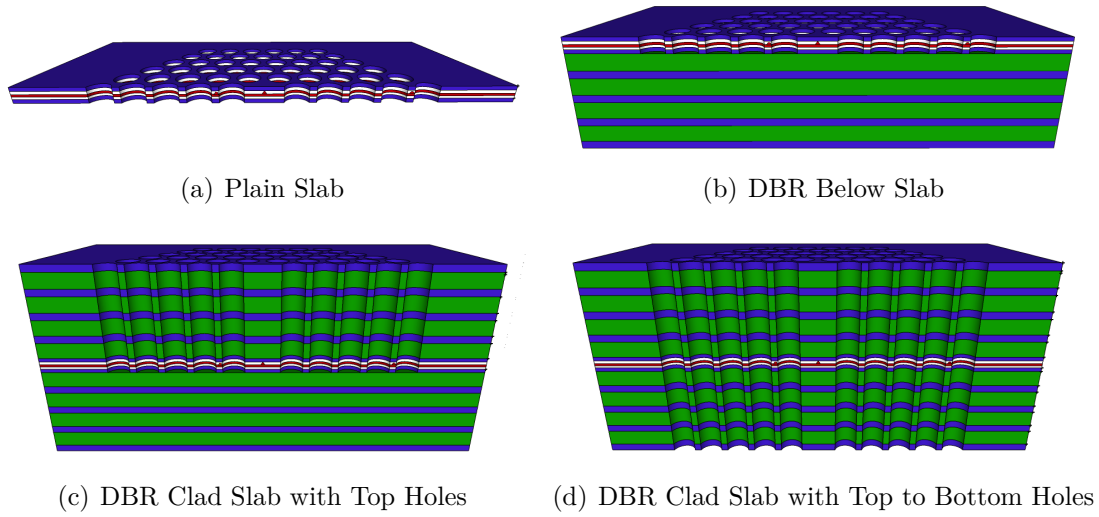


Figure 4.22: The various quasi-3D microcavities examined in this section. a) A GaAs slab suspended in air. b) A GaAs slab with a 4-period DBR made of GaAs and oxidized AlGaAs below. c) A GaAs slab with the 4-period DBR both above and below. Holes penetrate only the top layers. d) The same structure as c) but now the holes penetrate the entire structure.

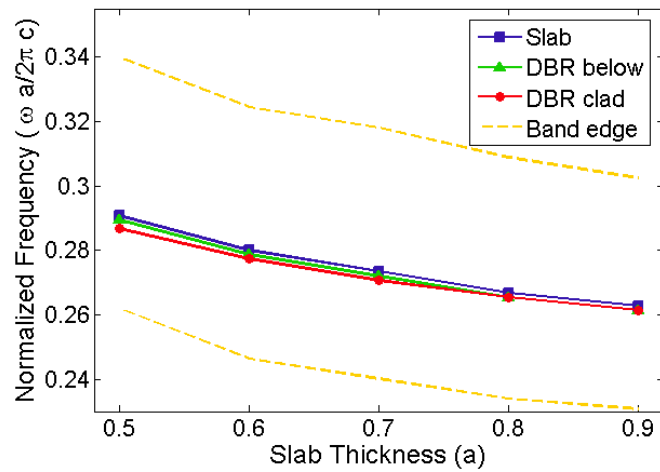


Figure 4.23: The mode frequencies for various configurations of the quasi-3D cavity are shown. As the DBR layers are added first to the bottom and then to the top, the mode frequencies decrease slightly.

air holes, $r = 0.3a$. A microcavity is made by removing a single hole from the lattice and a dipole mode is present inside the band gap. As the thickness of the slab is increased, the band edges and the mode frequency shift to lower frequency as shown in Fig. 4.23. In thicker slabs the volume of high dielectric material increases and the concentration of the fields in the air surrounding the slab decreases. This leads to lower mode frequencies. Figure 4.23 shows the change in mode frequencies when a 4 period GaAs/oxidized AlGaAs DBR is placed below or above and below the GaAs slab. When a DBR is placed below the 2D photonic crystal slab, as in Fig. 4.22 b, the resonant mode frequencies of the microcavity decrease slightly. The oxidized AlGaAs layer has an approximate refractive index, $n = 1.544$. Any fields that are not completely confined to the GaAs slab would spread into this oxidized layer on the bottom and to the air on the top. Because the index of the oxide is larger than the index of air, the effective dielectric of the structure is slightly increased and due to the variational theorem, we would expect the frequency of the mode to decrease. When a DBR is placed above and below the GaAs slab, as in the cavities of Fig. 4.22 (c) and (d), the mode frequencies are decreased further. The frequencies are however, unaffected by the depth of the holes. Because the field energy is easily confined to the high index material in thicker slabs, the mode frequencies for thicker slabs with and without DBRs do not differ as much.

Although changing the material surrounding the 2D photonic crystal slab does not have a dramatic effect on the resonant modes, the quality factor is significantly affected. The quality factor verses GaAs slab thickness for the 4 microcavities of Fig. 4.22 is shown in Fig. 4.24. For a dielectric slab surrounded by air, the quality factor decreases as the slab thickness increases. A slight change in Q for increasing slab thickness is expected because the fields filling the cavity encounter the dielectric interface at different angles for different slab thicknesses. While the quality factor is only moderately affected by variations in the slab thickness, it is highly dependent on the mirror types used above and below the slab. The two structures that are asymmetric, the slab with a DBR bottom mirror and the one

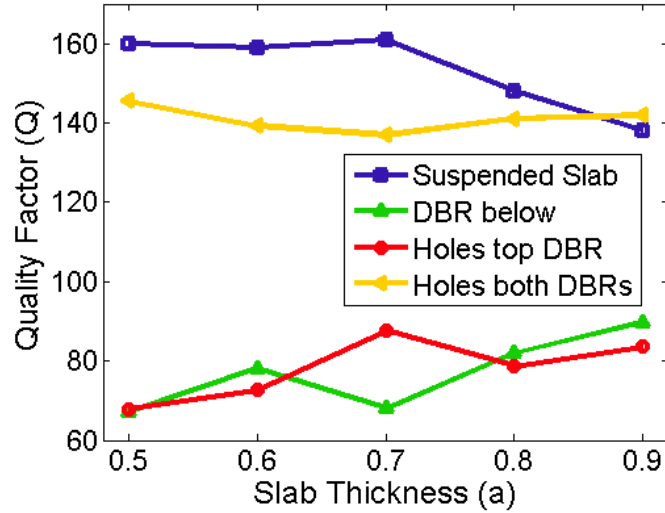


Figure 4.24: The quality factor for the microcavities of Fig. 4.22. The microcavity is made of GaAs with $r = 0.3a$ and $t = 0.5a$. When the microcavity has a DBR for the top or bottom mirror the structure is a quarter wave reflector with 4 repetitions.

with holes drilled only through the top DBR, see a large decrease in quality factor. The slab that is encased in a DBR, but has holes penetrating the entire structure, has a quality factor near that of the slab suspended in air.

When designing a practical device, fabrication limitations must be taken into consideration. Of the 4 microcavities shown in Fig. 4.22, the slab with a DBR below would be the easiest to fabricate. But as seen in Fig. 4.24 the quality factor is too low. Fig. 4.25 shows that the quality factor can be increased by drilling the holes through the dielectric slab and into at least one period of the DBR. For these simulations, the slab thickness was fixed to $t = 0.5a$ because it is a single mode structure and can be fabricated with relative ease. The improvement in the quality factor can be visualized by looking at the magnitude of the electric field through a slice along the y - z plane at the cavity center in Fig. 4.26. For the air holes penetrating only the dielectric slab, the fields couple into the first dielectric layer of the DBR where they are guided. When the air holes penetrate one or more layers of the DBR, the field leakage into the DBR slab is reduced and more of the power exits the device through the top surface.

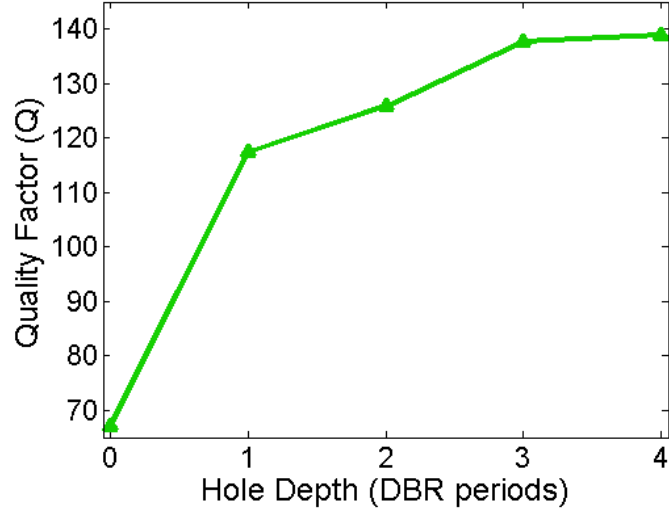


Figure 4.25: The quality factor increases as the holes penetrate more layers of the DBR that lies below the GaAs slab. The microcavity is made of GaAs with $r = 0.3a$ and $t = 0.5a$ and the DBR below the slab has 4 repetitions.

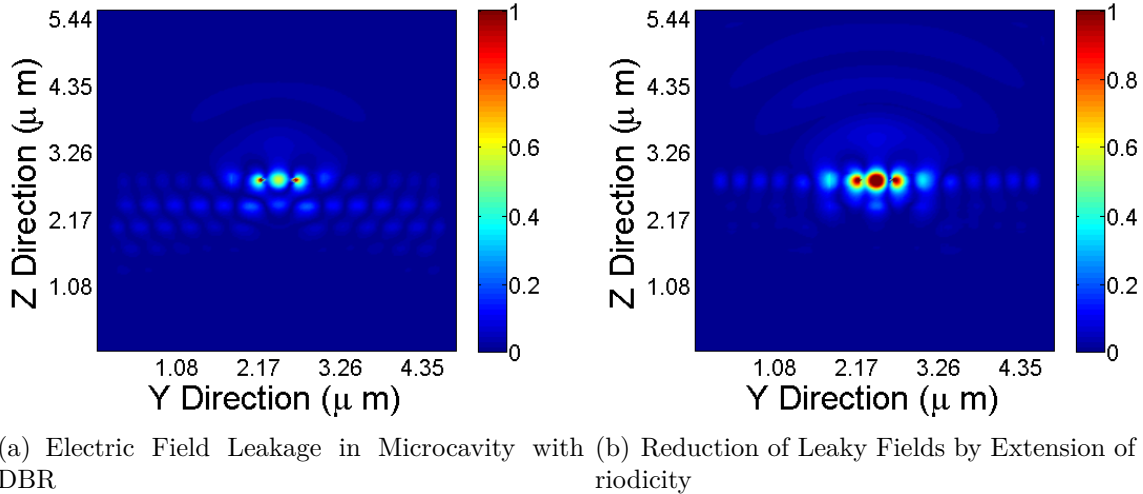


Figure 4.26: The normalized magnitude of the electric field along a yz slice through the center of the microcavity. a) Shows the fields for a photonic crystal slab with a DBR placed below. The electromagnetic fields are coupled to and then guided in the GaAs layers of the DBR causing significant leakage of energy. b) The fields for the same microcavity as in a) except that the air holes penetrate 3 layers of the bottom DBR. Here the fields are better confined to the GaAs slab and the leakage is reduced.

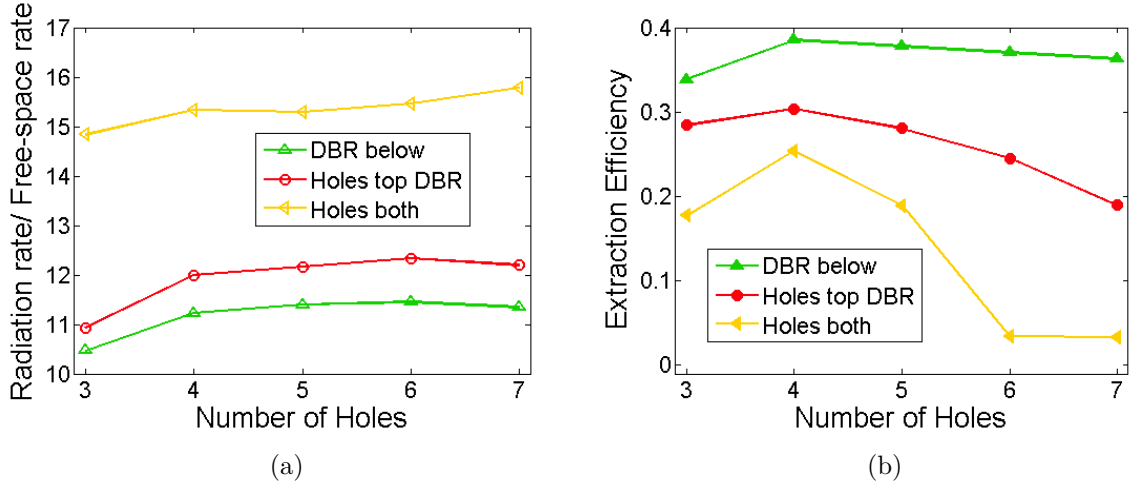


Figure 4.27: a) The spontaneous emission rate for the cavities of Fig. 4.22 for 3, 5 or 7 holes. b) The extraction efficiency for the cavities of Fig. 4.22 for 3, 5 or 7 holes.

The spontaneous emission rate is also affected by the presence of DBRs above and/or below the photonic crystal slab. Figure 4.27 shows the radiation rate and extraction efficiency for each of the microcavities in Fig. 4.22 b-d as a function of the rows of air holes surrounding the defect. In each case, an E_x -polarized dipole is placed at the cavity center. The spontaneous emission rate and extraction efficiency are lower than for the GaAs slab structure that was investigated in Sec. 4.1. The lowest radiation rate values are found for the asymmetric structures, which both have a DBR below the slab that is not penetrated by air holes. For these structures there is significant leakage of energy into the first GaAs layer of the DBR, as was illustrated in Fig. 4.26. This leakage reduces the magnitude of the electric field in the microcavity resulting in a lower spontaneous emission rate than for the dielectric slab. Because the leakage is only moderately affected by an increase in the extent of the periodic structure, these two cavities exhibit only a slight improvement in radiation rate as the periodicity of the 2D photonic crystal is increased from 3 to 7 rows of holes.

When the photonic crystal holes go through both the top and bottom DBR, there is an improvement in the spontaneous emission rate, however the rates are still much lower than

for the suspended slab. The DBR mirrors used above and below the GaAs slab are highly reflective even when only 4 periods are used. If a small number of holes are used to create the 2D photonic crystal, then the in-plane confinement is much weaker than the vertical confinement provided by the DBRs. Increasing the number of air holes, should provide better in-plane confinement and lead to improvement of both the spontaneous emission rate and the extraction efficiency.

Figure 4.27 shows only a modest improvement in the radiation rates for increasing numbers of holes, while the extraction efficiency actually decreases. Recall that the extraction efficiency is measured as the ratio of the radiation in the $|\hat{z}|$ direction to the outward radiation. A low extraction efficiency means that most of the energy is not leaving the cavity in the vertical direction. For each cavity, as the 2D periodicity is increased it is expected that the fields are not propagating out as far into the 2D photonic crystal. In the case of the suspended GaAs slab, this is what led to the asymptotically increasing extraction efficiency. Examination of the radiation data for the 3 cavities with the DBRs shows that there is still a significant portion of energy propagating in-plane for these devices even as the number of holes is increased. The majority of the $|\hat{z}|$ radiation is actually collected from along the sides of the box and not the top and bottom surfaces. Thus increasing the number of air holes actually decreases the $|\hat{z}|$ radiation at the sides and subsequently the extraction efficiency.

The dipole mode is located at a normalized frequency of $f = 0.288$. Referring to the band diagram for the quasi-3D photonic crystal with $r = 0.3a$ shown in Fig. 4.18(d), this frequency lies in the range where there are TE DBR states in the bulk photonic crystal. Specifically, there are states at the K point and half way between the M and K point. From the reciprocal space representation of the mode, it is possible to determine which wavevectors contribute most significantly to the mode profile. This is done by determining the reciprocal space representation of the mode through a spatial discrete Fourier transform. The magnitude of the wavevector along the Brillouin zone for each field can then be

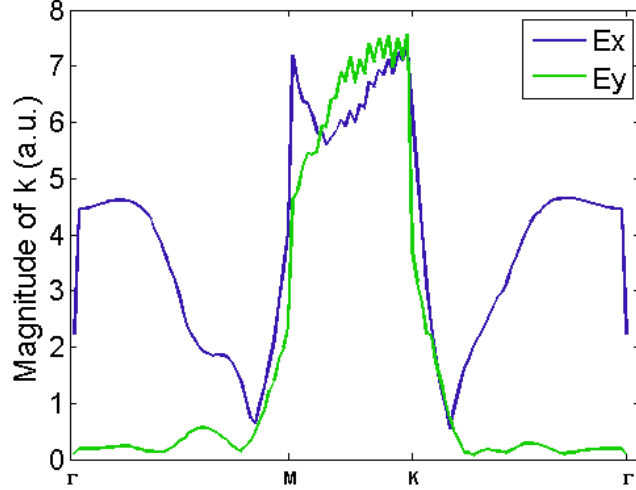


Figure 4.28: The magnitude of the wavevector found from the reciprocal space representation for the y-dipole mode along the edges of the Brillouin zone. The E_x field has maximums at the M and K points and the E_y field has a maximum near the K point.

plotted. For TE-like modes, the mode is primarily composed of E_x and E_y fields and we can neglect E_z in this analysis. Because the excitation was a x-oriented source, the mode has a y-dipole profile. The plot of the magnitude of the E_x and E_y field wavevectors are shown in Fig. 4.28 for the y-dipole mode at points along the Brillouin zone. Both the E_x and E_y fields have maximum values near the K point. The bulk quasi-3D crystal also supports a mode at this location and the fields are allowed to propagate through the crystal. This is what causes both the lower radiation rate and the poor extraction efficiency for this mode in comparison to the suspended slab.

Because the cavity with the DBR below the GaAs slab does not have a highly reflective mirror on the top, it has the highest extraction efficiency of the three cavities. The extraction efficiency also decreases the least as the number of holes is increased. The cavity with the holes penetrating the entire structure has the most dramatic decrease in extraction efficiency to nearly 0 once the number of holes has been increased to 6. The cavity with the holes only penetrating the top DBR and slab lies somewhere in the middle. All of the structures have a maximum extraction efficiency for 4 periods of holes. The modest

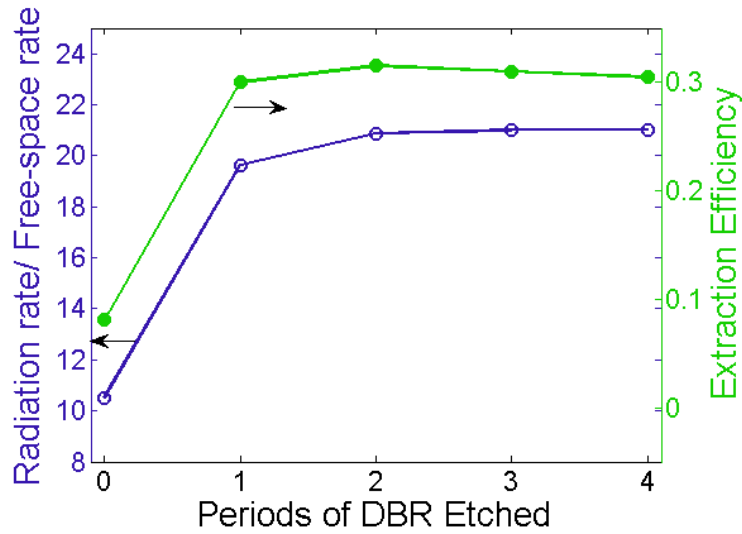


Figure 4.29: The spontaneous emission rate for an Ex-polarized dipole centered in a single defect GaAs slab microcavity with a DBR as the bottom mirror. The emission and extraction are plotted for the 2D triangular photonic crystal pattern penetrating between 0 and 4 periods of the DBR.

improvement gained by increasing the number of holes from 3 to 4 is likely due to a slight increase in the radiation leaving the top of the cavities.

For the microcavity with a DBR below the GaAs slab, there is significant improvement of the spontaneous emission rate and the extraction efficiency as the periodic pattern of air holes is etched down through the DBR. The trends are shown in Fig. 4.29 for the case of 3 rows of holes surrounding the defect. When the air holes penetrate one layer of the DBR there is a sharp rise in the extraction efficiency and the spontaneous emission rate. As the hole depth is increased, the values increase slightly. This structure comes the closest to achieving the high spontaneous emission enhancement of the suspended slab. When the number of holes surrounding the defect is increased, the performance of this structure is further improved. For 7 rows of holes, the relative radiation rate for the microcavity with holes drilled through three of the bottom DBR layers is 23.76. The extraction efficiency is 0.6296.

Instead of considering what happens as the 2D photonic crystal is etched further into

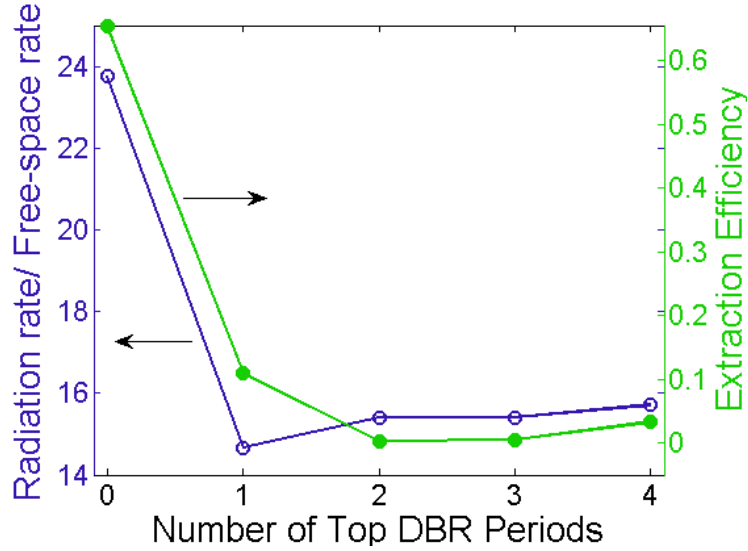


Figure 4.30: The spontaneous emission rate for an Ex-polarized dipole centered in a single defect GaAs slab microcavity with a DBR as the bottom mirror. The number of top DBR periods is varied between 0 and 4 and the 2D triangular photonic crystal pattern penetrates the entire structure.

the bottom DBR, it is also possible to examine the radiation rate and extraction efficiency for different periods of the top DBR as shown in Fig. 4.30. In this Figure, there are 7 rows of holes surrounding the single defect which are etched the entire way through the structure. When there are 4 DBR periods above the slab, the structure is the same as that of Fig. 4.22(d). As the number of top periods is decreased, the reflectivity of the top mirror is reduced. Because the DBR is highly reflective there is not a significant reduction in the reflectivity until the number of periods is ≤ 1 . At this point the extraction efficiency begins to increase. Once all of the DBR layers are removed the relative radiation rate is 23.76 and the extraction efficiency is 0.6296. Although this radiation rate is higher than for any of the other cavities with DBRs, it is still less than for the suspended slab.

The extraction efficiency at first seems to be poor in comparison to the value obtained for the GaAs slab of 0.9872, however it is actually better. Because the light exiting the top and bottom of the device are summed, the extraction efficiency out of only the top of the GaAs slab microcavity is $\approx 0.9872/2 = 0.4936$. Placing the DBR below the slab reduces

Table 4.1: Examination of Extraction Efficiency Calculations

Cavity Type	Mode Frequency(a/λ)	Total Extraction Efficiency	Top Extraction Efficiency
GaAs slab	0.2933	0.9872	0.4548
DBR below	0.2907	0.6546	0.5968

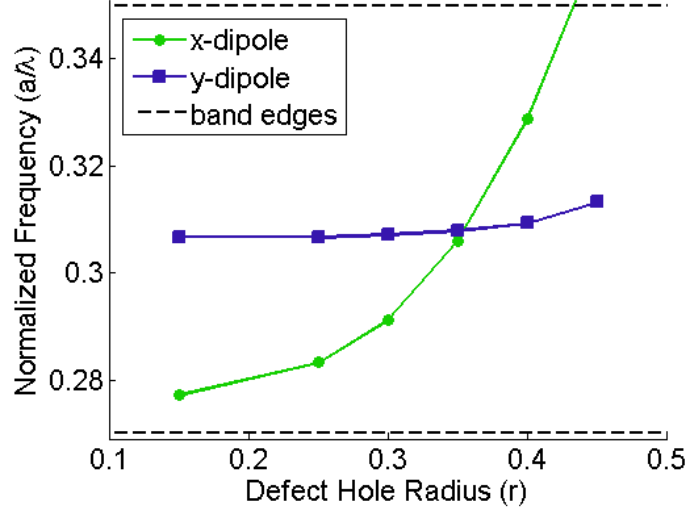


Figure 4.31: The mode frequencies for the quasi-3D cavity as the radii of the two inner holes along \hat{x} are varied. Because the perturbation is along \hat{x} the x-dipole mode is very sensitive to the change in hole radius while the y-dipole frequency remains relatively constant.

the amount of light that exits the device from the bottom. A more accurate method of calculating the extraction efficiency out of the top of the device is to sum the $|\hat{z}|$ component of the Poynting vector over the top half of the problem space only. The ratio of this value to the total power radiated will provide a more accurate view of the extraction efficiency. Consider the case of the DBR below with the 2D photonic crystal penetrating 4 periods of the DBR. The number of holes surrounding the defect is 7 and the data is summarized in Table 4.1. The microcavity with the DBR mirror below the GaAs slab has a higher top extraction efficiency than the GaAs slab in air. The cost of course is a lower spontaneous emission lifetime.

The results presented thus far imply that a mode in the quasi-3D microcavity has lower a radiation rate and extraction efficiency than the same mode in a suspended slab cavity. The only exception being a higher top extraction efficiency when the 2D photonic crystal

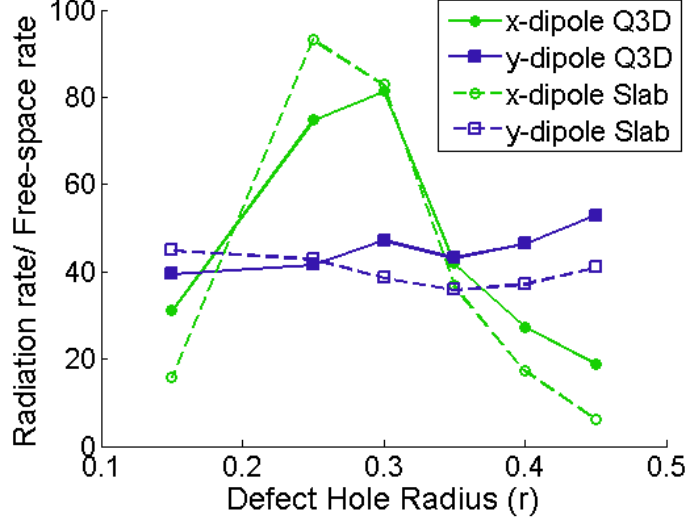


Figure 4.32: The radiation rates for the x (green circle) and y (blue square) dipole mode as a function of the radii of the two inner holes along \hat{x} . The solid line/filled data point are radiation rates in the quasi-3D cavity and the dashed line/open data point are radiation rates in the suspended slab. For each mode there are some r' where the radiation in the slab is greater than for the quasi-3D cavity.

is etched down into a DBR below the GaAs slab. To substantiate the claim that the poor performance of the y-dipole mode is due to the fact that the wavevector maximum corresponds to a TE DBR state, the spontaneous emission rate for the x and y-dipole modes can be found as the mode frequency is tuned. As discussed in Sec. 4.1, the degenerate dipole can be split by increasing or decreasing the radii of the nearest neighbor holes along the \hat{x} direction. This perturbation of the cavity also alters the mode frequencies. Because there is a quasi-3D band gap in the bulk structure with $r = 0.35a$ we will choose this bulk crystal as opposed to the $r = 0.3a$ photonic crystal structures that were examine thus far in this section. The mode frequencies for the quasi-3D cavity of Fig. 4.22(d) are shown in Fig. 4.31 as a function of the perturbed hole radius.

The radiation rate as a function of the perturbed hole radius is shown in Fig. 4.32. When the hole radii are reduced, the y-dipole frequency asymptotically approaches $f = 0.3067(a/\lambda)$. Once this frequency is reached, $r' \leq 0.25a$, the radiation rate in the quasi-

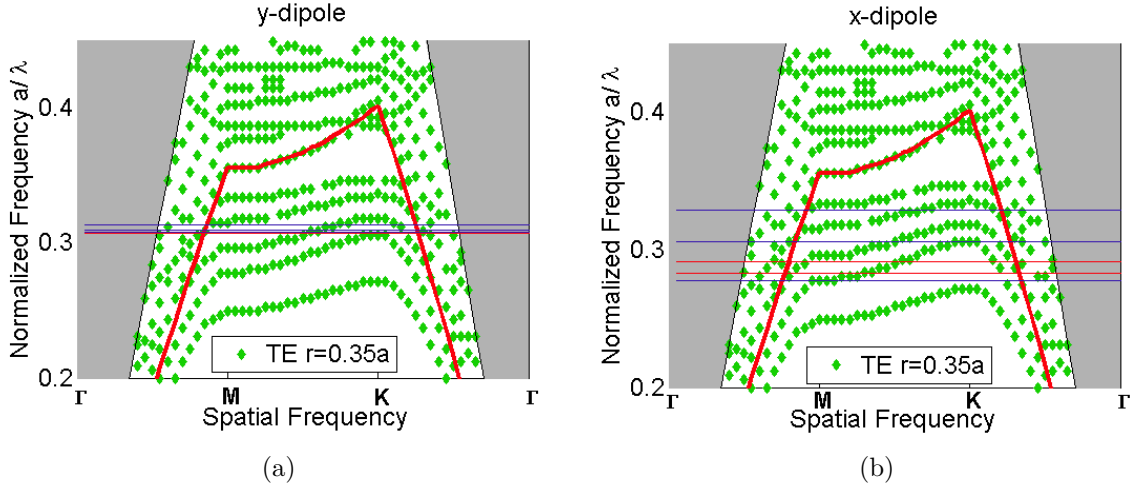


Figure 4.33: The mode frequencies for the a) y-dipole and b) x-dipole are shown as horizontal lines over the quasi-3D band diagram for the photonic crystal with hole radius, $r = 0.35a$. Depending on the mode frequency there will be between one and three TE DBR states to which the dipole mode can couple. Coupling efficiency depends on the magnitude of the mode wavevector at the TE DBR state locations. Red horizontal lines denote frequencies where the coupling is good and the spontaneous emission rate is less than in the slab, while blue horizontal lines denote frequencies where the spontaneous emission rate is greater than in the slab.

3D cavity is lower than in the suspended slab. There are several TE DBR states for $f = 0.3067(a/\lambda)$, including the first band at the K point and the second band about halfway between M and K. For the y-dipole mode, the maximum wavevector is at the K point as shown in Fig. 4.28. The mode couples efficiently to the DBR yielding a lower radiation rate. The placement of the y-dipole mode on the $r = 0.35a$ band diagram is the same as the degenerate dipole mode on the $r = 0.3a$ band diagram discussed previously, although the specific frequencies and cavity geometry differ. This helps to rule out the mode degeneracy or the absolute mode frequency as causes of the lower radiation rate. Instead it substantiates the claim that the lower radiation rate is due to TE DBR modes at locations of maximum wavevectors.

As the hole radius is increased above $r' > 0.25$, the y-dipole mode frequency increases from $f = 0.3072(a/\lambda)$ to $f = 0.3133(a/\lambda)$. At these frequencies there are two TE DBR states. One is located around half way between the K and M points and the other is to

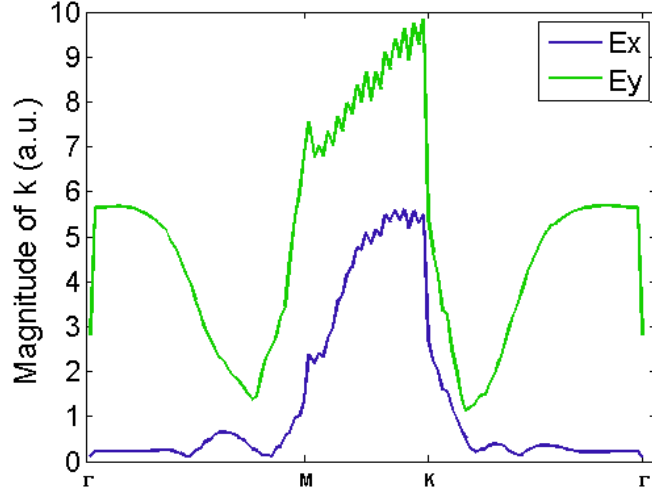


Figure 4.34: The magnitude of the wavevector found from the reciprocal space representation for the x-dipole mode along the edges of the Brillouin zone. The E_x and E_y fields have maximums at the K point.

the right of the K point, see Fig. 4.33(a). The magnitude of the y-dipole wavevectors at these locations are not maximums and the coupling to leaky DBR modes is not as good. Because there is less coupling to the DBR modes, the fields in the quasi-3D cavity will be larger leading to higher radiation rates than in the slab.

The magnitude of the wavevectors for the x-dipole along the Brillouin zone is shown in Fig. 4.34. Again there is a maximum at the K point, but between M and Γ and K and Γ the magnitude does not decrease as quickly as for the y-dipole mode. When the perturbed hole radius is $r' = 0.25a$ the mode frequency is $f = 0.2833$. At this frequency there are 3 TE DBR states: one to the left of the M point, one between M and K and another to the right of the K point, see Fig. 4.33(b). The magnitude of the wavevector is large at all of these locations and there is coupling to the DBR. As the hole radius is increased, the mode frequency increases, but there will still be 3 TE DBR states at points where the magnitude of the wavevector is large. When $r' = 0.35a$ the TE DBR state is very close to the K point which is the maximum wavevector location for the x-dipole mode. The mode frequency of the x-dipole for $r' = 0.4a$ is $f = 0.3287$. There is one TE DBR state between the M and

K points and one point just under the DBR light line to the right of K. Because the states are located at relatively low wavevector locations, the spontaneous emission rate is higher in the quasi-3D cavity. A similar situation occurs when $r' = 0.15a$. At this point there is one TE DBR band state near the M point and another near the light line to the left of the K point.

The presence of the TE DBR states in the quasi-3D band diagram does not necessarily mean lower radiation rates in these cavities. Instead the radiation rates can actually be higher as long as the states do not occur at the same locations as significantly contributing wavevectors of the mode. Design of microcavities in these quasi-3D photonic crystals must be handled with care to achieve the advantage of larger spontaneous emission enhancement.

Chapter 5

Photonic Crystal Microcavity

Single-Photon Emitter

This chapter combines the computational techniques discussed previously to fully characterize an optimal single-photon emitter. As stated in Chapter 1, the source must emit single polarized photons with as little wait time as possible. This wait time is governed primarily by the spontaneous emission lifetime and the photon lifetime. For the relatively low Q microcavities discussed so far, the photon lifetime will be on the order of picoseconds. The spontaneous emission lifetime of the InAs quantum dots in bulk studied in Chapter 3 was around half a nanosecond, making this the limiting factor for operating speed.

In order to emit single photons with high probability, it is beneficial to work with smaller quantum dots. These quantum dots have a single bound state for the electron to occupy. Any recombination in the dot of an electron in the conduction band state with a hole in the valance band state, then has a single transition energy and the photon can have only one frequency. If there are more energy levels, the ground state transition is still preferred, however there would be a finite probability of recombination from the excited states. The possibility of emissions from these states would degrade the quality of the single photon source. A major drawback of using smaller quantum dots is that the ground state transition

energy tends to be larger and the photon wavelength shorter. Designing a quantum dot with a single bound electron energy level and an emission wavelength of $\lambda = 1.3\mu\text{m}$, may then require the use of a novel materials system. Because photonic systems scale, it is possible to choose small InAs quantum dots that emit photons of wavelength $\lambda = 0.95\mu\text{m}$ to demonstrate the central ideas of this thesis while saving design at $\lambda = 1.3\mu\text{m}$ for future work.

To control the polarization of the photon, the quantum dot is placed inside a photonic crystal microcavity. When designing the microcavity, it is possible to perturb the nearest neighbor holes to control the resonant frequencies and field profiles. For single-photon source applications, it is desirable to have a single mode within the photonic band gap. The most obvious reason is that the quantum dot must couple to one mode that has the correct polarization while suppressing all other emissions. But the presence of additional modes also leads to less concentrated field profiles, lower Q and less spontaneous emission enhancement. This is a result of the fact that the field profiles of all of the resonant modes must be orthonormal to one another. Even if the photon frequency aligns perfectly with the desired cavity mode, the performance of a multi-mode cavity will not be as good as a single mode device.

The single mode requirement puts a constraint on the photonic crystal defect design. Not only must the mode have a distinct polarization, it should also be the only mode in the cavity. As we saw in Chapter 4, removal of a single hole creates a degenerate dipole mode in the band gap. Even as the cavity is further altered, this mode will remain inside of the band gap although it can shift in frequency. It is possible to push the mode down close to the dielectric band edge to mitigate its effect and create a nearly single mode cavity. A true single mode microcavity that does not have a dipole profile is not possible, the best option is to push the dipole mode towards the edge of the band gap.

Isolating a single mode poses new challenges for the quasi-3D microcavity with DBRs. Typically higher quality, more stable modes tend to lie near the center of the 2D photonic

crystal slab band gap. The band gap of the quasi-3D photonic crystal is smaller and lies towards the higher frequency side of the suspended slab gap. For a mode to lie in the quasi-3D photonic crystal band gap, it must be pushed up in frequency which generally means that there is less dielectric for the mode to occupy. If not properly designed, this can lead to less spontaneous emission enhancement. As was illustrated at the end of Chapter 4, modes that lie in the region where leaky TE DBR bands exist may still have higher radiation rates and quality factors than in a suspended slab, provided that there is not efficient coupling of the microcavity mode to the quasi-3D photonic crystal state. Whether or not the mode has to lie in the quasi-3D band gap will depend on the specific mode.

One additional concern when designing photonic crystal microcavities is the vertical loss, which tends to dominate the low quality factor in the cavities and also leads to longer spontaneous emission lifetimes. In order to combat this, researchers have used spatial frequency domain analysis to determine cavity geometries and modes which will have higher quality factors [1]. The modes in a photonic crystal microcavity are either pulled down from the air band or pushed up from the dielectric band and retain the characterizations of the band edge states from which they originate [2]. Dielectric band edge states tend to have a less significant portion of the reciprocal space wavevector located within the light cone and will therefore typically have less vertical loss [3]. Increasing the radius of a single hole is the most straightforward method of obtaining modes originating from the dielectric band. This approach is, however, not practical for semiconductor lasers and single photon sources grown by MBE because it will result in the removal of the active region. Instead, it is possible to remove a single hole and then grade the hole radii of several periods of holes around the central defect [1, 4, 5]. Further adjustments to the nearest neighbor holes to manipulate the mode frequencies and profiles may be more difficult for these cavities. Adding DBR mirrors to cavities that support modes pulled from the air band can provide better vertical confinement for any modes that lie within the quasi-3D photonic crystal band gap without compromising the tunability of the cavity geometry.

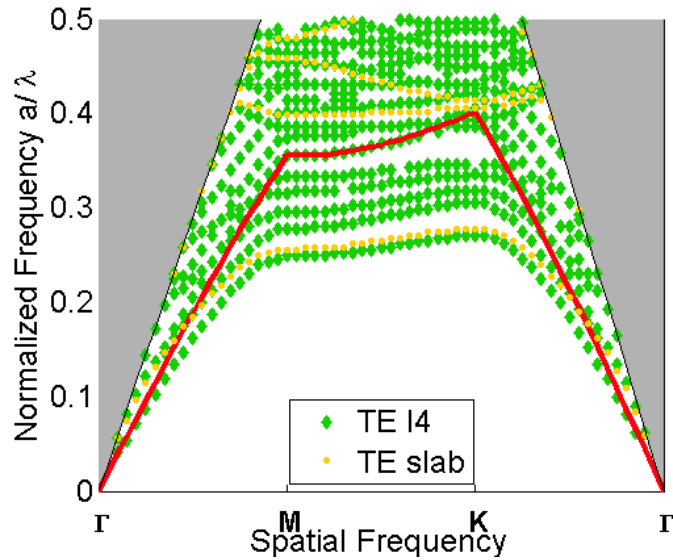


Figure 5.1: The quasi-3D photonic crystal TE band diagram for a photonic crystal with hole radius, $r=0.35a$. The corresponding suspended slab band diagram is shown the the yellow data points.

This chapter begins with an examination of modes which may work for a single-photon emitter. In order to justify the choice of modes, their field profiles, quality factors and photon lifetimes are examined. After the possible modes have been identified, the spontaneous emission lifetimes for small InAs quantum dot emitters in the most promising cavity will be investigated. Comparisons will be made between a suspended slab cavity and the quasi-3D geometry. The final section of this chapter accounts for fabrication non-idealities. Specifically, the spatial and spectral detuning of the quantum dot from the candidate microcavity will be examined.

5.1 Mode Identification and Cavity Analysis

At the end of Chapter 4, the band diagrams for quasi-3D photonic crystals with GaAs slab thicknesses of $t = 0.5a$ and 4 periods of highly reflective DBRs were presented. The DBR mirrors introduce additional bands to the band diagram and reduce the size of the gap. Designing a microcavity with a resonant mode lying in the band gap is no longer

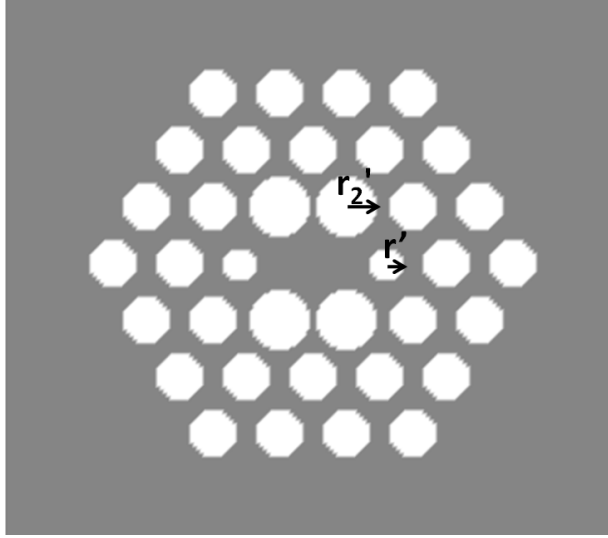


Figure 5.2: The photonic crystal microcavity geometry when a single hole is removed and the hole radii along \hat{x} are reduced, r' . The 4 holes above/below the defect can also be varied, r'_2 .

straightforward; the larger the band gap the less difficult the task. When the hole radius was set to $r = 0.35a$, the size of the band gap was maximized. This section focuses on the identification of candidate microcavities in the photonic crystal that have a mode of distinct polarization within the quasi-3D photonic band gap. Because the field distribution does not change when the DBRs are added to the microcavity, it is valid to first simulate the GaAs slab in air with $r = 0.35a$ and $t = 0.5a$ to obtain general trends for each defect. These computations typically require less time and therefore fewer resources. After the appropriate cavity geometries have been identified, one or two simulations can be done for the full quasi-3D structure. This approach also provides a set of GaAs slab data with which the quasi-3D cavity results can be compared.

The quasi-3D photonic crystal band diagram is shown in Fig. 5.1 where the GaAs slab is clad by two highly reflective quarter wave DBRs made of GaAs, $n = 3.6$ and Al_2O_3 , $n = 1.544$. In the Figure, the photonic bands corresponding to the GaAs slab in air are shown as overlays with yellow circles. The 2D suspended slab has a band gap for the normalized frequencies $0.2776 - 0.3992$ whereas the quasi-3D band gap lies between

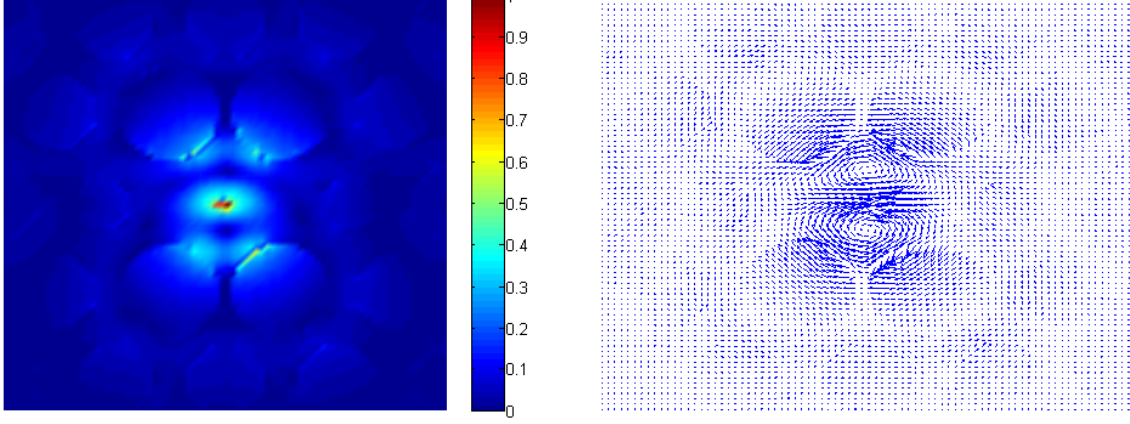


Figure 5.3: a) The normalized field distribution for the y-dipole mode at the slab center for the photonic crystal quasi-3D microcavity with $r' = 0.25a$ and $r'_2 = 0.45a$. This mode lies in the quasi-3D band gap. b) The vector field for the mode at the center of the slab.

0.3462 – 0.3556. This band gap is smaller and the center frequency is shifted upward compared to the slab structure. As discussed in Chapter 4, removal of a single hole in the photonic crystal results in a resonance slightly below the center of the band gap. In this case, the degenerate dipole mode frequency for a single defect cavity is 0.3094, which does not lie in the band gap of the quasi-3D photonic crystal. It is possible to push the resonance up in frequency by further perturbing the microcavity.

Previously it was shown that the degeneracy of the x and y dipole could be split by perturbing the two inner holes that lie along the \hat{x} direction, see Fig. 5.2. Increasing the size of the holes pushes the x-dipole up in frequency and eventually out of the band gap. The frequency could be tuned so that the mode lies in the quasi-3D band gap, but the mode would have a lower quality factor and less field confinement leading to longer spontaneous emission lifetimes. For this cavity, the y-dipole is the dominant mode and it will lie at the normalized frequency, 0.3094. The frequency of the y-dipole can be increased by increasing the radii of the 4 holes above/below the defect. When the holes along \hat{x} have a radius of $r' = 0.25a$ and the ones above/below the defect have a radius $r'_2 = 0.45a$, then the y-dipole mode lies at 0.3427, which is in the quasi-3D band gap. The x-dipole mode is now the dominant mode and remains at 0.3094. Because the y-dipole mode is no longer dominant,

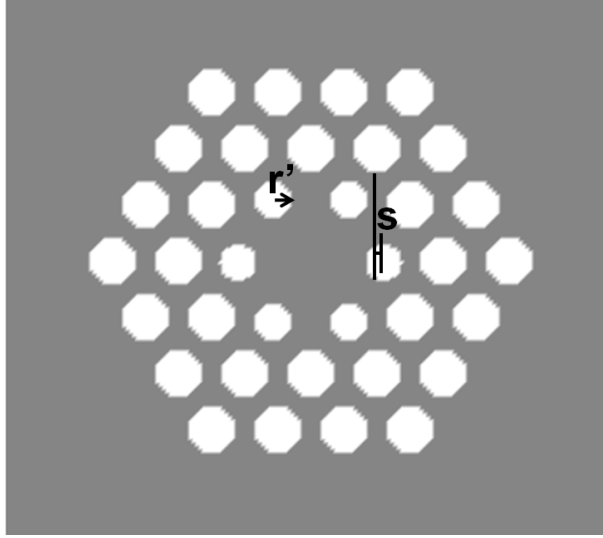


Figure 5.4: The photonic crystal microcavity geometry when a single hole is removed and the inner hole radii are reduced. Also, the holes are shifted outward slightly to align the edges of the holes with those of the bulk crystal. The varied parameters are r' and the corresponding shift, s .

it will have a lower Q.

The major issue with the dipole mode is that the polarization does not lie along one particular axis. Figure 5.3(a) shows the normalized magnitude of the electric field for the y-dipole mode in the perturbed quasi-3D cavity. The fields of the dipole mode are distributed almost equally between the E_x and the E_y components as shown in the field vector plot in Fig. 5.3(b). A directional polarization is desirable for the single photon source, where photons should be emitted along a particular axis in a chosen basis. The more directional the field, the higher the probability that the photon will align itself to the axis, leading to higher efficiency for the quantum key distribution system. Other perturbations of the microcavity are necessary to achieve different mode profiles that have a more directional polarization.

One popular photonic crystal cavity is formed when the radii of the nearest neighbor holes are reduced and the holes are shifted outward slightly. This cavity is shown in Fig. 5.4. Even slightly decreasing the size of the holes, increases the size of the cavity enough

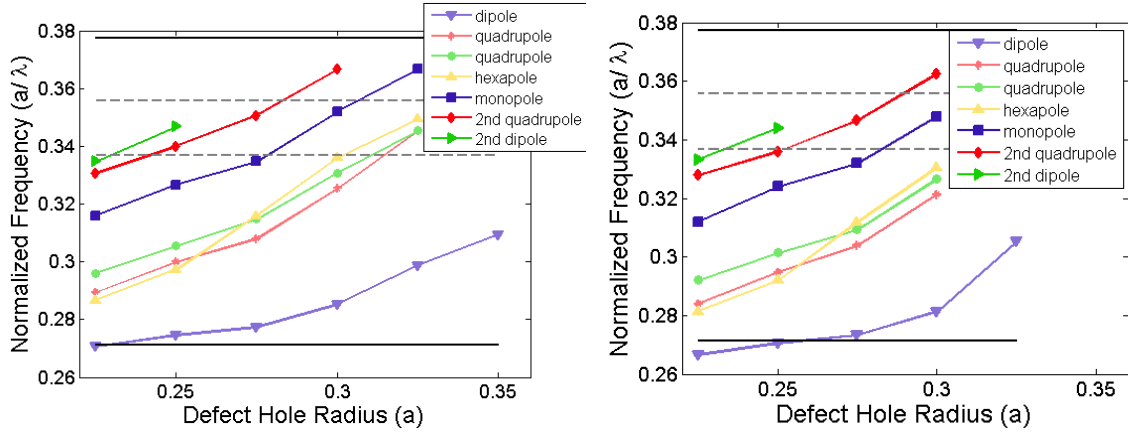


Figure 5.5: As the holes radii are reduced from the bulk photonic crystal value of $r = 0.35a$, the holes are pushed slightly outward enlarging the size of the cavity. Higher order modes begin to enter and traverse the band gap, denoted by the solid black lines. When $r = 0.300a$ and $r = 0.275a$ there is a single mode in the quasi-3D band gap, the gray dashed lines.

to pull additional modes from the air band into the band gap. The frequencies of the modes can then be tuned by further altering the radii as shown in Fig. 5.5. Here, the solid black lines denote the band edges for the 2D photonic crystal slab in air, while the gray dashed lines denote the quasi-3D photonic crystal band edges. Comparison of the modes for the 2D photonic crystal slab, Fig. 5.5(a), and those of the quasi-3D structure, Fig. 5.5(b) reveals that the modes follow the same trends but are slightly reduced in frequency for the quasi-3D case as expected. When the inner hole radii are set to $r' = 0.325a$, there are 4 modes in the 2D band gap and a set of 3 modes in the quasi-3D band gap. By further increasing the hole radii, the set of 3 modes is pushed down below the lower band edge and one by one, higher order modes enter the band gap region. For $r' = 0.3a$ or $r' = 0.275a$ there is a single mode within the quasi-3D band gap which is desirable for a single photon source.

The profiles of these modes are shown in Fig. 5.6, along with the electric field vectors at the slab center. The field magnitude is normalized to 1. For $r' = 0.3a$, the mode in the quasi-3D band gap is the monopole mode. When $r' = 0.275a$ the monopole mode drops out of the band gap and a second quadrupole mode emerges at 0.3507. The quality

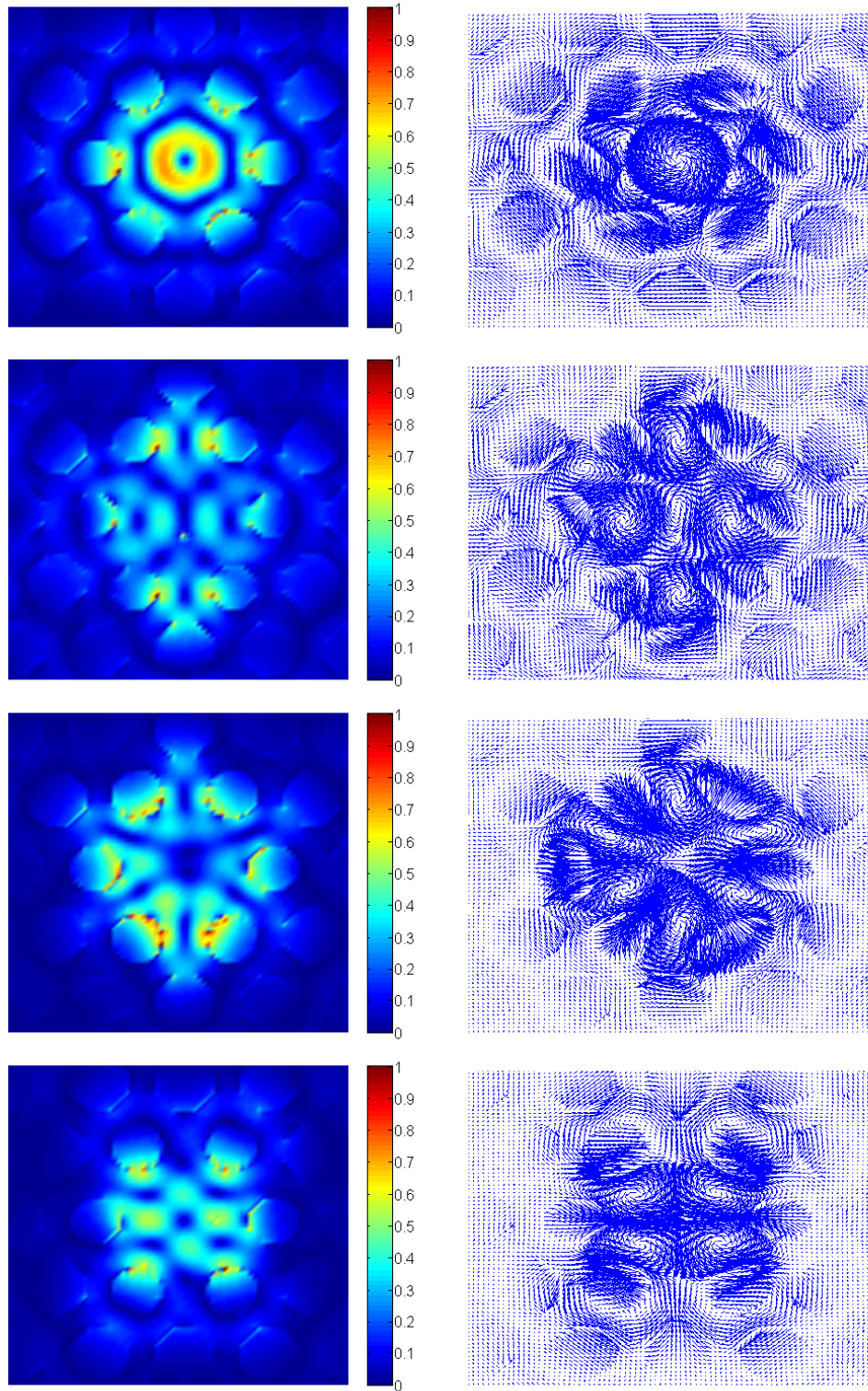


Figure 5.6: a) The magnitude of the electric field, normalized to 1, for the microcavity with $r = 0.300a$. The mode is a monopole mode. b) The quadrupole mode profile corresponding to the single mode in the quasi-3D band gap for $r' = 0.275a$. The vector fields for the c) monopole mode and d) the quadrupole are also shown.

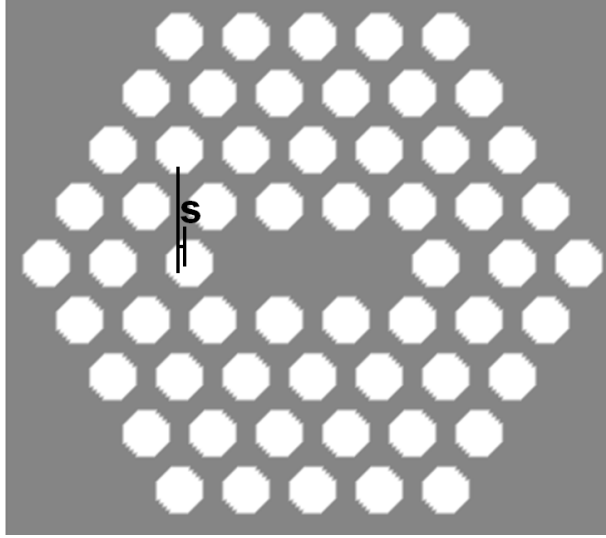


Figure 5.7: The photonic crystal microcavity geometry with 3 holes removed. The mode frequencies will be tuned by either shifting the holes by s along the \hat{x} direction or elongating the holes to form ellipses along that direction.

factor of the quadrupole mode is $Q = 664$, which for a frequency of $f = 317.2\text{THz}$ gives a photon lifetime of $\tau_{\text{photon}} = 0.42\text{ps}$. For the monopole mode, the cavity quality factor is $Q = 573$ and the photon lifetime $\tau_{\text{photon}} = 0.28\text{ps}$. Examination of the electric field vectors reveals that neither the monopole mode nor the 2nd quadrupole mode is highly polarized. Additional modes exist in this cavity, although they have frequencies corresponding to the leaky TE DBR bands. As was shown in Chapter 4, higher spontaneous emission rates are still possible in these regions. The hexapole and quadrupole field profiles are also shown in Fig. 5.6. For both modes, neither the E_x nor the E_y field is preferred. The lowest lying mode in this cavity is the degenerate dipole mode which has already been ruled out. None of the modes supported by this cavity geometry are suitable for single-photon source applications because they do not satisfy the polarization requirement.

Instead of creating a symmetric defect in the cavity, consider the geometry shown in Fig. 5.7. This is the L3 defect that was discussed briefly at the end of Chapter 3. Previously, the goal was to increase the operating wavelength and thus to decrease the mode frequency by shifting the holes along the \hat{x} direction outward from the cavity, so that s is a positive

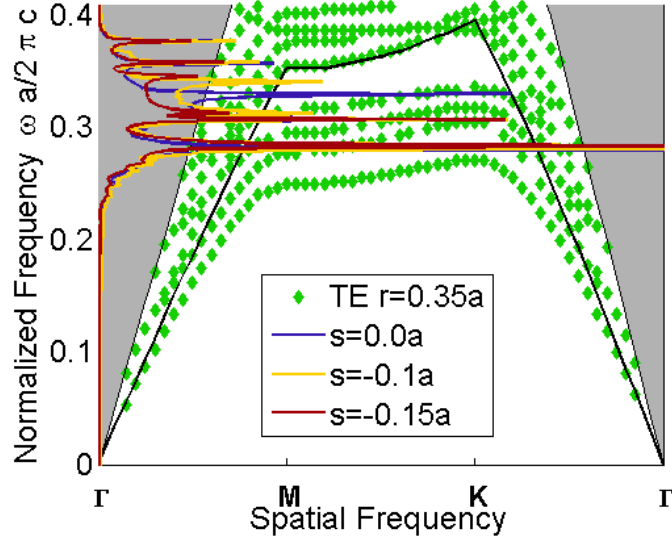


Figure 5.8: The mode frequencies in a L3 cavity for various hole shifts s are shown with the quasi-3D photonic crystal band diagram. Here the negative s denotes a shift of the holes towards the center of the cavity. The shift increases the frequency of the second mode, pushing it into the band gap.

number. For the quasi-3D photonic crystal microcavity, the frequency should be increased and the holes moved inward, making s negative. Figure 5.8 shows how the resonant mode frequencies in a suspended GaAs slab change as the size of the cavity is decreased along the \hat{x} direction. Note that the magnitude of these peaks is arbitrary. For illustrative purposes, the quasi-3D photonic crystal band diagram is also shown in the figure. Of the 3 cavity modes, the second one is the most sensitive to the perturbation of the cavity. The first and third modes are completely unaffected. This was also the case in Chapter 3 when positive values of s were considered. By shifting the holes inward, the second mode is pushed up into the quasi-3D photonic crystal band gap when $s = -0.1a$. Of course the mode frequencies will decrease slightly when the DBRs are included. To account for this frequency shift, it is wise to consider a cavity with $s < -0.15a$ so that the second mode lies in the quasi-3D band gap even when DBRs are added.

When $s = -0.15a$, the second mode has a normalized frequency of 0.3467. The mode profile at the center of the slab is shown in Fig. 5.9(a) with the corresponding electric

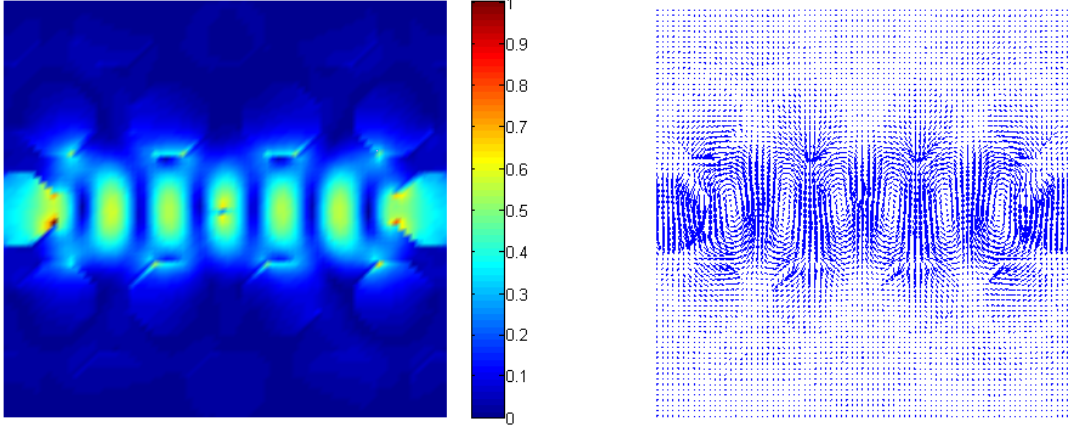


Figure 5.9: a) The normalized field distribution for the second mode at the slab center for the L3 photonic crystal microcavity with $s = -0.15a$. This mode lies in the quasi-3D band gap. b) The vector field for the mode at the center of the slab showing polarization along the \hat{y} direction.

field vector plot in Fig. 5.9(b). As the mode profile illustrates, the fields extend laterally along the \hat{x} direction. The mode is comprised mostly of E_y fields, as shown in the vector plot where the polarization is along \hat{y} . From energy decay measurements performed by calculating the total electric and magnetic field energy in the slab, the quality factor for this mode is $Q = 170$. For a mode frequency of $f = 317.2\text{THz}$, this corresponds to a photon lifetime of $\tau_{\text{photon}} = 0.08\text{ps}$. Because the perturbation of the cavity affects an additional period of the photonic crystal and the second resonance is further from the 2D mid gap frequency, the Q is lower than for the L3 defect with $s = 0$, $Q = 293$. Lower Q cavities are actually desirable for single-photon sources, so the ability to push the highly polarized mode into the quasi-3D band gap makes the L3 cavity an excellent candidate for use in the device. When DBRs are added above and below the slab, the resonant mode frequency drops to 0.3427 which is no longer above the quasi-3D band edge.

Instead of shifting the inner holes along \hat{x} , the holes can be stretched along the axis to form ellipses. This perturbation keeps the general alignment of the holes constant which tends to reduce the scattering of the fields. It also eliminates the small side cavities that form when s is large. The effect on the mode frequency is similar because the ellipse

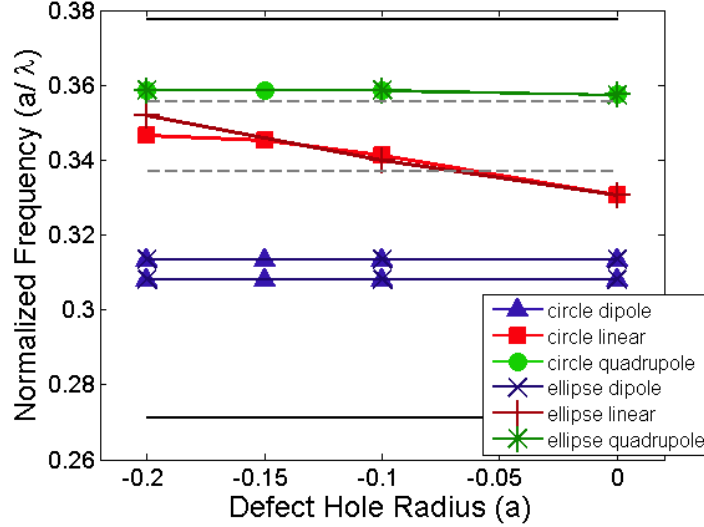
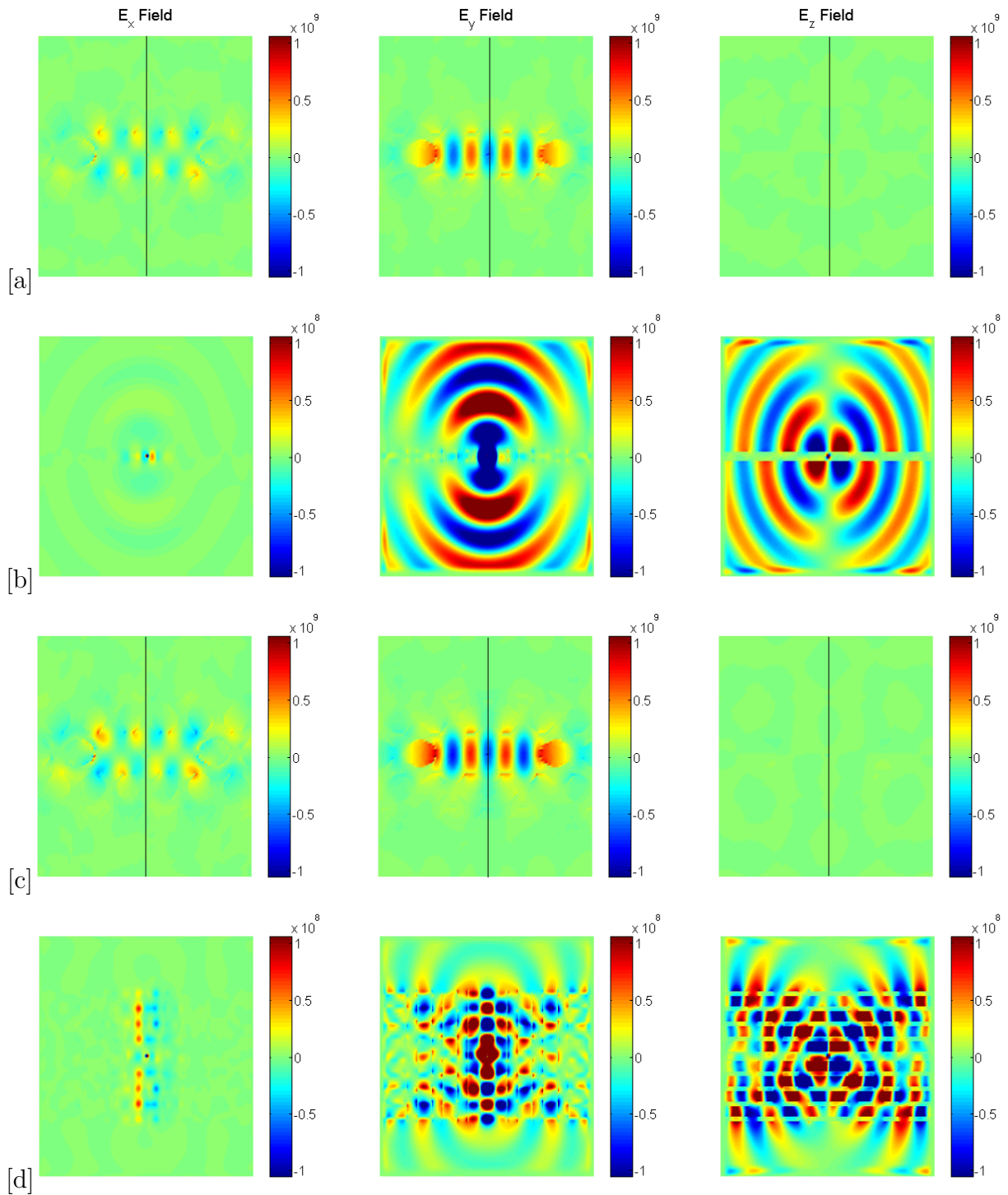


Figure 5.10: The mode frequencies for the 3 modes in a L3 cavity for various hole shifts s . A negative s corresponds to the holes being pushed in towards the center of the cavity. Also shown are the corresponding mode frequencies when the inner holes are elongated along the \hat{x} axis to form ellipses. The black solid lines are the 2D photonic crystal slab band edges and the gray dashed lines are the band edges of the quasi-3D photonic crystal.

increases the extent of the low index material into the region of the cavity. In fact, relatively small shifts or elongations result in nearly identical mode frequencies as illustrated in Fig. 5.10. As the holes are shifted further into the cavity, the corresponding ellipse becomes larger. The larger volume of low dielectric near the cavity region results in an increase of the mode frequency relative to that of the shifted hole mode. When the ellipse has a dimension of $0.44a$ along the semimajor axis and $0.35a$ along the semiminor axis, the mode frequency in a suspended slab is 0.352. This mode has a quality factor, $Q = 115$, and a photon lifetime, $\tau_{photon} = 0.058\text{ps}$. Placing the DBRs above and below the structure leads to a mode frequency of 0.3507, which is above the quasi-3D leaky band. For the quasi-3D cavity, the quality factor, $Q = 146$, is larger and the photon lifetime slightly longer, $\tau_{photon} = 0.073\text{ps}$.

The electric field components for the GaAs slab and the quasi-3D structure are shown in Fig. 5.11. Consider first the in-plane fields taken at the slab center. These field patterns



are similar to one another, and to the fields for the L3 cavity with shifted circular holes, but the fields are larger in the quasi-3D cavity. Examining the fields along the y axis of the photonic crystal, the cut plane is illustrated by the black line, the vertical confinement is also better with the DBRs. There is, however some vertical propagation. The origin of this leakage can be found by looking at the reciprocal space field profiles in Fig. 5.12. The plots have been normalized to the magnitude of the in-plane E fields. In the plots of Fig. 5.12, the circle denoted by the white dashed line corresponds to the light cone. A large magnitude inside of the circle denotes wavevectors that will lead to significant leakage. When the DBR is placed above and below the slab, the magnitude of the components within the light cone are reduced. The contribution by the wavevectors lying in the light cone are not completely eliminated and some leakage is, however, still expected. The higher field magnitude of the quasi-3D cavity fields should lead to larger spontaneous emission enhancement and the leakage may actually help to increase the light extraction efficiency from the device.

Of the cavity geometries discussed in this section, only the L3 cavity has a mode with a directional polarization. This mode also has lower Q factors and shorter photon lifetimes than many of the other modes including the monopole and quadrupole mode of the cavity in Fig. 5.4. Although the main concern is in shortening the spontaneous emission lifetime, this is nonetheless an advantage. The L3 cavity with elliptical holes along the \hat{x} axis is a better geometry than the cavity with shifted circular holes because the mode will remain well within the quasi-3D band gap once the DBRs are added. Narrowing down the selection, we see that the L3 cavity with elliptical holes possesses all of the requirements for the single-photon source. Before making any final conclusions regarding the microcavity, the spontaneous emission lifetimes of L3 cavities, both with and without DBR mirrors, must be calculated.

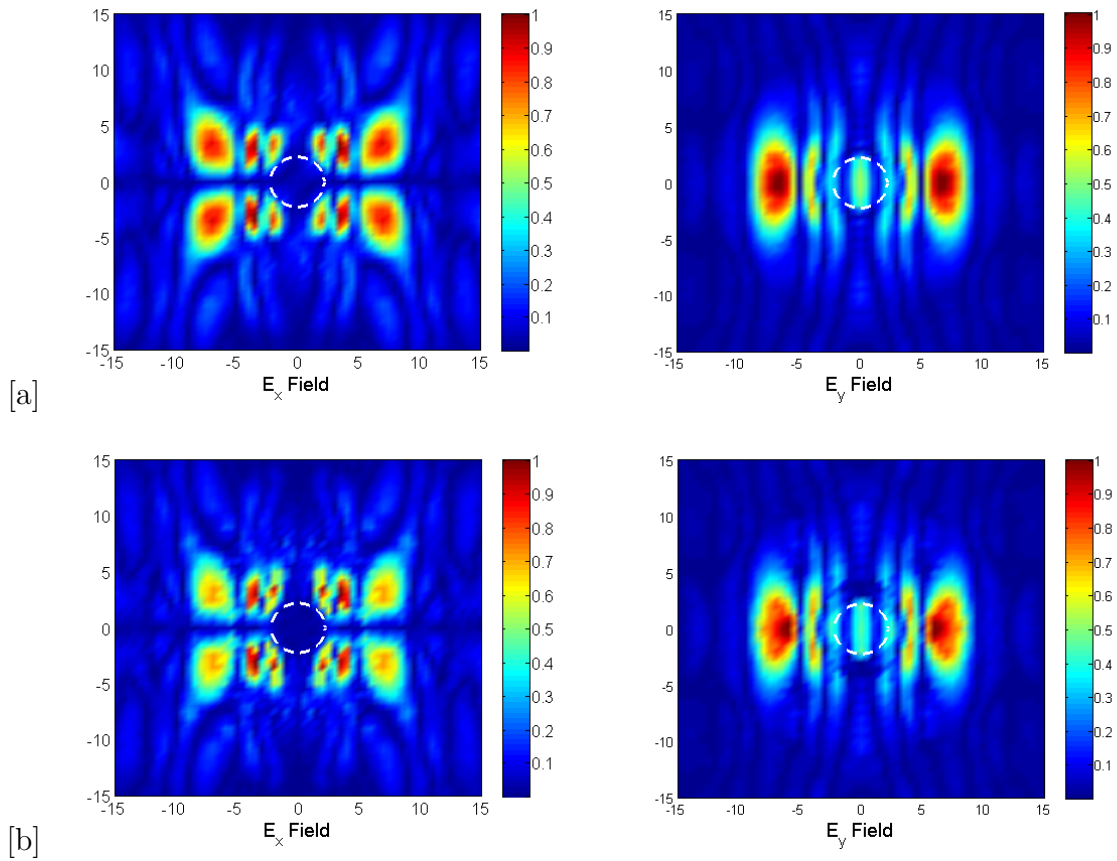


Figure 5.12: The reciprocal space representation of the E_x and E_y monopole mode fields are shown for a) the suspended slab and b) the quasi-3D structure. The dashed white circle is the light cone. Cladding the GaAs slab with highly reflective DBRs slightly decreases the contribution from wavevectors located inside the light cone.

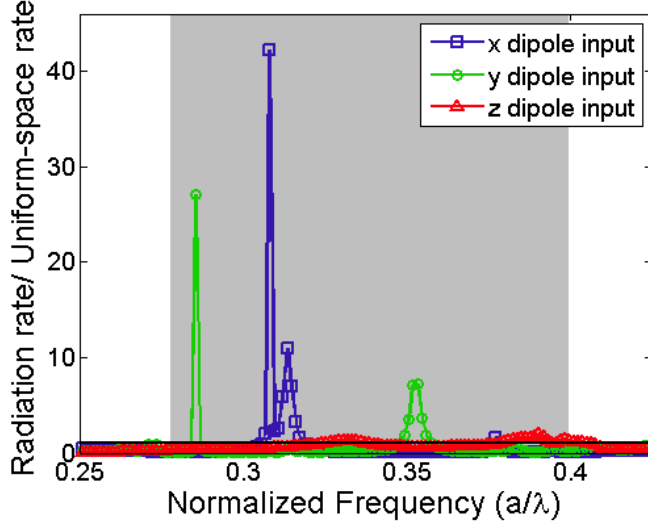


Figure 5.13: The radiation rates for a x-, y-, and z- oriented dipole source at the center of the L3 microcavity are given as a function of frequency. As expected there is good coupling of the y-dipole input to the cavity mode of interest, at $f = 0.352$. This sources also couples to a mode with x-dipole profile at $f = 0.2853$. An x-oriented input couples to two modes near $f = 0.3$ that have y-dipole-like mode profiles. The band gap is denoted by the gray shaded region and the solid black line at 1 denotes where the radiation in the cavity equals the radiation in bulk.

5.2 Spontaneous Emission Lifetimes

In experimental work, it is typical to report the spontaneous emission lifetime as extrapolated from time resolved μ PL measurements. For theoretical work, it is common to report the Purcell factor which is a dimensionless assessment of how significantly the cavity will change the lifetime. The method devised in this thesis and outlined at the end of Chapter 3 calculates the actual spontaneous emission lifetime. It was shown that these calculations are in good agreement with experimentally measured lifetimes both in bulk and on or off resonance with a cavity mode. The method will now be used to determine the spontaneous emission lifetimes when various quantum dots are placed at the center of the L3 cavity.

The spontaneous emission lifetime is given by

$$\tau_{spont} = 1/W_{fi} = \frac{3c^3}{4n\omega^3 (R_x d_{if}(x) + R_y d_{if}(y) + R_z d_{if}(z))} \quad (5.1)$$

where, c is the velocity of light in vacuum, n is the index of refraction, ω is the angular frequency, R_i ($i = x, y, z$) is the radiation rate for a dipole source oriented along the \hat{x} , \hat{y} , and \hat{z} directions in the microcavity respectively, and $d_{if}(i)$ is the dipole matrix element along the coordinate axis. Figure 5.13 shows the radiation rates for x-, y- and z- oriented dipole inputs at the slab cavity center. It is possible to choose other locations within the cavity for the source point, however to investigate the the minimum possible lifetime, the dipole must be placed at a maximum of the E_y field.

Throughout the band gap region, denoted by the gray shaded box, the radiation is suppressed except at cavity mode resonances. As expected, the y-dipole input couples to the second mode of the L3 cavity which lies at a normalized frequency of $f = 0.352$. The radiation rate of the y-dipole input in the cavity to the rate in bulk is 7.036. Because the E_x and E_z fields of the second mode have a small magnitude at the center of the cavity, as shown in Fig. 5.11, they do not couple to the resonant mode and the radiation rate is small for both inputs. The peaks at $f = 0.308$ and $f = .313$ both have a y-dipole-like mode profile and are not degenerate because the L3 cavity has reduced the symmetry of the defect. Although these modes have higher radiation rates which could lead to shorter spontaneous emission lifetimes, they were not as polarized as the second mode. Also, their mode frequencies were unaffected by the shifting or elongation of the holes along \hat{x} so it is not possible to push them into the quasi-3D photonic band gap. The peak from the y-oriented source at $f = 0.2853$ is due to the mode with a x-dipole profile. All of the quadrupole fields have a minimum at the cavity center so none of the inputs are coupling efficiently to the mode. There is a very small peak at $f = 0.3587$ in the x-dipoles radiation rate, which corresponds to the quadrupole mode.

When DBR mirrors are added above and below the GaAs slab with the L3 cavity, the radiation rates change. These rates are shown in Fig. 5.14. The same inputs couple to the same modes, which are shifted slightly lower in frequency. This agrees with the mode data presented in the previous section. Now the mode of interest lies at $f = 0.3507$ and has a

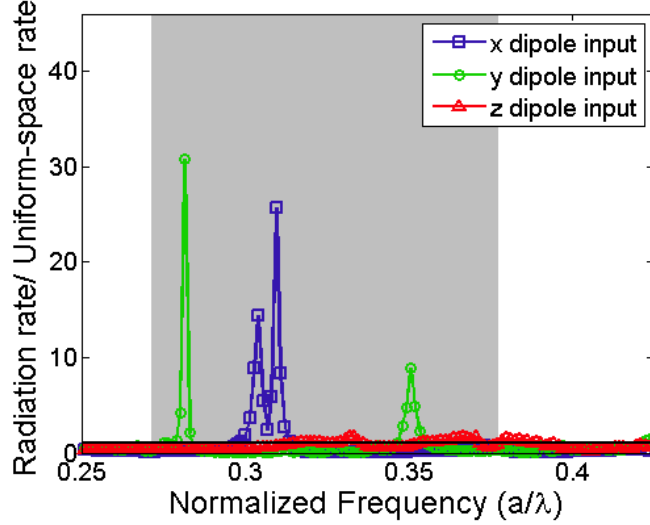


Figure 5.14: The radiation rates for a x-, y-, and z- oriented dipole source at the center of the L3 microcavity with DBR mirrors are given as a function of frequency. As expected there is good coupling of the y-dipole input to the cavity mode of interest, at $f = 0.3507$. The 2D photonic crystal band gap is denoted by the gray shaded region and the solid black line at 1 denotes where the radiation in the cavity equals the radiation in bulk.

Table 5.1: Spontaneous Emission Lifetimes L3 Microcavity with Elliptical Holes

Cavity	f (a/λ)	R_x	R_y	R_z	d_{fi_x}	d_{fi_y}	d_{fi_z}	τ_{spont} (ns)	τ_{photon} (ps)
slab	0.352	0.0446	7.036	0.6297	71.3687	47.3168	56.9332	0.31	0.058
quasi-3D	0.3507	0.1997	8.91	0.756	71.3687	47.3168	56.9332	0.24	0.073

higher radiation rate of 8.91 for a y-dipole input. This larger radiation rate should lead to shorter spontaneous emission lifetimes. Note that the quadrupole mode lies above the band gap of the quasi-3D structure and would not appear in the radiation rate plot even if the input was placed at field maximum. The gray shaded region in Fig. 5.14 denotes the 2D photonic crystal band gap, although the actual band gap for the quasi-3D structure lies only between 0.3462 and 0.3556.

A summary of the radiation rates for the x-, y-, and z-oriented dipole inputs for the mode of interest in the L3 cavity are shown in Table 5.1 for the slab and the quasi-3D structure. These values can be used to determine the spontaneous emission lifetime of quantum dots located at the center of the cavity. Focusing on small quantum dots that

have a single confined electron energy level in the conduction band will limit the InAs dots to base widths under $b = 10\text{nm}$ and dot heights of $h = 3\text{nm}$. Each dot will emit photons of a particular wavelength and a specific dot must be chosen before proceeding with the analysis. An InAs quantum dot with $b = 9\text{nm}$ and $h = 3\text{nm}$ emits photons of wavelength, $\lambda = 945.1\text{nm}$ or frequency $f = 317.2\text{THz}$. This choice is made so that the photon lifetimes calculated in Sec. 5.1 remain the same and because these values were discussed for the L3 slab case in Chapter 3. The spontaneous emission lifetime in bulk for this dot is $\tau_{spont} = 0.659\text{ns}$. In order to spectrally align the quantum dot with the cavity mode resonance, a specific lattice constant must be chosen. For the slab with $f = 0.352$, the lattice constant must be $a = 332.67\text{nm}$ and for the quasi-3D structure where $f = 0.3507$, $a = 331.4\text{nm}$.

Spontaneous emission lifetimes and photon lifetimes for the two cavities are listed in the last two columns in Table 5.1. The spontaneous emission lifetime of the quantum dot at the center of the suspended slab structure is $\tau_{spont} = 0.31\text{ns}$. For the quasi-3D structure this value decreases to $\tau_{spont} = 0.24\text{ns}$. The reason for the decrease is primarily due to the larger radiation rates that result from increased vertical confinement for a mode in the quasi-3D photonic band gap. By placing DBRs above and below the microcavity, the spontaneous emission lifetime is decreased by nearly 10%. There is a trade-off in the photon lifetime, which is slightly longer for the quasi-3D device. Since the photon lifetimes for both cavities are already significantly shorter than the spontaneous emission lifetime, the increase will have no real effect on the operating speed of the device. Neglecting the time to pump the device and considering only the sum of the spontaneous emission lifetime and the photon lifetime, the slab structure would have an operating speed of 3.2GHz. The quasi-3D cavity would have a speed of 4.2GHz when operated at the mode of interest.

As was done in Chapter 3 it is possible to consider the somewhat unrealistic situation of a tunable photonic crystal lattice constant to see how the lifetime for a particular dot changes as its photon frequency is scanned across the band gap. This provides an estimate

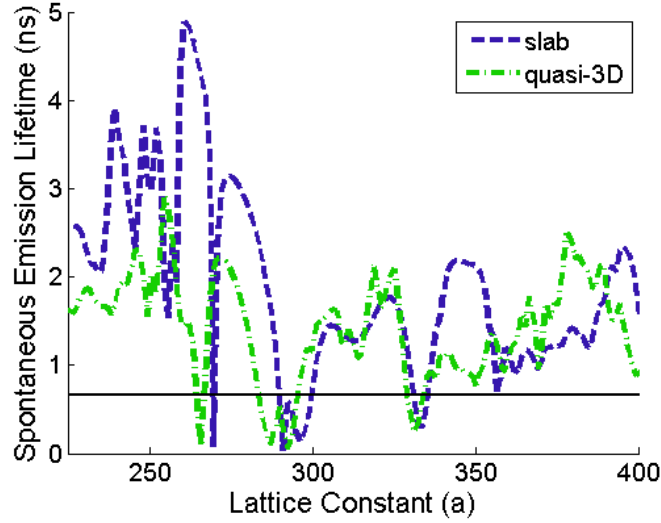


Figure 5.15: The spontaneous emission lifetime for a $b = 10\text{nm}$, $h = 3\text{nm}$ InAs quantum dot in the L3 cavity fluctuates as the photonic crystal lattice constant is changed. Certain choices of lattice constant will result in an alignment of a cavity mode frequency and the photon frequency leading to spontaneous emission lifetimes shorter than in bulk.

of the maximum and minimum spontaneous emission lifetimes for a particular dot in a cavity without having to do any additional calculations. The more realistic cases of tuning the quantum dot spectrally and spatially in and out of resonance will be considered in the next Section. Figure 5.15 illustrates the change in spontaneous emission lifetime for the InAs quantum dot at the center of the L3 cavity. In the Figure, the spontaneous emission lifetime for the $b = 9\text{nm}$, $h = 3\text{nm}$ quantum dot in bulk is shown as a solid black line. For both cavities, the emission wavelength will lie in the photonic band gap when the lattice constant is between about $255 - 360\text{nm}$. Consequently, the lifetime increases above the bulk lifetime in this range except when the dot is aligned with the cavity resonance. The spontaneous emission lifetime decreases when the lattice constant is chosen such that the resonant mode frequency matches the frequency of the photon emitted from the quantum dot.

Shown as a dashed blue curve in Fig. 5.15, the lifetimes in the suspended slab tend to be longer than those in the quasi-3D cavity, shown by the dashed green line. One exception is

Table 5.2: Extraction Efficiency from L3 Microcavity

Cavity	Radiation Rate	Total Extraction Efficiency	Top Extraction Efficiency
slab	7.03	0.9796	0.4927
quasi-3D	8.91	0.0152	0.003

for off-resonant modes in the quasi-3D band gap, for $a = 316 - 336\text{nm}$, where the lifetimes of the quasi-3D cavity are slightly longer than for the suspended slab. Most likely this is due to a decrease in the radiation rate for a z-oriented dipole in the quasi-3D gap. The minimum lifetime of $\tau_{spont} = 0.04\text{ns}$ is obtained in the slab for the lower frequency y-dipole mode, while the maximum, $\tau_{spont} = 3.13\text{ns}$, occurs off-resonance. The quasi-3D cavity has a minimum of $\tau_{spont} = 0.06\text{ns}$ for the higher frequency y-dipole mode and again a maximum off-resonance of $\tau_{spont} = 2.18\text{ns}$. Assuming that the photon lifetime will be much shorter than any of these lifetimes and can be neglected, the operating speed of the device would change from about 0.4GHz to 20GHz. For most modes, if the lattice constant is off by more than 0.6%, the quantum dot spontaneous emission lifetime will go from being shorter than the bulk lifetime to longer.

In addition to the spontaneous emission lifetime, the light extraction efficiency of the device is also important. For the L3 cavity, the E_y field is dominant and we need only focus our attention on the extraction efficiency from an E_y -oriented dipole source. When the number of holes around the defect is 6 or greater, the radiation rate and extraction efficiency remain relatively constant. The extraction efficiency for the slab and quasi-3D cavity are summarized in Table 5.2. The extraction efficiency from the slab is much higher than for the quasi-3D cavity. This is not surprising because the 4 periods of the highly reflective DBR are around 98% reflective and the vertical confinement is very strong. Although an extremely high extraction efficiency, around 98%, is possible in the slab structure, the photons are equally as likely to exit through the bottom of the device as they are at the top. For an actual practical device, there will be a substrate at some distance below one side of the device, so photons can only be collected from one side. In Chapter 4 it was noted

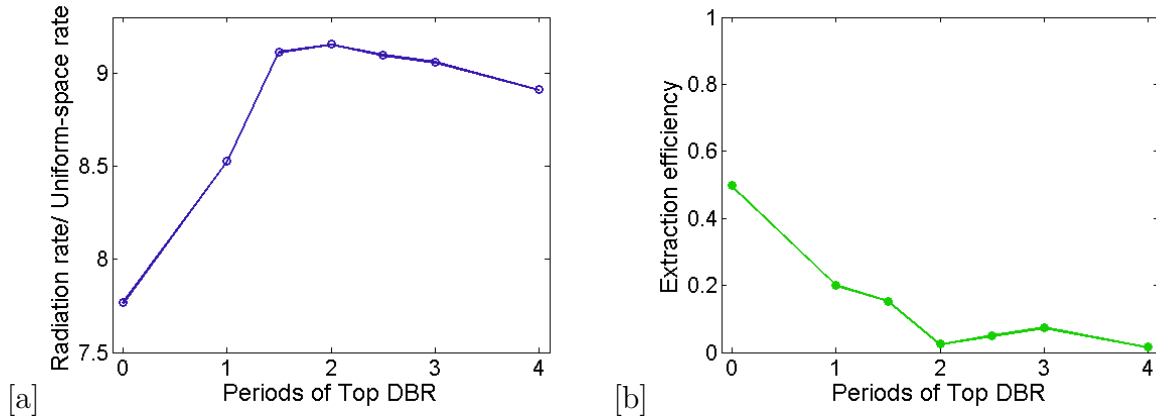


Figure 5.16: The extraction efficiency and radiation rate from an L3 cavity as the reflectivity of the top mirror is reduced.

that a better assesment of the real extraction efficiency of the source could be obtained by the ratio of the z component of the Poynting vector summed over the top half of the device divided by the total radiated power. The assumption is made that the photons will be collected from the top side of the device. When taking this into account, the extraction efficiency from the top of the slab cavity is reduced by approximately half to 49%. For the quasi-3D cavity, the extraction efficiency is reduced to less than 0.3%.

Of course, in the quasi-3D cavity with an equal number of DBR periods above and below the slab the photon will also have no preferential direction. The cavity's poor extraction efficiency as well as the directionality of the photon can be improved by reducing the reflectivity of the top mirror through reduction of the number of DBR periods. Figure 5.16 illustrates how the extraction efficiency and radiation rate are affected by the removal of layers of the top DBR. The extraction efficiency remains under 1% until the number of top DBRs is decreased to 2 periods. Then the efficiency begins to increase slowly reaching the maximum value of 49% when the top DBR is completely removed. Calculation of the top extraction efficiency yields a value of 49%, and reveals that nearly all of the vertically radiated fields are collected from the top. The radiation rate decreases when the number of DBR periods is less than 2 because there is less vertical confinement due to the reduced

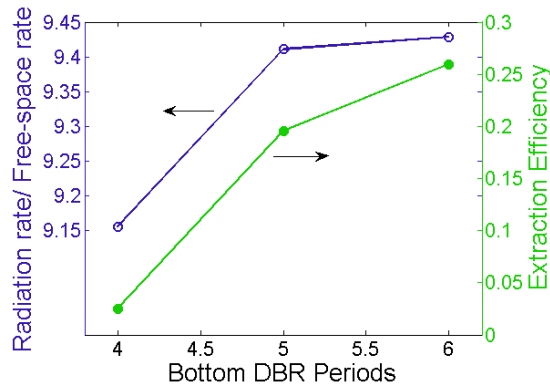


Figure 5.17: The extraction efficiency and radiation rate from an L3 cavity as the number of bottom mirrors is increased.

reflectivity. Even with no DBR on the top, however, the radiation rate remains slightly larger than for the slab suspended in air.

In order to improve the extraction efficiency further, more DBR periods can be added to the bottom of the device. Because the radiation rate was maximized when the number of top DBRs was chosen to be 2, we will add DBRs below the device to try to improve the extraction efficiency while maintaining the radiation rate. As DBR layers are added below, the radiation rate and the extraction efficiency increase, as shown in Fig. 5.17. The extraction efficiency is still much less than in the slab and it may be necessary to completely remove the top DBR to achieve efficient light extraction from this mode. Eliminating the top DBR mirror entirely, will lower relative radiation rate slightly.

5.3 Fabrication Non-idealities

When semiconductor devices are fabricated, even the best processing techniques will introduce non-idealities to the devices. The effect of fabrication errors is generally more pronounced for smaller devices and systems requiring high precision, both of which apply to the single-photon source. This section examines how significant deviations from an ideal device affect performance. The results of spectral detuning will be examined first, followed

by spatial variation of the dot position.

In photonic crystal fabrication, e-beam lithography and subsequent reactive-ion etching result in rough and non-uniform cylindrical air holes. This will affect the resonant mode frequencies and field patterns in the cavity as well as the bulk band structure. Considering that most FDTD calculations use a fairly coarse grid spacing, 20-30 points per lattice constant, the hole roughness is inherently accounted for during the simulation process. The holes are, however, generally uniform. To incorporate non-uniformity in the simulation, an SEM image of a fabricated photonic crystal can be imported and image processed. This approach is more valid for examining why a device has failed or for accurately modeling a fabricated device; it is not as applicable to simulating device performance.

For the single photon source, the main concern during the fabrication process is the alignment of the quantum dot's photon emission frequency with that of the desired cavity mode. The two key players here are the epitaxially grown InAs quantum dot and the fabricated photonic crystal. Because the variance in photonic crystal fabrication is more complicated to simulate, it is easier to consider how the device performance changes as the quantum dot emission wavelength is tuned over a reasonable range. This reasonable range can be deduced from examining photoluminescence data of real samples to determine the distribution in dot size as was discussed in Chapter 3. To examine the affect of spectral tuning this method will be employed.

The PL peak of a typical quantum dot sample will have a FWHM of around 30meV [6]. For the $b = 9\text{nm}$ and $h = 3\text{nm}$ InAs quantum dot examined in the previous section with a transition energy of 1.312eV this corresponds to transitions between 1.297 – 1.327eV. Assuming that the dot height remains at 3nm, the base width would vary from around 8.5nm to 9.5nm. The emission wavelength in this range is $\lambda = 938 - 953\text{nm}$. Figure 5.18 summarizes the change in transition energy and normalized frequency as a function of base width. The lattice constant, $a = 332.67\text{nm}$, used to determine the normalized frequency is chosen to align the $b = 9\text{nm}$ dot emission with the L3 suspended slab cavity mode of

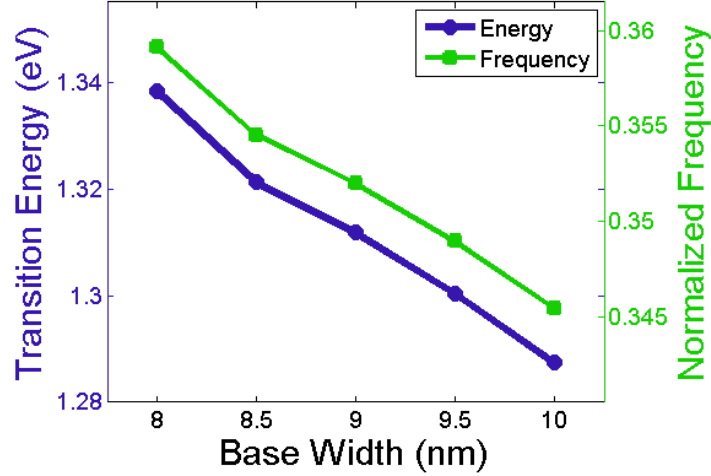


Figure 5.18: The spontaneous emission lifetime for a $b = 10\text{nm}$, $h = 3\text{nm}$ InAs quantum dot in the L3 cavity fluctuates as the photonic crystal lattice constant is changed. Certain choices of lattice constant will result in an alignment of a cavity mode frequency and the photon frequency leading to spontaneous emission lifetimes shorter than in bulk.

interest. In the figure, the data is given for dots with base widths between 8 – 10nm, to more than compensate for any realistic fabrication non-idealities.

The dots will emit photons that lie in the normalized frequency range from 0.345–0.359. A close up of the radiation rates in the L3 suspended cavity are shown in Fig. 5.19(a) with the dark gray area denoting the frequency range. At the edges of the frequency range, the radiation rates of a y-oriented dipole source are significantly lower than for the peak frequency of 0.352. The x- and z-oriented dipole radiation rates are relatively constant over the region. Shown at the right of Fig. 5.19(a), the spontaneous emission lifetime varies with the dot size. When the y-oriented dipole rate is greater than 1, as will be the case for dots with $b = 8.5 - 9\text{nm}$, the spontaneous emission lifetime is less than the bulk lifetime. For the other dots the emission is suppressed and the lifetime longer. The bulk spontaneous emission lifetime for each dot is shown by the red dashed line in the figure. Somewhat unexpectedly, the slightly off resonant quantum dot with $b = 8.5\text{nm}$ has a shorter lifetime, $\tau_{spont} = 28.97\text{ns}$, than the spectrally aligned dot. For this quantum dot the normalized frequency is approximately $f = 0.354$ and the y-dipole radiation rate is greater than 1.

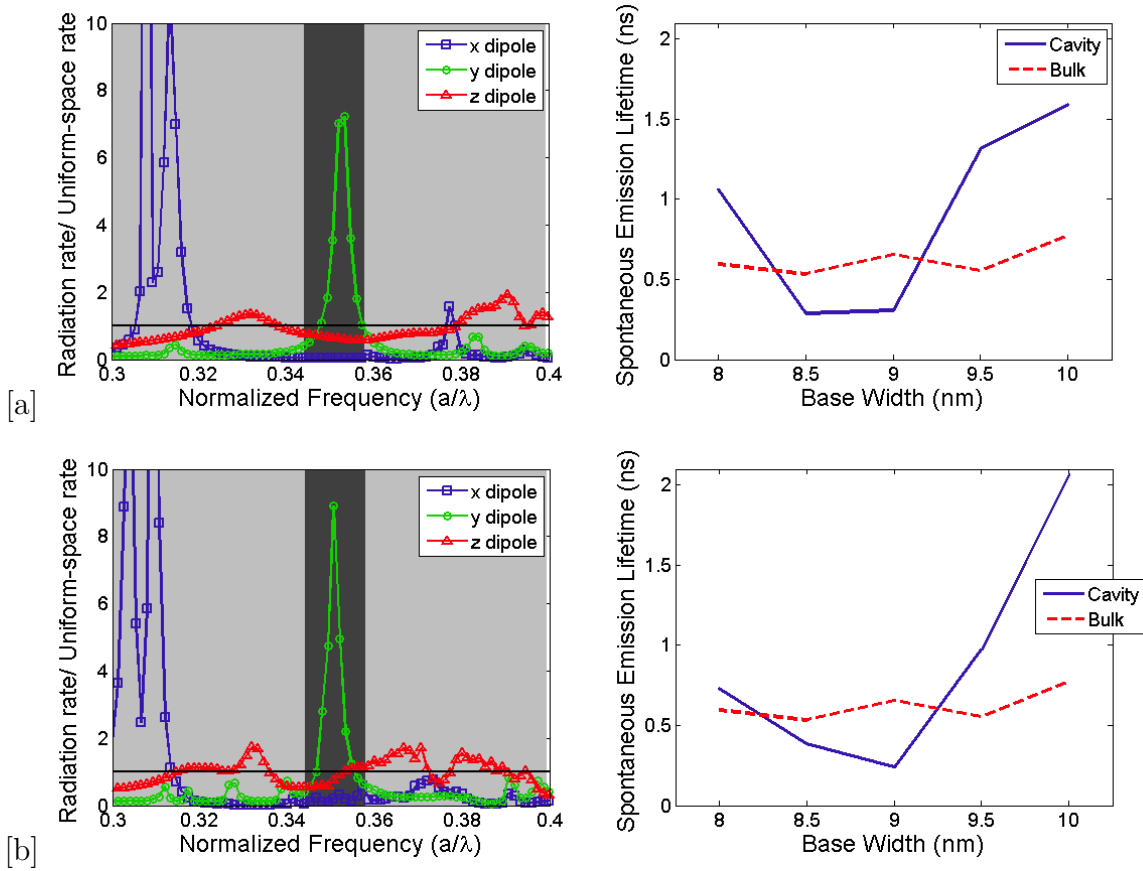


Figure 5.19: The reciprocal space representation of the E_x and E_y monopole mode fields are shown for a) the suspended slab and b) the quasi-3D structure. The dashed white circle is the light cone. Cladding the GaAs slab with highly reflective DBRs slightly decreases the contribution from wavevectors located inside the light cone.

The larger radiation rate along with the lower bulk lifetime is what leads to the shorter spontaneous emission lifetime for the $b = 8.5\text{nm}$ dot. The relative reduction in lifetime of 47%, however, is still greatest when $b = 9\text{nm}$.

When the quantum dot is placed in the quasi-3D cavity, the normalized frequencies change slightly because the lattice constant is now $a = 331.4\text{nm}$. The radiation rates in the frequency range of interest as well as the spontaneous emission lifetime as a function of dot base width are given in Fig. 5.19(b). Again the emission of the $b = 8.5 - 9\text{nm}$ dots are enhanced, however now the $b = 9\text{nm}$ dot has the shortest lifetime. The y-dipole radiation rate for the $b = 8.5\text{nm}$ dot is close to 1 and less than for the suspended slab cavity, which causes the increase. Comparison of the suspended slab and quasi-3D cavity results show that the quasi-3D cavity has a slightly larger range of quantum dot base width where emission enhancement occurs; it is $b \approx 8.25 - 9.25\text{nm}$.

An additional concern during the fabrication process is the spatial location of the quantum dot inside of the cavity. Positioning of the dot could be aided by a μPL setup that also has lithography capabilities. Once a quantum dot with the desired emission wavelength is identified, large fabrication markings can denote where the photonic crystal microcavity should be located. These markings can be used when performing e-beam lithography to pattern the photonic crystal. Still, there will be some error in the placement of the dot inside of the cavity. To investigate the significance of the dot placement, the spontaneous emission lifetime will be found as a function of space. This calculation is done only for in-plane or lateral variation of the dot position. Assuming that the device will be grown by MBE, there should not be any significant vertical variation of the dot placement.

As illustrated by the electric field patterns in Sec. 5.1, each field has its own distribution inside of the microcavity. In Chapter 4, the radiation rate was shown to vary proportionally with the magnitude of the field. By putting an x-dipole at the maximum of the E_x field, a y-dipole at the maximum of the E_y field and a z-dipole at the maximum of the E_z field it is possible to extrapolate the radiation rate of a dipole placed at any location inside of

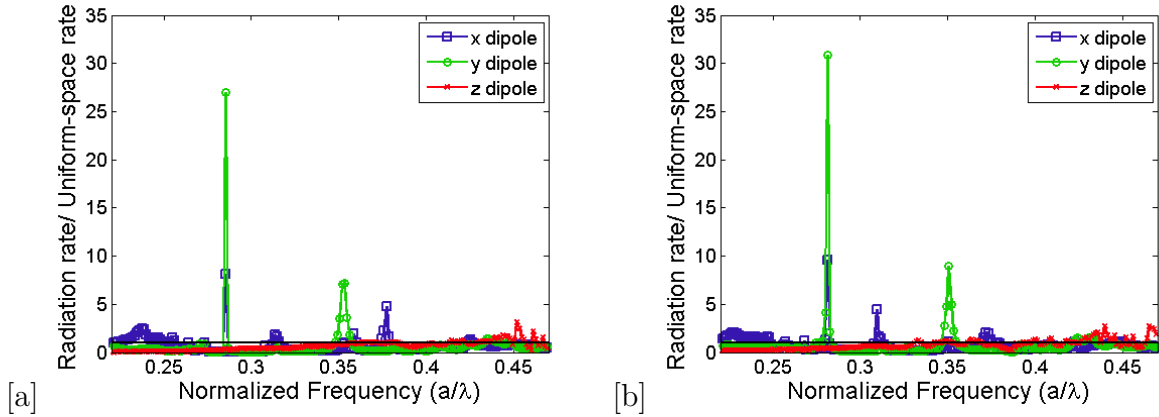


Figure 5.20: Radiation Rate for x, y and z dipoles as a function of normalized frequency. The dipoles are not co-located, but instead each dipole is placed at the corresponding field maximum.

the cavity. This is in contrast to all previous results which were obtained by placing the x-, y-, and z-dipole sources at the same spatial position in the cavity. The rates can not be accurately extrapolated from the initial, co-located source data because extrapolations of rates from field minimums leads to significant errors. During the extrapolation process, the magnitude of the field is normalized to the value at the input location. For minimum field locations, this leads to division by a small number and numerical instability. In the L3 cavity, for instance, the E_x and E_z fields have minimums at the cavity center. To simulate the spatial variation of the spontaneous emission lifetime in this cavity, two additional radiation rate calculations must be performed, one for the x input and one for the z input. The y-dipole is already chosen at the cavity center and the rates in the cavity can be directly extrapolated from this result.

Once the radiation rates have been determined at the x, y, and z field maximums, then the rates can be extrapolated to each position. The rates are found as a function of frequency and are shown in Fig. 5.20 for the suspended slab (a) and the quasi-3D slab (b). The field distributions can be found from quality factor calculations where the excitation frequency is the same as the mode of interest, for the L3 suspended slab $f = 0.352(a/\lambda)$. While the fields were initially taken after the mode had reached steady-state and before the

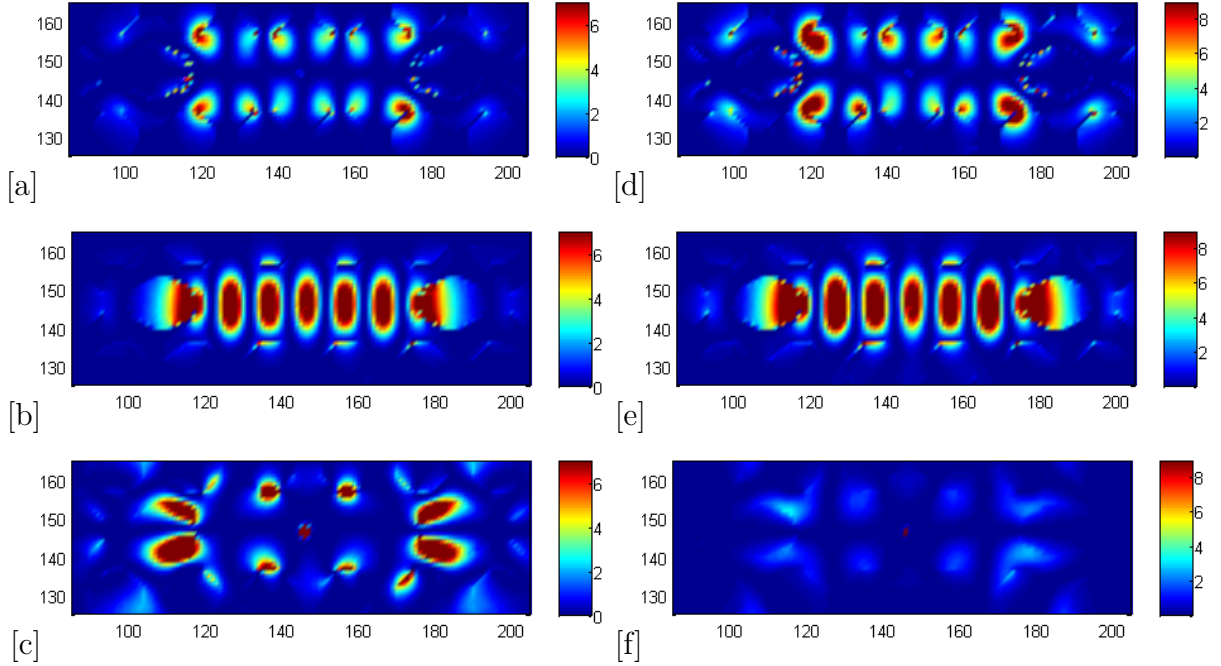


Figure 5.21: The radiation rate for a (a) x-dipole, (b) y-dipole, (c) z-dipole as its position is varied in the L3 suspended slab cavity. The radiation rates for the x, y, and z dipoles in the L3 quasi-3D cavity are shown in (d)-(f), respectively.

input was turned off, this actually introduced a small error because of the typical charging error that occurs from point sources in FDTD [2]. It was found that the results improved if the field distributions were taken after the source had been turned off. This minimized, although not completely eliminated, an abrupt spike in the spontaneous emission lifetime at the quality factor calculation injection site. It was verified that the general relative field distribution was not affected by this change and only the maximum value in absolute terms was affected. Since the fields are normalized, the actual value of the field is inconsequential.

The radiation rate for the x, y and z dipoles are shown as a function of position in the L3 suspended slab cavity in Fig. 5.21 (a)-(c). As expected these figures resemble the electric field distributions, and large radiation rates correspond to high electric fields. The radiation rates for the quasi-3D cavity are nearly identical, the only difference being the maximum rate, as shown in Fig. 5.21 (d)-(f). Next the spontaneous emission lifetime can be found for a specific quantum dot by substituting the spatially varying radiation rates

and the quantum dot axial dipole transition matrix elements into equation 5.1.

To illustrate this method, the spontaneous emission lifetimes for a $b = 9nm$ and $h = 3nm$ InAs quantum dot in the L3 slab and quasi-3D cavity are shown in Fig. 5.22 (a) and (b), respectively. The axial transition matrix elements for this dot were given in Table 5.1. In the Figure, the color scale ranges from 0 to the bulk spontaneous emission lifetime of the dot, $\tau_{spont} = 0.659ns$ for both structures. This choice is made to highlight the regions where the spontaneous emission is enhanced while assuming that all regions where the emission is suppressed are equally undesirable locations for the quantum dot. As a result, the dark red regions correspond to spontaneous emission lifetimes greater than or equal to the bulk lifetime. Although the images are zoomed in on the cavity region, outside of this region all spontaneous emission is suppressed. The lifetime in the photonic crystal air holes is set to 0, shown as white, because no dots can be present at those locations. To highlight that shorter lifetimes are possible for a quantum dot placed in the ideal location of the quasi-3D cavity than of the suspended slab cavity, the scales for both cavities are the same. From the Figure it also appears that there is a larger area where the quantum dot's emission is enhanced if the dot is placed in the quasi-3D cavity. Calculating the area where the emission is enhanced, and dividing by the total cavity area shows that this is in fact the case. For the suspended slab cavity, enhancement occurs over approximately 35% of the cavity area and for the quasi-3D cavity this is increased to 40%.

Figure 5.23 shows the spontaneous emission lifetime along two cut planes of the cavities. Also shown is a view of the cavity with a solid black line illustrating the location of the slice. The bulk lifetime is given by the dashed red line so that regions of enhancement and suppression can be easily identified. Consider first the lifetimes as the dot is shifted along the \hat{x} direction in the cavity. Outside of the cavity region, the lifetimes increase substantially above the bulk value. The emissions from dots not lying in the cavity will be suppressed enough that a single photon can be isolated. In the cavity region there are large segments of enhancement with several approximately equally spaced peaks where

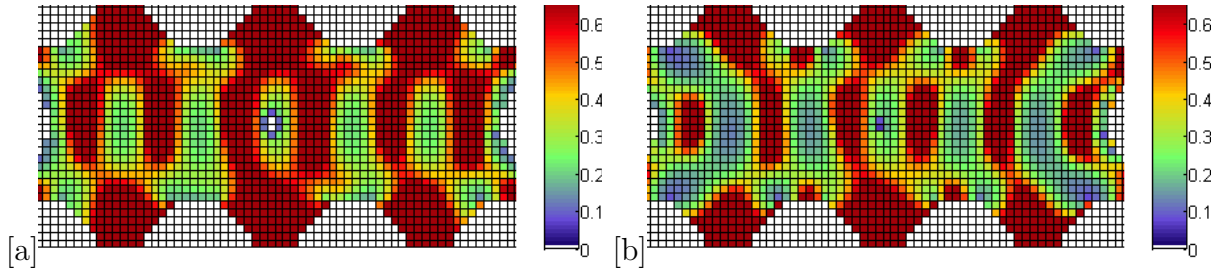


Figure 5.22: The spontaneous emission lifetime as a function of the $b = 9\text{nm}$, $h = 3\text{nm}$ InAs quantum dot location in the L3 (a) suspended slab and (b) quasi-3D cavity. The lifetimes are given in nanoseconds and the scale ranges from 0 to the bulk spontaneous emission lifetime. The white regions are the air holes of the photonic crystal where no emitter can be located.

the emission is suppressed. While the values of the minimum lifetime remains relatively constant, the maximum lifetimes in the cavities vary. The minimum lifetimes are dominated by the large radiation rates of the y-dipole and subsequently the E_y field distribution. Maximum lifetimes, however, occur when the radiation rates for all of the dipoles are low and depend fundamentally on the E_x , E_y and E_z field values. Since each field has its own symmetry in the cavity, the maximum lifetimes are expected to vary more with position.

Generally, the spontaneous emission lifetimes in the quasi-3D cavity are shorter than in the suspended slab cavity. This is easier to see from the plot of the lifetime as the dot is shifted along the \hat{y} direction as in Fig. 5.23. The extra dip at approximately cell 146 is due to a perturbation of the electric field value near the injection site for the quality factor calculations, and is an artifact of the simulation. As expected, the spontaneous emission enhancement occurs over a larger range for the quasi-3D cavity than for the suspended slab.

Although the requirement for directional polarization somewhat limits the maximum possible spontaneous emission enhancement, precise alignment of a quantum dot with the second mode of the L3 cavity will allow for faster operating speeds than a dot in bulk. Adding a DBR above and below the cavity further improves the spontaneous emission lifetime by about 10%. The quasi-3D cavity also has a larger cavity area over which

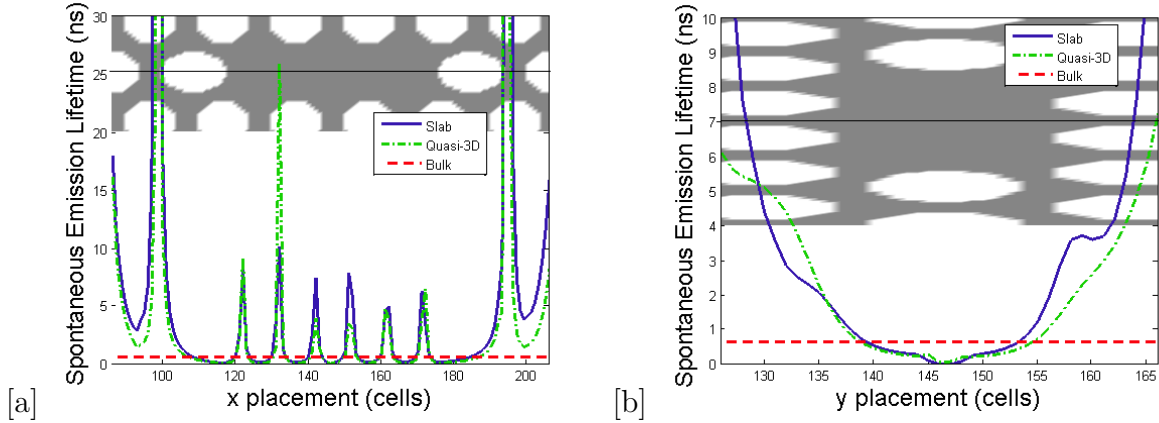


Figure 5.23: The spontaneous emission lifetimes of Fig. 5.22 are shown along 2 cut planes, (a) x and (b) y. At the top of each plot is image of the cavity with the cut location denoted by the solid black line. Lifetime of the $b = 9\text{nm}$, $h = 3\text{nm}$ InAs quantum dot in the suspended cavity is given by the solid blue line and the lifetime in the quasi-3D cavity is denoted by a dot-dash green line.

emission is enhanced, thus relaxing the condition for precise dot placement in the cavity. Tuning of the quantum dot spectrally in and out of resonance with the second mode of the L3 cavity is also slightly less sensitive for the quasi-3D structure. The poor extraction efficiency of the quasi-3D device is improved by adjusting the reflectivity of the mirrors above and below the GaAs slab. A higher top extraction efficiency than in a suspended slab is possible when the top DBR is removed and 2 periods are added to the bottom DBR. Although this reduces the radiation rate of the y oriented dipole slightly, the rate remains above that of the suspended slab. These advantages as well as the desirable mode polarization and short photon lifetime, make the single quantum dot in a L3 elliptical-hole quasi-3D cavity an excellent candidate for a single-photon source.

Chapter 6

Summary and Recommendation for Future Work

6.1 General Conclusions

This thesis has developed a computational model for designing and analyzing a single quantum dot inside of a photonic crystal microcavity for use as a single-photon source. Two main modeling tools are combined: the Finite-Difference Time-Domain method for characterizing the microcavity, and an 8-band $k \cdot p$ perturbation theory for determining the energy levels and wavefunctions in the quantum dot. For this research, we have implemented the Finite-Difference Time-Domain method in C using openMP directives to parallelize the computationally challenging portions of the code. The 8-band $k \cdot p$ calculations are done using Nextnano++.

A single-photon source is necessary to implement a quantum key distribution scheme. Quantum cryptography has emerged as a potential replacement of classical cryptography systems, which will no longer be secure if a quantum computer is developed. The quantum key distribution scheme relies on the generation, transmission and detection of single-polarized photons to establish a secure key that can be used to encode data sent through

classical channels. Working with single photons is not an easy task. Each portion of the system is complex and has its own unique challenges for practical implementation. In this thesis, the focus was on the generation of single-photons by investigating the interaction of a quantum dot with novel photonic crystal microcavities.

The ideal source would emit single polarized photons on demand with as little wait time as possible. At the beginning of the device design process, an operating frequency must be chosen. This frequency is used to determine the size of the quantum dot. Changing the size of the dot changes the energy levels, the transition energy, and the frequency of the emitted photon. The photonic crystal microcavity must also be designed to have a mode at the operating frequency. The polarization of the photon is determined by the microcavity geometry which supports one or a few modes, each having its own distinct field profile. Using finite-difference time-domain methods, the mode frequencies, mode profiles and cavity quality factors can all be determined.

To calculate the speed of the device, the model calculates both the spontaneous emission lifetime and the photon lifetime. The photon lifetime is inversely related to the quality factor. Because fast operating speed is a design goal, the cavity Q for the single-photon source should not be too large. For the spontaneous emission lifetime calculation, the dipole matrix element along each axis of the quantum dot is determined from the complex wavefunctions of the electron and hole. These results are multiplied by weighing factors and then summed to determine the new total dipole matrix element for the dot inside of a microcavity. When the quantum dot is in bulk, the weighing factors are 1 and the equations reduce to familiar form.

Using this method, both key lifetimes are determined. While this is not particularly challenging for the photon lifetime, theoretically determined spontaneous emission lifetimes have previously only been found in terms of relative quantities such as the Purcell factor. This is acceptable when the microcavities are used for lasers, because many randomly located and oriented emitters will collectively emit into the cavity. In the single-photon

source there is a single quantum dot at a particular location in the cavity and exact calculations of the lifetime make more sense. To validate the spontaneous emission lifetime calculations developed in this thesis, the results were compared with experimental data and found to be in good agreement.

In addition to developing the computational model, a novel photonic crystal microcavity is also investigated. The microcavity is formed by combining 2D distributed Bragg reflection for in-plane confinement while using 1D distributed Bragg reflection for vertical confinement. The band diagrams for the bulk photonic crystal are found using 3D Finite-Difference Time-Domain methods. Using a 3D instead of a 2D implementation allows us to fully determine the effect of the vertical DBRs without making any assumptions regarding the vertical component of the wavevector. When the DBRs were added above and below the GaAs slab, there were 4 bands that enter the 2D photonic crystal band gap. These bands originate from the continuum of TE modes for an unpatterned DBR.

The presence of the TE bands in the 2D photonic crystal band gap did not necessarily lead to lower radiation rates and longer spontaneous emission lifetimes. Instead, the propagation into the DBR depended on how large the wavevector of the mode was at the TE state locations. If the magnitude of the wavevectors were small, then the coupling to the DBR was inefficient and larger radiation rates than in the suspended slab cavity were observed. Splitting the degenerate dipole mode and tuning the mode frequencies over the band gap verified this theory.

For a single-photon source, the mode must be highly polarized along a single axis. Doing so requires creating a defect that is asymmetric. We investigated the second x-dipole-like mode of an L3 cavity which has a \hat{y} polarization. By adjusting the inner holes along the \hat{x} axis to form elliptical air holes, the mode frequency was pushed up into the quasi-3D band gap of the photonic crystal. The spontaneous emission lifetime was shorter for a quantum dot in the quasi-3D microcavity than in the suspended slab. To improve the extraction efficiency of the quasi-3D device, the top mirror reflectivity was reduced.

This resulted in a slightly lower radiation rate, but the rate was still higher than in the suspended slab. Using the quasi-3D cavity in a single photon source has the following advantages: a shorter spontaneous emission lifetime, faster operating speed, and a higher top extraction efficiency.

6.2 Recommendation for Future Work

To improve upon the computational model developed in this thesis, more complex quantum dot modeling could be used. For simplicity, the quantum dots were assumed to be made purely of InAs. In practice this is not the case and the dots are composed of $\text{In}_{1-x}\text{Ga}_x\text{As}$. Moreover the In content can vary throughout the dot. A more advanced model would take these variations into account. Nextnano++ should be capable of accounting for these situations; however, care must be taken when identifying the material constants that are used. In Nextnano++, many of the parameters are determined by linear interpolation between the constants for GaAs and InAs, although it is possible to use other interpolation schemes. It is recommended that new materials and grading be applied and tested on simple 1D structures before being used for quantum dots whenever possible. Incorporating these new materials may change the actual values of the energy levels, but the trends should remain the same.

The quantum dots were also pyramidal in shape. Real dots that are capped by GaAs tend to have flat tops and investigations using a truncated pyramidal geometry should also be conducted. Changing the shape will affect both the energy levels and the wavefunctions. Smaller dots may be more affected by the adjustment in the geometry.

For a single-photon source, the polarization requirement restricts which modes can be used. Other modes in the L3 microcavity and modes in other microcavity geometries have even more spontaneous emission enhancement than the \hat{y} polarized mode in the L3 cavity. Further investigation of candidate microcavities may produce other more advantageous

geometries and modes for use in the single-photon source. A mode that has even higher relative radiation rates and maintains a highly directional polarization is desirable.

The use of quasi-3D photonic crystal microcavities could also be explored for other applications such as LEDs. Photonic crystals have been proposed for use in LEDs to help improve the extraction efficiency from the slab membrane. Using a properly designed DBR below the suspended slab may help to improve the top extraction efficiency of the devices. The quasi-3D microcavities may also be useful in lasers because they can have higher quality factors than the suspended slab devices. They also offer the advantage of higher top extraction efficiency if the bottom mirror is more reflective than the top. The additional control over spontaneous emission enhancement and suppression in the quasi-3D microcavity may also be an advantage for thresholdless lasers.

Bibliography

- [1] C. Bennett and G. Brassard, “Quantum cryptography: Public key distribution and coin tossing,” in *Proceedings of IEEE International Conference on Computers, Systems and Signal Processing*, vol. 175, 1984.
- [2] R. Alleaume, J. Bouda, C. Branciard, T. Debuisschert, M. Dianati, N. Gisin, M. Godfrey, P. Grangier, T. Langer, A. Leverrier, *et al.*, “SECOQC White Paper on quantum key distribution and cryptography,” *Arxiv preprint quant-ph/0701168*, 2007.
- [3] Y. Zhao, B. Qi, X. Ma, H. Lo, and L. Qian, “Experimental quantum key distribution with decoy states,” *Physical review letters*, vol. 96, no. 7, p. 70502, 2006.
- [4] N. Gisin, G. Ribordy, H. Zbinden, D. Stucki, N. Brunner, and V. Scarani, “Towards practical and fast Quantum Cryptography,” *Arxiv preprint quant-ph/0411022*, 2004.
- [5] C. Gobby, Z. Yuan, and A. Shields, “Quantum key distribution over 122 km of standard telecom fiber,” *Applied Physics Letters*, vol. 84, p. 3762, 2004.
- [6] R. Ursin, F. Tiefenbacher, T. Schmitt-Manderbach, H. Weier, T. Scheidl, M. Lindenthal, B. Blauensteiner, T. Jennewein, J. Perdigues, P. Trojek, *et al.*, “Free-space distribution of entanglement and single photons over 144 km,” *eprint arXiv: quant-ph/0607182*, 2006.
- [7] R. Thew, S. Tanzilli, L. Krainer, S. Zeller, A. Rochas, I. Rech, S. Cova, H. Zbinden, and N. Gisin, “GHz QKD at telecom wavelengths using up-conversion detectors,” *New J. Phys*, vol. 8, p. 32, 2006.

- [8] H. Kimble, M. Dagenais, and L. Mandel, “Photon antibunching in resonance fluorescence,” *Physical Review Letters*, vol. 39, no. 11, pp. 691–695, 1977.
- [9] F. Diedrich and H. Walther, “Nonclassical radiation of a single stored ion,” *Physical review letters*, vol. 58, no. 3, pp. 203–206, 1987.
- [10] T. Basche, W. Moerner, M. Orrit, and H. Talon, “Photon antibunching in the fluorescence of a single dye molecule trapped in a solid,” *Physical review letters*, vol. 69, no. 10, pp. 1516–1519, 1992.
- [11] P. Michler, A. Imamoglu, M. Mason, P. Carson, G. Strouse, and S. Buratto, “Quantum correlation between photons from a single quantum dot at room temperature,” *Nature*, vol. 406, pp. 968–970, 2000.
- [12] Z. Yuan, B. Kardynal, R. Stevenson, A. Shields, C. Lobo, K. Cooper, N. Beattie, D. Ritchie, and M. Pepper, “Electrically driven single-photon source,” 2002.
- [13] A. Bennett, D. Unitt, P. See, A. Shields, P. Atkinson, K. Cooper, and D. Ritchie, “Microcavity single-photon-emitting diode,” *Applied Physics Letters*, vol. 86, p. 181102, 2005.
- [14] C. Monat, B. Alloing, C. Zinoni, L. Li, and A. Fiore, “Nanostructured current-confined single quantum dot light-emitting diode at 1300 nm,” *Nano Lett*, vol. 6, no. 7, pp. 1464–1467, 2006.
- [15] E. Yablonovitch, “Inhibited spontaneous emission in solid-state physics and electronics,” *Physical Review Letters*, vol. 58, no. 20, pp. 2059–2062, 1987.
- [16] Y. Miklyaev, D. Meisel, A. Blanco, G. Von Freymann, K. Busch, W. Koch, C. Enkrich, M. Deubel, and M. Wegener, “Three-dimensional face-centered-cubic photonic crystal templates by laser holography: fabrication, optical characterization, and band-structure calculations,” *Applied Physics Letters*, vol. 82, p. 1284, 2003.
- [17] M. Boroditsky, R. Vrijen, T. Krauss, R. Coccioli, R. Bhat, and E. Yablonovitch,

- “Spontaneous emission extraction and purcell enhancement from thin-film 2-d photonic crystals,” *J. Lightwave Technol*, vol. 17, pp. 2096–2112, 1999.
- [18] P. Michler, A. Kiraz, C. Becher, W. Schoenfeld, P. Petroff, L. Zhang, E. Hu, and A. Imamoglu, “A quantum dot single-photon turnstile device,” *Science*, vol. 290, no. 5500, pp. 2282–2285, 2000.
- [19] E. Moreau, I. Robert, J. Gerard, I. Abram, L. Manin, and V. Thierry-Mieg, “Single-mode solid-state single photon source based on isolated quantum dots in pillar microcavities,” *Applied Physics Letters*, vol. 79, p. 2865, 2001.
- [20] W. Chang, W. Chen, H. Chang, T. Hsieh, J. Chyi, and T. Hsu, “Efficient single-photon sources based on low-density quantum dots in photonic-crystal nanocavities,” *Physical review letters*, vol. 96, no. 11, p. 117401, 2006.
- [21] H. Park, S. Kim, S. Kwon, Y. Ju, J. Yang, J. Baek, S. Kim, and Y. Lee, “Electrically driven single-cell photonic crystal laser,” 2004.
- [22] A. Imamoglu and Y. Yamamoto, “Turnstile device for heralded single photons: Coulomb blockade of electron and hole tunneling in quantum confined pin heterojunctions,” *Physical review letters*, vol. 72, no. 2, pp. 210–213, 1994.
- [23] K. Yee *et al.*, “Numerical solution of initial boundary value problems involving Maxwell’s equations in isotropic media,” *IEEE Trans. Antennas Propagat*, vol. 14, no. 3, pp. 302–307, 1966.
- [24] J. Berenger, “A perfectly matched layer for the absorption of electromagnetic waves,” *Journal of computational physics*, vol. 114, no. 2, pp. 185–200, 1994.
- [25] Z. Sacks, D. Kingsland, R. Lee, and J. Lee, “A perfectly matched anisotropic absorber for use as an absorbing boundary condition,” *Antennas and Propagation, IEEE Transactions on*, vol. 43, no. 12, pp. 1460–1463, 1995.
- [26] W. Kuang, W. J. Kim, and J. O’Brien, “Finite-difference time domain method for

- nonorthogonal unit-cell two-dimensional photonic crystals,” *Lightwave Technology, Journal of*, vol. 25, pp. 2612–2617, sept. 2007.
- [27] A. Chutinan and S. Noda, “Waveguides and waveguide bends in two-dimensional photonic crystal slabs,” *Phys. Rev. B*, vol. 62, pp. 4488–4492, Aug 2000.
- [28] A. Umenyi, K. Miura, and O. Hanaizumi, “Modified Finite-Difference Time-Domain Method for Triangular Lattice Photonic Crystals,” *J. Lightwave Technol.*, vol. 27, pp. 4995–5001, 2009.
- [29] J. Proakis and D. G. Manolakis, *Digital Signal Processing: Principles, Algorithms, and Applications*. Prentice Hall, 4th edition ed., 2006.
- [30] H. Park, J. Hwang, J. Huh, H. Ryu, S. Kim, J. Kim, and Y. Lee, “Characteristics of modified single-defect two-dimensional photonic crystal lasers,” *IEEE Journal of Quantum Electronics*, vol. 38, no. 10, pp. 1353–1365, 2002.
- [31] J. Hwang, H. Ryu, and Y. Lee, “Spontaneous emission rate of an electric dipole in a general microcavity,” *Physical Review B*, vol. 60, no. 7, pp. 4688–4695, 1999.
- [32] E. Hinds, “Cavity quantum electrodynamics,” in *Suppliment 2* (D. Bates and B. Bederson, eds.), vol. 28 of *Advances In Atomic, Molecular, and Optical Physics*, pp. 237–289, Academic Press, 1990.
- [33] S. C. H. Allen Taflove, *Computational Electrodynamics: The Finite-Difference Time-Domain Method*. Artech House, 2005.
- [34] M. Burt, “The justification for applying the effective-mass approximation to microstructures,” *Journal of Physics: Condensed Matter*, vol. 4, p. 6651, 1992.
- [35] C. Van de Walle, “Band lineups and deformation potentials in the model-solid theory,” *Physical Review B*, vol. 39, no. 3, pp. 1871–1883, 1989.
- [36] Walter Schottky Institute. <http://www.nextnano.de/nextnano3/>.
- [37] T. Zibold, *Semiconductor based quantum information devices: Theory and simula-*

- tions. PhD thesis, Technische Universität München, 2007.
- [38] J. Bardeen, “An improved calculation of the energies of metallic Li and Na,” *The Journal of Chemical Physics*, vol. 6, p. 367, 1938.
- [39] F. Seitz, *The Modern Theory of Solids*. McGraw-Hill, 1940.
- [40] E. Kane, “The k-p Method,” *Semiconductors and Semimetals*, vol. 1, pp. 75–100, 1966.
- [41] P. Löwdin, “A Note on the Quantum-Mechanical Perturbation Theory,” *The Journal of Chemical Physics*, vol. 19, p. 1396, 1951.
- [42] O. Stier, M. Grundmann, and D. Bimberg, “Electronic and optical properties of strained quantum dots modeled by 8-band $k \cdot p$ theory,” *Phys. Rev. B*, vol. 59, pp. 5688–5701, Feb 1999.
- [43] V. Stoleru, D. Pal, and E. Towe, “Self-assembled (In, Ga) As/GaAs quantum-dot nanostructures: strain distribution and electronic structure,” *Physica E: Low-dimensional Systems and Nanostructures*, vol. 15, no. 3, pp. 131–152, 2002.
- [44] J. Eshelby, “The determination of the elastic field of an ellipsoidal inclusion, and related problems,” *Proceedings of the Royal Society of London. Series A, Mathematical and Physical Sciences*, pp. 376–396, 1957.
- [45] J. Altenbach and H. Altenbach, *Einführung in die Kontinuumsmechanik*. B.G. Teubner, 1994.
- [46] Walter Schottky Institute. <http://www.nextnano.de/nextnano>.
- [47] Landolt-Börnstein Database, *Group IV Elements, IV-IV and III-V Compounds. Part b - Electronic, Transport, Optical and Other Properties*, vol. 41A1b. Springer-Verlag, 2002.
- [48] C. Pryor, “Geometry and material parameter dependence of InAs/GaAs quantum dot electronic structure,” *Physical Review B*, vol. 60, no. 4, p. 2869, 1999.

- [49] I. Vurgaftman, J. Meyer, and L. Ram-Mohan, “Band parameters for III–V compound semiconductors and their alloys,” *Journal of applied physics*, vol. 89, p. 5815, 2001.
- [50] J. D. Joannopoulos, S. G. Johnson, J. N. Winn, and R. D. Meade, *Photonic Crystals: Molding the Flow of Light*. Princeton University Press, 2008.
- [51] S. Fan, P. R. Villeneuve, J. D. Joannopoulos, and E. F. Schubert, “High extraction efficiency of spontaneous emission from slabs of photonic crystals,” *Phys. Rev. Lett.*, vol. 78, pp. 3294–3297, Apr 1997.
- [52] O. Painter, J. Vučkovič, and A. Scherer, “Defect modes of a two-dimensional photonic crystal in an optically thin dielectric slab,” *J. Opt. Soc. Am. B*, vol. 16, no. 2, pp. 275–285, 1999.
- [53] J. N. Winn, Y. Fink, S. Fan, and J. D. Joannopoulos, “Omnidirectional reflection from a one-dimensional photonic crystal,” *Opt. Lett.*, vol. 23, no. 20, pp. 1573–1575, 1998.
- [54] K. Srinivasan and O. Painter, “Momentum space design of high-Q photonic crystal optical cavities,” *Opt. Express*, vol. 10, no. 15, pp. 670–684, 2002.
- [55] J. D. Joannopoulos, S. G. Johnson, J. N. Winn, and R. D. Meade, *Photonic Crystals: Molding the Flow of Light*. Princeton University Press, 2008.
- [56] Y. No, H. Ee, S. Kwon, S. Kim, M. Seo, J. Kang, Y. Lee, and H. Park, “Characteristics of dielectric-band modified single-cell photonic crystal lasers,” *Optics Express*, vol. 17, no. 3, pp. 1679–1690, 2009.
- [57] K. Srinivasan and O. Painter, “Fourier space design of high-Q cavities in standard and compressed hexagonal lattice photonic crystals,” *Phys. Lett*, vol. 80, pp. 3883–3885, 2002.
- [58] O. Painter and K. Srinivasan, “Localized defect states in two-dimensional photonic crystal slab waveguides: A simple model based upon symmetry analysis,” *Physical*

Review B, vol. 68, no. 3, p. 35110, 2003.

[59] A. Yariv, *An Introduction to Theory and Applications of Quantum Mechanics*. John Wiley & Sons, Ltd., 1982.

[60] N. Zettili, *Quantum Mechanics Concepts and Applications*. John Wiley & Sons, Ltd., 2005.

.1 Transition Rates with Time-Dependent Perturbation Theory

Time-dependent perturbation theory is used to study the interaction between atomic electrons and electromagnetic radiation. The Hamiltonian in this case has two parts, a time-independent part \hat{H}_0 and a time-dependent part $\hat{H}'(t)$. The corresponding Schrödinger equation is

$$i\hbar \frac{d|\Psi(t)\rangle}{dt} = (\hat{H}_0 + \hat{H}'(t)) |\Psi(t)\rangle \quad (1)$$

where $|\Psi(t)\rangle$ can be expanded in terms of the unperturbed eigenstates $|\psi_n\rangle$ as

$$|\Psi(t)\rangle = \sum_n c_n(t) e^{-iE_n^{(0)}t/\hbar} |\psi_n\rangle \quad (2)$$

It is assumed that solutions for the time-independent Hamiltonian,

$$i\hbar \frac{d|\psi(t)\rangle}{dt} = \hat{H}_0 |\psi(t)\rangle \quad (3)$$

can be found by solving the familiar eigenvalue problem

$$\hat{H}_0 |\psi_n\rangle = E_n^{(0)} |\psi_n\rangle \quad (4)$$

where $E_n^{(0)}$ are energy eigenvalues of the unperturbed system and $|\psi_n\rangle$ are eigenstates or wavefunctions.

If at $t = 0$ the energy, E_i is measured, then the coefficients must obey

$$c_i(0) = 1 \quad c_n(0) = 0. \quad (5)$$

Because the coefficients, $c_n(t)$, are time dependent, a subsequent measurement at time, t ,

may yield a value of E_f . The probability of such an event is $|c_f(t)|^2$. This is also the probability that the system, originally in state i at $t = 0$, is now in state f after time t . Solution of the time-dependent Schrödinger equation thus describes how the probability of finding the system in state $|\psi_n\rangle$ of \hat{H}_0 evolves due to the perturbation $\hat{H}'(t)$. Before determining the effect of a specific $\hat{H}'(t)$, the coefficients, $c_n(t)$ must be found. It is assumed that $\hat{H}'(t)$ will be small so that the time dependence of $c_n(t)$ can be treated perturbatively. Traditional perturbation theory can then be used where the parameter λ is introduced to keep track of the order of smallness of the perturbation.

First, the expansion of $|\Psi(t)\rangle$ given by equation (2) is substituted into equation (1) to obtain

$$i\hbar \sum_n \left[\frac{d}{dt} c_n(t) - \frac{iE_n^{(0)}}{\hbar} c_n(t) \right] e^{-iE_n^{(0)}t/\hbar} |\psi_n\rangle = \sum_n c_n(t) e^{-iE_n^{(0)}t/\hbar} (\hat{H}_0 + \hat{H}'(t)) |\psi_n\rangle \quad (6)$$

Taking the inner product with $\langle\psi_f| e^{iE_f^{(0)}t/\hbar}$ and using (4) on the right hand side, this equation becomes

$$\frac{d}{dt} c_f(t) = -\frac{i}{\hbar} \sum_n c_n(t) e^{i(E_f^{(0)} - E_n^{(0)})t/\hbar} \langle\psi_f| \hat{H}'(t) |\psi_n\rangle \quad (7)$$

Assuming again that the system is initially in an eigenstate of the unperturbed Hamiltonian $|\psi_i\rangle$ at time $t = 0$. Then the initial condition can be written concisely as

$$c_n(0) = \delta_{ni} \quad (8)$$

Now the parameter λ can be inserted into the Hamiltonian and the coefficients $c_n(t)$ can be expanded in a power series in λ . The coefficients are written as

$$c_n(t) = c_n^{(0)} + \lambda c_n^{(1)} + \lambda^2 c_n^{(2)} + \dots \quad (9)$$

which is substituted into (7) to obtain

$$\frac{d}{dt} (c_f^{(0)} + \lambda c_f^{(1)} + \lambda^2 c_f^{(2)} + \dots) = -\frac{i}{\hbar} \sum_n (c_n^{(0)} + \lambda c_n^{(1)} + \lambda^2 c_n^{(2)} + \dots) e^{i(E_f^{(0)} - E_n^{(0)})t/\hbar} \langle \psi_f | \lambda \hat{H}'(t) | \psi_n \rangle \quad (10)$$

Terms of the same order of λ on each side of the equation must be equal. Equating terms in λ^0 , leads to

$$\frac{d}{dt} c_f^{(0)} = 0 \quad (11)$$

because there is no λ^0 term on the right hand side of (10). The initial conditions are satisfied if $c_f^{(0)} = \delta_{fi}$ and $c_n^{(k)}(0) = 0$ for $k \geq 1$. Equating terms in λ^1 , results in

$$\begin{aligned} \frac{d}{dt} c_f^{(1)}(t) &= -\frac{i}{\hbar} \sum_n c_n^{(0)}(t) e^{i(E_f^{(0)} - E_n^{(0)})t/\hbar} \langle \psi_f | \hat{H}'(t) | \psi_n \rangle \\ &= -\frac{i}{\hbar} e^{i(E_f^{(0)} - E_i^{(0)})t/\hbar} \langle \psi_f | \hat{H}'(t) | \psi_i \rangle \end{aligned} \quad (12)$$

Integrating this equation $c_f^{(1)}$ is found to be

$$c_f^{(1)} = -\frac{i}{\hbar} \int_0^t e^{i(E_f^{(0)} - E_i^{(0)})t'/\hbar} \langle \psi_f | \hat{H}'(t') | \psi_i \rangle dt' \quad (13)$$

Using the equations for $c_f^{(0)}$ and $c_f^{(1)}$, $c_f(t)$ can be written to first order as

$$c_f(t) = \delta_{fi} - \frac{i}{\hbar} \int_0^t \left(e^{i(E_f^{(0)} - E_i^{(0)})t'/\hbar} \langle \psi_f | \hat{H}'(t') | \psi_i \rangle + \dots \right) dt' \quad (14)$$

To find the probability of the transition from some initial state of the unperturbed system to a different final state we write

$$P_{if} = |c_f(t)|^2 = \left| \delta_{fi} - \frac{i}{\hbar} \int_0^t e^{i(E_f^{(0)} - E_i^{(0)})t'/\hbar} \langle \psi_f | \hat{H}'(t') | \psi_i \rangle dt' \right|^2 \quad (15)$$

But the initial and final states must be different so $\delta_{fi} = 0$ and the transition rate becomes

$$P_{if} = |c_f(t)|^2 = \left| -\frac{i}{\hbar} \int_0^t e^{i(E_f^{(0)} - E_i^{(0)})t'/\hbar} \langle \psi_f | \hat{H}'(t') | \psi_i \rangle dt' \right|^2 \quad (16)$$

This is the first order approximation for the probability of the transition.

If the perturbing potential is a harmonic function, $\hat{H}'(t') = \nu e^{i\omega t'} + \nu^\dagger e^{-i\omega t'}$, as will later be shown to be the case for electromagnetic radiation, then we can write

$$P_{if}(t) = \left| \frac{-i}{\hbar} \int_0^t \langle \psi_f | \nu e^{i\omega t'} + \nu^\dagger e^{-i\omega t'} | \psi_i \rangle e^{i\omega_{fi}t'} dt' \right|^2 \quad (17)$$

After evaluating the integral and taking the magnitude, P_{if} becomes

$$P_{if}(t) = \frac{1}{\hbar^2} \left[\left| \langle \psi_f | \nu | \psi_i \rangle \right|^2 \left| \frac{e^{i(\omega_{fi} + \omega)t} - 1}{\omega_{fi} + \omega} \right|^2 + \left| \langle \psi_f | \nu^\dagger | \psi_i \rangle \right|^2 \left| \frac{e^{i(\omega_{fi} - \omega)t} - 1}{\omega_{fi} - \omega} \right|^2 \right] \quad (18)$$

To obtain this equation the cross terms were ignored because they will go to 0 as the time goes to infinity. Using $|e^{i\Theta} - 1|^2 = 4\sin^2(\Theta/2)$, the equation for the probability becomes

$$P_{if}(t) = \frac{4}{\hbar^2} \left[\left| \langle \psi_f | \nu | \psi_i \rangle \right|^2 \frac{\sin^2((\omega_{fi} + \omega)t/2)}{(\omega_{fi} + \omega)^2} + \left| \langle \psi_f | \nu^\dagger | \psi_i \rangle \right|^2 \frac{\sin^2((\omega_{fi} - \omega)t/2)}{(\omega_{fi} - \omega)^2} \right] \quad (19)$$

As the time goes to infinity the following relation results

$$\lim_{t \rightarrow \infty} \frac{\sin^2(yt)}{\pi y^2 t} = \delta(y) \quad (20)$$

Using this identity in (19) and multiplying by the necessary factors, the probability of a transition becomes

$$P_{if}(t) = \frac{2\pi t}{\hbar} \left| \langle \psi_f | \nu | \psi_i \rangle \right|^2 \delta(E_f - E_i + \hbar\omega) + \frac{2\pi t}{\hbar} \left| \langle \psi_f | \nu^\dagger | \psi_i \rangle \right|^2 \delta(E_f - E_i - \hbar\omega) \quad (21)$$

The transition rate is the transition probability per unit time and it can be written as

$$\Gamma_{if} = \frac{dP_{if}(t)}{dt} = \frac{2\pi}{\hbar} |\langle \psi_f | \nu | \psi_i \rangle|^2 \delta(E_f - E_i + \hbar\omega) + \frac{2\pi}{\hbar} |\langle \psi_f | \nu^\dagger | \psi_i \rangle|^2 \delta(E_f - E_i - \hbar\omega) \quad (22)$$

The transition rate is then only non-zero when $E_f - E_i = \hbar\omega$ or $E_i - E_f = \hbar\omega$. These conditions can not be met simultaneously. The first case corresponds to the final energy being higher than the initial energy and when acted on by the perturbation, a photon is absorbed. When the initial energy is higher than the final energy, as in the second condition, a photon is emitted. The transition rate for photon emission is

$$\Gamma_{if}^{emiss} = \frac{2\pi}{\hbar} |\langle \psi_f | \nu | \psi_i \rangle|^2 \delta(E_f - E_i + \hbar\omega) \quad (23)$$

So far only the general form for the transition rate in a harmonic potential is presented. The next step is to derive the precise form of the perturbing potential corresponding to an electromagnetic field and to show that it is of harmonic form. Consider a system in bulk that obeys the time-independent Schrödinger equation given in equation (3). Introducing an electric field with potential $\phi(\vec{r}, t) = -\int E(r, t) dr$ will increase the energy of the system by $|q|\phi(\vec{r}, t)$ where q is the charge on an electron. The time-independent Schrödinger equation becomes

$$i\hbar \frac{d|\Psi(t)\rangle}{dt} = (\hat{H}_0 - q\phi(\vec{r}, t)) |\Psi(t)\rangle. \quad (24)$$

In addition to the scalar potential introduced by the presence of the electric field, there is a corresponding vector potential due to the magnetic field. To account for the magnetic vector potential $\vec{A}(\vec{r}, t)$, equation (24) can be rewritten as

$$i\hbar \frac{d|\Psi(t)\rangle}{dt} + q\phi(\vec{r}, t) |\Psi(t)\rangle = \left(\frac{-\hbar^2}{2m_e} \nabla^2 + V(\vec{r}) \right) |\Psi(t)\rangle \quad (25)$$

where the substitution

$$H_0 = \frac{\vec{P}^2}{2m_e} + V(\vec{r}) = \frac{-\hbar^2}{2m_e} \nabla^2 + V(\vec{r}) \quad (26)$$

was made. The energy due to the magnetic vector potential can now be added to the right hand side of equation (25),

$$i\hbar \frac{d|\Psi(t)\rangle}{dt} + q\phi(\vec{r}, t) |\Psi(t)\rangle = \left(\frac{1}{2m_e} ((-i\hbar \vec{\nabla} + qA) \cdot (-i\hbar \vec{\nabla} + qA)) + V(\vec{r}) \right) |\Psi(t)\rangle \quad (27)$$

$$= \left(\frac{1}{2m_e} (\vec{P}^2 + q^2 A^2 + qA \cdot -i\hbar \vec{\nabla} - i\hbar \vec{\nabla} \cdot qA) + V(\vec{r}) \right) |\Psi(t)\rangle \quad (28)$$

$$= \left(\frac{\vec{P}^2}{2m_e} + \frac{q^2 A^2}{2m_e} + \frac{q}{2m_e} A \cdot \vec{P} + \frac{q}{2m_e} \vec{P} \cdot A + V(\vec{r}) \right) |\Psi(t)\rangle \quad (29)$$

When electromagnetic radiation with magnetic vector potential $\vec{A}(\vec{r}, t)$ and electric potential $\phi(\vec{r}, t)$ is applied to an atom the Hamiltonian describing the interaction of the electron and the radiation is then given by

$$H = H_0 + \frac{q^2 A^2}{2m_e} + \frac{q}{2m_e} A \cdot \vec{P} + \frac{q}{2m_e} \vec{P} \cdot A - q\phi(\vec{r}, t) \quad (30)$$

We will assume that there are no electrostatic sources so that $\phi(\vec{r}, t) = 0$. It is also valid to ignore the \vec{A}^2 term because it is smaller than the other terms by a factor of $q \approx E^{-19}$. Using the Coulomb gauge, $\nabla \cdot \vec{A} = 0$, the Hamiltonian can be simplified to

$$H = H_0 + \frac{q}{2m_e} \vec{A}(\vec{r}, t) \cdot \vec{P} = H_0 + \hat{H}'(t) \quad (31)$$

which is precisely the form of the Hamiltonian that was assumed when the time-dependent perturbation theory was developed earlier. The perturbation Hamiltonian in the presence

of an electromagnetic field is

$$\hat{H}'(t) = \frac{q}{2m_e} \vec{A}(\vec{r}, t) \cdot \vec{P}. \quad (32)$$

To determine the spontaneous emission lifetime, the field must be quantized. This means that the magnetic vector potential must be replaced with an operator. The process is similar to quantization of a classical harmonic oscillator and the electromagnetic field will be written in terms of creation and annihilation operators. First, the vector potential is expanded in a Fourier series

$$\vec{A}(\vec{r}, t) = \frac{1}{\sqrt{V}} \sum_k \sum_{\lambda=1}^2 \left[A_{\lambda,k} \vec{\epsilon}_\lambda e^{i(\vec{k} \cdot \vec{r} - \omega_k t)} + A_{\lambda,k}^* \vec{\epsilon}_\lambda^* e^{-i(\vec{k} \cdot \vec{r} - \omega_k t)} \right]. \quad (33)$$

The corresponding electric field, found through solution of

$$E(\vec{r}, t) = -\frac{\partial \vec{A}(\vec{r}, t)}{\partial t}, \quad (34)$$

can be written as

$$E = \frac{-1}{\sqrt{\epsilon V}} \sum_k \sum_{\lambda=1}^2 i\omega_k \sqrt{\epsilon} \left[A_{\lambda,k} \vec{\epsilon}_\lambda e^{i(\vec{k} \cdot \vec{r} - \omega_k t)} - A_{\lambda,k}^* \vec{\epsilon}_\lambda^* e^{-i(\vec{k} \cdot \vec{r} - \omega_k t)} \right]. \quad (35)$$

Similarly, the magnetic field can be found through solution of

$$H = \frac{1}{\mu} \nabla \times \vec{A}(\vec{r}, t) \quad (36)$$

as

$$H = \frac{1}{\sqrt{\mu V}} \sum_k \sum_{\lambda=1}^2 i\omega_k \sqrt{\epsilon} \left[A_{\lambda,k} (\vec{k} \times \vec{\epsilon}_\lambda) e^{i(\vec{k} \cdot \vec{r} - \omega_k t)} - A_{\lambda,k}^* (\vec{k} \times \vec{\epsilon}_\lambda^*) e^{-i(\vec{k} \cdot \vec{r} - \omega_k t)} \right]. \quad (37)$$

Introducing a set of variables, $P_{\lambda,k}$ and $Q_{\lambda,k}$, $A_{\lambda,k}$ and $A_{\lambda,k}^*$ can be written as a conjugate

pair,

$$A_{\lambda,k} = \frac{1}{2\sqrt{\epsilon}}Q_{\lambda,k} + \frac{i}{2\omega\sqrt{\epsilon}}P_{\lambda,k} \quad A_{\lambda,k}^* = \frac{1}{2\sqrt{\epsilon}}Q_{\lambda,k} - \frac{i}{2\omega\sqrt{\epsilon}}P_{\lambda,k}. \quad (38)$$

Substitution of equation (38) into equations (35) and (37) yield the following equations for the electric and magnetic field

$$E = \frac{-i}{\sqrt{4\epsilon V}} \sum_k \sum_{\lambda=1}^2 \omega_k \left[\left(Q_{\lambda,k} + \frac{i}{\omega_k} P_{\lambda,k} \right) \vec{\epsilon}_\lambda e^{i(\vec{k}\cdot\vec{r}-\omega_k t)} - \left(Q_{\lambda,k} - \frac{i}{\omega_k} P_{\lambda,k} \right) \vec{\epsilon}_\lambda^* e^{-i(\vec{k}\cdot\vec{r}-\omega_k t)} \right]. \quad (39)$$

$$H = \frac{i}{\sqrt{4\mu V}} \sum_k \sum_{\lambda=1}^2 \omega_k \left[\left(Q_{\lambda,k} + \frac{i}{\omega_k} P_{\lambda,k} \right) (\vec{k} \times \vec{\epsilon}_\lambda) e^{i(\vec{k}\cdot\vec{r}-\omega_k t)} - \left(Q_{\lambda,k} - \frac{i}{\omega_k} P_{\lambda,k} \right) (\vec{k} \times \vec{\epsilon}_\lambda^*) e^{-i(\vec{k}\cdot\vec{r}-\omega_k t)} \right] \quad (40)$$

which can be simplified to

$$E = \frac{-1}{\sqrt{4\epsilon V}} \sum_k \sum_{\lambda=1}^2 \left[(i\omega_k Q_{\lambda,k} - P_{\lambda,k}) \vec{\epsilon}_\lambda e^{i(\vec{k}\cdot\vec{r}-\omega_k t)} - (i\omega_k Q_{\lambda,k} + P_{\lambda,k}) \vec{\epsilon}_\lambda^* e^{-i(\vec{k}\cdot\vec{r}-\omega_k t)} \right]. \quad (41)$$

$$H = \frac{1}{\sqrt{4\mu V}} \sum_k \sum_{\lambda=1}^2 \left[(i\omega_k Q_{\lambda,k} - P_{\lambda,k}) (\vec{k} \times \vec{\epsilon}_\lambda) e^{i(\vec{k}\cdot\vec{r}-\omega_k t)} - (i\omega_k Q_{\lambda,k} + P_{\lambda,k}) (\vec{k} \times \vec{\epsilon}_\lambda^*) e^{-i(\vec{k}\cdot\vec{r}-\omega_k t)} \right]. \quad (42)$$

The energy density of the electromagnetic field is

$$H_r = \int d^3r \left(\frac{1}{2} \epsilon |\vec{E}(\vec{r}, t)|^2 + \frac{1}{2} \mu |\vec{H}(\vec{r}, t)|^2 \right). \quad (43)$$

Substitution of equation (41) and (42) into (43) and simplifying results in an energy density of

$$H_r = \int d^3r \frac{1}{4V} \sum_k \sum_{\lambda=1}^2 |i\omega_k Q_{\lambda,k} - P_{\lambda,k}|^2 + |i\omega_k Q_{\lambda,k} + P_{\lambda,k}|^2 = \sum_k \sum_{\lambda=1}^2 \frac{1}{2} |P_{\lambda,k}|^2 + \frac{\omega_k^2}{2} |Q_{\lambda,k}|^2 \quad (44)$$

where we have used the fact that ϵ_λ is normalized to 1 such that, $|\epsilon_\lambda|^2 = \epsilon_\lambda \cdot \epsilon_\lambda^* = 1$. This equation has a striking similarity to the Hamiltonian of a harmonic oscillator, which is

expressed as

$$H_{ho} = \frac{\vec{p}^2}{2m_e} + \frac{1}{2}\omega^2 m_e \vec{x}^2 \quad (45)$$

where m_e is the mass of the electron, \vec{p} is the momentum and \vec{x} is the position [1]. If $m_e = 1$, $\vec{p} = P_{\lambda,k}$, and $\vec{x} = Q_{\lambda,k}$, then Equation 44 is just an infinite sum of independent harmonic oscillators. This analogy allows us to proceed with the quantization of the electromagnetic fields by determining the appropriate operator representation for $Q_{\lambda,k}$ and $P_{\lambda,k}$ through the introduction of raising and lowering operators. The procedure is the same as that used for the harmonic oscillator where the momentum and position operators become

$$\vec{x} = \sqrt{\frac{\hbar}{2m_e\omega}}(a^\dagger + a) \quad (46)$$

and

$$p_{ho} = i\sqrt{\frac{\hbar m_e \omega}{2}}(a^\dagger - a) \quad (47)$$

where a^\dagger is the raising operator and a is the lowering operator.

The operators, $\hat{Q}_{\lambda,k}$ and $\hat{P}_{\lambda,k}$, will obey the canonical commutation relation given by

$$[\hat{Q}_{\lambda_1,k_1}, \hat{P}_{\lambda_2,k_2}] = i\hbar\delta_{\lambda_1\lambda_2}\delta_{k_1k_2} \quad (48)$$

The raising and lowering operators are then defined as

$$\hat{a}_{\lambda,k}^\dagger = \sqrt{\frac{\omega_k}{2\hbar}}\hat{Q}_{\lambda k} - \frac{i}{\sqrt{2\hbar\omega}}\hat{P}_{\lambda k}, \quad \hat{a}_{\lambda,k} = \sqrt{\frac{\omega_k}{2\hbar}}\hat{Q}_{\lambda k} + \frac{i}{\sqrt{2\hbar\omega}}\hat{P}_{\lambda k} \quad (49)$$

Writing $\hat{Q}_{\lambda,k}$ and $\hat{P}_{\lambda,k}$ in terms of the raising and lowering operators we have

$$\hat{Q}_{\lambda k} = \sqrt{\frac{\hbar}{2\omega_k}}(\hat{a}_{\lambda,k}^\dagger + \hat{a}_{\lambda,k}), \quad \hat{P}_{\lambda k} = i\sqrt{\frac{\hbar\omega_k}{2}}(\hat{a}_{\lambda,k}^\dagger - \hat{a}_{\lambda,k}) \quad (50)$$

Substitution into the Hamiltonian operator for the electromagnetic field, equation (44),

gives

$$\hat{H}_r = \sum_k \sum_{\lambda=1}^2 \frac{\omega_k^2}{2} \frac{\hbar}{2\omega_k} (a + a^\dagger)^2 - \frac{1}{2} \frac{\hbar\omega_k}{2} (a^\dagger - a)^2 \quad (51)$$

$$= \sum_k \sum_{\lambda=1}^2 \frac{\hbar\omega_k}{4} (aa + aa^\dagger + a^\dagger a + a^\dagger a^\dagger - (a^\dagger a^\dagger - a^\dagger a - aa^\dagger + aa)) \quad (52)$$

$$= \sum_k \sum_{\lambda=1}^2 \frac{\hbar\omega_k}{2} (aa^\dagger + a^\dagger a - a^\dagger a + a^\dagger a) \quad (53)$$

$$= \sum_k \sum_{\lambda=1}^2 \hbar\omega_k \left(a^\dagger a + \frac{1}{2} \right) \quad (54)$$

$$= \sum_k \sum_{\lambda=1}^2 \hbar\omega_k \left(\hat{N} + \frac{1}{2} \right) \quad (55)$$

The raising and lowering operators act on the state of the electromagnetic field to either create or annihilate a photon, respectively. If the electromagnetic field is in a state $|n_{\lambda k}\rangle$ the result of the raising and lowering operators are

$$\hat{a}_{\lambda k}^\dagger |n_{\lambda k}\rangle = \sqrt{n_{\lambda k} + 1} |n_{\lambda k} + 1\rangle \quad (56)$$

$$\hat{a}_{\lambda k} |n_{\lambda k}\rangle = \sqrt{n_{\lambda k}} |n_{\lambda k} - 1\rangle \quad (57)$$

This means that operating on a state of the electromagnetic field with $\hat{N} = a^\dagger a$ gives the number of photons in that state. The eigenstates of the Hamiltonian of the electromagnetic field are then given by

$$|n_{\lambda_1 k_1}, n_{\lambda_2 k_2}, \dots\rangle = \prod_j |n_{\lambda_j k_j}\rangle \quad (58)$$

and the energy eigenvalues are

$$E_r = \sum_k \sum_{\lambda=1}^2 \hbar\omega_k \left(n_{\lambda k} + \frac{1}{2} \right) \quad (59)$$

The operators corresponding to the Fourier coefficients of the vector potential can be

found by substituting equation (50) into equation (38). The result is

$$\hat{A}_{\lambda k} = \sqrt{\frac{\hbar}{2\omega_k \epsilon}} \hat{a}_{\lambda k} \quad \hat{A}_{\lambda k}^* = \sqrt{\frac{\hbar}{2\omega_k \epsilon}} \hat{a}_{\lambda k}^\dagger \quad (60)$$

Substitution of these equations into (33) gives the vector potential operator

$$\hat{\vec{A}}(\vec{r}, t) = \sum_k \sum_{\lambda=1}^2 \sqrt{\frac{\hbar}{2\omega_k \epsilon V}} \left(\vec{\epsilon}_\lambda \hat{a}_{\lambda k} e^{i(\vec{k} \cdot \vec{r} - \omega_k t)} + \vec{\epsilon}_\lambda^* \hat{a}_{\lambda k}^\dagger e^{-i(\vec{k} \cdot \vec{r} - \omega_k t)} \right) \quad (61)$$

Using the expression for $\hat{H}'(t)$ found in equation (32), the perturbing potential from the quantized electromagnetic field is

$$\hat{H}'(t) = \frac{q}{m_e} \hat{\vec{A}} \cdot \vec{P} = \sum_k \sum_{\lambda=1}^2 \sqrt{\frac{\hbar}{2\omega_k V \epsilon}} \frac{q}{m_e} \left(\hat{a}_{\lambda k} e^{i\vec{k} \cdot \vec{r}} \vec{\epsilon}_\lambda \cdot \vec{P} e^{-i\omega_k t} + \hat{a}_{\lambda k}^\dagger e^{-i\vec{k} \cdot \vec{r}} \vec{\epsilon}_\lambda^* \cdot \vec{P} e^{i\omega_k t} \right) \quad (62)$$

which takes the form of a harmonic potential.

$$\hat{H}'(t) = \sum_k \sum_{\lambda=1}^2 \left(\nu_{\lambda k}^\dagger e^{-i\omega_k t} + \nu_{\lambda k} e^{i\omega_k t} \right) \quad (63)$$

Recall from equation (23) that the emission rate due to a harmonic perturbation can be written as

$$\Gamma_{if}^{emiss} = \frac{2\pi}{\hbar} |\langle \Phi_f | \nu | \Phi_i \rangle|^2 \delta(E_f - E_i + \hbar\omega) \quad (64)$$

The initial and final states can be written as a combination of the electron state and the electromagnetic field state so that $|\Phi_i\rangle = |\psi_i\rangle |n_{\lambda k}\rangle$ and $|\Phi_f\rangle = |\psi_f\rangle |n_{\lambda k} + 1\rangle$. This leads to

$$\langle \Phi_f | \nu | \Phi_i \rangle = \langle \psi_f | \langle n_{\lambda k} + 1 | \sqrt{\frac{\hbar}{2\omega_k V \epsilon}} \frac{q}{m_e} e^{-i\vec{k} \cdot \vec{r}} \vec{\epsilon}_{\lambda k}^* \cdot \vec{P} \hat{a}_{\lambda k}^\dagger | n_{\lambda k} \rangle | \psi_i \rangle \quad (65)$$

$$= \sqrt{\frac{\hbar}{2\omega_k V \epsilon}} \frac{q}{m_e} \langle \psi_f | e^{-i\vec{k} \cdot \vec{r}} \vec{\epsilon}_{\lambda k}^* \cdot \vec{P} | \psi_i \rangle \langle n_{\lambda k} + 1 | \hat{a}_{\lambda k}^\dagger | n_{\lambda k} \rangle \quad (66)$$

Using equation (56) we find

$$\langle \Phi_f | \nu | \Phi_i \rangle = \sqrt{\frac{\hbar}{2\omega_k V \epsilon}} \frac{q}{m_e} \sqrt{n_{\lambda k} + 1} \langle \psi_f | e^{-i\vec{k}\cdot\vec{r}} \vec{\epsilon}_{\lambda k}^* \cdot \vec{P} | \psi_i \rangle. \quad (67)$$

Substitution of this result into (64) gives

$$\Gamma_{if}^{emiss} = \frac{\pi q^2}{m_e^2 \omega_k V \epsilon} (n_{\lambda k} + 1) \left| \langle \psi_f | e^{-i\vec{k}\cdot\vec{r}} \vec{\epsilon}_{\lambda k}^* \cdot \vec{P} | \psi_i \rangle \right|^2 \delta(E_f - E_i + \hbar\omega_k) \quad (68)$$

For spontaneous emission, the number of photons is initially 0 so $n_{\lambda k} = 0$. The spontaneous emission rate therefore is given by

$$\Gamma_{if}^{spon} = \frac{\pi q^2}{m_e^2 \omega_k V \epsilon} \left| \langle \psi_f | e^{-i\vec{k}\cdot\vec{r}} \vec{\epsilon}_{\lambda k}^* \cdot \vec{P} | \psi_i \rangle \right|^2 \delta(E_f - E_i + \hbar\omega_k) \quad (69)$$

To find approximate solutions for this equation, it is convenient to expand the exponential $e^{-i\vec{k}\cdot\vec{r}}$.

$$e^{-i\vec{k}\cdot\vec{r}} = 1 \pm i\vec{k}\cdot\vec{r} - \frac{1}{2}(\vec{k}\cdot\vec{r})^2 \mp \dots \quad (70)$$

Typically this approximation is used for the case of an atomic electron where the term, $\vec{k}\cdot\vec{r}$, will be small because the wavelength is much larger than the atom. This is also applicable to quantum dots which are $\approx 10 - 20nm$. In this case the term will be on the order of $kr = 2\pi d/\lambda = 2\pi \times 10^{-9}/10^{-6} \approx 10^{-3}$ and $e^{-i\vec{k}\cdot\vec{r}} \approx 1$. Using this electric dipole approximation we obtain

$$\langle \psi_f | e^{-i\vec{k}\cdot\vec{r}} \vec{\epsilon}_{\lambda k}^* \cdot \vec{P} | \psi_i \rangle = \vec{\epsilon}_{\lambda k}^* \cdot \langle \psi_f | \vec{P} | \psi_i \rangle \quad (71)$$

This can be simplified further by using the commutator relationships of the position oper-

ator and the unperturbed Hamiltonian. Specifically

$$[\hat{X}, \hat{H}_0] = \left[\hat{X}, \frac{\hat{P}^2}{2m_e} + \vec{V}(r) \right] = \left[\hat{X}, \frac{\hat{P}_X^2}{2m_e} \right] = \frac{i\hbar}{m_e} \hat{P}_X \quad (72)$$

which can be generalized to $[\hat{r}, \hat{H}_0] = \frac{i\hbar}{m_e} \hat{P}$. Using this in (71) we obtain

$$\vec{\epsilon}_{\lambda k}^* \cdot \langle \psi_f | \vec{P} | \psi_i \rangle = \vec{\epsilon}_{\lambda k}^* \cdot \langle \psi_f | \frac{m_e}{i\hbar} [\hat{r}, \hat{H}_0] | \psi_i \rangle \quad (73)$$

$$= \vec{\epsilon}_{\lambda k}^* \cdot \langle \psi_f | \frac{m_e}{i\hbar} (\hat{r} \hat{H}_0 - \hat{H}_0 \hat{r}) | \psi_i \rangle \quad (74)$$

$$= \frac{m_e}{i\hbar} \vec{\epsilon}_{\lambda k}^* \cdot (E_i \langle \psi_f | \hat{r} | \psi_i \rangle - E_f \langle \psi_f | \hat{r} | \psi_i \rangle) \quad (75)$$

$$= im_e \omega_{fi} \vec{\epsilon}_{\lambda k}^* \cdot \langle \psi_f | \hat{r} | \psi_i \rangle \quad (76)$$

with $\omega_{fi} = (E_f - E_i)/\hbar$. Using these approximations the spontaneous emission rate becomes

$$\Gamma_{if}^{spon} = \frac{\pi}{\omega V \varepsilon} \omega_{fi}^2 |\vec{\epsilon}_{\lambda k}^* \cdot \langle \psi_f | (-q\hat{r}) | \psi_i \rangle|^2 \delta(E_f - E_i + \hbar\omega) \quad (77)$$

$$= \frac{\pi}{\omega V \varepsilon} \omega_{fi}^2 |\vec{\epsilon}_{\lambda k}^* \cdot \vec{d}_{fi}|^2 \delta(E_f - E_i + \hbar\omega) \quad (78)$$

where $\vec{d}_{fi} = -q \langle \psi_f | \hat{r} | \psi_i \rangle$ is the dipole matrix element. The total transition rate is found by summing the transition rate (78) over the final photonic states.

$$W_{i \rightarrow f}^{spon} = \int \Gamma_{if}^{spon} \rho(\omega) d\omega \quad (79)$$

$$= \int \frac{\pi}{\omega V \varepsilon} \omega_{fi}^2 |\vec{\epsilon}_{\lambda k}^* \cdot \vec{d}_{fi}|^2 \delta(E_f - E_i + \hbar\omega) \rho(\omega) d\omega \quad (80)$$

$$= \int \frac{\pi}{\omega V \varepsilon \hbar} \omega_{fi}^2 |\vec{\epsilon}_{\lambda k}^* \cdot \vec{d}_{fi}|^2 \delta(\omega_{if} - \omega) \rho(\omega) d\omega \quad (81)$$

$$= \frac{\pi}{\varepsilon \hbar} \omega_{fi} |\vec{\epsilon}_{\lambda k}^* \cdot \vec{d}_{fi}|^2 \rho(\omega_{if}) \quad (82)$$

The density of photonic states $\rho(\omega_{if})$ is dependent on the surrounding environment of the emitter. For a quantum dot in a photonic crystal microcavity, $\rho(\omega_{if}) = \rho_C(\omega_{if})$, which is

the density of photon modes in the cavity. Solution of equation (82) gives the spontaneous transition rate.

As an example, consider the spontaneous transition rate into some bulk material with refractive index, n . The density of modes per unit frequency per unit volume in bulk is given by

$$\rho_b(\omega) = \frac{2\omega^2 n^3}{\pi c^3} \quad (83)$$

Substitution of equation (83) into (82) then gives

$$W_{i \rightarrow f}^{bulk} = \frac{2n}{\hbar c^3} \omega^3 |\vec{\epsilon}_{\lambda k}^* \cdot \vec{d}_{fi}|^2 \quad (84)$$

This expression is valid only for a single polarization, because $\vec{\epsilon}_{\lambda k}^*$ has a specific value for the chosen k . By summing over the two possible polarizations of the photon, it is possible to obtain an expression for the transition rate corresponding to any polarization [2]. Averaging over the polarizations gives

$$\sum_{\lambda=1}^2 |\vec{\epsilon}_{\lambda k}^* \cdot \vec{d}_{fi}|^2 = \frac{2}{3} |\vec{d}_{fi}|^2 \quad (85)$$

Substitution of equation (85) into (84) gives

$$W_{i \rightarrow f}^{bulk} = \frac{4n\omega^3}{3\hbar c^3} |\vec{d}_{fi}|^2 \quad (86)$$

Similarly, we can determine the spontaneous transition rate into a cavity. In a cavity the density of modes per unit volume is

$$\rho_c(\omega) = \frac{1}{\Delta\omega} \quad (87)$$

The mode is considered to be non-degenerate in this case. Substituting this expression

directly into equation (82) the transition rate becomes

$$W_{i \rightarrow f}^{cavity} = \frac{\pi}{\hbar \varepsilon} \omega_{fi} |\vec{\epsilon}_{\lambda k}^* \cdot \vec{d}_{fi}|^2 \frac{1}{\Delta \omega} \quad (88)$$

Rearranging the terms of equation (88), the equation for the transition rate becomes

$$W_{i \rightarrow f}^{cavity} = \frac{\pi}{\hbar^2 \Delta \omega} \left(\frac{\hbar \omega_{fi}}{\varepsilon} |\vec{\epsilon}_{\lambda k}^* \cdot \vec{d}_{fi}|^2 \right) \quad (89)$$

For emission into bulk, we were able to simply average $|\vec{\epsilon}_{\lambda k}^* \cdot \vec{d}_{fi}|^2$ over the two polarizations. In the case of emission into a cavity, the value of $|\vec{\epsilon}_{\lambda k}^* \cdot \vec{d}_{fi}|^2$ will depend on the profile of the mode with frequency ω_{fi} and we write

$$\sum_{\lambda=1}^2 \frac{\hbar \omega_{fi}}{\varepsilon} |\vec{\epsilon}_{\lambda k}^* \cdot \vec{d}_{fi}|^2 = 8 |\vec{d}_{fi}|^2 |\alpha E_{max}|^2 \quad (90)$$

The factor of $\hbar \omega_{fi}$ is necessary for correct dimensions, E_{max} is the maximum electric field of the mode, and α is the field normalization factor [3]

$$\alpha^2 = \frac{\hbar \omega_{fi}}{2 \int \varepsilon(r) E^2(r) d^3 r} \quad (91)$$

Substituting equation (90) into (89) the transition rate for emission into a microcavity becomes

$$W_{i \rightarrow f}^{cavity} = \frac{8\pi}{\hbar^2 \Delta \omega} |\vec{d}_{fi}|^2 |\alpha E_{max}|^2 \quad (92)$$

Bibliography

- [1] A. Yariv, *An Introduction to Theory and Applications of Quantum Mechanics*. John Wiley & Sons, Ltd., 1982.
- [2] N. Zettili, *Quantum Mechanics Concepts and Applications*. John Wiley & Sons, Ltd., 2005.
- [3] M. Boroditsky, R. Vrijen, T. Krauss, R. Coccioli, R. Bhat, and E. Yablonovitch, “Spontaneous emission extraction and purcell enhancement from thin-film 2-d photonic crystals,” *J. Lightwave Technol*, vol. 17, pp. 2096–2112, 1999.